Transparent Silver Nanowire Bottom Electrodes in Organic Solar Cells

Dissertation
zur Erlangung des wissenschaftlichen Grades
Doctor rerum naturalium
(Dr. rer. nat.)

vorgelegt von

Jan Ludwig Bormann
geboren am 29. Juni 1985 in Erfurt

– IAPP –
Dresden Integrated Center for Applied Physics and Photonic Materials

Technische Universität Dresden

2016

Dissertation eingereicht: 13. Juli 2016
Verteidigung absolviert: 25. November 2016

1. Gutachter: Prof. Dr. Karl Leo
2. Gutachter: Prof. Dr. Frank Nüesch

Abstract

Organic solar cells (OSCs) is an emerging photovoltaic technology that opens up new application areas where common inorganic techniques are not able to score. Some of those key features are flexibility, light weight, semitransparency, and low cost processing. The current industry-standard for the transparent electrode, indium tin oxide (ITO), cannot provide these properties because it is brittle and expensive. This thesis aims to investigate an alternative type of promising transparent electrode: silver nanowire (AgNW) networks. They exhibit similar or even better optical and electrical performance than ITO down to a sheet resistance of $12\,\Omega/\square$ at 84 % transmission (including the glass substrate). Furthermore, AgNWs are more flexible, solution-processable, and more cost-effective than ITO. However, two challenges occur during implementation as bottom electrode in OSCs. First, their inherently high roughness causes devices to shunt. Second, the AgNW network structure exhibits – in contrast to the continuous ITO – μm^2-sized voids that have to be bridged electrically by the organic layers.

In the first part of this thesis, solution-processed small molecule charge transport layers are investigated. In the case of hole transport layers (HTL), the host BF-DPB and the dopant NDP9 are investigated using tetrahydrofuran as a solvent. It is shown that BF-DPB is already doped by NDP9 in solution via the formation of a hybrid molecule complex. Solution-processed layers exhibit similar conductivities as compared to the reference deposition, which is thermal evaporation in high vacuum. The layers sufficiently smoothen the AgNW electrode such that DCV5T-Me:C_{60} organic solar cells with an efficiency up to 4.4 % are obtained. Moreover, the influence of the square micrometer large network voids is investigated using HTLs of varying conductivity. As a result, a minimum conductivity of 1×10^{-4} S/cm is needed to avoid macroscopic performance losses. Equivalent circuit simulations are performed to confirm these results.

As a second planarization method, the AgNWs are buried in an insulating polymer that serves concurrently as flexible and ultrathin substrate. Out of three different polymers tested, the optical adhesive 'NOA63' gives the best results. The roughness is strongly reduced from 30 nm down to (2 ± 1) nm. Two different OSC types are employed as testing devices with fully-flexible alumina encapsulation against moisture ingress. Maximum power conversion efficiencies of 5.0 % and 5.6 % are achieved with a fullerene-free cascade layer architecture and a DCV5T-Me:C_{60} OSC, respectively.

To evaluate the applicability of these fully-flexible and encapsulated devices, degradation studies are performed under continuous illumination and a humid climate. Although employing the intrinsically stable DCV5T-Me:C_{60} stack design, within one day a fast degradation of the fully-flexible solar cells is observed. The degradation is attributed to AgNW electrode failure that results from photo-oxidation and -sulfurization, photo-migration, and electromigration. It is further shown that the cascade organic solar cell lacks intrinsic stability.

In summary, efficient, fully-flexible, and encapsulated devices are shown. However, in terms of competitive OSCs, the low stability of AgNW electrodes is a challenge to be taken care of. In current research, this issue needs to be addressed more frequently.

Kurzdarstellung

Organische Solarzellen (OSZ) sind ein junges Forschungsgebiet der Photovoltaik, welches neue Anwendungsgebiete erschließt, für die herkömmliche anorganische Solarzellen nicht einsetzbar sind. Einige der Haupteigenschaften sind Flexibilität, niedriges Gewicht, Teiltransparenz und geringe Herstellungskosten. Indiumzinnoxid (ITO), der aktuelle Industriestandard transparenter Elektrodentechnologie, ist nicht in der Lage, diese Eigenschaften zu gewährleisten. Dies liegt vor allem an der Brüchigkeit von ITO und der begrenzten Verfügbarkeit von Indium, welche mit einem hohen Preis einhergeht.
Das Ziel dieser Dissertation ist die Integration einer alternativen und vielversprechenden Elektrodentechnologie: Netzwerke aus Silbernanodrähten (AgNWs). Mit einem Schichtwiderstand von $12\,\Omega/\Box$ bei einer Transmission von 84 % (inklusive Glassubstrat) besitzen sie ähnliche oder sogar bessere optische und elektrische Eigenschaften als ITO. Des Weiteren sind AgNW-Elektroden flexibler und kostengünstiger als ITO und aus flüssiger Phase prozessierbar. Es gibt allerdings zwei Herausforderungen, welche die Integration als Grundelektrode in OSZ erschweren. Zum einen sind AgNW-Netzwerke sehr rauh, sodass organische Bauteile kurzgeschlossen werden. Zum anderen weisen AgNW-Elektroden, im Gegensatz zu einer vollflächigen ITO-Schicht, Lücken zwischen den einzelnen Drähten auf. Diese Lücken müssen von den organischen Schichten der OSZ elektrisch überbrückt werden.

Im ersten Teil der Arbeit werden daher flüssigprozessierte Ladungsträgertransportschichten aus kleinen Molekülen untersucht, welche die AgNW-Elektroden glätten und die verhältnismäßig großen Lücken füllen sollen. Im Falle von Lochleitschichten (HTL) wird BF-DPB als Matrix und NDP9 als Dotand in Tetrahydrofuran gelöst und zur Anwendung gebracht. BF-DPB wird dabei schon in Lösung von NDP9 dotiert, wobei sich ein Hybridmolekülkomplex ausbildet. Die Leitfähigkeit der entstehenden Schichten ist ähnlich zu Referenzschichten, die durch thermisches Verdampfen im Hochvakuum hergestellt wurden. Die erhaltenen HTLs glätten die AgNW-Elektroden, sodass DCV5T-Me:C_{60}-Solarzellen mit einer Effizienz von maximal 4.4 % hergestellt werden können. Weiterhin wird der Einfluss der quadratmikrometergroßen Löcher auf die makroskopische Effizienz der Solarzelle in Abhängigkeit der HTL Leitfähigkeit untersucht. Um signifikante Effizienzverluste zu verhindern, muss der HTL eine minimale Leitfähigkeit von etwa 1×10^{-4} S/cm aufweisen. Simulationen eines Ersatzschaltkreises bestätigen hierbei die experimentellen Ergebnisse.

Im zweiten Teil der Arbeit wird eine Planarisierungsmethode untersucht, in welcher die AgNWs in nichtleitfähigen Polymeren eingebettet werden. Diese Polymere fungieren anschließend als flexibles Substrat. Der optische Kleber "NOA63" erzielt hierbei die besten Ergebnisse. Die Rauheit der AgNW-Elektroden wird von etwa 30 nm auf 1 bis 3 nm stark reduziert. Anschließend werden diese AgNW-Elektroden in zwei unterschiedlichen OSZ-Konfigurationen getestet und mit einer vollflexiblen Schicht aus Aluminiumoxid gegen Wasserdampfpermeation verkapselt. Somit können maximale Effizienzen von 5 % mithilfe einer organischen Kaskadenstruktur und 5.6 % mit DCV5T-Me:C_{60} OSZ erreicht werden.
Um die Anwendbarkeit dieser vollflexiblen und verkapselten OSZ zu bewerten, werden Alterungsstudien unter konstanter Beleuchtung und feuchtem Klima durchgeführt. Es wird gezeigt, dass die in das Polymer eingebettete AgNW-Elektrode aufgrund von Photooxidation

und -schwefelung und Photo- und Elektromigration instabil ist. Dieser Sachverhalt ist für die Anwendung von AgNW-Elektroden in kommerziellen OSZ von großer Bedeutung und wurde in der Forschung bisher nicht ausreichend thematisiert.

Contents

Publication List

Articles

[A1] L. Bormann, F. Nehm, L. Sonntag, F.-Y. Chen, F. Selzer, L. Müller-Meskamp, A. Eychmüller, and K. Leo. "Degradation of Flexible, ITO-Free Oligothiophene Organic Solar Cells". *ACS Applied Materials & Interfaces* 8.23 (2016). DOI: 10.1021/acsami.6b02363.

[A2] L. Bormann, F. Nehm, N. Weiß, V. C. Nikolis, F. Selzer, A. Eychmüller, L. Müller-Meskamp, K. Vandewal, and K. Leo. "Degradation of Sexithiophene Cascade Organic Solar Cells". *Advanced Energy Materials* 6.9 (2016). DOI: 10.1002/aenm.201502432.

[A3] L. Bormann, F. Selzer, N. Weiß, D. Kneppe, K. Leo, and L. Müller-Meskamp. "Doped Hole Transport Layers Processed from Solution: Planarization and Bridging the Voids in Noncontinuous Silver Nanowire Electrodes". *Organic Electronics* 28 (2016). DOI: 10.1016/j.orgel.2015.10.007.

[A4] Y. Park, L. Bormann, L. Müller-Meskamp, K. Vandewal, and K. Leo. "Efficient Flexible Organic Photovoltaics using Silver Nanowires and Polymer Based Transparent Electrodes". *Organic Electronics* 36 (2016). DOI: 10.1016/j.orgel.2016.05.032.

[A5] F. Selzer, C. Floresca, D. Kneppe, L. Bormann, C. Sachse, N. Weiß, A. Eychmüller, A. Amassian, L. Müller-Meskamp, and K. Leo. "Electrical Limit of Silver Nanowire Electrodes: Direct Measurement of the Nanowire Junction Resistance". *Applied Physics Letters* 108.16 (2016). DOI: 10.1063/1.4947285.

[A6] F. Selzer, N. Weiß, D. Kneppe, L. Bormann, C. Sachse, N. Gaponik, A. Eychmüller, K. Leo, and L. Müller-Meskamp. "A Spray-Coating Process for Highly Conductive Silver Nanowire Networks as the Transparent Top-Electrode for Small Molecule Organic Photovoltaics". *Nanoscale* 7.6 (2015). DOI: 10.1039/c4nr06502f.

[A7] N. Weiß, L. Müller-Meskamp, F. Selzer, L. Bormann, A. Eychmüller, K. Leo, and N. Gaponik. "Humidity Assisted Annealing Technique for Transparent Conductive Silver Nanowire Networks". *RSC Adv.* 5.25 (2015). DOI: 10.1039/C5RA01303H.

[A8] L. Müller-Meskamp, F. Selzer, L. Bormann, A. Schubert, S. Schubert, N. Weiss, and K. Leo. "Transparent Electrodes for Organic Photovoltaics and OLEDs". *Asia Communications and Photonics Conference* (2014).

[A9] F. Selzer, N. Weiß, L. Bormann, C. Sachse, N. Gaponik, L. Müller-Meskamp, A. Eychmüller, and K. Leo. “Highly Conductive Silver Nanowire Networks by Organic Matrix Assisted Low-Temperature Fusing”. *Organic Electronics* 15.12 (2014). DOI: 10.1016/j.orgel.2014.09.030.

[A10] C. Sachse, L. Müller-Meskamp, L. Bormann, Y. H. Kim, F. Lehnert, A. Philipp, B. Beyer, and K. Leo. “Transparent, Dip-Coated Silver Nanowire Electrodes for Small Molecule Organic Solar Cells”. *Organic Electronics* 14.1 (2013). DOI: 10.1016/j.orgel.2012.09.032.

Patents

[P1] L. Bormann, L. Müller-Meskamp, F. Selzer, N. Weiss, C. Sachse, N. Gaponik, A. Eychmüller, and D. Kneppe. *Verfahren zur Herstellung einer Nanodrahtelektrode für optoelektronische Bauelemente sowie deren Verwendung.* URL: https://www.google.com/patents/DE102013226998B4?cl=de.

[P2] F. Selzer, L. Müller-Meskamp, L. Bormann, N. Weiss, C. Sachse, N. Gaponik, and A. Eychmüller. *Transparente Nanodrahtelektrode mit Funktionaler organischer Schicht.* URL: https://www.google.com/patents/WO2015090395A1.

[P3] N. Weiß, L. Müller-Meskamp, F. Selzer, L. Bormann, N. Gaponik, and A. Eychmüller. *Verfahren zur Herstellung einer Elektrodenschicht eines elektrischen Bauelements.*

Oral Conference Contributions

[O1] L. Bormann, F. Selzer, K. Leo, and L. Müller-Meskamp. “A Solution-Doped Small Molecule Hole Transport Layer for Efficient ITO-Free Organic Solar Cells”. In: *SPIE Optics and Photonics 2015.* San Diego, USA, 2015.

[O2] L. Bormann, F. Selzer, N. Weiß, L. Müller-Meskamp, and K. Leo. “Organic Solar Cells with Silver Nanowire Electrodes and Solution Processed Small Molecule Hole Transport Layers”. In: *ISFOE 2014.* Thessaloniki, Greece, 2014.

[O3] L. Bormann, F. Selzer, N. Weiß, L. Müller-Meskamp, and K. Leo. “Solution-Based Planarization Layers for Organic Solar Cells on Transparent Silver Nanowire Electrodes”. In: *DPG Spring Meeting.* Dresden, Germany, 2014.

1. Introduction

Animate nature is a fascinating thing. It arose over billions of years using a complex interplay of trial and error, called *evolution*. Mankind searches for ways to mimic patterns in nature evolution for their benefit. Famous examples are the adaption of bird flight mechanisms and physics to develop aviation, or the imitation of the lotus effect to keep surfaces clean. Even the concept of artificial light sources has a natural equivalent; so-called *bioluminescence*. Further, the oriental hornet (*vespa orientalis*), shown in Figure 1.1, provides a concept that mankind has employed – what exactly will follow in a bit.

Figure 1.1.: Photograph of the oriental hornet. From http://www.uniprot.org/taxonomy/7447, accessed on 06/13/2016.

It is indisputable that our current lifestyle needs a huge amount of energy to run all the computers, light sources, cars, ships, factories, et cetera. In 2015, the worldwide energy consumption was 550×10^{18} J, and continues to increase.[9] This thirst is mainly satisfied by exploiting fossil fuels like mineral oil, natural gas, or coal. However, the use of these energy sources is profoundly unsustainable and is the main driving force for the exponentially increasing CO_2 content in our atmosphere, which is one cause of global warming. As depicted in Figure 1.2, a fluctuation of atmospheric CO_2 has been observed in geological history before, but not in such a short timescale or with such strength as we are currently facing it.

Renewable energy sources like wind, water, and sunlight are able to reduce the need for fossil fuels although their part of the whole energy production currently is only 2.8 %.[9] The utilization of the sun as an energy source for generating electricity, called *photovoltaics*, is an important and promising renewable energy form, as the sun gives us a lot of it for free. *A lot* means 20 times of the annual world consumption – per

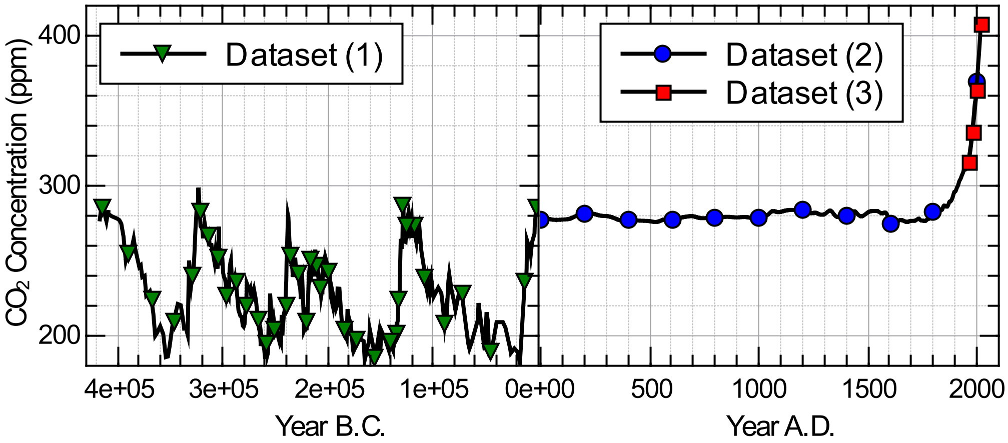

Figure 1.2.: Atmospheric CO_2 concentration over time. Datasets are from (1) N. I. Barkov, Arctic and Antarctic Research Institute (Russia), (2) [243], and (3) Station at Mauna Loa, Hawaii, USA - `http://www.esrl.noaa.gov/`, accessed on 06/09/2016.

day. This is the point where the oriental hornet comes into play: its cuticle is capable of transforming sunlight into electricity, working as a little biological solar cell that has been invented by nature.[294] Most of the solar cells we use today are made of inorganic semiconductors, for example silicon or gallium arsenide. Despite the similar outcome of transforming sunlight into electricity, they are quite far from the oriental hornet in terms of the materials used.

Organic solar cells (OSCs) (one example is shown in Figure 1.3 left) are not only much more close to the basic building blocks of the animate nature; they utilize *the same* basic elements as the organic world, which consists mostly of the elements carbon, nitrogen, hydrogen, and oxygen. Thereby, carbon is of great importance, as its tetravalence allows for myriads of different molecules with many different properties. Due to the potential of high absorption coefficients of these materials, layers with thicknesses below 100 nm are sufficient for strong light absorption. Thus, OSCs, which consist of several sandwiched organic layers, can be made extremely thin – the total layer thickness is approximately a thousand times less than a human hair. Further, high flexibility of the materials allows for the employment of roll-to-roll fabrication processes to achieve large area devices with low-cost methods. However, roll-to-roll fabrication requires that every layer of the organic device is flexible. Consequently, not only organic materials but also substrate, electrodes, and encapsulation layers against moisture ingress require flexibility.

So far, the transparent electrode presents the biggest challenge. Indium tin oxide (ITO), the currently used industry-standard, provides good optical and electrical performance, but is stiff and expensive. A valuable alternative is needed that offers comparable optical and electrical performance than ITO, enables flexibility, and comes along with inexpensive material and fabrication cost.

In the last several years, silver nanowire (AgNW) electrodes emerged as a promising alternative to ITO. As shown in Figure 1.3 (right), they consist of randomly oriented silver nanowires, which are deposited in-plane on an arbitrary substrate. Their electrical conductivity is high due to the fact that silver is the best conductor among the metals. AgNW networks further offer high transparency, as light can pass through the open spaces inbetween the wires. With these properties, they achieve better optical and electrical performance than ITO. Moreover, their structure and the high ductility of silver allows flexibility and stretchability. As the silver nanowires are usually dispersed in organic solvents like ethanol or water, simple and cheap solution-based deposition methods can be used at low temperatures, which are compatible with roll-to-roll processes.

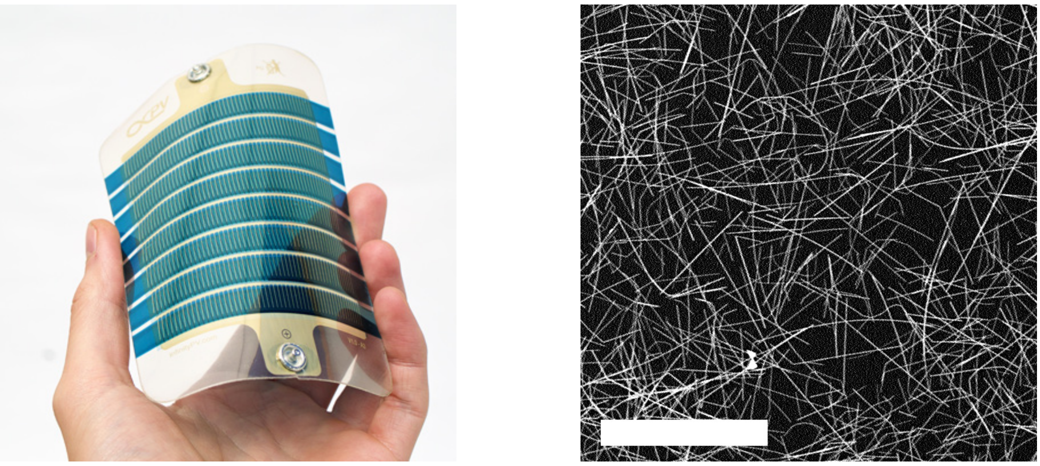

Figure 1.3.: Left: Flexible and semitransparent organic solar cell. Courtesy of infinityPV. Taken from `http://www.infinitypv.com/infinitypro/opv/demonstrator`, accessed on 06/13/2016. **Right:** Scanning electron microscopy image of a silver nanowire network. The scalebar represents 20 µm.

However, this thesis would not exist if the implementation of AgNW electrodes in organic solar cells would work without any issues. Silver nanowire networks exhibit huge roughnesses. A junction of two nanowires is twice as high as one silver nanowire in diameter and with this often higher than the total organic layer stack. This leads to shunt paths and shortcuts in the device. Consequently, a planarization is needed. Furthermore, the structure contains square micrometer large voids inbetween the nanowires, which have to be bridged electrically by the organic layers. If the lateral conductivity of the organic materials is too low, the macroscopic device performance suffers. Additionally, the longterm stability of OSC devices is important for commercial applications. Although there are many studies adressing this issue on ITO and ITO-free devices, the stability of AgNW electrodes in OSC operation is only marginally adressed in current research.

This thesis discusses the implementation of silver nanowire networks as transparent bottom electrode in organic solar cells. Thereby, the focus is on the issues introduced above.

Prior to discussing the results of this PhD thesis, Part I provides fundamental background information. In Chapter 2, basic properties and concepts of organic semiconductors are introduced. The working principle of organic solar cells, state-of-the-art device types, and degradation mechanisms are discussed. Chapter 3 focuses on transparent electrodes in terms of general requirements and different electrode types. Roughly half of this chapter is dedicated to silver nanowires, as they are the core element of the investigations within this thesis. Percolation is introduced as the theory explaining the conductivity of AgNW networks. Further, a short look is taken into the synthesis and an overview over AgNW network properties and the aforementionend challenges that occur upon implementation in OSCs is given.

Part II of this thesis explains the methods of sample preparation (Chapter 4), sample characterization (Chapter 5), and the model used for equivalent circuit simulations (Chapter 6).

In Part III, the results are presented. Two fundamentally different techniques of AgNW network planarization are evaluated. In Chapter 7, the silver nanowires are planarized with solution-processed small molecule charge carrier transport layers. Three different material systems are investigated: BF-DPB:NDP9, Spiro-TTB:NDP9, and n-doped NTCDA. With focus on the first system, optical, electrical, and topographical analysis of the single layers and AgNW electrodes is carried out. Organic solar cells are fabricated on this planarized electrode. Further, the impact of the void-like network structure on the macroscopic OSC performance in dependence of HTL conductivity is analyzed. Therefore, experiments and equivalent circuit simulations are used.

In Chapter 8, another concept of planarization is investigated. Thereby, the silver nanowires are buried in an insulating polymer that concurrently serves as flexible and ultrathin substrate. They are implemented in two different organic solar cell configurations, which are highly efficient on ITO. As this planarization concept enables fabrication of flexible devices, the aging behavior in air of devices that are encapsulated with a flexible alumina barrier against moisture ingress is studied.

In the last Part IV, the work is shortly summarized (Chapter 9) and an outlook is given in Chapter 10.

Part I.

Fundamentals

2. Basics of Organic Semiconductors

This chapter gives an introduction to organic semiconductors. Basic molecule properties like the π conjugation are discussed in Section 2.1 as well as doping and charge carrier transport in organic molecular crystals. In Section 2.2, organic solar cells as one important application of organic semiconductors are introduced by discussing their basic working principle, deposition techniques, different types of organic solar cells, and degradation mechanisms due to intrinsic or extrinsic influences. The chapter mainly follows the monographs [239, 245, 254] and further publications as cited in the text.

A first evidence of the semiconducting properties of organic molecular crystals was already observed in the early 20th century with the measurement of dark- and photoconductivity of anthracene. This happened long before inorganic semiconductors started a revolution of (micro-)electronics by the implementation of transistors. Nowadays, life as it is would be unimaginable without inorganic semiconductors. Organic semiconductor physics has been a field of basic research for a long time, but has recently entered new applications beyond microelectronics with their unique properties. Flexibility, light weight, low-cost and low-energy production, and recyclability are promising properties for sustainable products.

To understand why organic solar cells (OSCs) or organic light emitting diodes (OLEDs) are a considerable addition to inorganic counterparts like silicon solar cells or light emitting diodes, one has to start at the fundamental building block of organic semiconductors – the carbon atom.

2.1. Organic Semiconductors - from Atoms to Molecules to Solids

Tetravalent carbon is the element that gives the organic semiconductor its first name, as the living, *organic* world is only possible because of its rich bond diversity. In ground state, the electron configuration of a free carbon atom is $1s^2 2s^2 2p^2$. To form a bond with another atom, the valence electron orbitals hybridize. The wave functions

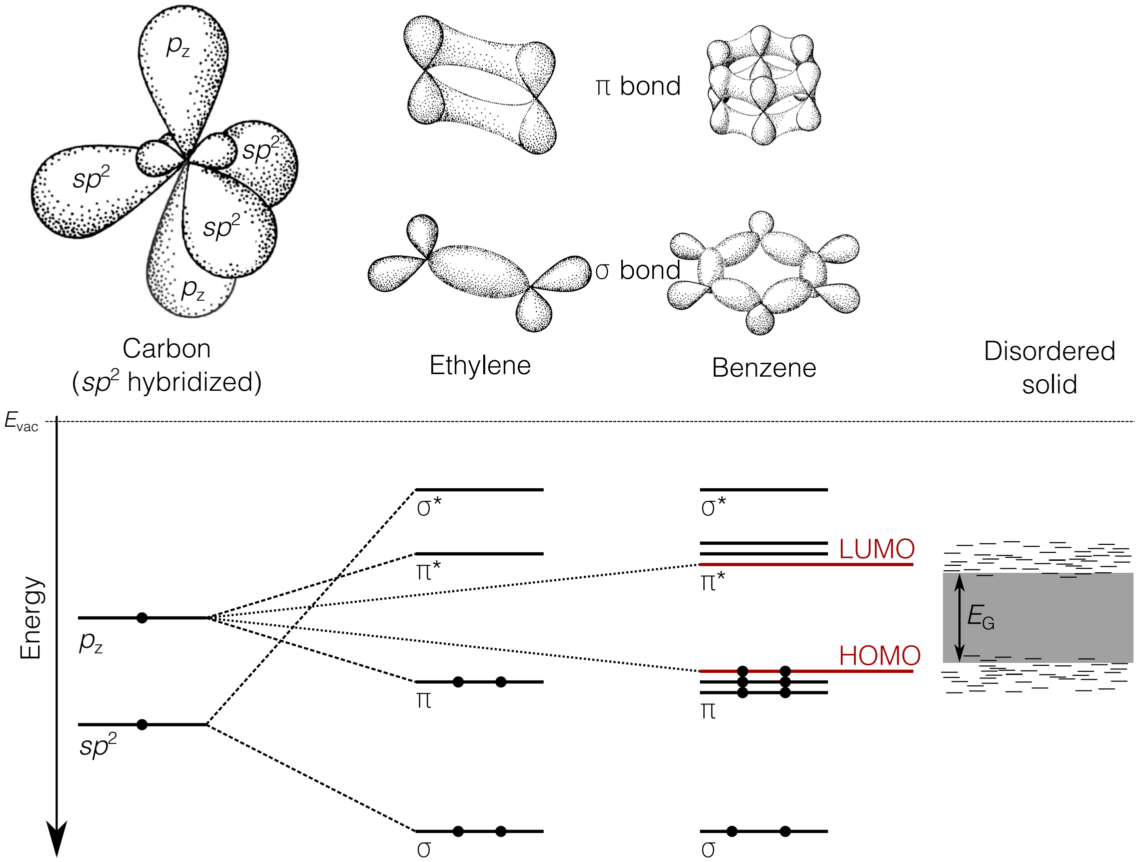

Figure 2.1.: Top: Electron orbitals of sp^2 hybridized carbon, ethylene and benzene. **Bottom:** Schematic representation of energy levels and their splitting during the transition from atom to molecule to an amorphous solid. The sp^2 orbitals transfer to localized σ bonds, the p_z orbital transfers to delocalized π bonds. In an amorphous solid, the energy levels are broadened due to disorder-induced statistical polarization energy deviations.

of one $2s$ and one, two, or three $2p$ electrons form linear superpositions, which result in sp (e. g. carbon monoxide (CO) or ethine (C_2H_2)), sp^2 (e. g. ethylene (C_2H_4) or benzene (C_6H_6), both depicted in Figure 2.1 top), or sp^3 hybridization (e. g. diamond or methane (CH_4)), respectively. If the sp orbital overlaps with an electron orbital of another atom, the wave functions degenerate (Fig. 2.1 bottom). A bonding σ orbital and an antibonding σ^* orbital arise whereby only the bonding σ orbital is occupied due to its lower energy. The σ orbital is localized and constitutes a strong, intramolecular, covalent bond. The remaining $2p$ electrons form bonding π and antibonding π^* orbitals which are more delocalized and weaker as compared to the σ orbitals. In sp^2 hybridization, three sp^2 orbitals arise which are coplanar with angles of 120° between each of the orbitals as depicted in Figure 2.1. The remaining $2p$ orbital lies perpendicular to the sp^2 plane. Ethylene or benzene are bound due to sp^2 hybridization.

In the case of organic semiconductors, the sp^2 hybridization is the reason for their semiconducting properties. The strong σ bond is responsible for the covalent bonds of atoms while the π bond develops into a delocalized electron cloud. The term scheme in

Figure 2.1 shows the transition from carbon's electron orbitals to the molecule orbitals of ethylene and benzene as well as the resulting populations with electrons. Bonding π and σ states are populated with electrons up to a certain energy level – the *highest occupied molecule orbital* (HOMO), usually being a π state. The antibonding π^* and σ^* states are not occupied, starting with the *lowest unoccupied molecule orbital* (LUMO), which is a π^* state. Thus, the $\pi \rightleftharpoons \pi^*$ transition is the one with the smallest energy difference that leads to the energetic gap E_G wherein no states are present. The difference in energy is then $E_\mathrm{G} = E_\mathrm{HOMO} - E_\mathrm{LUMO}$. For many organic semiconductors, E_G is in the range of a few electron volts. This results in basic interactions with photons in or close to the visible part of the spectrum – one important requirement to build organic optoelectronic devices like OLEDs and OSCs.
It is possible to determine the position of HOMO and LUMO by measuring the ionization potential (IP) and the electron affinity (EA) according to Koopmans' theorem. In this approximation, the removal of an electron is only marginally changing the energy level landscape such that ($E_\mathrm{HOMO} \approx$ IP, $E_\mathrm{LUMO} \approx$ EA) is valid.

2.1.1. Conjugated π Systems

One basic building block of organic semiconductors is benzene, whose delocalized π orbitals are not confined to a single carbon atom or a C-C bonding but extend over the whole molecule leading to a *conjugated* π system. The energies of the π_n states can be calculated by using the Hückel approximation: the π electrons are assumed to be in a square well potential. The benzene circumference L must satisfy the condition $n\lambda = L$ (λ: electron's de Broglie wavelength).[255, p. 260] For the energies of level n,

$$E_n = \frac{n^2 h^2}{2 m_\mathrm{e} L^2} \tag{2.1}$$

is obtained with electron mass m_e and planck constant h. The lowest possible transition $n = 1 \rightarrow n = 2$ leads to an energy difference of

$$\Delta E = \frac{h^2(2n+1)}{2 m_e L^2} = 6.5\,\mathrm{eV} \ , \tag{2.2}$$

which results in a value ΔE of 6.5 eV in benzene (with $L = 840\,\mathrm{pm}$) corresponding to an excitation wavelength of 191 nm. This is in fair agreement with experimental results where a minimum excitation wavelength of approximately 220 nm is obtained. With increasing conjugation length (and increasing L), the energy gap gets smaller. In Figure 2.2, the energy gap is depicted for different aromatic hydrocarbons with an increasing number of benzene rings. A pentacene bulk exhibits an energy gap of approximately 2 eV. Another effect is visible in Figure 2.1 and 2.2: the energy gap varies depending on whether an isolated molecule – sometimes called *oriented gas* –

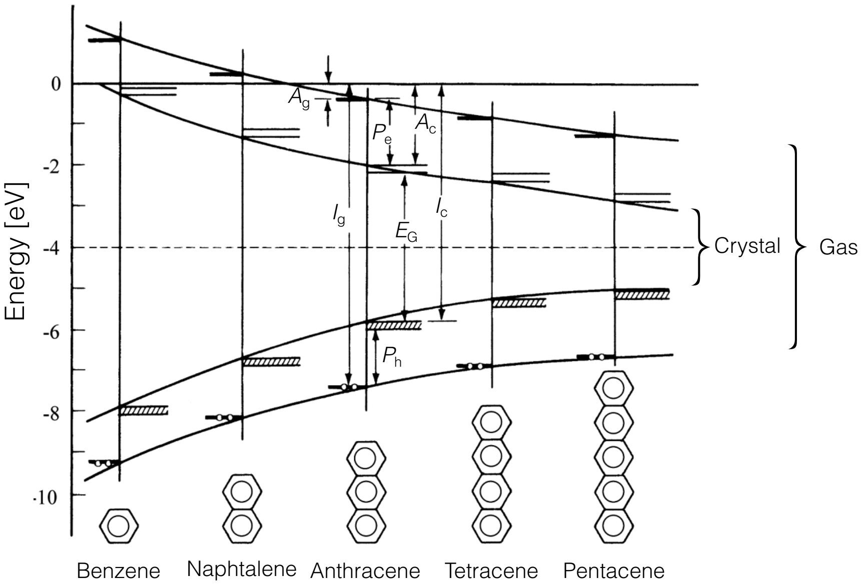

Figure 2.2.: Term scheme of various aromatic hydrocarbons with different conjugation lengths. Compared are ionized states of the crystal (subscript 'c') with energy levels of the isolated molecule (subscript 'g'). $A_{\mathrm{g/c}}$: electron affinity, $I_{\mathrm{g/c}}$: ionization energy, $P_{\mathrm{e/h}}$: polarization energy for electrons and holes, E_{G}: energy gap. Adapted from [239].

or a crystal is considered. In a crystal, neighboring molecules polarize, reducing the energetic gap. In a disordered solid, like most thin-films that are used in this study, energy levels are additionally broadened due to statistical variations of the polarization energies.

The intermolecular interplay is dominated by the π system due to electric dipole interaction which leads to intermolecular forces, so-called Van der Waals forces. In contrast to e. g. covalent, metallic, or ionic bond, the Van der Waals forces are short-ranged and have relatively low binding energies in the meV regime. Therefore, these forces lead to bulk properties such as a lower melting point, a lower binding energy, and a higher compressibility as compared to inorganic materials. Furthermore, many organic materials exhibit high extinction coefficients in the regime of $1 \times 10^5\,\mathrm{cm}^{-1}\,\mathrm{M}^{-1}$ enabling a strong light absorption even at layer thicknesses smaller than 100 nm.

2.1.2. Charge Carrier Transport in Organic Semiconductors

Charge carrier transport can be described using Ohm's law

$$\vec{j} = \widehat{\sigma}\vec{F} \,, \tag{2.3}$$

where $\vec{j}$ represents the current density, $\widehat{\sigma}$ the conductivity tensor, and $\vec{F}$ the electric field strength. To simplify matters, $\widehat{\sigma}$ is assumed to be scalar. If only one charge carrier type (e. g. electrons) with free charge carrier density n is involved in current flow, the current density can be derived using $\vec{v}_\mathrm{D}$ as average charge carrier drift velocity and q as elementary charge:

$$\vec{j} = q\, n\, \vec{v}_\mathrm{D} \; . \tag{2.4}$$

By introducing the important and widely used charge carrier mobility μ via

$$\vec{F}\, \mu = \vec{v}_\mathrm{D} \; , \tag{2.5}$$

the conductivity σ is obtained using the equation

$$\sigma = q\, n\, \mu \; . \tag{2.6}$$

The mobility exhibits values ranging from $1 \times 10^{-7}\,\mathrm{cm^2/(V\,s)}$ for disordered organic semiconductors up to $400\,\mathrm{cm^2/(V\,s)}$ for extremely purified molecular crystals at low temperatures.[267] Note, that mobilities of organic semiconductors are usually much lower as compared to inorganic materials. Germanium for example exhibits an electron mobility of approximately $4000\,\mathrm{cm^2/(V\,s)}$ at room temperature.
The charge carrier transport in organic molecular solids can be described in analogy to the energy-band model from Bloch in inorganic solids. This model is only valid, if the molecular solid is a single crystal, highly purified, and kept at low temperatures far below room temperature. Transport bands are formed due to long-range periodicity of the molecules. However, most organic solids at room temperature are disordered, contaminated, or doped (cf. Section 2.1.3). In these cases, charge carrier transport is dominated by *hopping* from molecule to molecule. Reasons for this kind of transport are localized and energetically broadened states induced by disorder. This leads to a certain probability for a charge carrier to *hop* to neighboring molecules.

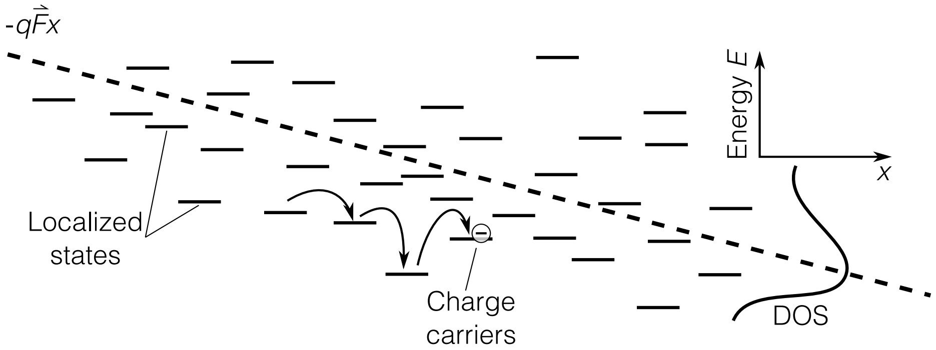

Figure 2.3.: Schematic hopping transport in a disordered organic semiconductor according to the Bässler model with a Gaussian energy distribution of the density of states (DOS). Adapted from [239].

Different models have been reported explaining the hopping transport. The Bässler model, which is illustrated in Figure 2.3, is physically well-founded and fairly simple. It assumes that the density of localized energy states $g(E)$ is broadened by a Gaussian distribution with a width Σ, given by

$$g(E) = \frac{N}{(\sqrt{2\pi}\Sigma)} \exp\left[-\frac{E^2}{2\Sigma^2}\right] \ . \tag{2.7}$$

(N: total density of hopping sites, E: energy measured in the center of the density of states)

Hopping probabilities can be determined using Monte Carlo simulation, leading to a thermally activated charge transport. The mobility at low electric fields equals

$$\mu(\Sigma, T) = \mu_0 \ \exp\left[-\left(\frac{2\Sigma}{3k_\mathrm{B}T}\right)^2\right] \ . \tag{2.8}$$

Here, μ_0 is the mobility of a perfect semiconductor without any disorder at temperature $T \rightarrow \infty$, and k_B is the Boltzmann constant.

2.1.3. Electrical Doping[1]

Two charge carrier species usually occur in semiconductors: electrons and holes. If an electron is lifted from the ground state up to higher lying energy levels, a positively charged vacancy is left-behind which moves through the semiconductor like a charge carrier with a certain mass m_p and mobility μ_p – the so-called *hole*. Hence, the overall conductivity of an organic semiconductor is determined by contributions from free electrons (subscript 'n') and free holes (subscript 'p') such that Equation 2.6 needs to be modified to

$$\sigma = q(\mu_\mathrm{n} n_\mathrm{n} + \mu_\mathrm{p} n_\mathrm{p}) \ . \tag{2.9}$$

Purified organic materials usually exhibit very low conductivities in the range of 1×10^{-10} to 1×10^{-7} S/cm at room temperature. Due to Fermi-Dirac statistics, charge carriers in the ground state are not able to overcome the bandgap of a few electron volts just by thermal activation, which is around 25 meV. Only due to optical excitation or high external applied voltages can electrons be excited from the HOMO into the LUMO forming an exciton (cf. Sec. 2.1.4) that can be split into free charge carriers.

By introducing the concept of electrical doping to organic semiconductors, the density of a specific charge carrier type can be increased drastically leading to conductivities that are several orders of magnitude higher than in the undoped case. For example, C_{60} experiences an increase upon n-doping up to 1 to 10 S/cm.[116] The basic principle is analog to inorganic semiconductors: the semiconductor is impurified with a small amount of a different element or molecule – the so-called *dopant* – which raises the absolute number of free charge carriers n_n and/or n_p. For this purpose, a charge transfer from dopant to matrix molecule is necessary. Figure 2.4 shows the case of

---

[1] Main reference for this section is [87].

p-doping: the EA of the dopant (*acceptor*) has to lie energetically below the IP of the matrix molecule. An electron located in the matrix is transferred to the dopant but still bound with the generated hole via Coulomb interaction. After charge separation, a free hole is created in the matrix molecule which can now diffuse through the organic semiconductor. For n-doping, the IP of the dopant needs to be energetically higher than the matrix EA such that a dopant electron is transferred to the matrix material. This implies, for typical n-dopants, that the IP is located close to the vacuum level. The molecules are much more prone to oxidation and thus not as stable in air as common p-dopants. Approaches have been made introducing air-stable but inactive precursor molecules (e. g. dimers) that incorporate the actual n-dopant. By thermal treatment (e. g. during vacuum evaporation), the molecule breaks up and the n-dopant gets activated.[74, 143, 157]

Although the basic principle of doping is relatively simple, an exact understanding of molecular doping processes has not yet been achieved. This is reasonend by observations which suggest significant differences to the inorganic world. The doping efficiency is strongly concentration dependent. At low doping concentrations, nearly no enhancement in conductivity is observed.[156] In this regime, the additional charge carriers fill trap states in the organic material. Doping efficiency is also lower at higher doping concentrations, meaning that not every dopant molecule leads to an additional free charge carrier. This necessitates much higher doping concentrations in the magnitude of weight percent with respect to the matrix material. The doping concentrations for inorganic materials often lie around 1×10^{-4} to 1×10^{-8} per host atom. Different models of the molecular doping process are reported trying to explain the low doping efficiency. They differ from the easy picture drawn in Figure 2.4. One prevailing model assumes that the doping takes place in two steps. First, a charge transfer complex of e. g. p-dopant and matrix molecule forms and the electron is transferred from matrix to

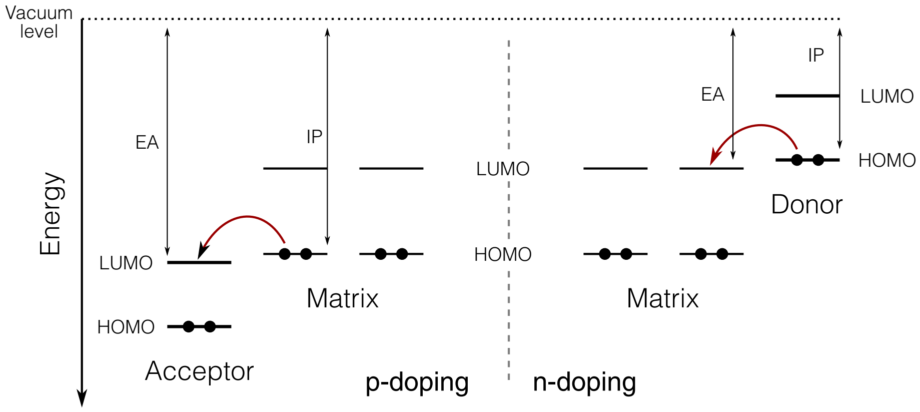

Figure 2.4.: Schematic p- and n-doping process. In case of n-doping, an electron is transferred due to thermal excitation from a donor molecule to a neighboring matrix molecule. P-doping takes place, if an acceptor molecule takes an electron and generates a free hole in the matrix.

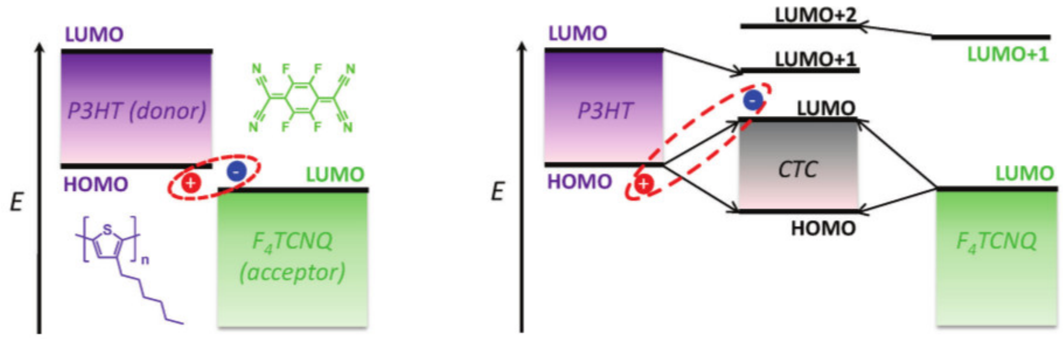

a) Integer charge transfer

b) Hybrid charge transfer complex

Figure 2.5.: Different reported models of the charge transfer process between P3HT (matrix) and F_4TCNQ (p-dopant). **a)** Isolated molecules are ionized after the charge transfer. **b)** A hybrid molecule is formed with new emerging HOMO und LUMO energies as supramolecular orbitals. Adapted from [117].

dopant. Second, the complex dissociates leaving an ionized dopant and matrix molecule behind (Fig. 2.5 a).[207, 273] In this case, electron and hole are strongly bound via Coulomb interaction, explaining the lower doping efficiency.

Another model, reported by Aziz et al., states the formation of a hybrid molecule prior to the charge transfer (Figure 2.5 b).[115, 235] Staying at the exemplary p-doping, the HOMO of the matrix molecule overlaps with the LUMO of the dopant. An additional host molecule is necessary for giving the electron to the hybrid complex which needs to overcome an activation energy. This activation energy is assumed to be responsible for the low doping efficiency in this case, as it is around 0.5 eV. Recently, Salzmann et al. reported that, depending on the specific material combination, both models can occur.[16]

Charge carrier transport layers (cf. Section 2.2.1) profit from doping due to a high conductivity enabling the free choice of layer thickness. Additionally, doping is also beneficial as it helps to provide ohmic contacts at e. g. metal/organic interfaces by reducing the width of the space charge region, allowing charge carriers to tunnel through the primal energetic barrier.

2.1.4. Excitons

Another important concept for understanding the generation of free charge carriers in organic semiconductors is the so-called *exciton*. Excitons are neutral quasiparticles consisting of an electron and a hole that are bound due to Coulomb interaction. Thus, their binding energy can be calculated as

$$E_{\mathrm{B}} = \frac{q^2}{4\pi\,\epsilon\,\epsilon_0}\frac{1}{r}\,, \tag{2.10}$$

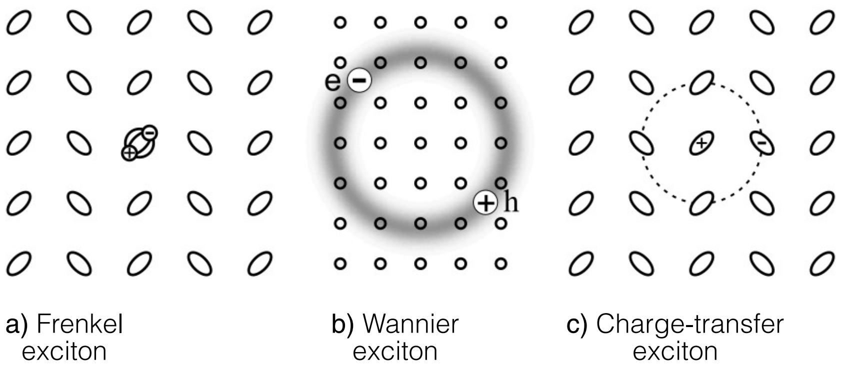

Figure 2.6.: Different excitons and their local expansion. **a)** The Frenkel exciton is mostly located at a single molecule while **b)** a Wannier exciton is much more delocalized over several lattice constants ($r \approx 4$ to 10 nm). **c)** Electron and hole of a charge-transfer exciton are located on two adjacent molecules. Adapted from [239].

with ϵ_0 being the vacuum permittivity, r the distance of the charges, and ϵ the permittivity of the material. E_B usually differs quite strongly in organic and inorganic materials for two reasons. On the one hand, $\epsilon_\mathrm{organics}$ is usually lower (values ranging from 1 to 6) than in e. g. silicon ($\epsilon_\mathrm{Si} \approx 12$).[217, p. 415] On the other hand, electron and hole are usually located on the same molecule, resulting in a charge carrier distance r of just a few nanometers. These excitons are so-called *Frenkel excitons* (Fig. 2.6 a). In the case of inorganic semiconductors, the *Wannier exciton* (Fig. 2.6 b) is delocalized over the distance of several atoms, usually in the range of 4 to 10 nm. The differences in ϵ and r result in binding energies in the meV regime in inorganic semiconductors – corresponding excitons are easily separated by thermal activation. For organic materials, E_B usually exhibits values between 0.5 to 1 eV. Hence, it needs some additional energy to split the exciton into free charge carriers. A third species is the *charge-transfer exciton* (Fig. 2.6 c). It lies in terms of charge carrier distance r and binding energy E_B between Frenkel and Wannier exciton, since electron and hole are located on neighboring molecules. The charge-transfer exciton is one requirement for the exciton splitting mechanism used in organic solar cells (see Section 2.2).

Excitons are able to diffuse through the bulk by transferring their energy to adjacent molecules. Two non-radiative possibilites of diffusion occur: The *Foerster resonant energy transfer* uses dipole-dipole coupling of the involved molecules, while electrons are exchanged at the *Dexter energy transfer*.[311] The corresponding exciton diffusion length L_D can be calculated using the material-dependent diffusion coefficent D_exc and the lifetime τ until hole and electron recombine:

$$L_\mathrm{D} = \sqrt{D_\mathrm{exc}\,\tau}\ . \tag{2.11}$$

For commonly used, amorphous, organic semiconductors, L_D lies in the range of 5 to 20 nm.[223] Organic solar cell design and the device performance is strongly influenced by the short diffusion lengths.

2.2. Organic Solar Cells

The first two-layer organic solar cell (OSC) was reported by C. W. Tang in 1986.[295] The layer stack was fairly simple: a donor (CuPc) and an acceptor (a perylene tetracarboxylic derivative) were placed consecutively between two electrodes. However, a respectable PCE of 0.95 % was achieved.[2]

Since then, a lot of research activity improved organic solar cells drastically such that first consumer products are now available on the market. The basic understanding of charge carrier generation influenced design principles for new organic absorber materials as well as rules for the architecture of the OPV devices. Vice versa, new material combinations and processing differences created unpredictable improvement and challenged the need for further basic understanding.

Organic solar cells offer many differences as compared to inorganic (e. g. silicon) solar cells which can be both advantegeous and detrimental for later OPV applications. Usually, organic absorber materials have a high absorption coefficient α greater than $1 \times 10^5\,\mathrm{cm}^{-1}$ [279] due to the conjugated π electron system. A layer thickness of only 100 nm already absorbs most of the incoming visible light. Silicon provides an absorption coefficient α of only $1 \times 10^3\,\mathrm{cm}^{-1}$,[297] leading to a thousandfold higher thickness of greater than 100 µm. Low organic layer thickness and weak intermolecular Van der Waals forces enable flexible devices, which opens up the door for novel application scenarios.

Further, the carbon building block allows for the synthesis of a nearly infinite variety of organic materials – each individually tailored for a specific absorption spectrum or absorption intensity. With the absorption spectrum, the visible color of the device also changes. This makes it very appealing for architects as a colorful design element in building facades, which is already realized, for instance at the EPFL Lausanne, Switzerland (see Figure 2.7).

The fabrication of OSCs can be carried out with low temperature deposition processes like vacuum-deposition or solvent-based deposition techniques, e. g. spin coating or inkjet printing (more details can be found in Section 2.2.2). This enables device fabrication with low energy consumption and on a large substrate area using roll-to-roll processing technologies. However, two issues need to be adressed where inorganic devices outperform the organic ones. Power conversion efficiency records remain at the moment in the region of 10 to 13 % – for lab-scale research devices.[1, 15, 19] During upscaling, the module efficiency is usually lower due to busbar shadowing.[209] This is a big challenge when aiming for applications that need a high power conversion efficiency.

Secondly, nearly all organic devices need to be encapsulated against moisture ingress,

---

[2] Illumination was $75\,\mathrm{mW/cm}^2$ under AM2 condition.

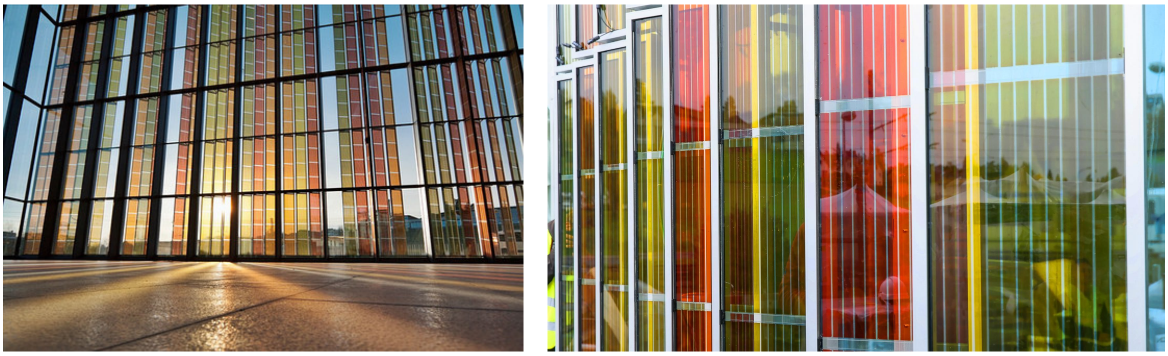

Figure 2.7.: Large area organic-inorganic solar cells on the facade of the 'École polytechnique fédérale de Lausanne' (EPFL) in Switzerland. [Taken from `http://actu.epfl.ch`, accessed on 04/01/2016.]

mechanical stress, and incident UV light.[3] Organic materials often decompose in moist environments, electrodes oxidize or detach during water and/or oxygen diffusion.[232] A solar cell in a realistic outdoor application needs to withstand humidity, temperature and mechanical stress for years. A detailed discussion of several degradation mechanisms and encapsulation techniques can be found in Section 2.2.4.

In the following, the basic working principle of an organic solar cell is introduced. As many different types of OSCs exist and are used within the scope of this thesis, the main differences and advantages are briefly explained.

2.2.1. Working Principle

In the simplest approximation, a solar cell is a device where incident photons with a certain energy $h\nu$ (h: Planck constant, ν: photon frequency) generate free charge carriers that are collected at cathode and anode. Inorganic solar cells simply necessitate a p-n junction – realized for example as homojunction by p- and n-doping of silicon – leading to an electric field in the space charge region between p- and n-doped area. Upon charge carrier excitation from valence into conduction band, electron and hole are separated at the p-n junction and dragged into their region of majority. Through drift and diffusion processes, the charge carriers are then transferred to the contacts.[4]

Organic semiconductors are similar but a bit more complicated. It is explained using a simplified picture shown in Figure 2.8 (a) and an energetic state diagram in Figure 2.8 (b). First, an incoming photon does not generate a free charge carrier directly in an absorber molecule. Instead, a bound pair of electron and hole emerges, the previ-

---

[3] At least, no air-stable, continuously illuminated OSC has been reported with device lifetimes longer than some days.[62, 218] Lifetimes of unencapsulated devices of one year are reported, but in dark ambient environment.[12]

[4] A comprehensive description of solar cell physics is given in the book of P. Würfel.[284]

ously introduced exciton (cf. Section 2.1.4).[5] This process is depicted as the transition of an excitonic singlet ground state S_0 into the first excited state S_1 and takes place with a probability η_A, which is close to 100 % but reduced due to reflection losses and parasitic absorption in other layers.[270] To split this exciton into free charge carriers,

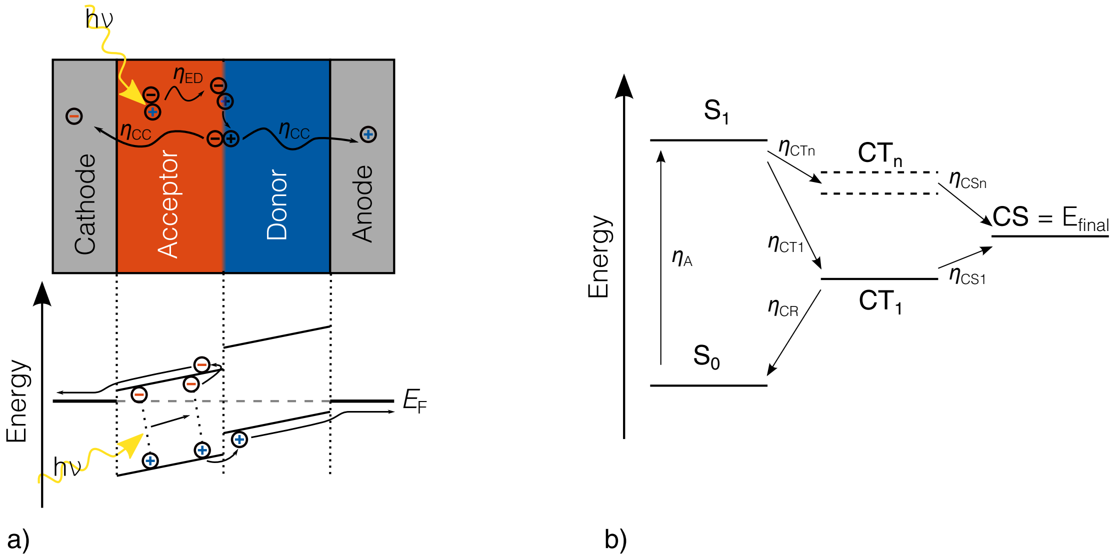

Figure 2.8.: a) Charge carrier generation in organic solar cells under short-circuit condition. Incoming photons generate Frenkel excitons, which diffuse to the donor-acceptor interface, in either the donor or acceptor material. The excitons split up into electrons and holes. Disregarding further loss mechanisms, the free charge carriers drift to the respective contacts. **b)** Electronic state diagram. The first excited singlet state S_1 of a donor or acceptor molecule is reached from the singlet ground state S_0 after optical excitation. Intermolecular charge-transfer creates a charge-transfer (CT_n) state; holes and electrons are now located on a donor and acceptor molecule, respectively. If a charge separation (CS) state is reached, hole and electron are free from mutual binding. Transfer rates between different electronic states are indicated by the η_i terms. Adapted from [219].

it is necessary to locally separate electron and hole. That is usually done at an interface of two absorber molecule species with slightly different HOMO and LUMO energies – they are called *donor* and *acceptor* molecules. If an exciton reaches such, a so-called *heterojunction* (which happens with a probability η_{ED}) a charge-transfer (CT_n) state is occupied. It is energetically favorable that the electron moves onto the acceptor material with a lower LUMO energy and the hole stays at the donor with a higher HOMO. Now, the charges are locally separated and the exciton is able to dissociate – a charge-separation state (CS) emerges with a probability η_{CS}. At this point, it becomes clear why the different absorber molecule types are called acceptor and donor: one absorber *accepts* the electron while the other material *donates* one. Typically, acceptor and donor are n-type and p-type materials, respectively. It is further noted that these materials are intrinsic and need to be highly purified. Any defect or dopant acts as a

---

[5] Strictly speaking, the exciton occurs also in inorganic semiconductors but its binding energy E_B is so small that a splitting is possible only due to thermal activation energy.

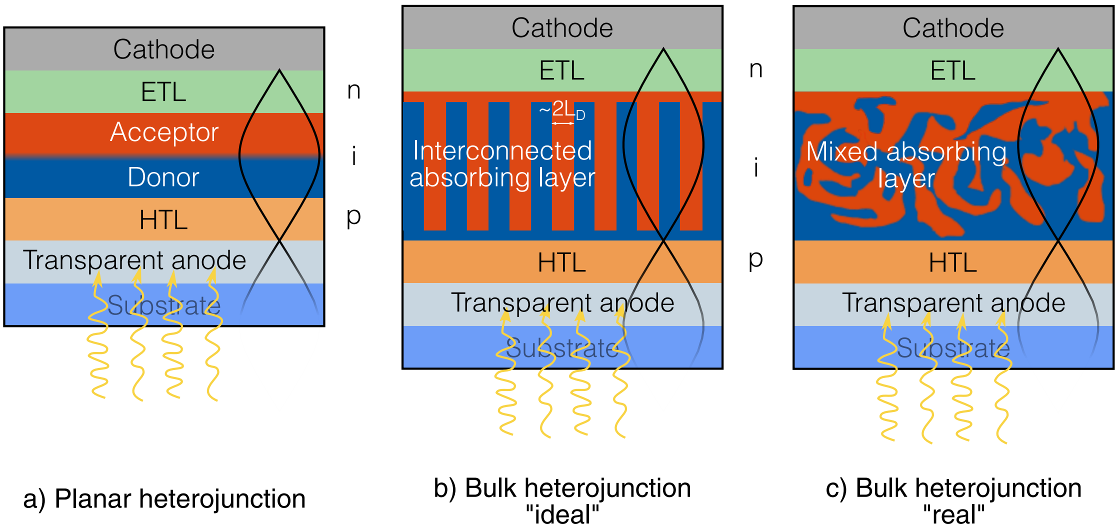

Figure 2.9.: Schematic representation of different heterojunction p-i-n concepts in organic solar cells with the electric field distribution of incident light within the device (black lines). **a)** The planar heterojunction comprises of subsequent deposited donor and acceptor layers. **b)** The ideal bulk heterojunction employs two interconnected layers of donor and acceptor with a finger width of approximately twice the diffusion length in the respective material. **c)** Donor and acceptor material are mixed in the case of a real bulk heterojunction. Random percolation paths ensure a connection of the domains to the ETL/HTL interface such that generated charge carriers can be collected.

charge carrier trap, leading to increased recombination. As a last step, the charges are transported to the contacts with transport efficiency η_{CC}.
Summing up all reaction probabilities, one ends up with the *external quantum efficiency* (EQE)

$$\eta_{\mathrm{EQE}} = \eta_{\mathrm{A}} \cdot \eta_{\mathrm{ED}} \cdot \eta_{\mathrm{CT}} \cdot \eta_{\mathrm{CS}} \cdot \eta_{\mathrm{CC}} \ . \tag{2.12}$$

η_{EQE} describes the probability that an incident photon generates a collected charge carrier.

Many of those probabilites are close to 100 %. However, one bottleneck is η_{ED}, as it is limited by the exciton diffusion length L_{D} which is only a few nm and thus much smaller than the optimal thickness for complete light absorption. Hence, two concepts are introduced in order to strongly improve the EQE.
The first one is the so-called *p-i-n concept* that has been invented at the IAPP (Figure 2.9).[240, 264] Both intrinsic absorber materials are hereby sandwiched between a p- and an n-type organic semiconductor material. They are usually doped and exhibit a bandgap greater than 3 eV[6] such that they are transparent in the visible range of the electromagnetic spectrum. The transport levels are designed to fit with the adjacent absorber material and transport only one charge carrier type while blocking the other one. In the case of the acceptor side, the LUMO energies of acceptor and n-type organic

---

[6] They are sometimes called *window layer*.

semiconductor need to match such that electrons are easily transported through the *electron transport layer* (ETL). The ETL HOMO should be situated deep enough to efficiently block holes. Similarly, all these considerations are also valid for the donor side where a *hole transport layer* (HTL) is used to efficiently transport holes and block electrons.

The conductivity of these layers can be strongly improved via doping (cf. Section 2.1.3), enabling a fairly free choice of layer thickness. By carefully considering the optical constellation of the whole device (including organic layer thicknesses and reflective contacts), the electric field maximum of the propagating light can be placed at the absorbing layer position. Thereby, the absorption and, consequently, the efficiency of the device is enhanced (the electric field distribution is schematically sketched in Figure 2.9).

To bypass the limited L_D, the *planar heterojunction* absorbing layer morphology (Fig. 2.9 a) is modified. The interfacial donor-acceptor area is increased in such a way that more excitons find an interface for dissociation before they relax. In a perfect situation, this would be achieved by realizing interconnected donor-acceptor fingers as depicted in Figure 2.9 (b) with a finger width of $2L_\mathrm{D}$. This ideal scenario is not achievable with present deposition techniques. Consequently, researchers invented the *bulk heterojunction* (BHJ) where both materials are randomly mixed with each other.[226, 269] The result is nanometer-sized domains within the blend increasing the interfacial area. Charge carrier collection is ensured through percolation pathways to the respective ETL/HTL. Especially for this concept, the charge carrier blocking property of the transport materials is important. The bulk heterojunction is a powerful concept with many adjustable parameters to obtain a favorable morphology for efficient charge carrier generation. Some of them are: the donor-acceptor ratio, substrate or material temperature during deposition, deposition speed, side chain manipulation, et cetera.

All the processes and reactions described above explain the working principle of an organic solar cell on a microscopic level. However, a macroscopic device is obtained in the end. Thus, to evaluate the efficiency of an OSC, also a macroscopic access is needed, which is normally found by simply recording a current density versus voltage (jV) characteristic under illumination. Figure 2.10 depicts a schematic jV curve of an organic solar cell. The most prominent feature is the diode-like behavior which is shifted to negative current densities by j_ill under illumination. Such a jV relation can be described in first approximation by the Shockley equation

$$j(V) = j_\mathrm{S}\left(\exp\left[\frac{qV}{n_\mathrm{i}k_\mathrm{B}T}\right] - 1\right) - j_\mathrm{ill} \tag{2.13}$$

with j_S being the saturation current and n_i the diode ideality factor. Such a jV curve exhibits some characteristic points. The *short circuit current density* $j_\mathrm{SC} = j(0\,\mathrm{V}) \approx j_\mathrm{ill}$ represents the extracted current at zero volts and is a measure for the amount of charge carriers generated under illumination. A connection to the microscopic description is

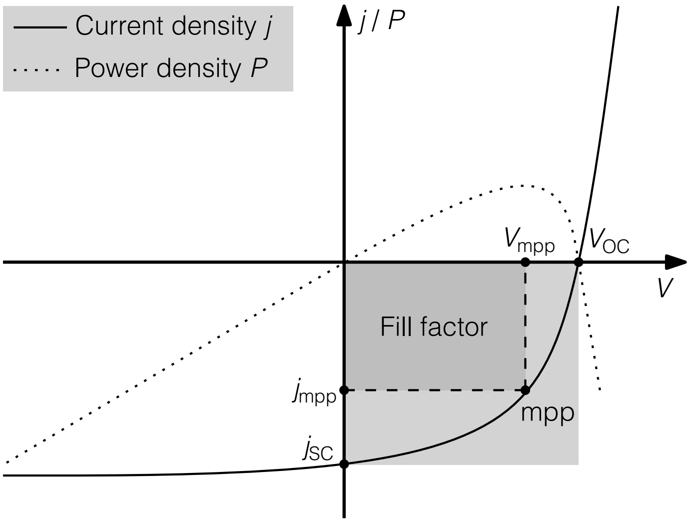

Figure 2.10.: Schematic jV curve of an organic solar cell with characteristic parameters for determining the performance of an OSC. Additionally, the power density $P = j \cdot V$ is plotted (dotted line).

given with the spectral resolved EQE(λ) and the incident photon flux $\Phi(\lambda)$:

$$j_{\mathrm{SC}} = q \int \Phi(\lambda)\mathrm{EQE}(\lambda)\mathrm{d}\lambda \tag{2.14}$$

Another important parameter is the *open-circuit voltage* V_{OC} at which charge injection compensates the photo-generated current density: $j(V_{\mathrm{OC}}) = 0$. It follows from Equation 2.13 under consideration of $j_{\mathrm{SC}} \approx j_{\mathrm{ill}}$

$$V_{\mathrm{OC}} = \frac{n_{\mathrm{i}} k_{\mathrm{B}} T}{q} \ln\left[\frac{j_{\mathrm{SC}}}{j_{\mathrm{S}}} + 1\right] \ , \tag{2.15}$$

which means that the V_{OC} is also dependent on the j_{SC} and thus on the illumination intensity.

The V_{OC} is also related to the microscopic configuration, in particular to the distance of the quasi-Fermi levels of donor-acceptor heterojunction. However, the correlation is not easy and many different approaches try to predict the open-circuit voltage of various donor-acceptor blends under consideration of recombination losses (geminate or non-geminate, radiative or non-radiative).[129, 161, 225] Scharber et al. predicted the following calculation for polymer solar cells (cf. Section 2.2.3), whereby 0.3 eV refers to the energy loss due to exciton dissociation.

$$qV_{\mathrm{OC}} = (E_{\mathrm{HOMO,\,donor}} - E_{\mathrm{LUMO,\,acceptor}}) - 0.3\,\mathrm{eV} \ .[251] \tag{2.16}$$

An elaborate description of the V_{OC} has been given by Vandewal et al. who relate the V_{OC} to donor-acceptor interface properties and radiative and non-radiative loss mechanisms.[206] (E_{CT}: effective band gap, h: Planck constant, c: speed of light in vacuum,

f: density of donor-acceptor contacts, λ: reorganization energy associated with the charge-transfer absorption process, $\mathrm{EQE_{EL}}$: electroluminescence EQE)

$$qV_\mathrm{OC} = E_\mathrm{CT} + k_\mathrm{B}T\,\ln\left[\frac{j_\mathrm{SC}\,h^3\,c^2}{f\,q\,(E_\mathrm{CT}-\lambda)\,2\pi}\right] + k_\mathrm{B}T\,\ln\left[\mathrm{EQE_{EL}}\right] \tag{2.17}$$

By multiplying j and V, the device's power density is obtained (Figure 2.10, dotted line) with a *maximum power point* (mpp) at V_mpp and j_mpp. The power conversion efficiency equals

$$\eta = \frac{P_\mathrm{mpp}}{P_\mathrm{illumination}} = \frac{V_\mathrm{mpp}\,j_\mathrm{mpp}}{P_\mathrm{illumination}}\ . \tag{2.18}$$

To correlate η with j_SC and V_OC, the dimensionless *fill factor* (FF) is defined as the ratio between maximum power density and ideal power density $FF = (V_\mathrm{mpp}\,j_\mathrm{mpp})/(V_\mathrm{OC}\,j_\mathrm{SC})$. The FF reflects the 'rectangularity' of a jV curve. Applying the FF to Equation 2.18, an efficiency of

$$\eta = \frac{V_\mathrm{OC}\,j_\mathrm{SC}\,FF}{P_\mathrm{illumination}} \tag{2.19}$$

is obtained.

The Shockley equation (Eq. 2.13) describes a perfect diode and neglects several loss mechanisms. A more appropriate approximation is achieved by including shunt paths, or resistances within the device which affect the jV curve of an OSC. An easy equivalent circuit model as shown in Figure 2.11 accounts for such losses by implementing serial and parallel resistances R_ser and R_par, respectively. Equation 2.13 can be modified to

$$j(V) = j_\mathrm{S}\left[\exp\left(\frac{q(V-j(V)R_\mathrm{ser})}{n_\mathrm{i}k_\mathrm{B}T}\right)-1\right] + \frac{V-j(V)R_\mathrm{ser}}{R_\mathrm{par}} - j_\mathrm{ill}\ . \tag{2.20}$$

This equation is recursive and cannot be solved analytically. In comparison to the ideal case with $R_\mathrm{par} = \infty$ and $R_\mathrm{ser} = 0$, the impact of R_ser and R_par on a solar cell jV curve is depicted in Figure 2.12. With increasing serial resistance, the slope in forward direction decreases, thereby reducing FF and j_SC. Series resistances in an organic solar cell can be caused by insufficient charge carrier transport in organic layers. Also a high sheet resistance of the electrode adds series resistances, as discussed in Chapter 3, Section 3.1. If the parallel resistance decreases, the jV slope in backward direction increases. j_SC stays constant while V_OC and FF is reduced. Shunt paths cause lower parallel resistances e. g. due to a rough surface or a crystalline layer growth.

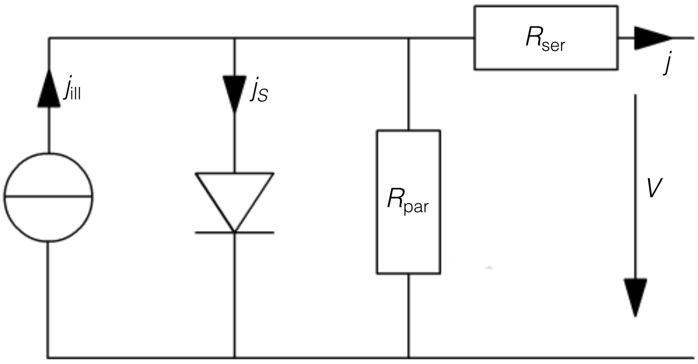

Figure 2.11.: Equivalent circuit description of an organic solar cell containing series resistances R_{ser} and parallel resistances R_{par}.

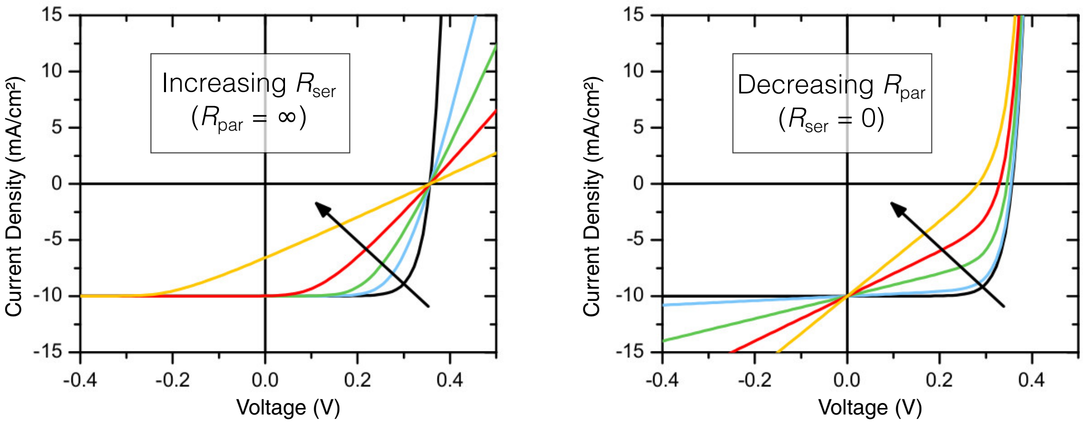

Figure 2.12.: Influence of serial and parallel resistances on the jV characteristic of organic solar cells. **Left:** An increasing serial resistance R_{ser} reduces FF and j_{SC} while $R_{\text{par}} = \infty$. **Right:** With $R_{\text{ser}} = 0$, a decreasing R_{par} leads to reduced FF and V_{OC}. Adapted from [148].

2.2.2. Deposition Techniques

Organic optoelectronic devices consist of stacked thin-films of organic materials, metal oxides, and metals. These layers have to be deposited using a method that gives good control over thickness, morphology, mixing ratio, structure, and homogeneity. Two fundamentally different deposition categories are used for device fabrication: gas or liquid phase deposition. The first case involves only the material (or precursors) aimed for deposition, either as a physical or a chemical vapour deposition. Liquid phase deposition involves many different techniques. All have in common that the target material is either a liquid or is dissolved/dispersed in a carrier solvent which has to be removed afterwards.

Both categories have advantages and drawbacks, which will be discussed for selected deposition techniques frequently used within this thesis. Additionally, upscaling is an important question to be raised. For mass production of OPV, deposition processes which are compatible with large area fabrication like roll-to-roll processing are needed. Information in this section is mainly based on the references [100], [289], and [263].

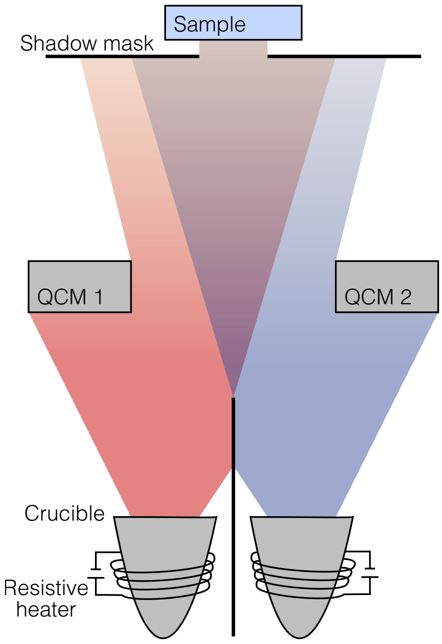

Figure 2.13.: Representation of thermal co-evaporation. Two materials are indepently heated and their evaporation rate is monitored by quartz crystal microbalances (QCMs). The coni of material flow overlap such that a mixture of the primal components condenses at the substrate.

Thermal Evaporation

Physical vapor deposition (PVD) is a deposition process whereby the material is transferred from solid phase into gas phase followed by a subsequent condensation on the substrate's surface. This process usually takes place in high vacuum ($p < 1 \times 10^{-5}$ mbar) to enhance the mean free path of the particle to a value greater than the distance source-to-sample. The particle transport is from ballistic nature, enabling the use of shadow masks for structuring. Many different PVD techniques exist. They are predominantly differentiated by the method of material desorption such as sputtering, electron beam evaporation, pulsed laser deposition, or arc evaporation.

In the case of *thermal evaporation*, the material – organic molecules or metals – is resistively heated in a crucible such that the sublimation temperature is exceeded. For this purpose, the decomposition temperature T_{dec} of the material has to be higher than the sublimation temperature T_{sub}. Typically, small molecule organic semiconductors are evaporable while polymers decompose because their T_{dec} is smaller than T_{sub}.

Thermal evaporation offers several advantages as compared to solution-processing. First, no carrier solvent is needed which increases the purity of the deposited materials. Second, the deposition rate and thickness can be monitored with quartz crystal microbalances (QCMs), allowing for high deposition accuracy down to 1 Å. Third, two materials can be deposited at the same time as shown in Figure 2.13. This so-called *co-evaporation* is used for depositing the BHJ with high control over the donor-acceptor ratio and for creating doped transport layers with ultra-low doping concentrations down to a molar ratio of 1×10^{-5}.[44] Nevertheless, some drawbacks exist: the need for (high) vacuum necessitates sophisticated tools and complicates sample handling.

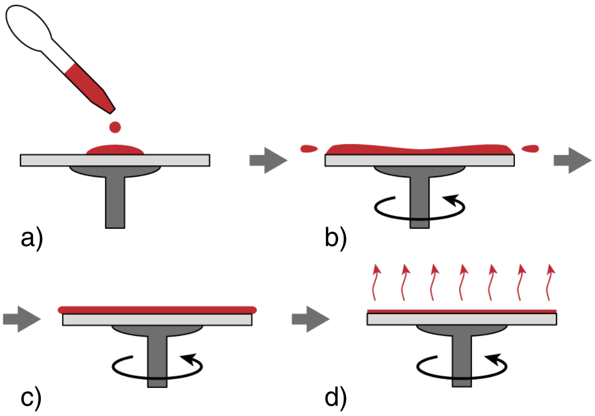

Figure 2.14.: Schematic representation of the spin coating procedure. **a)** The solution is dispensed onto a substrate that is mounted on a vacuum chuck. **b)** Upon chuck rotation, the solution spreads over the whole sample. **c)** By varying the spin speed, solution thickness can be adjusted. **d)** The solvent evaporates under continued sample spinning. Taken from [8].

Spin Coating

Figure 2.14 depicts the basic *spin coating* principle. A material-containing solution is dispensed onto a sample which is mounted on a rotatable chuck via vacuum suction. The chuck starts to rotate with a frequency f, leading to a homogeneous material distribution over the whole sample. With further increasing spinning frequency f, the thickness of the remaining solution is adjusted. Upon solvent evaporation, only a thin-film of material remains on the substrate. After spin coating, the sample is annealed to remove residual solvent. The final layer thickness d further depends on the initial solid content, the solution viscosity ν_0, and the solvent evaporation rate e according to a model reported by Meyerhofer.[298]

$$d \propto f^{-2/3}\, \nu_0^{1/3}\, e^{1/3} \tag{2.21}$$

Spin coating is a widely used liquid phase deposition technique and finds application in many lab-scale OPV manufacturing sites and in the microelectronics industry. Polymers like PEDOT:PSS or absorber materials are usually spin-coated as well as photo resists in photolithography. The main advantages are the easy process handling and good control over resulting film thicknesses over a wide range, from several micrometers down to nanometers. However, drawbacks are high material waste, as 90 % of the initial material is removed from the substrate during rotation. Furthermore, the substrate size is limited to approximately 8 inch, making spin coating not suitable for large-area device fabrication.

Spray Coating

Spray coating is a solution-based deposition technique whereby the material solution or dispersion (the *ink*) is atomized into small droplets which settle down in a continuous flow on a substrate. Two methods for atomization and droplet transfer are commonly used. Pressurized carrier gas (air or nitrogen) can be used to atomize the ink at the nozzle and blow it onto the substrate (Figure 2.15 a) or the nozzle vibrates with ultrasonic speed thereby atomizing the ink (Figure 2.15 b). No carrier gas is needed in this case.

Spray coating is highly promising for OPV fabrication. Advantages of spray coating are low material waste and good possibility of upscaling. It has been successfully utilized for all layers of an OPV device separately:

- **Transparent bottom electrode:** metal nanowires, highly conductive PEDOT:PSS [94, 118, 125]
- **Charge carrier transport layers:** zinc oxide, PEDOT:PSS, molybdenum oxide [59, 94, 146]
- **Absorber blends:** polymer:PCBM [104, 128]
- **Top electrode:** silver nanowires, silver nanoparticles [39, 108, 215]

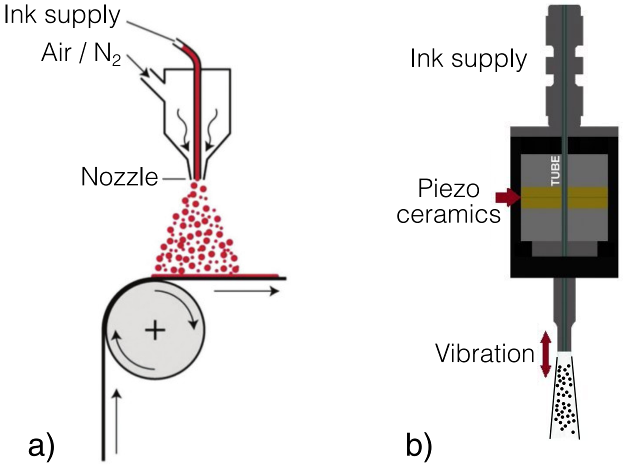

Figure 2.15.: Schematic spray coating process. **a)** Spray coating in a roll-to-roll setup with pressurized air for suction and atomization of the ink. Taken from [123]. **b)** Ultrasonic spray coating. The ink gets atomized through vibration of the tip with ultrasonic frequency. Adapted from `http://www.sonozap.com/Atomizer_HIW.jpg`, accessed on 04/07/2016.

Roll-to-Roll Processing

One key advantage of organic compared to inorganic electronics is the ability to use inexpensive, low-energy, large-scale fabrication methods. Roll-to-roll (R2R) processing is a fundamental technology enabling all the aforementioned aspects. A schematic representation is given in Figure 2.16. A polymer substrate (e. g. PET or PEN) is furled like wrapping film on a roll. Between unwinding and refurling the web on another roll, it successively runs through various processing steps including layer deposition, layer treatment, layer structuring, et cetera. This allows for high fabrication speed up to approximately 100 m/min.[26] Many solution-based processes are suitable for implementation in R2R fabrication lines, for example printing techniques (inkjet, screen, flexographic, or gravure printing), blade or slot-die coating, or spray coating. However, spin coating, the standard solution process in lab-scale device fabrication, is not transferable to R2R coating. A pioneer in the field of solution-processed R2R OSCs is Frederik C. Krebs from Denmark Technical University (DTU) who published many studies and also founded an OPV company (InfinityPV, Denmark).[109, 123, 162]

Thermal evaporation of organics can also be used in R2R fabrication, as successfully demonstrated by companies (e. g. Heliatek GmbH, Germany) and other research institutions.[42]

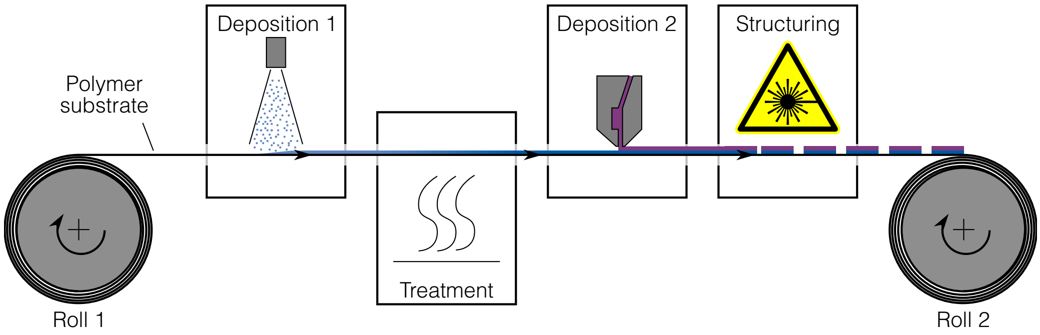

Figure 2.16.: Sketch of a roll-to-roll process. The substrate is transferred from roll 1 to roll 2. Inbetween, it runs through a plurality of processes for material deposition, post-treatment, structuring, et cetera. The depicted processes are chosen exemplarily.

2.2.3. Different Types of Organic Solar Cells

Figure 2.17 gives an overview of the temporal development of power conversion efficiency records. It is annually published by the National Renewable Energy Laboratory (NREL, USA). Common inorganic solar cells are depicted where maximum PCEs of nearly 50 % are reached for some very sophisticated and expensive concepts. Since the 1990s, organic solar cells have been monitored and significant improvements have been included from time to time. Over the last few decades, a huge variety of organic solar cell types emerged. They differ in many aspects such as the used organic material class (polymers or small molecules), the predominant layer deposition process (thermal evaporation or solvent-based processing), the solar cell architecture (single- or multijunction), et cetera. Below, widely used OPV types which will be used within this thesis are briefly introduced.

For the sake of being thorough, dye-sensitized solar cells (DSSCs) should be mentioned at this point. They were invented by Michael Grätzel et al. and utilize a slightly different concept than previously discussed.[197, 252, 278] A liquid electrolyte and a dye is used in combination with a mesoporous, nanocrystalline metal oxide layer, often titanium oxide (TiO_2). The charge carrier generation takes place at the dye-TiO_2 interface. Recently, the liquid dye is replaced by solid organohalide perovskites, reaching efficiencies close to 15 %.[92]

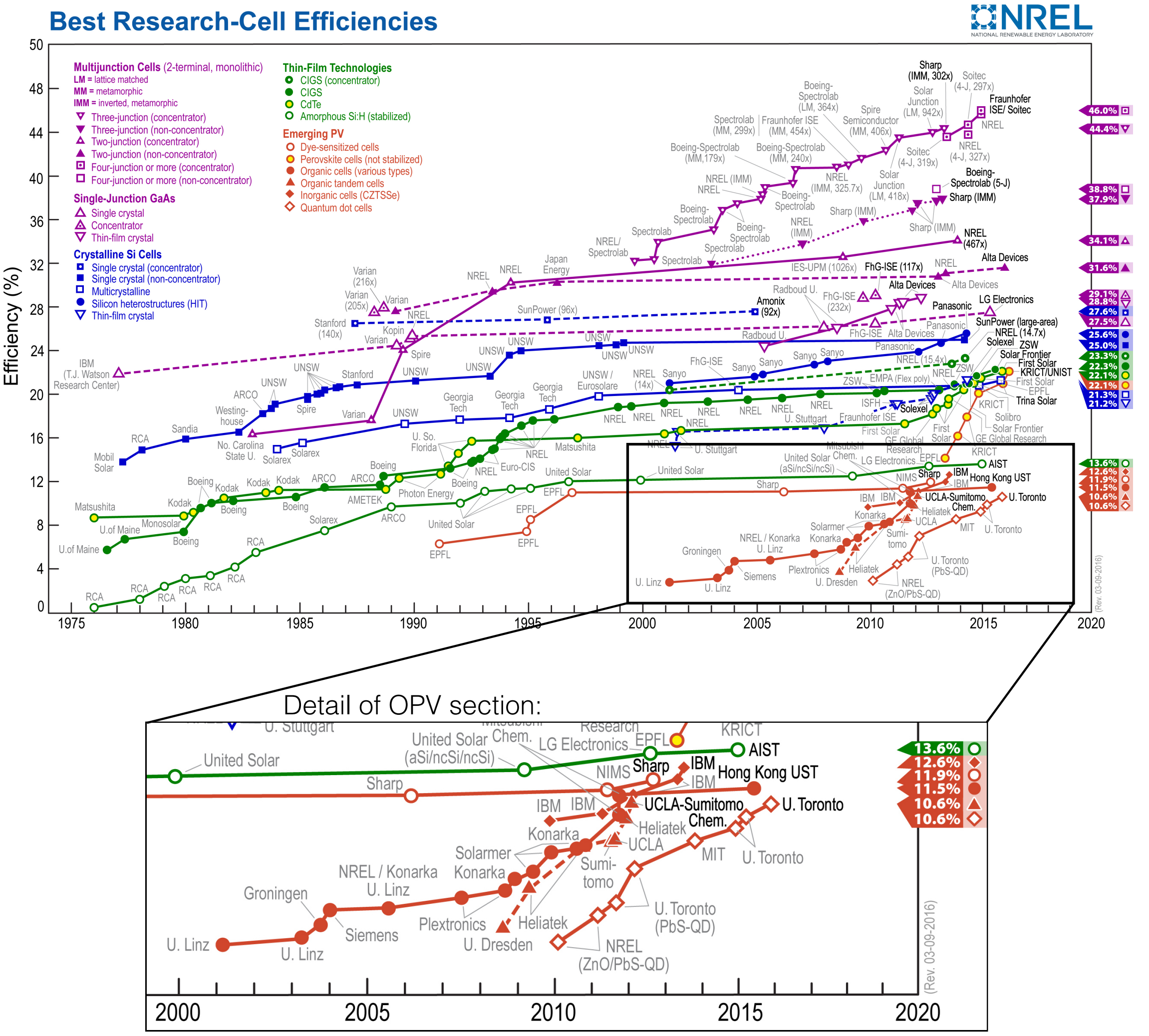

Figure 2.17.: Overview of record efficiencies of different solar cells from research laboratories. The efficiencies are confirmed by independent, recognized test labs. The section of emerging photovoltaics (including OPV) is enlarged in the detail view. This plot is courtesy of the National Renewable Energy Laboratory, Golden, CO. Version from year 2016.

Small Molecule Organic Solar Cells

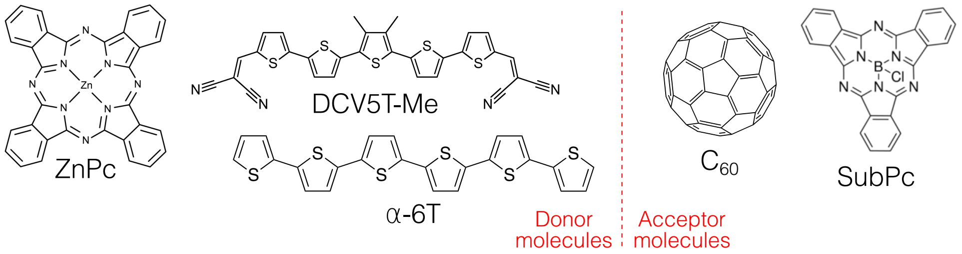

Figure 2.18.: Commonly used organic molecules as donor and acceptor in small molecule OPV.

A typical differentiation of OSCs arises from the nature of employed molecules. If organic semiconductors with a typical molecular weight smaller than approximately 1500 u are used, they are called *small molecules*. Common small molecules are usually monomers or oligomers. Some widely used materials and highly efficient donor molecules are depicted in Figure 2.18. The fullerene C_{60} is a frequent acceptor in combination with the well-studied zinc phtalocyanine (ZnPc) or the methylated oligothiophene derivative DCV5T-Me. Their low molecular weight allows for thermal evaporation in high vacuum, which is the commonly used deposition technique for small molecule OPV. A huge variety of solar cell architectures can be created, as different small molecules can easily be deposited one after another. Planar heterojunctions are possible as well as bulk heterojunctions which reach efficiencies up to 8.3 % in a single DCV5T-Me:C_{60} BHJ [72] and 10.4 % as multijunction with three stacked BHJs.[15]

However, also small molecule solar cells have recently been reported with solution-processed absorbing layers reaching efficiencies around 10 %.[27, 160] The record efficiency at the moment for an evaporated multijunction device is reported by Heliatek and lies at 13.2 %.[1]

Small molecules offer several advantages as compared to polymer materials; they will be discussed in the next section. The defined molecular structure allows for high purification, reproducibility, and low batch-to-batch variations. They usually exhibit higher hole mobilities than polymer donors and the molecular structure can be easily controlled for good energy level manipulation.[166]

A different architecture, which mostly employs small molecules, utilizes a cascade layer sequence of three or more organic absorber materials instead of a BHJ.[55, 180, 227] One example with four active layers is given in Figure 2.19.[60] Three donor materials with monotonically decreasing optical gap from anode to cathode transfer the excitons via Foerster processes to the donor-acceptor heterojunction. The cascade OSC with highest reported efficiency uses sexithiophene (α-6T, see Fig. 2.18) as donor and non-fullerene acceptor materials (SubNc[7], SubPc[8]) and reaches a maximum PCE of 8.4 %.[55] Further, these kind of solar cells can have high V_{OC} values, above 1 V.[88]

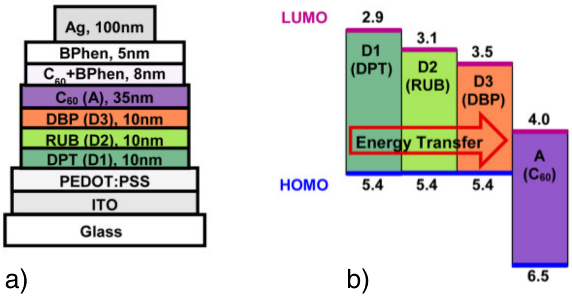

Figure 2.19.: A cascade organic solar cell comprising of three donor materials: diphenyltetracene (DPT), rubrene (RUB), and tetraphenyldibenzoperiflanthene (DBP). C_{60} is chosen as the acceptor layer. This solar cell architecture exhibit PCEs up to 7.1 %. **a)** Schematic layer sequence. **b)** Energy level diagram. Adapted from [60].

Polymer Organic Solar Cells

The second big group of organic materials are – in contrast to the small molecules – polymers with high molecular weight M_{w} greater than 50×10^3 g/mol. Famous examples of polymers are depicted in Figure 2.20. The absorbing layer commonly consists of a donor polymer in combination with a soluble derivative of C_{60} or C_{70}, namely phenyl-C_x-butyric acid methyl ester (PC_xBM with $x = 61$ or 71). Two examples of donor polymers are poly(3-hexylthiophene-2,5-diyl) (P3HT) and PTB7,[9] yielding efficiencies up to 4 to 5 % (P3HT) and approximately 10 % (PTB7).[24, 144, 165, 228] As the molecules are heavy compared to small molecules, it is not possible to deposit them via thermal evaporation. Their decomposition temperature is lower than their volatilization temperature resulting in damage before they evaporate from the crucible. Hence, the predominant deposition is carried out from liquid phase. It implies that the materials need to be soluble, impacting their molecular design. Halogenated solvents like chloroform or chlorobenzene are often used for dissolving donor-acceptor blends with high boiling point solvent additives (e. g. diiodooctane) which improve layer morphology. Recently, highly efficient single junction devices with halogen-free hydrocarbon solvents are reported yielding efficiencies up to 11.7 %.[19, 71] Two issues result in detrimental properties of polymers when compared to small molecules. On the one hand, if many layers are deposited one after another from solution, it is crucial to choose orthogonal solvents and/or insoluble layers for subsequently deposited layers. Otherwise, the sublayer might partially dissolve and mix with the actual layer. On

---

[7] boron subnaphtalocyanine chloride

[8] boron subphtalocyanine chloride

[9] The full chemical name is very long: poly[[4,8-bis[(2-ethylhexyl)oxy]benzo[1,2-b:4,5-b']dithiophene-2,6-diyl][3-fluoro-2-[(2-ethylhexyl)carbonyl]thieno[3,4-b]thiophenediyl]].

the other hand, exact control over polymer chain length is difficult. This leads to batch-to-batch variations of the polymer's molecular weight, significantly influencing the device performance.[70]

Poly-3,4-ethylenedioxythiophene doped with polystyrene sulfonate (PEDOT:PSS) is a water-dispersable polymer used as hole transport layer in a plurality of reported small molecule and polymer solar cells. The work function between 4.8 to 5.2 eV is suitable for providing good contact to the donor material and the anode. Further, its conductivity can be tuned from approximately 1×10^{-4} S/cm up to 4×10^{3} S/cm, making it suitable as an electrode itself (cf. Chapter 3).[47]

On the ETL side, polyelectrolytes like PFN[10] and others are often used as thin surface modifiers. The work function of the cathode is decreased due to the strong interface dipole of the polyelectrolytes.[144, 163]

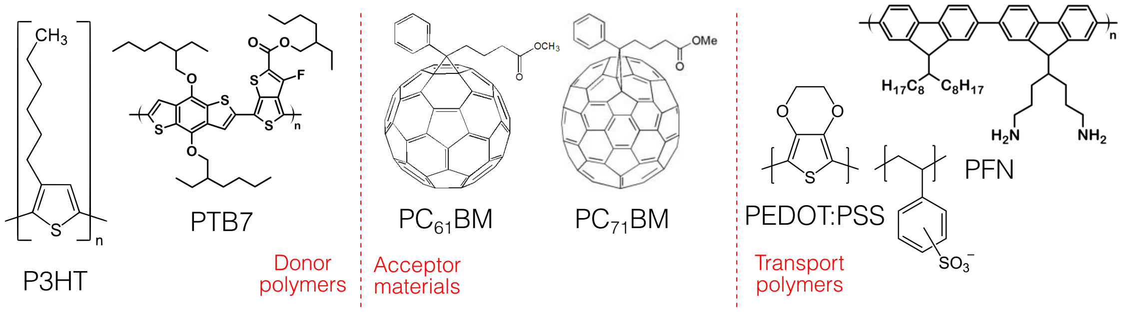

Figure 2.20.: Common organic molecules used in polymer solar cells as donor, acceptor, or charge carrier transport material.

Perovskite Solar Cells

The third discussed OPV technology – the perovskite solar cell (PSC) – is a rather new and rapidly growing research field. A drastic efficiency improvement has been observed from 3.8 % in 2009 [221] to over 10 % in 2012 [150]. Nowadays, it is already surpassing 20 %.[3] This solar cell type is based on a compound with a perovskite structure as depicted in Figure 2.21 (a) containing organic compounds in an inorganic backbone. A common perovskite for solar cell application is the methylammonium lead trihalide $CH_3NH_3PbX_3$ with X representing halogen atoms like iodine, bromine or chloride. Two PSC architectures are present: On the one hand, it is used as sensitizer in combination with mesoporous TiO_2 in DSSCs. On the other hand, flat layer architectures with perovskite thicknesses greater than 100 nm are used as presented in Figure 2.21 (b).

Similar to small molecule OPV, the perovskite can be deposited from liquid phase or via thermal co-evaporation which gives the free choice of optimal processing technology for the desired architecture and handling.

In contrast to small molecule and polymer OPV, the basic working principle seems to

---

[10] poly[(9,9-bis(3-(N,N-dimethylamino)propyl)-2,7-fluorene)-alt-2,7-(9,9–dioctylfluorene)]

be fundamentally different, although the community has not achieved a well-founded consensus. The nature of charge carrier generation is most likely *non-excitonic* because no interface for exciton dissociation is needed within the perovskite. The measured exciton binding energies are below or similar to the thermal activation energy $k_\mathrm{B}T$ at room temperature.[22]

Until now, the perovskite solar cell concept is not entirely ready for entering the market even if processing and material costs are promisingly cheap. Toxicity of lead, stability concerns and the issue of strong hysteresis have to be investigated, understood, and solved.[58]

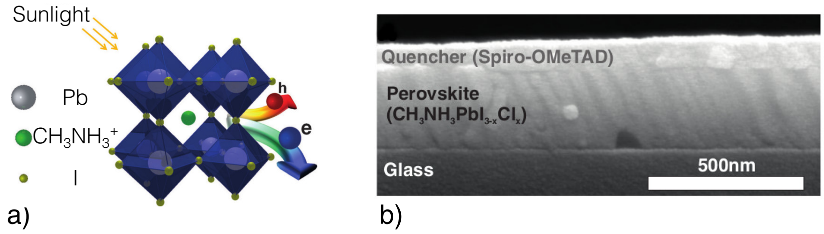

Figure 2.21.: a) Chemical structure of a perovskite crystal $CH_3NH_3PbI_3$ with a methylammonium cation in the center which is surrounded by 12 nearest-neighbor iodide ions. Taken from [22]. **b)** Cross-sectional SEM image of a thin-film perovskite solar cell. Taken from [124].

2.2.4. Degradation of Organic Solar Cells

Key properties for competitive OPV devices are not only sufficient efficiency and cheap mass production. At least of similar importance is a decent device lifetime. In the most extreme application scenario – in the jungle or a desert –, an OPV device must withstand high temperatures up to 60 or 70 °C, relative humidities (RH) up to 100 %, constant sun illumination and mechanical stress due to rain, wind, and dust deposit. All these factors make high demands on the OSC durability itself and on proper encapsulation.

In the following, typical degradation mechanisms are discussed and encapsulation technologies are introduced on the basis of the references [33, 145, 158, 232].

Degradation Mechanisms

Figure 2.22 displays possible degradation paths in OPV devices using the example of a polymer solar cell. Basically, two categories can be classified: *intrinsic* and *extrinsic degradation*.

If a device is kept under inert environment, for instance in an N_2 atmosphere or in vacuum, any degradation can be referred to *intrinsic* mechanisms. Photodegradation takes place when high energy photons (notably UV light) induce structural changes in organic layers or electrodes. This is especially crucial for polymers, which might occur in OSCs as substrate, electrode, donor, or transport layer. Donor polymer chains can break apart leading to a decrease in mobility and charge carrier generation. Polymer substrates like PET or PEN yellow and become brittle under UV illumination. A reduction of flexibility and transmission is a likely consequence. Also, migration occurs, activated by temperature or electric fields, independently from extrinsic factors. Indium migration from the indium tin oxide (ITO) transparent electrode is observed through nearly the whole device due to etching reactions with the adjacent acidic PEDOT:PSS layer. Further, aluminum migration from the top electrode into absorber blends is reported but can be slowed down by the insertion of metal oxide or organic interlayers.[184, 232]

A device that is kept in ambient air experiences ingress of oxygen and water molecules. This brings along a variety of *extrinsic* degradation pathways, additionally decreasing the device performance. Predominantly, water and oxygen ingresses through defects in the top electrode layer. Typically, these are holes of up to several micrometers in diameter, so-called *pinholes*. A first device deterioration happens already at the interface between top electrode (made from e. g. aluminum or silver) and subjacent organic layers. The electrode metal locally oxidizes to AlO_x or AgO_x. Due to a low adhesion of the metal on organic layers, the top electrode detachment leads to a reduced active device area.

If water and oxygen molecules diffuse further into the device, oxidation of the organic materials is possible. In interaction with incoming UV light, this effect is pronounced and known as photo-oxidation. The oxidation is additionally linked to their energy levels. Materials with a low ionization potential (e. g. n-dopants) are more prone to oxidation than p-type materials.

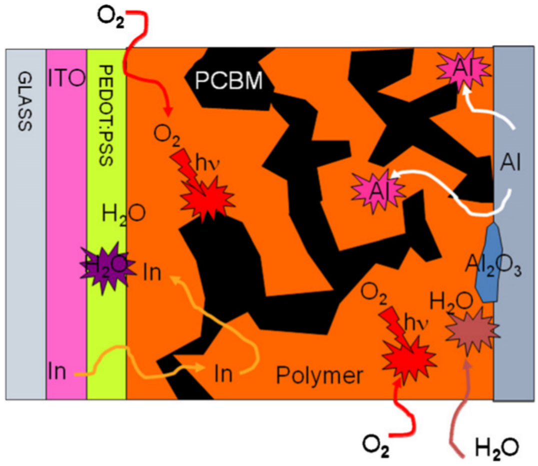

Figure 2.22.: Cross sectional view of an organic solar cell with a polymer:PCBM absorbing layer. Depicted are the many processes involved in device degradation. Taken from [232].

Encapsulation Technology

To efficiently prevent organic devices from water and oxygen ingress and thus increase the device lifetime, they have to be encapsulated. For this purpose, water and oxygen *barriers* are employed on both device faces. The barrier quality is often determined by the *water vapor transmission rate* ($WVTR$) which describes the amount of water diffusing through a certain barrier area in a certain amount of time. It is typically given in $\mathrm{g/(m^2\,d)}$. OPV devices require extremely low $WVTR$ values – already a water amount of $20\,\mathrm{mg/m^2}$ (roughly one drop of water) is able to decrease the active area of an OSC down to 50 %.[69] Figure 2.23 shows a comparison of $WVTR$ values required for various applications. For instance, OPV devices with 5 years of expected lifetime necessitate a value in the range of $1 \times 10^{-5}\,\mathrm{g/(m^2\,d)}$. The measurement of such low $WVTR$ values is challenging and takes long time. An extremely sensitive setup is needed that is well protected against environmental influences. Several techniques are known such as laser absorption, coulometrical measurement, mass spectrometry, tritium test, and electrical or optical calcium test. Within this thesis, the electrical calcium test is used for determining $WVTR$ values (see Experimental Section 5 for details). Moreover, additional impact factors have to be considered for applicable barrier technologies. For optoelectronic devices, at least one device side has to be transparent which necessitates barrier layers with high transparency. In addition, the barrier should be flexible to enable device flexibility, and materials should be non-toxic, inexpensive, and easily processable also on large area.

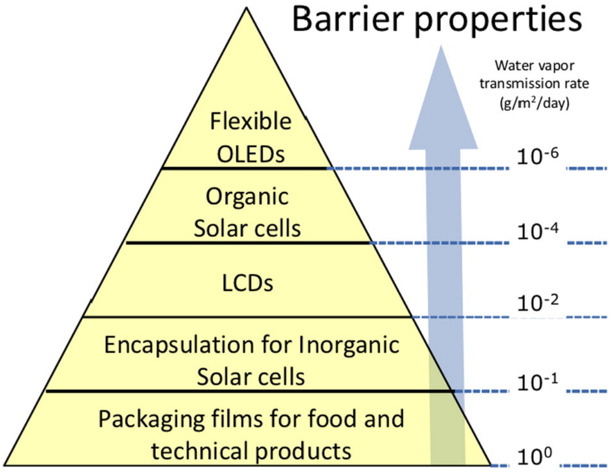

Figure 2.23.: $WVTR$ requirements of the barrier for various applications. Taken from [41].

Closing this section, a short overview of up-to-date barrier technologies is given. The most common encapsulation material is glass with $WVTR$ values lower than the resolution limit of most measurement techniques. It can be used as substrate itself and meets high transparency but has drawbacks in terms of rigidity and high weight. Single thin-film layers of metal oxides, for example alumina (AlO_x), provide low $WVTR$ values down to $1 \times 10^{-5}\,\mathrm{g/(m^2\,d)}$ and can be deposited via sputtering or conformal atomic layer deposition.[34, 122, 247, 262] They are highly transparent as well and additionally provide flexibility and light weight. However, the risk of having pinholes in the layer is high and is not reduced just by thickening the layers which would reduce flexibility and stability at the same time. Therefore, multilayer stacks are developed that make use of micrometer thick polymer interlayers to decouple multiple metal oxide layers from each other.[96, 277] Commercially available multilayer barriers are for example POLO® or BARIX®. Rather new technologies include nanoclay or graphene oxide flakes [90, 110] which provide only $WVTR$s in the range of $1 \times 10^{-3}\,\mathrm{g/(m^2\,d)}$ at the moment.

3. Basics of Transparent Electrodes

Within this chapter, an introduction to transparent electrodes (TEs) is given. Basic requirements and evaluation methods of TEs are discussed in Section 3.1. An overview about different technologies, classified in thin-films or structured films, is presented in Section 3.2. Section 3.3 is dedicated to silver nanowire (AgNW) networks. As the focus of this thesis is the optimization of AgNW networks in organic solar cells, a comprehensive description of percolation theory, synthesis, and state-of-the-art technology is given.

Nowadays, transparent electrodes are an important but invisible part of our life. Basically every electronic consumer product (flat screen displays, smartphones, digital indicators on watches or temperature sensors, et cetera) and even window defoggers need transparent electrodes. The first transparent conducting layers were discovered by Bädeker in 1907,[312] long before electronic products with transparent electrodes became widespread.

For organic optoelectronic devices, at least one transparent electrode is a necessary requirement. The light generated inside of an OLED needs to be outcoupled through the organic layers and electrodes. Organic photovoltaic devices require one transparent electrode sucht that light can enter the active layer. Moreover, two transparent electrodes can be used to create semitransparent devices, for example as application on windows or semitransparent roofs.[99, 121]

3.1. Requirements of Transparent Electrodes

Various properties need to be considered when evaluating a transparent electrode in view of competitive OPV. It is indisputable that optical and electrical properties have to be optimized. However, they are not independent from each other: an optimization of one parameter often negatively affects the other one. These interdependencies are shown in the following.

Generally speaking, a high optical transmittance in the active spectral region of a device is needed. For example, OLEDs need a high electrode transmittance at the emission wavelengths. In OSCs, sun emission needs to be considered additionally to device absorption. Figure 3.1 shows the spectral irradiance of the sun under AM1.5G

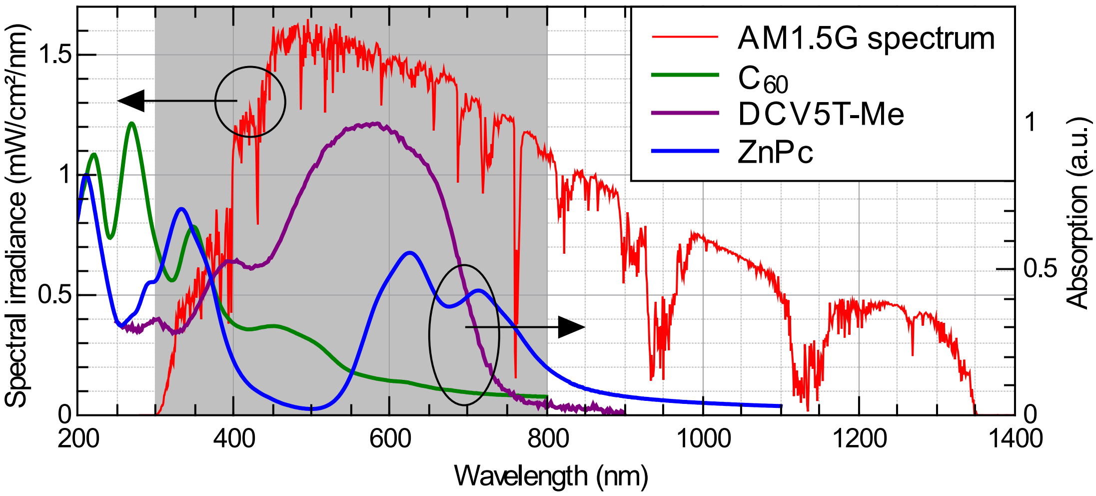

Figure 3.1.: Spectral irradiance of the sun under AM1.5G condition and absorption spectra of C_{60}, DCV5T-Me, and ZnPc (cf. Section 4.1 for long names). These small molecules are frequently used as absorber materials within this thesis.

condition and absorption spectra of small molecule absorbers employed within this thesis. The required spectral region of the electrode transparency is determined by the spectral overlap of sun emission and device absorption, as illustrated by the grey area. It approximately covers the visible part of the spectrum from 300 to 800 nm.

The transmission T can be described by the ratio of electromagnetic radiation intensity before entering (I_0) a layer on one side and after leaving (I) it on the other side. It equals an exponential decay of intensity through a layer with thickness d and absorption coefficient α (the BEER-LAMBERT law) as follows:

$$T(\lambda, d) = I/I_0 = e^{-\alpha(\lambda)\, d} \; . \tag{3.1}$$

Consequently, a high electrode transmission is obtained by minimizing the absorption coefficient α, which is a material property, or reducing the layer thickness d. A criterion for electrode transmission is rather simple: as high as possible. Industry came to the agreement that an electrode technology in OPV should have a transmission T greater than 90 % to be competitive in most applications of optoelectronic devices.[179, 195]

For improving the electrical properties of transparent electrodes, a high conductivity is favorable. On the basis of Equation 2.6, the conductivity σ is linearly proportional to the free charge carrier concentration $n_{\mathrm{e/h}}$ and the mobility $\mu_{\mathrm{e/h}}$. Nonetheless, the benchmark for determining the electrical performance is the sheet resistance R_{S} which depends on electrical conductivity σ and film thickness d:

$$R_{\mathrm{S}} = \frac{1}{\sigma\, d} \qquad [R_{\mathrm{S}}] = \Omega/\square \; . \tag{3.2}$$

In order to maximize the electrical performance, R_{S} needs to be minimized. This is possible by raising conductivity σ, thickness d, or both. At this point, it gets obvious

that T and R_S are competing against each other due to the conflictive impact of the layer thickness d.
Stating a maximum value for the sheet resistance tolerable in TE applications is not as easy as in the case of the transmission. It can be condensed into the following question: what R_S of the TE is needed to transport charge carriers over a certain distance without significantly deteriorating the device performance by a voltage or current drop?
Several publications address this issue by performing equivalent circuit modeling as well as experimental verification.[120, 209, 212, 220] Equation 3.3 is derived to associate a power loss density P_TE in dependence on the sheet resistance R_S of the electrode.

$$P_\mathrm{TE} = \frac{1}{\beta}\, R_\mathrm{S}\, L^2\, j_\mathrm{SC}^2 \tag{3.3}$$

Hereby, L is the length of the device in respect to the current collector contact and β is a factor that considers the geometry if the device is interconnected in a module. For a single device with one collector contact, β equals 3.[209]
Lungenschmied et al. report that a cell length of 1 cm leads to efficiency losses of 5 % with a transparent electrode R_S of 15 Ω/□ while a R_S of 60 Ω/□ results in a PCE loss of 26 %.[237] Schubert et al. calculated a necessary sheet resistance of 10 Ω/□ for a width of 38.8 mm to keep efficiency losses below 1 %.[120]
Nevertheless, it is possible to extend OPV device area over the above stated lengths without further reducing R_S or accepting efficiency losses. A common way is to insert highly conductive but opaque metal grids as intermediate current collector. This kind of metal grid is usually called *busbar* in large area solar cell modules.[141, 179, 209] In this case, the distance of the busbar fingers determines the maximum sheet resistance of the transparent electrode. It has to be considered as well that the insertion of these busbars leads to a device shadowing, which reduces the effective active area and thus the perfomance. A calculation of T is given in Equation 3.8. Consequently, a carefully chosen balance between busbar density and sheet resistance of the transparent electrode is needed. Jacobs et al. recently reported on the impact of busbars on OPV performance.[11] They conclude that it is better to include busbars and thereby reduce R_S requirements of the TE to enhance the electrode's transparency.

Apart from a high transparency T and a low sheet resistance R_S, further factors are relevant for the application transparent electrode.
First, an OPV application under outdoor conditions not only requires OSC stability, as discussed in Section 2.2.4, but also a stable transparent electrode under light exposure, humidity, and heat. Second, a flexible organic device necessitates a flexible transparent electrode as well. This further enables cost-effective processing via R2R methods.
Third, organic photovoltaics is meant to be a *green* technology. This is fulfilled on the one hand by producing renewable energy, but on the other hand by using earth-abundant, non-toxic, recyclable resources with energy-saving fabrication processes.

Consequently, a *sustainable* transparent electrode technology needs to fulfill the same requirements.[138]
Fourth, the total OSC layer thickness is often below 100 nm with single layer thicknesses down to 5 nm. This requires a low roughness of the electrode to prevent shunts and short circuits.

3.1.1. Figure of Merit

From the discussion of crucial requirements for transparent electrodes, it becomes clear that an evaluation of TE suitability in organic devices is complex. A comparison of different electrode technologies is not easily possible as every technology exhibits advantages and disadvantages in different domains. To overcome this issue, an evaluation factor called *figure of merit* (FOM, Φ) is introduced. The aim is to obtain one value that states the electrode perfomance. Transmission and sheet resistance are chosen as starting points.
A first proposal of a FOM was made by Haacke.[299] He simply calculated the ratio of T and R_S leading to

$$\Phi_\mathrm{H} = \frac{T^x}{R_\mathrm{S}} \overset{3.1,\,3.2}{=} \sigma\, d\, e^{-x\,\alpha\, d}\ . \tag{3.4}$$

By adding the exponent x with $x > 1$, the transmittance could be assessed with regard to the specific application requirement. Usually, x equals 10 because it leads to a optimum film thickness for $T = 90\,\%$, which previously has been stated to be the minimum requirement for a transparent electrode. In Figure 3.2, Φ_H values are plotted for different metals and transparent conductive oxides (TCOs) (see Sec. 3.2) using the absorption coefficient α at 550 nm. It shows that ITO outperforms metals in terms of Φ_H by roughly one order of magnitude. The TCO thickness is for maximum Φ_H values a thousand times higher than for metals. Moreover, the theoretical optimum for metals is at thicknesses below 2 nm. Growth of continuous metal films for such small thicknesses is almost impossible.[76]
In conclusion, the model of Haacke is based on a rather arbitrary definition and leads to unrealistic perceptions of optimal layer thicknesses.

Consequently, a different model for the FOM is needed that is thickness independent and is more generally valid. De et al. reintroduced a formula based on the work of Glover and Dressel that relates T and R_S to each other in the following way: [196, 275, 307]

$$T(\lambda, R_\mathrm{S}) = \left(1 + \frac{Z_0}{2\,R_\mathrm{S}}\,\frac{\sigma_\mathrm{op}(\lambda)}{\sigma_\mathrm{dc,b}}\right)^{-2}\ . \tag{3.5}$$

Hereby, Z_0 is the vacuum impedance (377 Ω) and $\sigma_\mathrm{dc,b}$ is the electrical conductivity of bulk-like thin-films. The optical conductivity σ_op is related to the absorption coefficient α via $\sigma_\mathrm{op} \approx 2\alpha/Z_0$ in first order.[210] The FOM Φ_De is defined as the ratio between

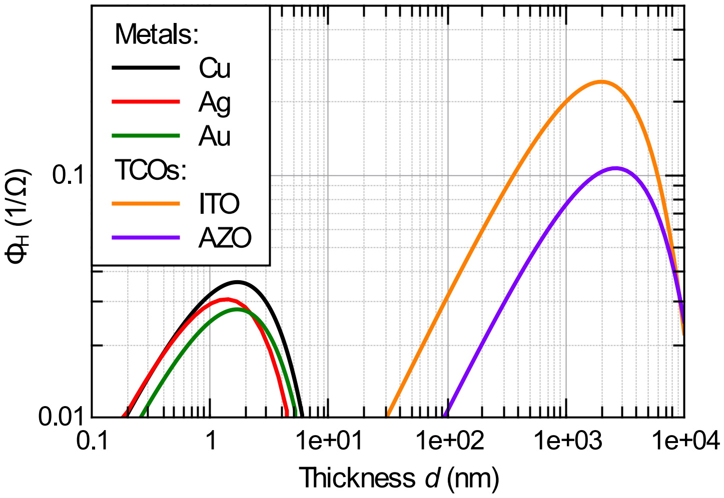

Figure 3.2.: Figure of merit Φ_H of different metals and doped metal oxides. For calculation, absorption coefficients at 550 nm wavelength are taken from `http://refractiveindex.info/`, accessed on 04/25/2016. Electrical conductivity values are taken from `https://webelements.com`, accessed on 04/25/2016 (Au, Ag, Cu), [303] (ITO), and [244] (AZO).

electrical and optical conductivity $\Phi_{De} = \sigma_{dc,b}/\sigma_{op}$ and is only dependent on material properties.

If a substrate has to be taken into account, Equation 3.5 is modified to

$$T(\lambda, R_S) = \frac{16n^2}{(1+n)^2}\left((1+n) + \frac{Z_0}{R_S}\,\frac{\sigma_{op}(\lambda)}{\sigma_{dc,b}}\right)^{-2} \tag{3.6}$$

with the refractive index n of the substrate.[133] However, Equation 3.5 and 3.6 are only valid for bulk-like thin-films. In case of percolation-type electrodes (cf. Section 3.3), the T-R_S dependency follows different mechanisms such that further modifications are necessary. These are described in Section 3.3.

Two concluding comments are given at this point. First, defining a reasonable wavelength for $T(\lambda)$ always depends on the electrode application and their spectral region of interest. Hence, a general comparability of electrode technologies among themselves is not possible. Many publications use $T(\lambda = 550\,\mathrm{nm})$ assuming a more or less homogeneous spectral distribution over the important spectral region, which is not always given.

Second, although Equation 3.5 is used for evaluation in many publications,[137, 170, 196] deviating FOM definitions exist.[133] A unification or standardization has not happened up to now. Therefore, a direct comparison of FOM values stated in different publications is not possible.

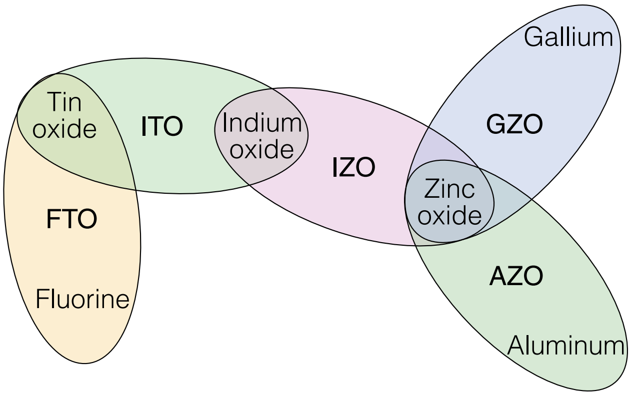

Figure 3.3.: Various TCO combinations typically used as thin-film transparent electrode: fluorine-doped tin oxide (FTO), indium tin oxide (ITO), indium-doped zinc oxide (IZO), gallium-doped zinc oxide (GZO), and aluminum-doped zinc oxide (AZO).

3.2. Transparent Electrode Types

A huge variety of transparent electrode technologies exist today with many different properties and application areas. It is possible to classify them by the materials used, mainly leading to three categories:

- **Metal-based systems:** Thin metal films, metal grids and nanowire networks, dielectric-metal-dielectric sandwiches
- **Transparent conductive oxides (TCOs):** doped metal oxides
- **Carbon-based systems:** PEDOT:PSS, graphen, carbon nanotubes (CNTs), highly n-doped C_{60}

However, it is shown later in this thesis that the geometry can be a crucial factor for the OSC performance, depending on whether the electrode is a thin-film or a structured one. For this reason, TEs are categorized in the following by their geometry.

3.2.1. Thin-Films

Thin-film transparent electrodes consist of laterally continuous thin layers or layer stacks. In this case, the TE material combines the functionalities of transparency and conductivity.

Inorganic Thin-Films

A widely used group of thin-film TEs is *transparent conductive oxides* (TCOs).[257] They usually consist of an n-type semiconducting metal oxide such as tin oxide (SnO_2), zinc oxide (ZnO), or indium oxide (In_2O_3). The bandgap E_G of these metal oxides is greater than 3 eV such that they are transparent in the visible part of the spectrum. To increase the intrinsically low free charge carrier concentration n_e, doping with other metals or metal oxides (e. g. aluminum, indium, fluorine, gallium, et cetera) is applied. Figure 3.3 lists some well-known examples of those TCOs: indium tin oxide (ITO), aluminum-doped zinc oxide (AZO), fluorine-doped tin oxide (FTO), gallium-doped zinc oxide (GZO), and indium-doped zinc oxide (IZO). Doping enhances n_e to values in the range of $1.5 \times 10^{21}\,\mathrm{cm}^{-3}$.[137, 258, 286] With mobilities of 20 to $100\,\mathrm{cm}^2/(\mathrm{V\,s})$, indium tin oxide (ITO) exhibits a conductivity of approximately $5 \times 10^{3}\,\mathrm{S/cm}$.[137, 303]. For thicknesses in the range of 100 nm, TCOs offer a sheet resistance down to $25\,\Omega/\square$ at a transparency over 85 % in the visible spectrum. In the near infrared region, transparency is reduced due to collective plasma excitation of the charge carriers according to the Drude model.[137] All in all, Φ_De values for TCOs are in the range of 120 to 240.

These outstanding optical and electrical properties are responsible for an overarching use of TCOs in most applications with transparent electrodes. ITO is thereby the most common material. It is implemented in many kinds of flat-panel displays, low-emissivity coatings,[296] and thin-film photovoltaics.

Nonetheless, ITO and other TCOs also have some significant drawbacks. First, they are brittle such that their performance on flexible substrates is reduced or even destroyed under strain or repeated bending, as shown in Figure 3.4 (left).[169, 186, 224] This property makes ITO unsuitable in flexible device applications.

Second, especially indium is a scarce element. As Figure 3.4 (right) illustrates, worldwide production steadily increases, but the statistical reserve coverage is estimated to be only 17 years.[167, p. 45] Thus, the price increased significantly in the past 20 years with negative effect on the device fabrication cost. Nowadays, roughly one fourth of module fabrication cost is related to the ITO electrode.[138]

Another inorganic representative is *thin metal electrodes* (TMEs). Typical metals like silver (Ag), aluminum (Al), or gold (Au) exhibit very high free charge carrier concentrations which are greater than $5 \times 10^{22}\,\mathrm{cm}^{-3}$, but only average mobilities of 10 to $50\,\mathrm{cm}^2/(\mathrm{V\,s})$. The resulting bulk conductivity $\sigma_\mathrm{dc,b}$ of at least $3 \times 10^{5}\,\mathrm{S/cm}$ is two orders of magnitude higher than in TCOs. However, in thin metal films, the conductivity is lower as compared to the bulk due to electron scattering on the surfaces and grain boundaries.[304, 305] Metals exhibit high absorption coefficients above $5 \times 10^{5}\,\mathrm{cm}^{-1}$ such that the transmission at a film thickness of 50 nm is already below 10 %. This results in typical TME thicknesses of 6 to 20 nm where the TME still transmits more than 70 % of the light.[121, 238, 249]

Two different layer architectures are commonly used. On the one hand, single TME films exhibit high R_S values but transmittances below average.[80, 265] On the other hand, a metal layer is sandwiched between two metal oxide layers, which enhance the optical transparency due to a favorable light interference.[107, 121, 238, 249] In both cases, morphology control over the metal layer is the crucial factor for obtaining a

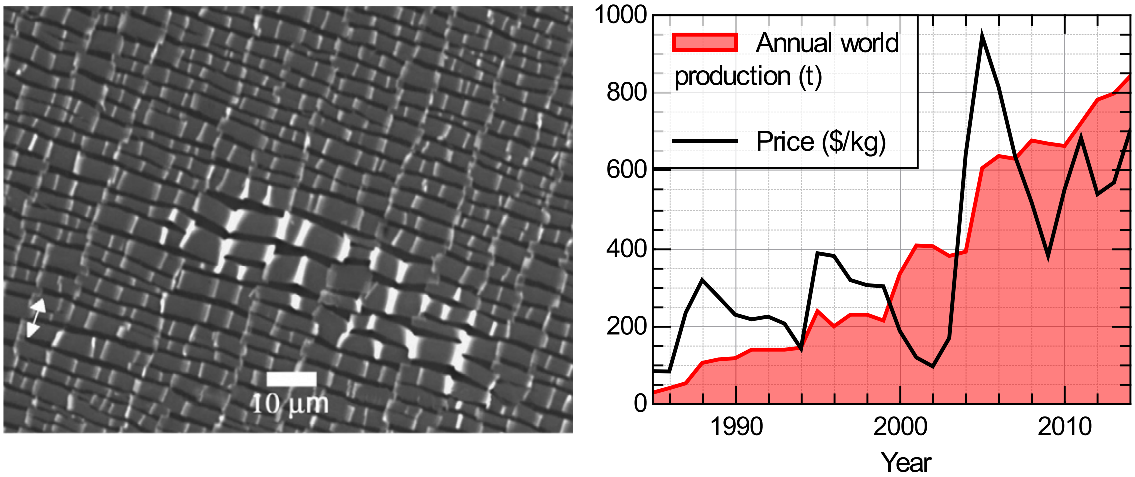

Figure 3.4.: Left: SEM image of cracks and delamination of ITO on a PET substrate. The sample has been strained by 6 %, the arrow indicates strain direction. With permission from [224]. **Right:** Development of indium price and world production. Data from `http://minerals.usgs.gov`, accessed on 04/19/2016.

good electrode perfomance. Unfavorable island-like growth of the metal is prevented by inserting an ultrathin seed layer into the stack. It enhances substrate wetting of the metal and dramatically improves growth behavior, conductance, and transparency.[76, 121, 310]

Very low sheet resistances of TMEs down to 3 Ω/□ are reported.[249] However, in comparison to TCOs, the transparency is lower and spectrally more narrow. This results in FOM values between 90 and 240.

Organic Thin-Films

Beneath metals or metal oxides, also organic materials are used as transparent thin-film electrode. A prominent representative is *PEDOT:PSS*. It has been already introduced as HTL (Section 2.2.3) that covers a wide range of conductivities. PEDOT is a conductive polymer mixed with the insulating PSS (ratios ranging from 1:2 to 1:10), serving as doping counterion and solubilizer in water.[201]

For the application as transparent electrode, the conductivity needs to be maximized to meet the requirement of low R_S values with a simultaneously high transparency. Different routes have been reported improving conductivity. The addition of high boiling point solvents like ethylene glycole (EG) or dimethylsulfoxide (DMSO) in a volume fraction of 5 to 10 % in respect to the dispersion leads to a strong phase separation of PEDOT and PSS during solvent evaporation. By applying further post-treatment steps, conductivities up to 1400 S/cm are reported.[132, 171] High metal-like conductivities above 3500 S/cm have been reported using vapor phase deposition (in this case without PSS addition) or a solution-shearing method.[47, 139]

Through its solution-processibility, PEDOT:PSS is easily deposited and also the transfer to R2R-compatible processes has been demonstrated.[37, 123] Once the PEDOT:PSS layer is dry, it is rather insoluble in common organic solvents. This makes it a common choice when depositing subsequent layers from solution.

However, PEDOT:PSS has also some unfavorable properties. Its sheet resistance is often above $100\,\Omega/\square$ [154, 171] at a transparency greater $90\,\%$, which leads to a relatively low Φ_{De} value below 50. This necessitates additional busbar or metal grid implementation for large area solar cells. Furthermore, PSS is acidic. Reports show that PEDOT:PSS might be an additional factor of OSC degradation when used as HTL, standalone electrode, or in combination with silver nanowires.[31, 37, 79, 232]

Two further organic thin-films are briefly mentioned at this point. Figure 3.5 depicts one very promising representant: *graphene*.[170, 190, 236] It is a two-dimensional material consisting of a planar honeycomb carbon structure and provides a two-dimensional electron gas at room temperature, leading to high electron mobilities greater than $5 \times 10^3\,\mathrm{cm}^2/(\mathrm{V\,s})$.[137] Due to its thinness, it also provides a high transparency of $97.7\,\%$ per monolayer and homogeneity in the visible light spectrum.

In terms of sheet resistance, pure graphene is inferior to other TE technologies because of a rather low charge carrier concentration of only $0.3 \times 10^{21}\,\mathrm{cm}^{-3}$ leading to R_{S} values above $100\,\Omega/\square$.[137, 194] However, the conductivity can be enhanced via doping. Bae et al. report a R2R-processed graphene-based electrode. Via wet-chemical doping with nitric acid, they achieved a remarkable performance of $30\,\Omega/\square$ at $90\,\%$ transmission excluding the substrate (cf. Fig. 3.5 right). This results in a Φ_{De} value of 115.[192]

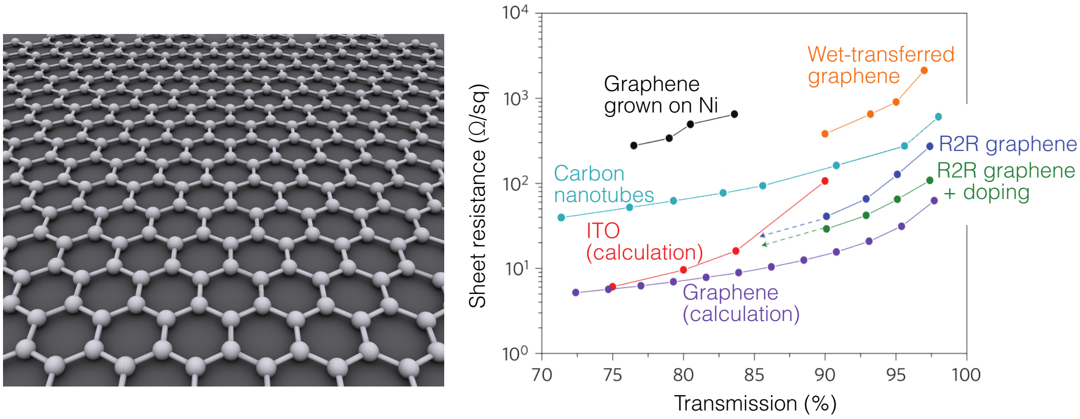

Figure 3.5.: Left: Graphene. Courtesy of AlexanderAIUS under Creative Commons license BY-SA 3.0. Taken from `https://de.wikipedia.org/wiki/Graphen/media/File:Graphen.jpg`, accessed on 04/17/2016. **Right:** Sheet resistance vs. transmission plot of different graphene processes and other transparent electrodes for comparison purposes. Adapted from [192].

Moreover, the fullerene C_{60}, which is commonly used as acceptor molecule and electron transport material, is reported as transparent electrode.[120] As it usually exhibits very low conductivities, doping has been utilized to achieve a conductivity of $5\,\mathrm{S/cm}$ and a resulting sheet resistance of $10\,\mathrm{k}\Omega/\square$. The transmittance for the doped C_{60} layer has been greater than 70 %. Despite low electrode performance ($\Phi_{\mathrm{De}} < 1$) and limited OSC efficiency, the publication is a proof of principle for using evaporated organic small molecules as transparent electrode.

3.2.2. Structured Transparent Electrodes

Metal can be employed as transparent electrode even if the thicknesses are greater than 50 nm. Structural changes have to be made to still contain transparency. Instead of using a material that is transparent and conductive at the same time, like in the case of thin-films, the functionality is spatially divided. The highly conductive metal efficiently transports charge carriers while voids inbetween the material let the light pass trough. A nanostructure needs to be employed to achieve this kind of transparent electrode.

Commonly, two approaches are established for realizing nano-structured films. On the one hand, one- or twodimensional, periodic metal grids are used as shown in Figure 3.6 (left). Several methods emerged for fabrication, often using nanoimprint lithography [84, 233] in combination with physical vapor deposition [65, 172] or solution-processed formation of silver nanoparticles.[13, 36] On the other hand, randomly distributed, disordered structures are reported, which will be discussed below.

Transparent electrodes made from metal grids often exhibit very good optical and electrical properties, reaching Φ_{De} values up to approximately 500. Rosamond et al. reported a gold grid TE with R_{S} of 3.1 Ω/□ and a transmission of 84 % excluding the substrate.[178] Basic formulas for the calculation of sheet resistance and transmission are displayed in Equation 3.7 and 3.8. The metal grid is represented with thickness t,

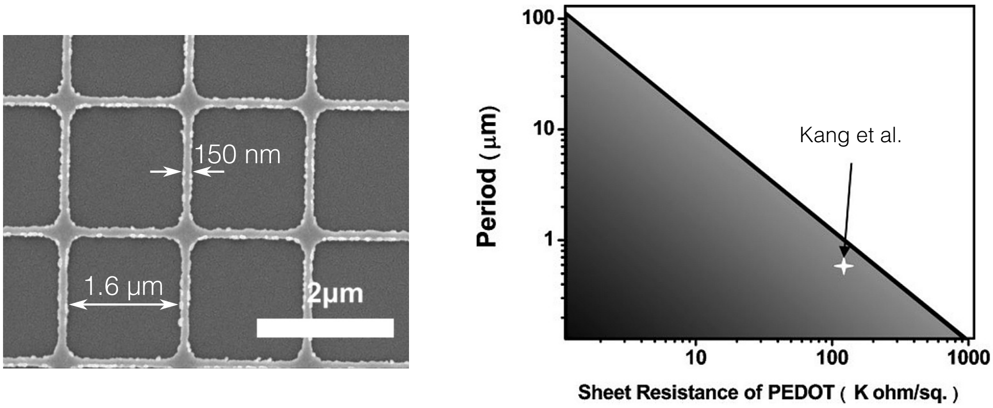

Figure 3.6.: Left: A metal grid fabricated via thermal evaporation of 60 to 100 nm silver and transfer process from prestructured polyurethane acrylate mold. With permission from [84]. **Right:** Calculated performance loss in dependence on grid period p and the sheet resistance of the filler material (PEDOT:PSS in their case). In the grey area, losses are negligible while losses are significant in the white area. With permission from Kang et al.[233]

width w, periodicity p, and bulk conductivity $\sigma_{\mathrm{dc,b}}$ of the material.

$$R_{\mathrm{S}} = \frac{1}{t\,\sigma_{\mathrm{dc,b}}}\,\frac{p}{w} \tag{3.7}$$

$$T \propto \frac{w}{w+p} \tag{3.8}$$

Note, that the transmission is strongly simplified and only considers metal grid geometry, plasmonic activity and scattering are neglected. On the one hand, metal structures in the nanoscale generate surface plasmons that are likely to further reduce the transmittance. On the other hand, based on optical simulations, Zeng, Kafafi, and Bartoli reported that surface plasmon excitation can be used to strongly enhance absorption in the active layer of organic solar cells.[91]
Although the performance of metal grids is outstanding, the implementation in organic solar cells requires substantial considerations. The fabrication involves many steps and is therefore error-prone, time-consuming, and expensive. Furthermore, grid thicknesses are usually greater than 60 nm, making a planarization necessary. The distance between the grid lines reaches from several micrometers up to several millimeters.[51, 103] In the case of large distances, the space inbetween has to be filled with an intermediate transparent conductive material to efficiently transport charges to the metal grid, similar to the busbar and R_{S} requirement discussed in Section 3.1. As shown in Figure 3.6 (right), Kang et al. provided a calculation of necessary filler sheet resistance in dependence on metal grid period p. For PEDOT:PSS, which was used in this publication, it is rather simple to achieve a necessary R_{S} value to prevent losses, as PEDOT:PSS is able to provide low R_{S}. However, low conductive filler materials require a small period, which consequently leads to a lower grid transmission (cf. Equation 3.8).

In contrast to ordered metal structures, many approaches use randomly distributed microstructures. The fabrication is more simple, as nano- or microscale building blocks are utilized. For example, Han et al. take inspiration from nature and use real leaf or spiderweb networks as metallization template for the fabrication of transparent electrodes.[61] The leaf electrode is shown in Figure 3.7 and nicely visualizes the random, quasi-fractal structure. High Φ_{De} values greater than 1000 are reported for this kind of network (excluding the substrate). A similar approach of metallizing nanostructures is reported by Wu et al. who use an electrospun polymer fiber web as template. The so-achieved *nanotrough* network exhibit lengths up to 1 mm and high optoelectrical performance ($< 10\,\Omega/\square$ at $> 90\,\%$ transmission).[130]

Another representant of randomly structured TEs are nanowires and nanotubes. Usually, they consist of isolated nanowires or nanotubes in dispersion or gas phase that are deposited in plane on a substrate. They form an interconnected *percolative* network that is electrically conductive. Two material systems are used to obtain this

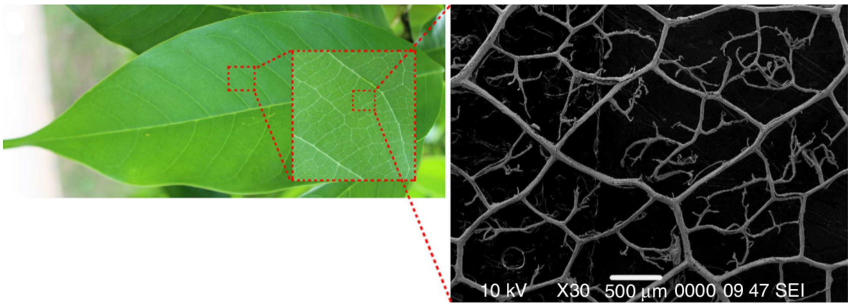

Figure 3.7.: Bio-inspired transparent electrode. The quasi-fractal structure relates to the leaf veins. With permission taken from [61].

kind of TE: on the one hand, *carbon nanotubes* with diameters and lengths of 1 to 10 nm and 3 to 20 µm are used, respectively.[49, 147, 259] These CNT networks are not as conductive as systems previously introduced due to a high contact resistance between the tubes. Sheet resistances down to 50 to 100 Ω/□ are achieved at 80 to 90 % transmission.[49, 198] An example of a CNT network is shown in Figure 3.8 (left). Dr. Franz Selzer (IAPP) implemented CNT networks as bottom electrode into OSCs within his PhD thesis.[38]

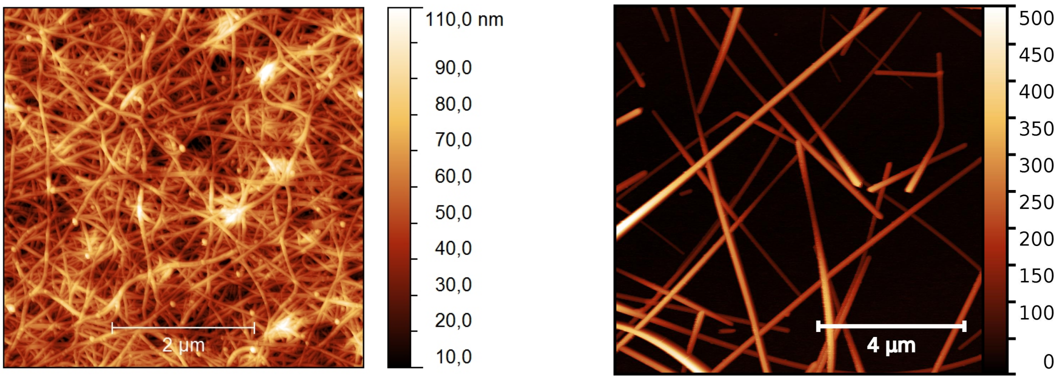

Figure 3.8.: Atomic force microscopy image of a **Left:** CNT (courtesy of Dr. Franz Selzer) and **Right:** AgNW network (scalebar in nm).

A further promising technology utilizes metallic nanowires as transparent electrode. Figure 3.8 (right) depicts such a network. Similarly to CNTs, metallic nanowires are randomly deposited on a substrate via liquid-phase methods like spin, spray, or dip coating and form a conducting network via percolative processes. Several metals are reported for this purpose, mainly silver,[111, 211, 234] copper,[7, 119, 177] and recently nickel.[14]

The implementation of metallic nanowires in organic solar cells has already been reported: For copper nanowires (CuNW), a small number of articles are published. Efficiencies reach 3 to 4 % with small molecule and polymer solar cells.[48, 119] In case of silver nanowires (AgNWs), polymer solar cells with AgNWs as bottom electrode with efficiencies up to 8.6 % are reported.[28, 29] However, with small molecules as

absorbing layer, efficiencies stay below 5 %.[6, 82, 234] The implementation as top electrode is reported as well.[108, 203] For polymer-based solar cells, the processing does not need further modifications and can be done in air. In contrast, for small molecule OSCs, AgNWs need a modification to be dispersed in solvents that do not harm the organic materials. Selzer et al. reported the use of a highly fluorinated ether as solvent for AgNW dispersions and successfully demonstrated OPV with AgNW top electrodes.[39]
As silver nanowires are a substantial element of this thesis, the next section discusses AgNW electrodes in detail.

3.3. Silver Nanowire Networks

In 2008, Lee et al. first reported the implementation of randomly distributed silver nanowire networks as transparent bottom electrode. They raised several points like thermal annealing, optical simulation, and planarization, as well as building OPV devices as proof of principle. Nowadays, the research in silver nanowires is a broad field of interest with applications to OPV and OLED devices,[28, 56] touch panels,[149] and transparent heaters.[106] Key advantages of silver nanowire electrodes are facile synthesis, low production and fabrication cost, and the ability of simple upscaling due to solution-based deposition methods.

This section gives an overview over silver nanowire networks as a special case of randomly structured transparent electrodes. The formation of a conductive network by randomly located silver nanowires is grounded on percolation theory. It will be described in Section 3.3.1 as basic theoretical model and also in the aspect of real nanowire networks. Furthermore, the standard route of template-free AgNW synthesis, which is the foundation of AgNWs used in this thesis, is outlined (Section 3.3.3). In a last part (Section 3.3.4), basic properties of AgNW networks and challenges to overcome are summarized and a short state-of-the-art review is given.

3.3.1. Percolation[1]

The formation of a conductive network by randomly located silver nanowires in two dimensions (e. g. on a substrate) can be described with the mathematical model of *percolation theory.* First percolative models were considered by Flory and Stockmayer in the 1940s, who described gelation processes of single molecule clusters to large macromolecules. The name 'percolation theory' first appeared in a publication of Broadbent and Hammersley in 1956 [306] and originates from the latin word *perco-*

---

[1] This chapter is based on the book 'Introduction to Percolation Theory' by D. Stauffer and A. Aharony.[292]

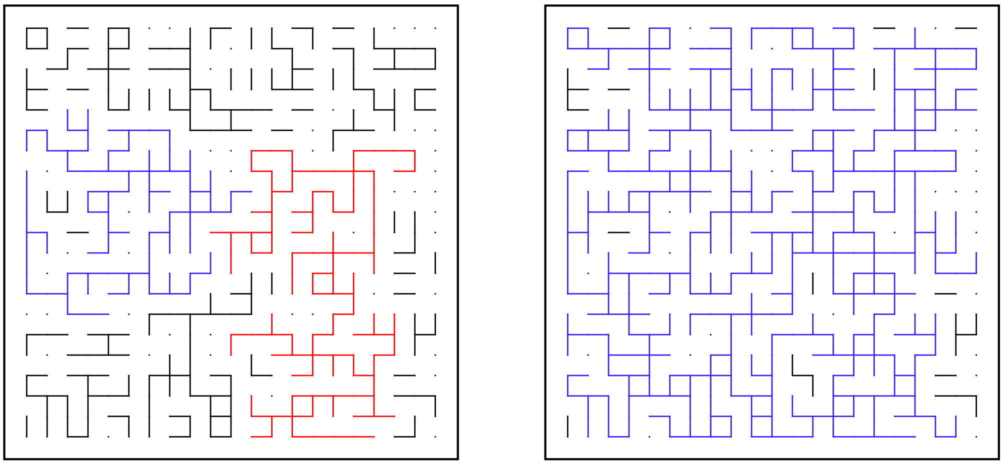

a) $p = 0.45 < p_c$ b) $p = 0.55 > p_c$

Figure 3.9.: Bond percolation of a 21 × 21 point grid in two dimensions with different connection probability p. Large clusters are colored. **a)** $p = 0.45$ is smaller than the percolation treshold $p_c = 0.5$. Many isolated clusters are present. **b)** $p = 0.55$ is above percolation threshold p_c. One large cluster emerges, reaching all borders of the grid.

lare, which means to filter, to interfuse, or to permeate. Percolative processes and phenomenons can be observed in manifold examples covering nature (e. g. forest fires), society, physics, chemistry, and even our daily life is pervaded with percolation theory: a cup of coffee comes off by water trickling through a porous coffee powder volume.[193] The basic problem of percolation is described with the help of a simple model, visualized in Figure 3.9. A twodimensional grid consists of $n \cdot n$ points, which are connected to a nearest neighbor with the probability p, independently of its neighbors. If connected, a *bond* is formed between two points. The probability that a bond is open equals $1 - p$. A continuous connection of bonds is called a *cluster*; two larger clusters are colored in Figure 3.9 (a). At a critical connection probability p_c, the *percolation threshold*, the clusters get so large that they all get connected and percolate through the whole area, which is shown in Figure 3.9 (b) as the blue cluster. p_c strongly depends on the geometry of the grid. The example of bond percolation in a 2D square lattice gives $p_c = 1/2$.

For $p > p_c$, the probability that an arbitrary point belongs to the huge cluster is given by

$$P(p) \propto (p - p_c)^{\beta} \tag{3.9}$$

with $P(p)$ reflecting the 'strength of the network'. The *critical exponent* β is defined by convergence of Equation 3.9 for $p \rightarrow p_c^+$ and depends on the specific percolation system.

3.3.2. Conductivity of Silver Nanowire Networks

The concept described in Section 3.3.1 can be adapted to describe the electrical conductivity σ_{dc} of a percolating system with conductive bonds. It seems obvious that σ_{dc} follows a similar law as Equation 3.9 but with a different exponent μ because dead ends of pathways do not contribute to the overall conductivity. Using Kirchhoff's current law leads to

$$\sigma_{\mathrm{dc}} \propto (p - p_{\mathrm{c}})^{\mu} \ . \tag{3.10}$$

For nanowire networks, the percolation problem gets more complicated: instead of fixed bond locations, the AgNWs are randomly distributed in location and orientation with a wire density N_{A}. This leads to a *continuum percolation* that can only be solved using numerical methods like Monte-Carlo simulation.[301] If two nanowires overlap at any point, they are connected electrically. 'Percolation' happens when it is possible to find at least one pathway from one side of the covered area to another. Two example networks are shown in Figure 3.10. The exemplary contact pads need to be connected by a continuous path to be over the percolation threshold. Fig. 3.10 (a) is below percolation while the network in Fig. 3.10 (b) percolates. In the latter case, the conductivity σ_{dc} equals

$$\sigma_{\mathrm{dc}} \propto (N_{\mathrm{A}} - N_{\mathrm{A,c}})^{\alpha} \tag{3.11}$$

with the percolation threshold density $N_{\mathrm{A,c}}$ and α as another critical exponent. This equation is only valid for $N_{\mathrm{A}} > N_{\mathrm{A,c}}$ close to the percolation threshold. D. Langley stated $\alpha = 4/3$ for ideal 2D percolating stick systems.[30] Obviously, $N_{\mathrm{A,c}}$ has to be dependent on the wire length, as longer nanowires have a higher ability to connect with wires more far away. A calculation of $N_{\mathrm{A,c}}(l)$ for a 2D stick system is given in the following equation:[53, 300]

$$N_{\mathrm{A,c}} = \left(\frac{4.236}{l}\right)^2 / \pi \ . \tag{3.12}$$

The above used σ_{dc} is a network parameter and is smaller than the bulk-like thin-film conductivity $\sigma_{\mathrm{dc,b}}$. However, while adding more and more wires to the network ($N_{\mathrm{A}} \gg N_{\mathrm{A,c}}$), a transition will take place where the network behaves like a bulk with $\sigma_{\mathrm{dc}} = \sigma_{\mathrm{dc,b}}$. De et al. report the development of σ_{dc} by introducing an equivalent network film thickness d.[196] Figure 3.11 (left) depicts the conductivity measurements of AgNW networks for different film thicknesses d. An equation for $\sigma_{\mathrm{dc}}(d)$ in this regime is given as

$$\sigma_{\mathrm{dc}}(d) = \sigma_{\mathrm{dc,b}} \left(\frac{d}{d_{\mathrm{min}}}\right)^n \ . \tag{3.13}$$

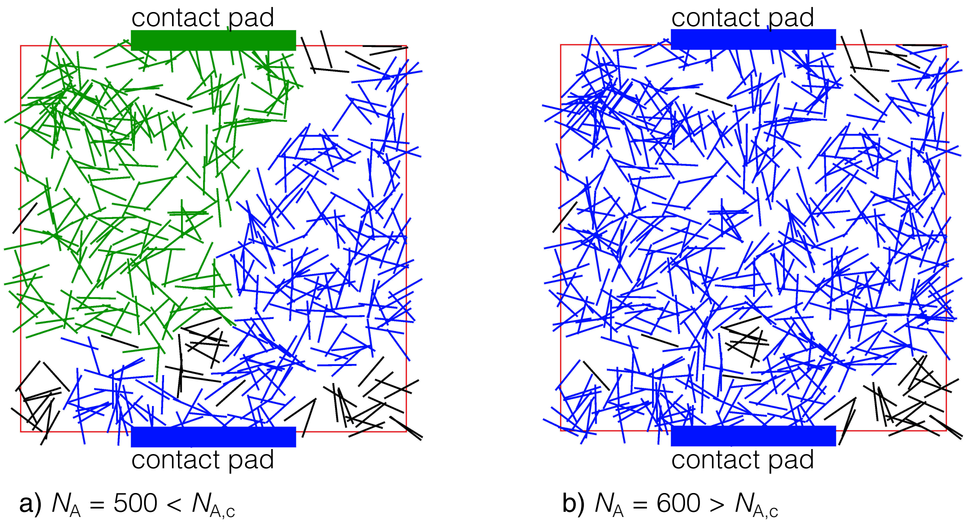

Figure 3.10.: Schematical nanowire network with density N_A in one unit area, the nanowire length l equals 0.1 length unit. With Equation 3.12, $N_\mathrm{A,c}$ equals 571. Every NW that is connected to one of the contact pads has the same color as the respective contact pad. **a)** N_A is below the percolation threshold. No continuous path exists between the two contact pads. **b)** With a density N_A greater than the percolation threshold, both contact pads are connected through a nanowire pathway.

The increase in Equation 3.11[2], which follows a power law, is now slowed down until $d = d_\mathrm{min}$, which is the thickness where transition from percolative to bulk-like behavior occurs.
Considering the percolation behavior of the network as discussed above, a modification of Equation 3.5 for the dependence on T and R_S is derived by substituting $\sigma_\mathrm{dc,b} \rightarrow \sigma_\mathrm{dc}$ in Equation 3.2 and leads to the following expression with a new *percolative figure of merit* Π:

$$T = \left(1 + \frac{1}{\Pi}\left(\frac{Z_0}{R_\mathrm{S}}\right)^{1/(n+1)}\right)^{-2} \tag{3.14}$$

$$\Pi = 2\left(\frac{\sigma_\mathrm{dc,b}/\sigma_\mathrm{op}}{(Z_0\, d_\mathrm{min}\, \sigma_\mathrm{op})^n}\right) . \tag{3.15}$$

Consequently, the T-R_S behavior of percolative networks close to the 'sweet spot' for electrode application ($10\,\Omega/\square$ at $90\,\%$ transmission) can be described by the two Equations 3.5 and 3.14. Figure 3.11 (right) displays for different percolative systems like AgNWs, carbon nanotubes, graphene, or silver flakes that experimentally obtained data fits well with the calculated dependence.[196] In the percolation regime, significant differences occur for different network types while the behavior in the bulk regime is very similar and only shifted by the R_S regime.

---

[2] This equation can also be written in terms of equivalent film thickness: $\sigma_\mathrm{dc} \propto (d - d_\mathrm{c})^n$. d_c is the thickness above which percolation sets in.[196]

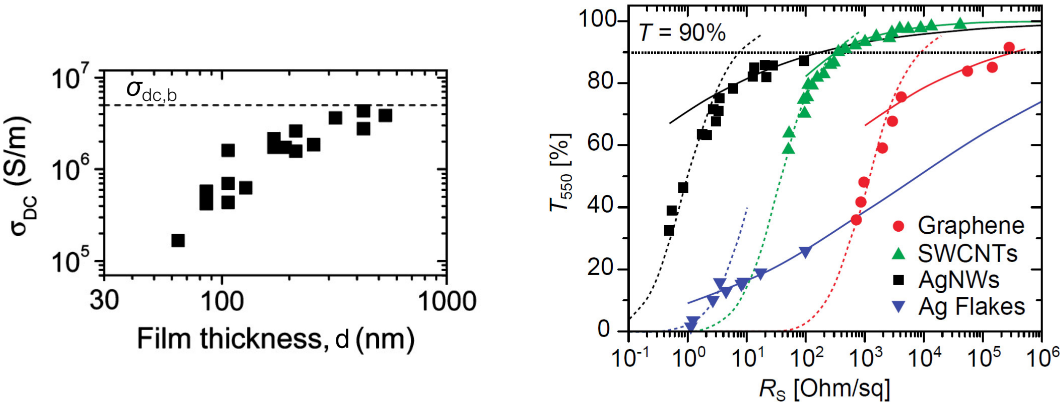

Figure 3.11.: Left: Silver nanowire network conductivity σ_{dc} in dependence on equivalent film thickness d. The dashed line represents the bulk conductivity of silver (5×10^6 S/m). **Right:** Plot of transmission at 550 nm wavelength over sheet resistance R_{S} for different network types. The solid line represents percolative fits according to Equation 3.14, the dotted lines are fits with the thin-film equation (Eq. 3.5). Adapted with permission from [211] and [196]. Copyright 2009 and 2010 American Chemical Society.

3.3.3. Synthesis of Silver Nanowires

Many methods are known to fabricate metal nanowires with diameters smaller than 100 nm, which are reviewed by D. Natelson.[268] Used techniques cover *top-down* approaches like electron beam lithography, step-edge and molecular beam epitaxy templating, or nanotube templating. Also *bottom-up* methods are reported, e. g. electrodeposition into etched porous media, strain-mediated self-assembly, or step-edge decoration. A boost in research with metal nanowires started when Y. Sun and B. Wiley reported a polyol route for direct chemical synthesis of silver nanowires utilizing the all-round polymer polyvinylpyrrolidone (PVP).[260, 276] Many subsequent publications dealing with silver nanowires for electrode applications use variations of the AgNW synthesis proposed by Sun et al.[50, 142, 189] As also the silver nanowires used within this thesis are synthesized following the aforementioned route, the synthesis is sketched in Figure 3.12 (a) and briefly summarized in the following.

1. Silver nitrate ($AgNO_3$), oxidizing scavenger iron chloride ($FeCl_3$), and capping agent PVP are merged in 160 °C hot ethylene glycole (EG), the polyol. EG serves as solvent and reduction agent at the same time that reduces the silver salt to neutral silver.

2. The silver atoms nucleate and form nanoparticles with different forms and shapes, for instance single crystal cubooctahedrons or multi-twinned particles (MTPs). As only decahedral, fivefold MTPs are required for further steps, the oxidizing agent etches unwanted nanoparticles and prevents undesired oxygen etching.

3. PVP caps anisotropically on the MTP due to a higher affinity of PVP to the (100) face of the MTP. PVP prevents growth of the MTP in (100) direction

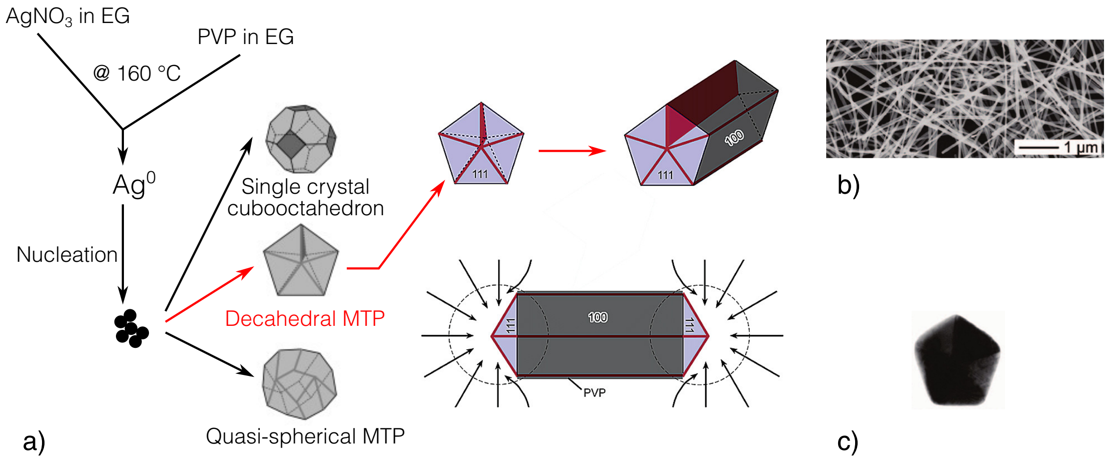

Figure 3.12.: a) Polyol synthesis of silver nanowires. **b)** SEM image of AgNWs. **c)** TEM cross-section of a fivefold twinned nanowire. Adapted with permission from [272], [260] and [241]. Copyright 2003 and 2007 American Chemical Society and 2005 John Wiley and Sons.

leading to further silver adsorption only in (111) direction. This results in the growth of silver nanowires.

4. The dispersion is washed several times for attenuating the PVP shell, removing residuals, and exchanging the solvent to a desired solvent (e. g. ethanol, isopropyl alcohol, or water) for further processing steps. Figure 3.12 (b) depicts an SEM image of the final AgNWs. The fivefold, pentagonal shape of the AgNWs is contained during the whole synthesis, as shown by the TEM image in Figure 3.12 (c) (no scale is given in the article).

This synthesis route allows for silver nanowires with approximately 20 to 200 nm diameter, adjusted by variation of AgNO$_3$ and PVP ratio and reaction temperature.[134, 188] The length, reported by Sun et al., did not exceed ≈ 50 µm. Nowadays, synthesis of very long AgNWs with a length up to 500 µm is reported employing a modified multistep growth.[149, 151] Yields for AgNW synthesis are very high with values of 70 % in the original article of Sun et al. and even 99 %, reported by Zhu et al.[188] This simple, fast, and scalable synthesis of ready-to-use dispersions, high yield, and low cost materials make this route for AgNW fabrication suitable for commercial applications.

3.3.4. Properties, Challenges, and State-of-the-Art Technology

This section discusses basic properties and recent progress of silver nanowire networks. Several challenges that occur during implementation of AgNWs into organic devices are presented and state-of-the-art solutions are described.

In general, the geometrical shape of AgNWs is responsible for electrical as well as optical properties.[134] It is favorable to achieve an aspect ratio, meaning the ratio of length to diameter, that is as high as possible. Currently, aspect ratios greater than 1000 are reported.[21, 151]

Optical Properties

Figure 3.13 shows the total and diffuse transmission in the visible wavelength regime for nanowires with different diameters. The spectral shape in the wavelength regime between 440 and 800 nm is homogeneous, leading to a greyish impression for the bare eye. However, around 350 nm, a strong absorption dip occurs that strongly depends on the diameter. This dip is associated with collective electron oscillations, called localized surface plasmon resonances. The transverse plasmon mode is responsible for it while the longitudinal plasmon mode leads to an absorption at approximately 2600 nm.[174] Furthermore, AgNW electrodes are transparent in the near infrared regime up to 2000 nm. At 1500 nm, the transmission of ITO decreases to 35 % while AgNWs stay at 80 %.[137, 199]

Another important optical property is the scattering of silver nanowires. Depending on AgNW diameter, light passing through the AgNW layer is scattered into different angles. The amount of scattered light reaches between 7 and 10 % depending on diameter and wavelength (cf. Fig 3.13 right).

Plasmonic activity and scattering can be utilized to optimize the absorption in OPV devices.[191] On the one hand, scattered light leads to an increased light path length through the active layer and therefore enhances absorption. On the other hand, a near-field enhancement is expected via finite difference time domain calculations.[45, 105, 174] Wang et al. experimentally show an absorption enhancement and thus an increase in OPV device efficiency.[45] Khanarian et al. report Mie theory as basis for calculating the scattering of AgNW networks.[105]

Conductivity Optimization

The sheet resistance R_S of the AgNW network is determined by resistive contributions of the nanowire itself and the junction resistance between two nanowires. With Pouillet's law, the nanowire resistance can be approximated by the resistance of a conductive cylinder.

$$R_\mathrm{wire} = \frac{4\,l}{\sigma_\mathrm{wire}\pi\, d^2} \tag{3.16}$$

For wire diameters smaller than approximately 100 nm, the conductivity is restricted due to 2D confinement of the electrons. Electron scattering at the metal surface reduces the conductivity such that $\sigma_\mathrm{wire} < \sigma_\mathrm{dc,b}$. Dingle and Chambers calculated the conductivity σ_wire for thin metal wires using the electron mean free path λ_e and the scattering strength q_S, which is between 0 (diffuse scattering, high losses) and 1

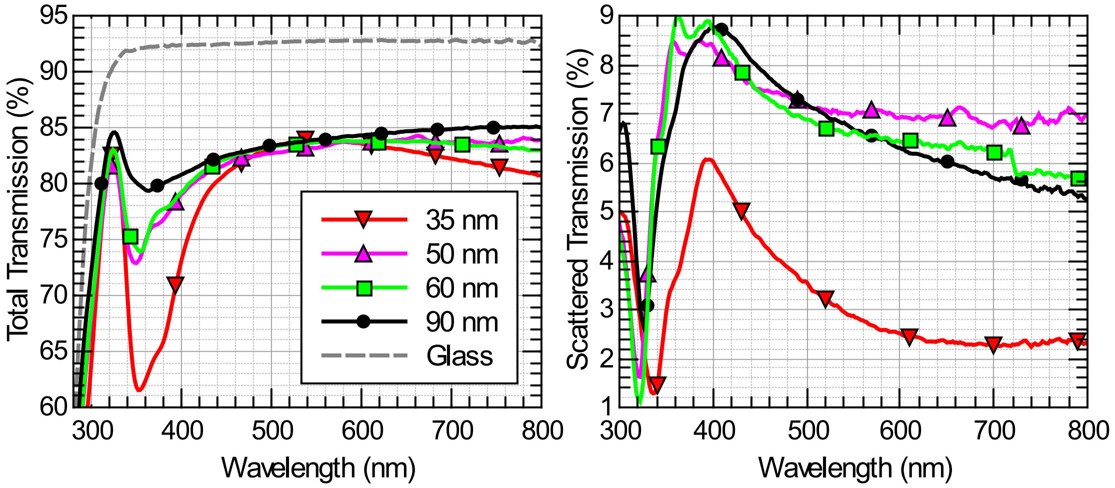

Figure 3.13.: Transmission of silver nanowires with different diameters. **Left:** Total transmission T_t. **Right:** Scattered transmission ($T_\mathrm{s} = T_\mathrm{t} - T_\mathrm{d}$) with direct transmission T_d.

(specular scattering, low losses):[308, 309]

$$\sigma_\mathrm{wire} = \sigma_\mathrm{dc,b}\left[1 + (1 - q_\mathrm{S})\frac{\lambda_\mathrm{e}}{d}\right]^{-1} . \tag{3.17}$$

For silver nanowires with a diameter of 100 nm and 40 nm, σ_wire is approximately 3.6×10^5 and 0.8×10^5 S/cm, respectively.[17, 276] Values of $R_\mathrm{wire}(d = 100\,\mathrm{nm})/l \approx 4.4\,\Omega/\mu\mathrm{m}$ and $R_\mathrm{wire}(d = 40\,\mathrm{nm})/l \approx 99.5\,\Omega/\mu\mathrm{m}$ are obtained with Equation 3.16. Dr. Franz Selzer (IAPP) reported the direct measurement of the silver nanowire resistance R_wire for wires with $d = 90$ nm and found good agreement ($R_\mathrm{wire} = (4.96 \pm 0.18)$ $\Omega/\mu\mathrm{m}$).[17]

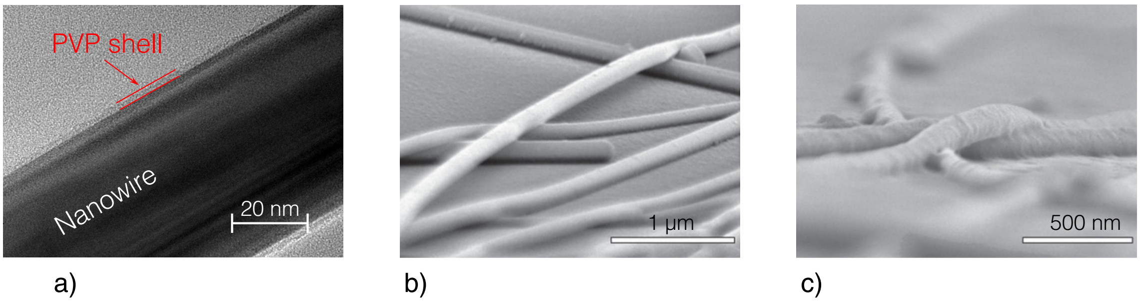

a)

b)

c)

Figure 3.14.: a) Transmission electron microscopy image of silver nanowire and PVP shell. Courtesy of Dipl. Chem. Luisa Sonntag (TU Dresden). **b)** and **c)** Scanning electron microscopy images of AgNWs and junctions before (a) and after (b) post treatment (in this case, a nanosoldering step was executed). Adapted with permission from [114].

However, not only the nanowire resistance but also the junction resistance is of particular importance for the overall network conductivity. After AgNW synthesis, a several nanometer thick layer of the insulating PVP remains around the wires (Figure 3.14 a). Thus, it hinders the charge carrier transport between the wires and leads to an initial junction resistance with large and unpredictable spread of the R_S values.[46] Consequently, post treatment methods have to be applied to reproducibly minimize the sheet resistance. A simple and successful annealing step has already been introduced by Lee et al. in the first publication of silver nanowires as transparent electrode.[234] At elevated temperatures (200 °C for $d = 100$ nm), the PVP ligand shell desorps and silver nanowires merge together.[30, 118] Nevertheless, in view of flexible transparent electrodes, flexible polymer substrates like PET or pPEN destabilize or even melt at temperatures above 120 °C, making such a high temperature unsuitable for these kind of substrates. Therefore, alternative approaches are developed that give similar results at lower temperatures or even room temperature. N. Weiß et al. (IAPP) report a humidity-assisted low temperature ($\leqq$ 80 °C) fusing of silver nanowires because of the hydrophilic nature of PVP.[46] Garnett et al. make use of self-limited plasmonic activity of silver nanowires.[142] By short and highly intense white light illumination, the nanowires heat up at the junctions and fuse together. F. Selzer et al. (IAPP) facilitate a thin polymeric sublayer that leads to enhanced hydrophobic interaction between substrate and silver nanowires already at room temperature.[82] Another room temperature process is introduced by Lee et al. who nanosolder the silver nanowires with PEDOT:PSS.[114] Figure 3.14 (b), (c) show the AgNW network before and after fusing, respectively.

Roughness Reduction

Another unwanted property of AgNW networks is its inherently high roughness. As nanowires necessarily overlap to form electrical connections, the height at a junction is roughly twice the height of a single nanowire. For example, a diameter of 90 nm leads to a junction height of 180 nm. Considering that the thickness of organic layers is below 100 nm, such electrode steps are fatal for a well working device, as shunt paths or short circuits get present.

This issue has been adressed in many publications about AgNW electrodes in organic devices.[75, 94, 169, 234] Using PEDOT:PSS as hole-transporting planarization layer is a frequently applied technique for planarization.[28, 45, 94, 118, 234] However, as stated previously (Section 3.2.1), the acidic and hydrophilic nature of PEDOT:PSS may lead to a worsening of the electrode and/or the device lifetime.[31, 37, 79] PSS is reported to be the driving force of degradation in PEDOT:PSS. Consequently, attempts have been made to either neutralize PEDOT:PSS [52] or to utilize a dry transfer to keep the PSS-rich side of the PEDOT:PSS layer away from other organic layers.[66] The reports show improved stability, but do not investigate the influence of continuous illumination and climate.

Further planarization methods without PEDOT:PSS are reported that employ low conductive metal oxides, e. g. zinc oxide or titanium dioxide.[85, 173, 176]

A different way of planarization is carried out in recent publications by burying the silver nanowires in an insulating polymer.[29, 57, 75, 152] A schematic process description is plotted in Figure 3.15. The insulating polymer is spin-coated on top of the silver nanowires on an arbitrary substrate. After curing the polymer, it is peeled off from the substrate and includes the AgNWs at the bottom. The substrate is turned and a perfectly smooth surface is achieved with nanowires being directly below this surface. Polyimide,[57] polydimethylsiloxane,[53] polyvinyl alcohol,[208] and NOA63 [56, 75] are reported as insulating polymers for this purpose. Advantages of this process are high AgNW adhesion, good flexibility and stability, and low roughness. However, in terms of upscaling to R2R production, the peel-off might be not as suitable as simple solution-processed planarization methods.

Some further approaches are reported for reducing the roughness of AgNW electrodes, e. g. pressing the network into a subjacent polymer layer [169] or letting the silver nanowires sink into an acrylic resin under elevated temperatures of 80 °C.[45]

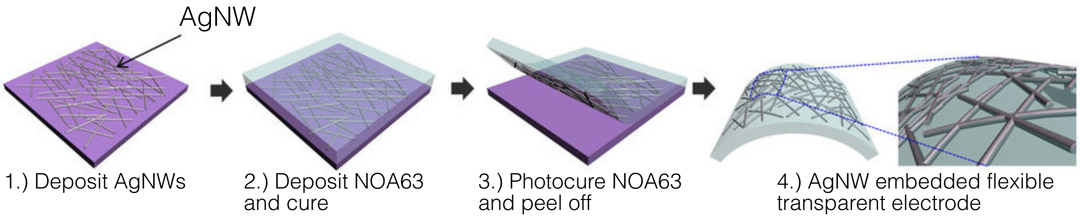

Figure 3.15.: Sketch of the process for burying nanowires on the bottom of an insulating polymer. Adapted from [75] under Creative Commons CC-BY license.

Stability

Considering the degradation of an organic device (cf. Sec. 2.2.4), stability of the AgNW electrode is of equal importance as all the other device parts. Two facets of electrode stability are relevant: mechanical robustness and chemical durability.

Due to the inherent structure of AgNW networks, they exhibit high flexibility without significantly changing its conductivity.[57, 75, 112, 149] Bendability down to 40 µm is reported by Kim et al. without destroying the conductive film.[29] Hence, AgNW electrodes are suitable for R2R processes and flexible consumer products. However, AgNWs also have a low adhesion to their substrate, if simply deposited on top without further treatment. For example, they are easily removed with conventional adhesive tape, which is exploited as a standard adhesion test, called *tape test*. The low adhesion complicates handling; every mechanical contact needs to be avoided to not harm the layer. Further, solvent-based treatment like sonication is hardly possible. Consequently, methods that increase the adhesion are necessary. Many post- or pre-treatments used for increasing conductivity or reducing roughness have the positive side-effect of also improving the adhesion.[53, 57, 64, 189]

Moreover, AgNW networks have to withstand additional factors that degrade the electrode. In an OPV application, elevated temperatures might be present due to a constant sun illumination and the surrounding temperature. Mayousse et al. broadly investigated the impact of these and other factors on the AgNW electrode.[31] They show that many factors are worsening the electrode performance. UV illumination leads to particle formation, which might destroy the electrode.[25] Oxidization and sulfurization occurs in the presence of light, oxygen, and sulfur.[25, 31] Electromigration is also a possible degradation pathway of silver nanowire electrodes.[101, 187] Moreover, PEDOT:PSS is identified to fasten up degradation.[31]

Attempts to increase the stability are reported. Idier et al. use triphenylphosphine (PPh_3) and prevent nanowire oxidation because of PPh_3 adsorption at the AgNWs. In other publications, AgNWs are covered with graphene or graphene oxide for improved stability.[93, 112, 131]

3.3.5. Conclusion

Silver nanowire networks is an important transparent electrode technology. With its high transmission at low sheet resistances, sufficient flexibility, and cost-effectiveness, AgNW networks outperform ITO. The polyol synthesis is relatively simple, allows for a wide range of wire diameter and length, and offers high yields. Silver nanowire dispersions in various organic solvents enable solution-based deposition techniques like spin, spray, or dip coating. Only moderate temperature application is necessary to achieve high conductivity. Hence, an implementation into R2R processes for large area electrodes is possible.

In view of thin-film organic devices, planarization of the AgNW network is required; several methods are reported for a successful planarization. The most promising and universal method thereby is the embedment in an insulating polymer which improves not only smoothness but also mechanical stability.

An important issue is the longterm stability in an OPV application scenario. To date, only two publications address the degradation in the presence of light, whereby one publication states that light is not harming the AgNWs strongly [31] and the other publication identifies light as driving factor for AgNW degradation.[25] Therefore, more investigations are necessary to get deeper insight into AgNW degradation pathways and possible prevention.

Part II.

Experimental

4. Sample Preparation and Manipulation

Sample fabrication takes place on various substrates. Glass substrates ('BK7', Schott, Germany) with $(2.5 \times 2.5)\,\mathrm{cm}^2$ size and pre-structured[1] ITO-coated glass substrates ($(2.5 \times 2.5)\,\mathrm{cm}^2$ or $(15 \times 15)\,\mathrm{cm}^2$, 'Corning Eagle XG', Thin Film Devices, USA) with 1.1 mm thickness are cleaned according to the following procedure:

1. Substrates are cleaned with acetone, ethanol, and a cotton tissue (ITO only).
2. Ultrasonic bath in n-methylpyrrolidone 15 min.
3. Rinse with deionized water 5 min.
4. Ultrasonic bath in deionized water 10 min.
5. Ultrasonic bath in ethanol 15 min.
6. Spin rinser with pure water and nitrogen flow.
7. Oxygen plasma, 10 min at 2×10^{-1} mbar (directly before sample usage).

Plasma cleaning is executed with a 'PDC-002' (Harrick, USA). Oxygen or argon is used as working gas at a pressure of 2×10^{-1} mbar for several minutes at radio frequency level *high*. For argon plasma cleaning, the chamber is purged three times with argon to ensure the absence of oxygen.

A laser scribing system ('WorkstationProfessional', ACI, Germany) with a pulsed, frequency-doubled Nd:YAG laser (1064 nm wavelength) is used for AgNW sample structuring. The transparent electrode layout according to Figure 4.3 is written with following parameters: 100 % power, 150 mm/s moving speed, 5 kHz pulse frequency, 3 µs pulse width, and 10 µm line distance.

4.1. Materials

Table 4.1 lists all relevant materials used within this thesis and their respective suppliers. Non-polymeric organic materials are purified at least twice by gradient sublimation, done in-house by Annette Petrich or Tina Träger (both IAPP).

---

[1] The structure is shown in Figure 4.3.

Table 4.1.: Overview about materials used within this thesis. They are sorted alphabetically by abbreviation and by application field.

Short name	Long name	Supplier
Electrode materials & special solvents		
AI4083	PEDOT:PSS 'P VP AI 4083'	Heraeus Clevios, Germany
EG	ethylene glycol, 99.8 % purity	Sigma Aldrich, Germany
NOA63	Norland Optical Adhesive 63	Norland Products, USA
NW35	SLV-NW-35 (diameter 35 nm, length $(12 \pm 3)\,\mu m$), 10 mg/ml in ethanol, serial number SN BN 30125146	BlueNano, USA
NW90	SLV-NW-90 (diameter 90 nm, length 30 µm), 10 mg/ml in ethanol, serial number SN 4011000141	BlueNano, USA
PDMS	polydimethylsiloxane 'Sylgard® 184'	Dow Corning Corporation, USA
PI	polyimide 'VTEC PI-080-051'	Richard Blaine International, Inc., USA
THF	anhydrous tetrahydrofuran > 99.9 % with 250 ppm butylhydroxytoluene as stabilizer	Sigma Aldrich, Germany
OSC materials		
$(2\text{-cyc-DMBI})_2$	2-cyclohexyl-N,N'-dimethylbenzimidazoline	Z. Bao group, USA
α-6T	sexithiophene	TCI Europe, Belgium
Ag	silver	Lesker, UK
Al	aluminum	Lesker, UK
Au	gold	Allgemeine Gold- und Silberscheideanstalt AG, Germany
BF-DPB	N,N'-((diphenyl-N,N'-bis)9,9,-dimethylfluoren-2-yl)-benzidine	Synthon, Germany
Bis-HFl-NTCDI	N,N-bis(fluoren-2-yl)-naphtalenetetracarboxylic diimide	synthesized in-house
BPAPF	9,9-bis(4-(N,N-bis-biphenyl-4-yl-amino) phenyl)-9H-fluorene	Lumtec, Taiwan
BPhen	bathophenanthroline	ABCR, Germany
C_{60}	fullerene	CreaPhys, Germany
$Cr_2(hpp)_4$	tetrakis(1,3,4,6,7,8-hexahydro-2H-pyrimido[1,2-a]pyrimidinato) dichromium	Lumtec, Taiwan

DCV5T-Me	2,2-((3,4-dimethyl-[2,2:5,2:5,2:5,2-quinquethiophene]-5,5-diyl)bis(methanylylidene))dimalononitrile	Synthon, Germany
F$_6$-TCNNQ	2,2'-(perfluoronaphthalene-2,6-diylidene)dimalononitril	Novaled AG, Germany
Spiro-TTB	spiro-tetra(p-methyl-phenyl)-benzidine	Lumtec, Taiwan
MeNH$_3$I	methylammonium iodide	synthesized in-house
MoO$_3$	molybdenum oxide	Sigma Aldrich, Germany
NDP9	Novaled hole dopant 9	Novaled AG, Germany
NTCDA	napthtalenetetracarboxylic dianhydride	TCI Europe, Belgium
PbCl$_2$	lead(II) chloride, 99.999 % purity	Sigma Aldrich, Germany
PC$_{71}$BM	[6,6]-phenyl-C$_{71}$-butyric acid methyl ester	1-Materials, Canada
PFN	[(9,9-bis(3'-(N,N-dimethylamino)propyl)-2,7-fluorene)-alt-2,7-(9,9-dioctylfluorene)]	1-Materials, Canada
PTB7	poly[[4,8-bis[(2-ethylhexyl)oxy]benzo[1,2-b:4,5-b']dithiophene-2,6-diyl][3-fluoro-2-[(2-ethylhexyl)carbonyl]thieno[3,4-b]thiophenediyl]]	1-Materials, Canada
Rh-D	dimeric rhodocene	S. Marder group, USA
SubPc	boron subphtalocyanine chloride	Lumtec, Taiwan
SubNc	boron subnaphtalocyanine chloride	Lumtec, Taiwan
W$_2$(hpp)$_4$	tetrakis(1,3,4,6,7,8-hexahydro-2H-pyrimidol[1,2-a]pyrimidinato)ditungsten	Novaled AG, Germany
ZnPc	zinc phtalocyanine	CreaPhys, Germany
Other materials		
pPEN	planarized Teonex polyethylene napthalene PQA1M	Dupont Teijin Films Ltd., UK
TMA	trimethylaluminum	Sigma Aldrich, Germany
XNR	epoxy glue XNR 5590	Nagase, Japan
	proprietary barrier glue	tesa SE, Germany

4.2. Spin Coating

The basic spin coating principle is explained in Section 2.2.2. Consequently, only specific information of the setup and the process parameters are given here. Two spin coaters (Sawatec, Switzerland) are used, one in ambient atmosphere under a fume hood, one in a nitrogen-filled glovebox. Following processes are used for the layer preparation with each of the materials:

- The initial **silver nanowire** dispersion (NW35 or NW90) is diluted with pure ethanol to a concentration of 2 mg/ml. A defined volume of this dispersion is dispensed onto the spinning sample at 4000 rpm 'drop by drop' (7.5 µl per drop) with 5 to 10 s between each drop to let the ethanol evaporate. Processing is done in air.
- The **PEDOT:PSS** formula AI4083 is used as received and in air. The solution is filtered through a PVDF syringe filter with 0.45 µm pore size (Sigma Aldrich, Germany). After deposition at various spin speeds, the sample is placed on a hot plate at 120 °C for 15 min.
- **Doped BF-DPB and Spiro-TTB:** Processing is done in a UV-protected N_2-filled glovebox. BF-DPB, Spiro-TTB, F_6-TCNNQ, and NDP9 are individually dissolved in tetrahydrofuran with 10 mg/ml concentration (if not stated otherwise) and annealed on a hotplate at 55 °C to fully dissolve. After 5 min of BF-DPB or Spiro-TTB sonication (closed vial in air), the materials are blended either with NDP9 or F_6-TCNNQ with different weight ratios, such that a total concentration of 10 mg/ml is preserved. Spin coating takes place at 1000 rpm for 45 s, followed by an annealing step (55 °C, 10 min). Layer thicknesses of 100 ± 10 and 55 ± 3 nm are obtained for p-BF-DPB and p-Spiro-TTB, respectively.
- **NTCDA** and corresponding n-dopants are dissolved in dimethylformamide with a concentration of 10 mg/ml, if not stated otherwise. To fully dissolve, the material is heated at 90 °C and magnetically stirred for more than 10 min. After merging dopant and NTCDA solution, the solution is spin-coated at 2000 rpm|60 s on various substrates through a 0.2 µm syringe filter, and continued to use without further treatments. Layer thickness is 15 to 20 nm. Prior to spin coating, the substrates are treated with argon plasma.
- **NOA63** is used as received. 1 ml is dispensed on glass or glass/AgNW samples and spin coating is subsequently executed (500 rpm|20 s followed by 1200 rpm|30 s). Subsequently, the samples are transferred to a no-name commercial nailcuring device with 4 UV lamps (9 W each) and cured within 30 min. The layer is then peeled off from the glass substrate for further layer deposition or characterization.
- **Polyimide** is used as received. After spin coating (500 rpm|20 s followed by 800 rpm|90 s), the sample is transferred to a hotplate and cured at 100 °C|10 min and 110 °C|50 min. Subsequently, it is peeled off from the substrate for further steps.

4.3. Spray Coating

Spray coating is undertaken using a XYZ-table ('F7300N', Fisnar, USA), a needle valve ('SV1000SS', Fisnar, USA), an automatic pressure controller ('VC1200', Fisnar, USA) and a hotplate ('HT 40', LAC, Czechia). Figure 4.1 shows the setup. The silver nanowire dispersion is diluted with pure ethanol to a concentration of 0.2 mg/ml, sonicated for 15 min (NW90) or 1 min (NW35), filled into a cartridge, and continuously stirred. The cartridge is further connected with a vacuum pump to generate an underpressure of approximately 2×10^4 Pa relative to the atmospheric pressure.

The spraying distance and the pressure are 12.5 cm and 2×10^4 Pa, respectively. The nozzle moves computer-assisted in a meander movement over the samples with a line distance of 7 mm and a speed of 1.5 cm/s. To guarantee fast ethanol evaporation, the samples are heated to 80 °C. The AgNW thickness is adjusted by repeatedly executing identical meander movement (alternating forward and backward direction) and checking transmittance manually from time to time until the desired value is obtained.

A maximum size of $(20 \times 20)\,\mathrm{cm}^2$ or simultaneous coating of several $(2.5 \times 2.5)\,\mathrm{cm}^2$ substrates is possible with a homogeneous AgNW coating.

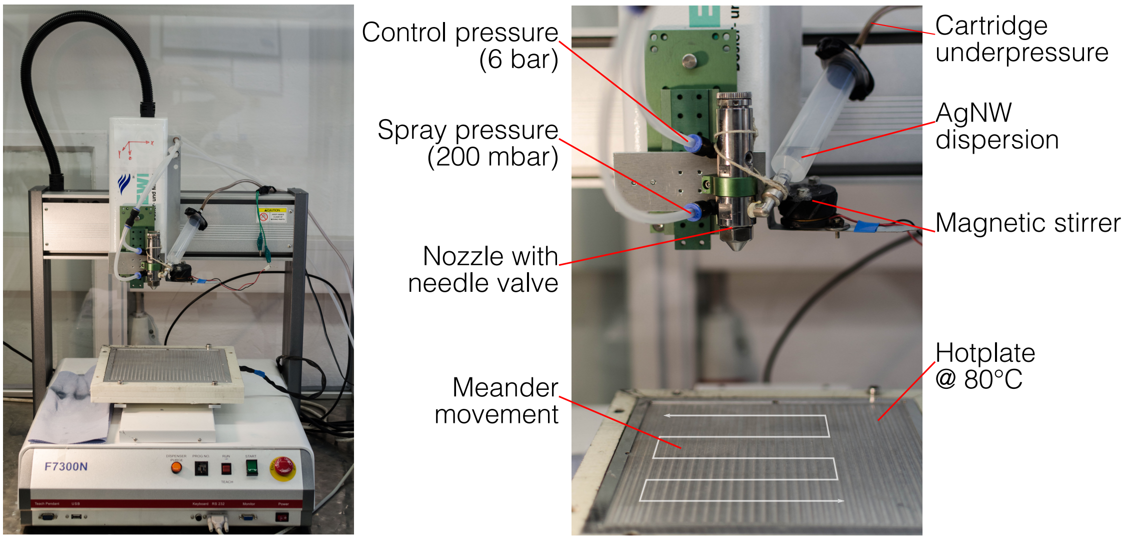

Figure 4.1.: Spray coating setup. The AgNW dispersion is sprayed through a needle-valve-controlled nozzle onto the substrates, which lie on a 80 °C hotplate. Through meander-like nozzle movement, a big and homogeneous area can be coated. **Left:** Overview. **Right:** Detailed photograph of nozzle and parts.

4.4. Electrode Fabrication

As different routes are used for every different type of electrode, they are shortly described in the following.

Glass/ITO: 1.) O_2-plasma is carried out 10 min. 2.) PEDOT:PSS is spin-coated on top with 4000 rpm|30 s.

Glass/AgNW/PEDOT:PSS: 1.) The glass sample is O_2-plasma-treated for 10 min. 2.) Diluted AgNW dispersion is spray- or spin-coated until the desired transmission is reached. 3.) Optional: The sample is layouted with the laser system. 4.) Glass/AgNW sample is treated with Ar-plasma for 10 min. 5.) PEDOT:PSS is spin-coated with 800 rpm|45 s.

Glass/AgNW/BF-DPB or Spiro-TTB: 1.) The glass sample is O_2-plasma-treated for 10 min. 2.) Diluted AgNW dispersion is spray- or spin-coated until the desired transmission is reached. 3.) The sample is heated out in air 90 min at 210 °C for NW90 or 30 min at 140 °C for NW35. 4.) Optional: The sample is layouted with the laser system. 5.) Glass/AgNW sample is treated with Ar-plasma for 10 min and subsequently transferred into N_2-glovebox. 6.) Doped or undoped BF-DPB or Spiro-TTB solution is spin-coated onto the sample.

NOA63/AgNW: 1.) The glass sample is O_2-plasma-treated for 10 min. 2.) Diluted AgNW dispersion is spray- or spin-coated until the desired transmission is reached. 3.) Optional: The sample is layouted with the laser system. 4.) Glass/NW35 sample is treated with Ar-plasma for 10 min. 5.) Glass/NW90 is heated (210 °C|90 min). 6.) NOA63 is spin-coated on top and cured. 7.) The NOA63/AgNW layer is peeled off from the glass substrate. 8.) Ar-plasma for 5 min (no PEDOT:PSS afterwards) or 10 min (PEDOT:PSS afterwards). 9.) Optional: PEDOT:PSS is spin-coated (2000 rpm|45 s).

PI/AgNW: 1.) The glass sample is O_2-plasma-treated for 10 min. 2.) Diluted AgNW dispersion is spray- or spin-coated until the desired transmission is reached. 3.) Optional: The sample is layouted with the laser system. 4.) Optional: Glass/AgNW samples are coated with PEDOT:PSS (1000 rpm|45 s). 5.) PI is spin-coated on top and cured. 6.) PI/AgNW is peeled off from the substrate, turned around and mounted on another glass substrate with capton tape. 7.) Argon-plasma 5 min 8.) PI/AgNW sample is spin-coated with PEDOT:PSS (2000 rpm|60 s).

4.4.1. Silver Nanowire Electrode Characterization

An electrical and optical characterization of the silver nanowires used within this study is necessary to classify their performance. Figure 4.2 shows the dependence of sheet resistance and total transmission at 550 nm for the nanowires with a diameter of 35 nm (NW35) and 90 nm (NW90), respectively. Moreover, the Equations 3.5 (p. 40) and 3.14 (p. 52) are used to fit the bulk regime and the percolative regime of the nanowire networks. A datapoint for the ITO electrodes used at the IAPP is plotted as a reference and fitted with the bulk equation (Eq. 3.5). The fit values are stated in Table 4.2.
The bulk behavior for NW90 electrodes with $\Phi_{\mathrm{De}} = 525$ is valid for transmission

values below approximately 82 %. Above 82 %, the percolative behavior dominates. A direct comparison of Φ_{De} values for ITO and NW90 is rather unpractical because the electrode perfomance used later on is set in the percolative regime. Consequently, the Φ_{De} value of NW90 electrodes is overestimated. For NW35 electrodes, the bulk behavior with $\Phi_{\mathrm{De}} = 215$ is valid up to approximately 88 %. Here, a direct comparison with ITO is possible as the NW35 electrode is used in the bulk regime. Φ_{De} for NW35 is approximately twice as high as for ITO.

Summarizing, it is found that the silver nanowire electrodes of both types exhibit a better optoelectrical performance than the ITO electrodes used at the IAPP as reference electrodes.

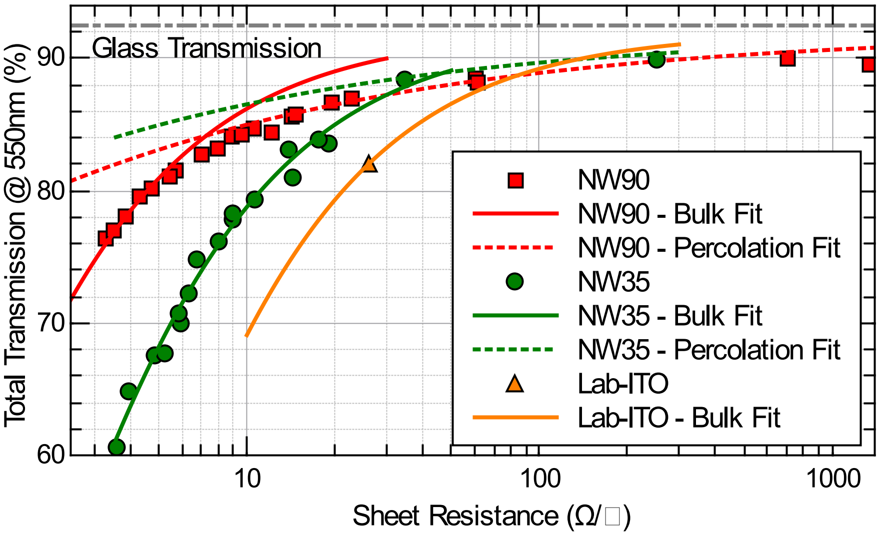

Figure 4.2.: Total transmission at 550 nm wavelength versus sheet resistance for various NW90 and NW35 samples. The bulk and percolation fit equation relate to Equation 3.5 (p. 40) and 3.14 (p. 52), respectively.

Table 4.2.: Fit values of ITO, NW90, and NW35 electrodes for the bulk regime and the percolative regime of T-R_S dependency. As ITO is a bulk electrode, it is only fitted with the bulk equation (Eq. 3.5).

Type	Φ_{De}	Π	n
ITO	113	-	-
NW90	525	95	1.7
NW35	215	130	1.6

4.5. Organic Solar Cell Fabrication

4.5.1. Small Molecule Solar Cells

All small molecule OSCs are fabricated using thermal (co-)evaporation (cf. Section 2.2.2) in ultra-high vacuum (UHV) chambers. The layout of one sample, which contains 4 identical pixels with approximately 6.44 mm^2 area, is depicted in Figure 4.3. Two different systems are used for layer deposition.

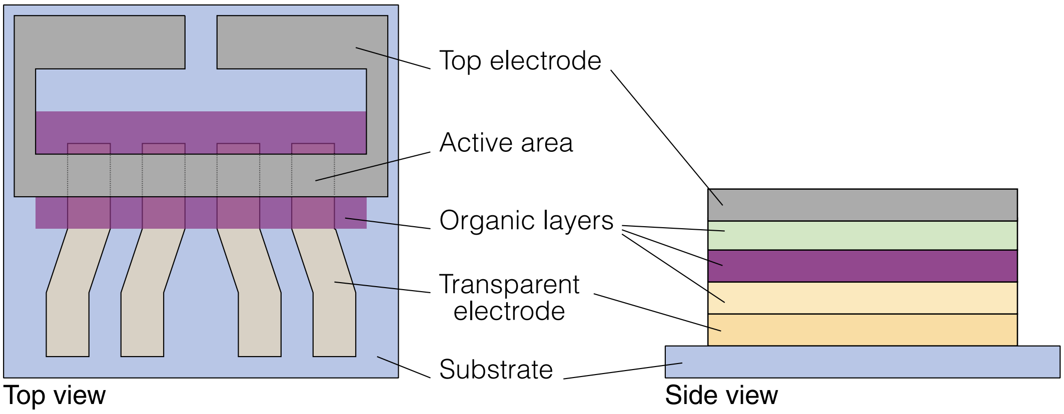

Figure 4.3.: Layout and side view of fabricated small molecule organic solar cells.

Evaporation Tool 'UFO1'

The 'UFO1' is a multi-chamber evaporation system (BesTec GmbH, Germany) with a base pressure of 1×10^{-8} mbar, mainly operated by the researchers themselves. Mounting of the sample into a teflon holder is carried out in a flow box under laminar air flow to avoid dust particles on the sample. Subsequently, the sample is transferred through a N_2-glovebox into the UHV evaporation system. Five evaporation chambers for different material classes (ETLs, HTLs, two for absorber materials, and metals) and one UPS/XPS measurement system are connected to a handler, such that the sample can be moved inbetween the chambers without breaking the vacuum. An evaporation chamber can handle one sample ($(2.5 \times 2.5)\,\text{cm}^2$) at a time. Different layer layouts are achieved using various shadow masks. The QCMs are calibrated after every change of material and/or chamber configuration to ensure high accuracy and they are exchanged after a shift of eigenfrequency by approximately 5 % (organic materials) or 20 % (metals).
Maintenance of the 'UFO1' is done by Sven Kunze and Andreas Büst (both IAPP).

The following solar cells are fabricated with 'UFO1', layer thicknesses in brackets:

- **Section 7.2.1:** Glass/ITO or Glass/AgNW | s-HTL[100] | ZnPc:C_{60}(1:2)[30] | C_{60}[30] | BPhen[6] | Al[100].

- **Section 7.4:** Glass/ITO | (2-cyc-DMBI)$_2$[1](e-ETL only) | s-ETL[15] or e-ETL[20] | C_{60}[5] | ZnPc:C_{60}(1:2)[30] | BF-DPB[5] | BF-DPB:NDP9(5 wt%)[25] | NDP9[1] | Al[100].
- **Section 8.4.1:** Glass/ITO or PI/NW35 | α-6T[60] | SubNc[12] | SubPc[18] | BPhen[7] | Al[150] or Ag[100].

Evaporation Tool 'Lesker'

A sophisticated evaporation system is the 'Lesker' (Lesker, UK). It is a single-chamber evaporation system with a base pressure of 1×10^{-8} mbar, connected to a N_2-glovebox. Sample preparation, handling, and maintenance of this system is done by a crew of experienced technicians – Tobias Günther, Andreas Wendel, and Caroline Walde (all IAPP). The 'Lesker' system allows for simultaneous fabrication of up to 36 samples – either on a $(15 \times 15)\,\mathrm{cm}^2$ wafer or as single samples (only 18 samples possible). To customize layout and layer structure of the samples, different shadow masks and a wedging tool are available. After fabrication, the solar cells are inertly transferred to a glovebox, where a top encapsulation against moisture ingress is attached: a cavity glass, which contains a getter (Dynic Corporation Minato-Ku, Japan), is epoxy glued with XNR on top of the active device area and UV-cured.

The following solar cells are fabricated with 'Lesker', layer thicknesses in brackets:

- **Section 7.2.4:** Glass/ITO or Glass/AgNW | s-HTL[100] or e-HTL[30] | ZnPc:C_{60} (1:2)[30] | C_{60}[30] | BPhen[6] | Al[100]. (OSOL-1284)
- **Section 7.2.5:** Glass/ITO or Glass/AgNW | s-HTL[100] or e-HTL[90] | NDP9[1] | BPAPF: NDP9(10 wt%)[5] | BPAPF[5] | DCV5T-Me:C_{60}(2:1)[40 at 80 °C substrate temperature] | C_{60}[20] | C_{60}:$Cr_2(hpp)_4$(4 wt%)[15] | Al[100]. (OSOL-1328)
- **Section 8.4.2:** Glass/ITO/AI4083 or NOA63/NW35/AI4083 | α-6T[60] | SubNc [12] | SubPc[18] | BPhen[7] | Al[150]. (OSOL-1625)
- **Section 8.4.2:** Glass/ITO/AI4083 | α-6T[30,45,60,75] | SubNc[12] | SubPc[18] | BPhen[7] | Al[150]. (OSOL-1624)
- **Section 8.5:** Glass/ITO or NOA63/NW35 or NOA63/NW90, each with and without AI4083 | $W_2(hpp)_4$[1] | C_{60}[15] | DCV5T-Me:C_{60}(2:1)[40 at 90 °C substrate temperature] | BPAPF[5] | BPAPF:NDP9(10 wt%)[40] | NDP9 [1] | Al[100]. (OSOL-1669)

4.5.2. Polymer Solar Cells

Polymer solar cells are fabricated at the King Abdullah University of Science and Technology (KAUST) in Saudi Arabia during a research stay in the 'Organic Electronics

& Photovoltaics Group' of Professor Aram Amassian.
Substrates have a size of $(2 \times 2)\,\mathrm{cm}^2$ with prestructured ITO coating (5 mm width). PTB7 and $PC_{71}BM$ are mixed with a weight ratio of 1:1.5 and a concentration of 25 mg/ml in chlorobenzene with 3 vol% diiodooctane (DIO) in inert N_2 atmosphere. The solution is heated and stirred at 60 °C overnight. A solution volume of 60 µl is spin-coated with 800 rpm for 45 s. The layer is afterwards evacuated in a vacuum-chamber with a base pressure of 1×10^{-7} mbar for 45 min. Subsequently, ITO contacts are partly freed from the absorbing layer using a razorblade. The samples are transferred into a thermal evaporation system (Angstrom Engineering, Canada) and 7 nm of MoO_3 followed by 80 nm of silver are evaporated. One substrate contains 10 diodes with an active area of $10\,\mathrm{mm}^2$.

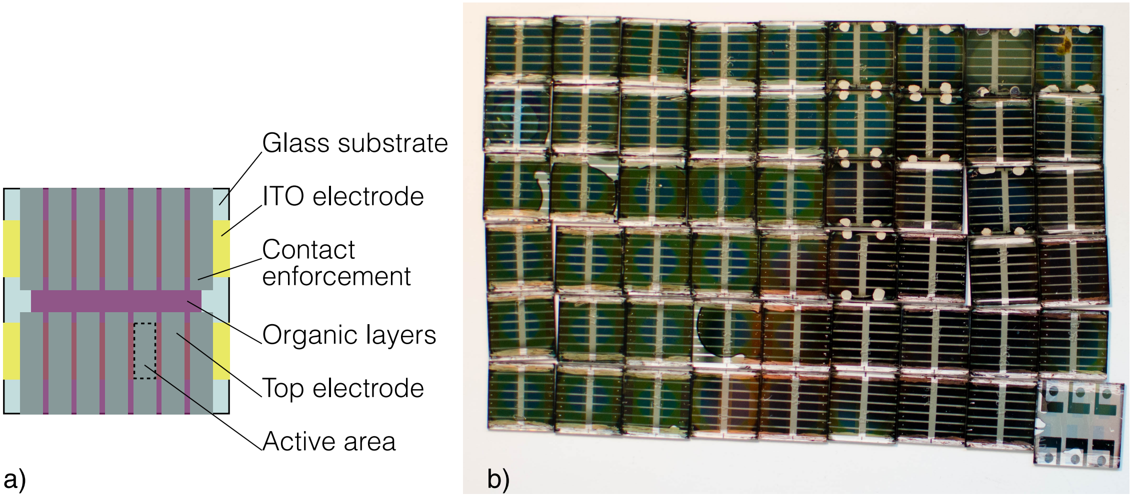

Figure 4.4.: a) Schematic sample layout. Each sample contains 10 diodes with an active area of $10\,\mathrm{mm}^2$. **b)** Photograph of 53 PTB7:$PC_{71}BM$ solar cell substrates according to the schematic layout and one cuckoo's egg (it is a sample from a different solar cell fabrication facility).

4.5.3. Perovskite Solar Cells

HTL layers are deposited using the 'Lesker' evaporation system (cf. Section 4.5.1) or spin-coated in inert atmosphere. Perovskite layers are fabricated in a custom-made multi-chamber evaporation system 'ESK' (CreaPhys, Germany) with a base pressure of 1×10^{-7} mbar. $PbCl_2$ and $MeNH_3I$ are co-evaporated and monitored with three quartz crystal microbalances: one for each source and one at the height of the substrate holder to monitor layer thickness. Subsequently, the samples are transferred to another chamber of the 'ESK' to evaporate C_{60} and silver. The device architecture is shown in Figure 7.20, p. 105.
The perovskite solar cells are prepared by M. Sc. Enkhtur Erdenebileg (IAPP).

4.5.4. Flexible Encapsulation

AlO_x with a thickness of 20 nm is either deposited on a pPEN substrate or directly on the finished OSC stack via atomic layer deposition in a plasma-enhanced deposition system ('SI ALD LL', Sentech Instruments GmbH, Germany) with 100 °C electrode temperature. As precursors, TMA and ozone are used. Purging gas is nitrogen with 99.9999 % chemical purity.

As bottom encapsulation, the pPEN/AlO_x substrate is laminated in a N_2-glovebox below the NOA63/AgNW electrode utilizing the UV-curing barrier glue (tesa SE) using a no-name commercial nailcuring device (4 UV lamps, 9 W each). The barrier glue contains a latent getter against lateral moisture diffusion and resulting edge degradation. For top encapsulation, two routes are followed: On the one hand, the pPEN/AlO_x substrate is laminated directly on top of the device as described above. On the other hand, for the case of directly deposited AlO_x, an additional PET substrate, which protects the ALD layer from water adsorption and mechanical stress, is glued on the AlO_x layer with UV-curing XNR epoxy glue inside a glovebox.

4.6. Climate Cabinet

Solar cell and electrode aging takes place in a climate chamber 'PL-3 J' (Espec, Japan) with mounted solar simulator 'SOL2000' (Hönle AG, Germany) under AM1.5G illumination at $(100 \pm 10)\,\mathrm{mW/cm^2}$. A steady climate can be generated within the chamber up to values of 90 °C and 80 % RH. A custom-built circuit board in the chamber electrically connects up to 88 samples to a source measurement unit (Keithley, USA). A measurement PC records IV curves from −1 V to 1 V for two pixels of each sample every hour. During measurement down-times, the samples are kept in open-circuit condition.

Figure 4.5.: Left: Photograph of climate chamber. **Right:** Photograph of custom-made circuit board for electrically connecting up to 88 samples.

5. Sample Characterization

Sheet Resistance / Conductivity

Generally, the resistance through a conductive cuboid is defined as

$$R = \rho \frac{l}{w \cdot d} \tag{5.1}$$

with material resistivity ρ, length l, width w, and thickness d. A sheet resistance can be expressed for square-shaped film over

$$R_{\mathrm{S}} = \rho / d \ . \tag{5.2}$$

The four-point-probe (4PP) setup '302 Resistivity Stand' (Lucas Labs, USA) is used for measuring the sheet resistance with a connected source meter unit 'SMU 2400' (Keithley, USA) to supply and measure voltage V and current I. Figure 5.1 depicts the measurement principle. A current of typically 1 mA is applied between the outer two probes and the voltage drop is measured between the inner two probes. Probe material is tungsten carbide, probe radius is 0.04 mm, and probe distance t equals 1.6 mm.
For calculating the sheet resistance, following approximation is valid, if the layer thickness is much smaller than the probe distance t:

$$R_{\mathrm{S}} \approx 4.4 \frac{V}{I} \qquad [R_{\mathrm{S}}] = \Omega / \square \ . \tag{5.3}$$

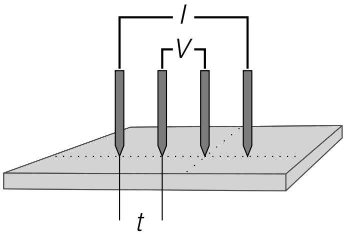

Figure 5.1.: Sketch of the four-point-probe-setup. Between the outer two probes, a current is applied. The inner two probes measure the voltage drop.

The measurement of low conductivities in the range of 1×10^{-9} to 1×10^{-3} S/cm (e. g. for s-HTL conductivies, Section 7.2.2) is carried out with a different technique due to measurement limitations of the 4PP setup. A silver film with $d = 60\,\mathrm{nm}$ is thermally evaporated through a shadow mask onto a glass substrate to obtain interdigitated silver fingers. A channel is created with a total width w of 111 mm and a length l of 0.5 mm. Subsequently, the target material is deposited on top of it, and a IV curve is recorded with a SMU '236' (Keithley, USA) to obtain R. The conductivity $\sigma = 1/\rho$ is calculated using Equation 5.1.

Solar Cell Characterization

Organic solar cells are characterized in air using two automated self-made measurement systems.

First, the external quantum efficiency is measured with the 'EQE Robot'. The sample is illuminated through an aperture ($2.96\,\mathrm{mm}^2$) with monochromatic light in the spectral region from 300 to 900 nm, generated by a combination of xenon lamp and monochromator ('Oriel Xenon Arc-Lamp Apex Illuminator' and 'Cornerstone 260', Newport Corporation, USA). Further, a chopper at approximately $(220 \pm 10)\,\mathrm{Hz}$ and a lock-in amplifier ('7265', Signal Recovery, USA) are used to detect the spectrally resolved response $\mathrm{SR_{osc}}(\lambda)$. The EQE is calculated and a corresponding spectral mismatch factor M is obtained (Equation 5.4). The mismatch factor is necessary to correct the illumination intensity with respect to the measurement system and the specific solar cell, as the sun simulator spectrum $\Phi_{\mathrm{sim}}(\lambda)$ is not identical to the standardized AM1.5G sun spectrum $\Phi_{\mathrm{AM1.5G}}(\lambda)$. $\mathrm{SR_{ref}}(\lambda)$ is the spectral response of the silicon reference solar cell ('S1337-33BQ', Hamamatsu, Japan), calibrated by the Fraunhofer Institute for Solar Energy Systems (ISE, Germany). It yields a current $I_{\mathrm{ref}}^{AM1.5G}$ of 0.78 mA at $100\,\mathrm{mW/cm}^2$ AM1.5G illumination intensity.

$$M = \frac{\int \mathrm{SR_{osc}}(\lambda) \cdot \Phi_{\mathrm{sim}}(\lambda)\,\mathrm{d}\lambda}{\int \mathrm{SR_{osc}}(\lambda) \cdot \Phi_{\mathrm{AM1.5G}}(\lambda)\mathrm{d}\lambda} \cdot \frac{\int \mathrm{SR_{ref}}(\lambda) \cdot \Phi_{\mathrm{AM1.5G}}(\lambda)\,\mathrm{d}\lambda}{\int \mathrm{SR_{ref}}(\lambda) \cdot \Phi_{\mathrm{sim}}(\lambda)\mathrm{d}\lambda} \tag{5.4}$$

Second, the dark and illuminated jV characteristic of the solar cell is recorded using the 'LIV-Robot', which can measure up to 36 samples automatically. A sun simulator ('16S-003-300-AM1.5', Solar Light Co., USA), a SMU '2400' (Keithley, USA), and the above stated silicon reference solar cell are used. The illumination intensity is adjusted with the mismatch factor M such that the measured current I_{ref}^{sim} under the sun simulator equals $I_{\mathrm{ref}}^{AM1.5G}/M$.

To obtain an exact active area, either an aperture of $2.35\,\mathrm{mm}^2$ is inserted (Chapter 7) or the active area is precisely measured with an optical microscope.

Atomic Force Microscopy

Acquring atomic force microscope (AFM) images is carried out using a 'CombiScope1000' (AIST, USA). TAP-Al-G tips (BudgetSensors, Bulgaria) with 300 kHz resonance frequency and a force constant of 40 N/m in standard tapping mode are used. The AFM is assembled on an optical table to avoid external vibrations.

Scanning Electron Microscopy

Two scanning electron microscopes (SEMs) are employed. A Phenom table top SEM (FEI, USA) is used in Section 7.3. All other pictures are acquired with a 'GSM 982 Gemini' SEM (Zeiss, Jena, Germany), operated by Susanne Goldberg (Physical Chemistry, TU Dresden). To avoid sample charging, 1 to 2 nm of gold are sputtered onto the sample before SEM analysis.

Spectroscopy

Transmission and reflection measurements are carried out using a 'SolidSpec 3700 UV-VIS-NIR Spectrophotometer' (Shimadzu, Japan) with PbS or InGaAs detectors for the visible or near infrared spectrum, respectively. For all measurements, air is used as reference baseline. Consequently, all electrode spectra include the substrate.

Water Vapour Transmission Rate Measurement

WVTRs of bent barriers are measured using electrical calcium corrosion tests. Here, the following layer stack is evaporated directly onto the flexible barrier film: 20 nm of C_{60} for mechanical decoupling,[68] 60 nm Ca as the sensor material, and 100 nm Al electrodes in a four-point-probe conductivity measurement geometry.[181] After deposition, encapsulation glasses are glued onto the backsides of the samples with UV-curing XNR-5592 epoxy in an inert environment. Samples are then introduced to a custom measurement setup and measurements are taken every 5 min. A current is sent through the outer electrode fingers until a voltage of 20 mV is measured between the inner sensing electrodes. During measurement down-times, no voltage is applied. A constant RH of 90 % is applied using a saturated, aqueous Na_2SO_4 solution. This setup is described in detail elsewhere.[67]

6. Equivalent Circuit Simulation

Equivalent circuit simulations in Section 7.2.4 are done with distributed elements using the SPICE software 'LTSpice IV' (Linear Technology, USA) and an adapted python script, written by Dr. Sylvio Schubert (IAPP).[120] Figure 6.1 depicts, how the simulation is conducted. The area of $(1 \times 1)\,\mu\mathrm{m}^2$ within one nanowire void is represented by 50×50 ideal, photo-generating, parallel connected diodes with a parallel resistance R_P of $0.5 \times 10^{-15}\,\Omega$ and a serial resistance R_ser of $60\,\Omega$. Using the Shockley equation

$$I(V) = I_\mathrm{S}\left(\exp\left[\frac{qV}{n_\mathrm{i}\,k_\mathrm{B}T}\right] - 1\right) - I_\mathrm{ph}\ , \tag{6.1}$$

the diode behavior is modeled and fitted to the best experimentally obtained curve of this experiment on NW90 with 10 wt% doping concentration (cf. Fig 7.13 on p. 95). Saturation current I_S of 0.43 pA, photo current I_ph of 0.76 pA, and ideality factor n_i of 3.75 are obtained from fitting.

All diodes are interconnected with series resistances $R_\mathrm{S} = 1/(\sigma\, d)$, which equal the sheet resistance of the HTL layer for 100 nm thickness d and various conductivities σ. The outer diodes are connected to the nanowire frame with a resistance of $10\,\Omega$ according to the nanowire resistance.

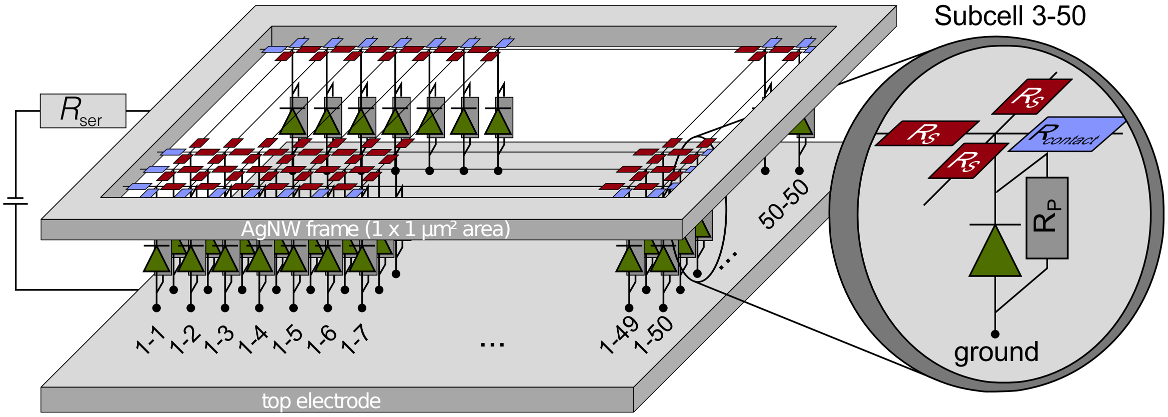

Figure 6.1.: Sketch of equivalent circuit simulation. The series resistances (red) are correlated with the conductivity of the HTL via $R_\mathrm{S} = 1/(\sigma\, d)$. The diode (green) represents the photo-generating solar cell subdivision. Picture is courtesy of Dr. Sylvio Schubert.

Part III.

Results

7. Doped Charge Carrier Transport Layers Processed From Solution

This chapter introduces a novel approach for the planarization of silver nanowire networks. Three different small molecule charge carrier transport materials are dissolved in various solvents and spin-coated onto glass substrates, ITO electrodes, or silver nanowire electrodes. The conductivity of hole and electron transport materials is controlled via doping with small molecule p- and n-dopants, respectively. The doping process in solution is investigated and compared to reference layers that are deposited via thermal evaporation in vacuum. Moreover, the planarization capability of the solution processing is evaluated.

In Section 7.2, organic solar cells are fabricated onto silver nanowire bottom electrodes and planarized with a solution-processed hole transport layer (s-HTL). The mesh-like structure of AgNW networks leads to micrometer-large voids within the electrode. Thus, a certain HTL conductivity is necessary to sufficiently transport charge carriers between electrode and organic device. The impact of this phenomenon on OPV performance parameters is investigated and verified using equivalent circuit simulations.

Further, another solution-processed HTL is investigated with perovskite solar cells (Section 7.3). A solution-processed electron transport layer is investigated with polymer solar cells in Section7.4.

7.1. Motivation

Organic thin-film devices offer some key advantages as compared to inorganic counterparts (e. g. silicon photovoltaics, light emitting diodes, et cetera): They exhibit high flexibility and enable the possibility of low-cost processing on a large area. For both properties, the bottleneck for realization is not the organic layer stack itself. In fact, all layers of the device need to be flexible, inexpensive, and processable on large areas. Indium tin oxide (ITO) is commonly used as transparent bottom electrode. It exhibits a high optical transmittance and a good electrical conductivity, but suffers from brittleness and high material cost (cf. Section 3.2.1).

Silver nanowires (AgNWs) are a promising technology for ITO-free organic solar cells. Employed as transparent electrode, they show a better electrical conductivity and a similar optical transmittance than ITO electrodes. Inherent flexibility, low fabrication cost, and the advantage of solution-processing make AgNW networks a key technology for a successful market entry of OPV. However, the main challenge of integration into organic thin-film devices is the high roughness of AgNW networks which usually leads to shunts in organic devices. For planarization, many different approaches are reported in literature (cf. Section 3.3.4, p. 57). Thereby, PEDOT:PSS is a frequently used material and many publications show sufficient planarization, allowing efficient devices.[45, 94, 118, 189] Although PEDOT:PSS is a good choice for AgNW planarization, several aspects indicate a decrease of OPV performance. Kawano et al. report on fast degradation of polymer solar cells in air due to hydrophilicity of PEDOT:PSS.[246] The acidity of PEDOT:PSS leads to etching of adjacent layers and thus to an instable interface.[282] In small molecule OPV, the energy level alignment is crucial for obtaining maximum V_{OC} and high fill factors. For example, the absorber systems DCV5T-Me:C_{60} exhibits a DCV5T-Me HOMO level of 5.75 eV,[72] and necessitates an HTL with a similar value, which PEDOT:PSS with a HOMO of 4.8 to 5.1 eV cannot provide. Therefore, additional HTL layers have to be implemented, leading to increased parasitic absorption.

In this study, a novel approach for planarization of AgNW networks is investigated. Instead of using PEDOT:PSS, small molecule charge carrier transport layers are introduced that are processed from solution. Figure 7.1 sketches the comparison of a conventionally planarized AgNW electrode with PEDOT:PSS and the approach presented in this section. Two aspects have to be considered. First, small molecule organic materials are usually thermally deposited in high vacuum. Thereby, the molecule transport is ballistic, which leads to a directional deposition.[266] Due to this directional evaporation, some sample areas are overshadowed by silver nanowires so that no continuous, closed organic layer is possible. Figure 7.2 shows this effect. Especially crucial are junctions and wires that do not lie on the substrate. Consequently, a proper layer sequence cannot be assured if more than one organic material is deposited consecutively.

Second, an important requirement is the finding of a suitable combination of solvent and organic material that dissolves but does not harm the organic material. Fur-

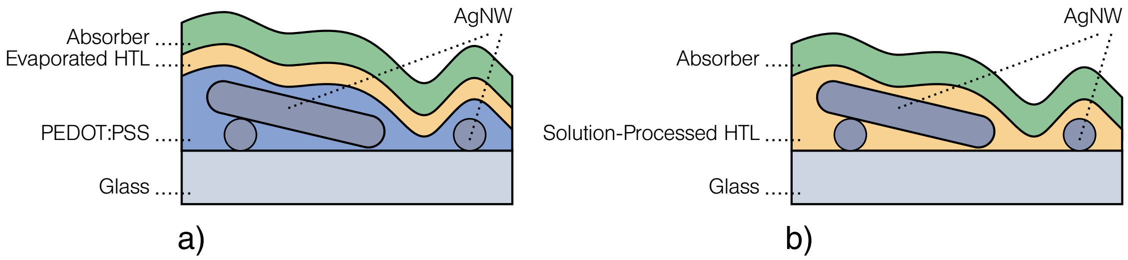

Figure 7.1.: Schematic layer sequence of an organic solar cell until the absorbing layer. **a)** Conventional structure with PEDOT:PSS as planarization layer. **b)** New approach with the solution-processed charge transport layer as planarization layer. The drawing is plotted exemplarily for the HTL. An ETL planarization layer is possible as well.

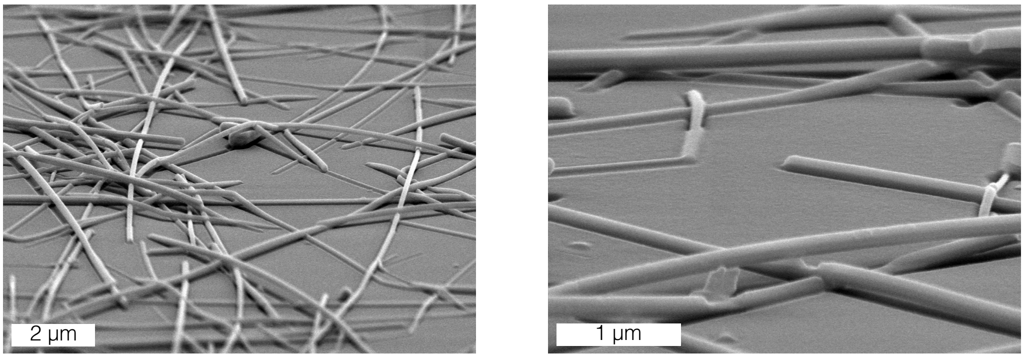

Figure 7.2.: SEM images of NW90 electrode with 100 nm BF-DPB evaporated on top of it.

thermore, HTL conductivity is usually controlled via co-deposition of small molecule dopants. The solvent has to dissolve the dopant as well and the doping process needs to work in solution.
One advantage of this process is that the solution-processed small molecules act as both, planarization layer and HTL or ETL, as schematically shown in Figure 7.1. Thus, no additional layers are needed to align energy levels with the absorbing system, leading to decreasesd parasitic absorption. Moreover, the device stability is increased by the removal of the hydrophilic and acidic PEDOT:PSS. Charge carrier transport materials usually exhibit wide band gaps greater than 3 eV such that they are highly transmissive in the visible part of the spectrum. If non-aqueous solvents are used, the processing may take place in inert atmosphere and, consequently, increases processing reproducibility.

The following small molecules are tested in respect to the aforementioned approach: BF-DPB [175, 216] or Spiro-TTB [250, 281] are used as hole transport materials with the p-dopants F_6-TCNNQ [202] or 'NDP9', which is proprietary. NTCDA and Bis-HFl-NTCDI,[72] doped with 2-Cyc-DMBI [74] or a rhodium dopant (Rh-D),[143] are investigated as electron transport material and n-dopants, respectively (Figure 7.3).

7.2. BF-DPB as Hole Transport Material[1]

BF-DPB is a wide band gap material with a HOMO level of 5.23 eV and an optical bandgap of 3.02 eV. It is chosen due to its successful implementation as hole transport material in small molecule OPV with ZnPc, F_4-ZnPc, or DCV5T-Me as donor, and OLEDs with favorable transmission and stability.[73, 171]
Different solvents like dimethylformamide (DMF), toluene, o-xylene, dichlorobenzene, acetonitrile and tetrahydrofuran (THF) are investigated for dissolving BF-DPB. THF, DMF and o-xylene are able to dissolve BF-DPB up to a concentration of 10 mg/ml, resulting in a clear, colorless solution. Dichlorobenzene – a common solvent for polymer

---

[1] The content of this chapter is published in [6].

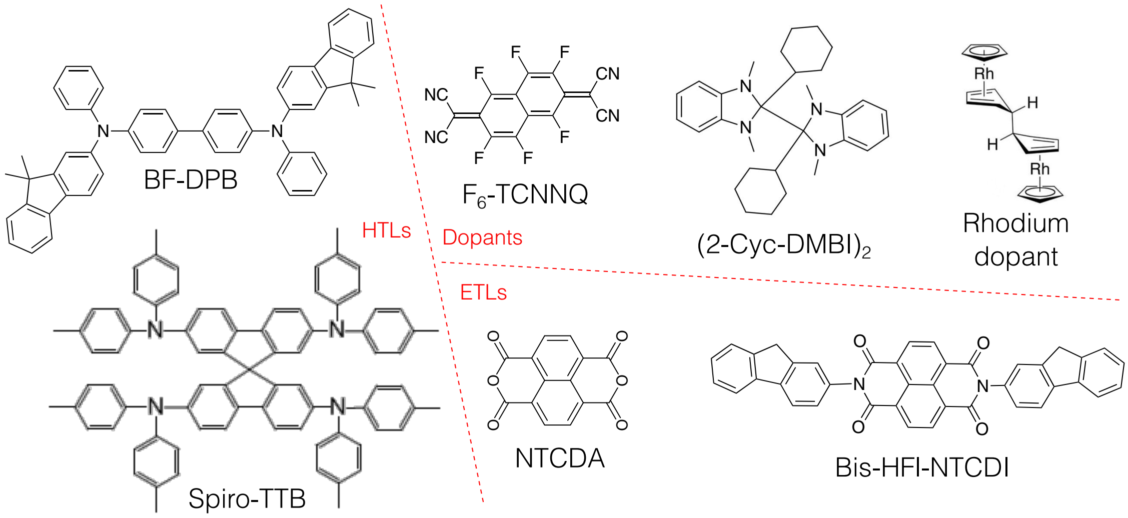

Figure 7.3.: Chemical structures of organic materials used in this study. NDP9 is a proprietary molecule and consequently not depicted. The rhodium dopant molecule picture is taken from [143].

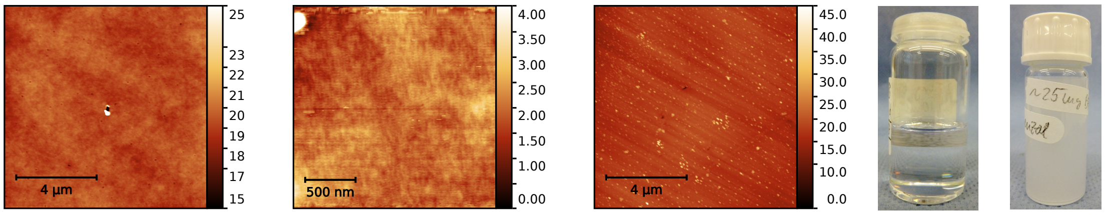

a) b) c) d) e)

Figure 7.4.: AFM images of BF-DPB, spin-coated from **a)** o-xylene, **b)** THF or **c)** dichlorobenzene. Z-scale values are given in nm. Photograph of BF-DPB solution in **d)** o-xylene and **e)** dichlorobenzene.

solar cells – is not able to dissolve BF-DPB. A milky dispersion is obtained even after heating to 100 °C and stirring overnight (Fig. 7.4 e). Consequently, spin-coated films from THF and o-xylene exhibit smooth surfaces (Figure 7.4 a, b) while films that are spin-coated from dichlorobenzene show a grainy structure (Figure 7.4 c).

Spin-coated thin-films of BF-DPB are tested in respect to its electronic functionality. Simple organic solar cells are prepared on ITO and enable a sufficient examination of the lateral HTL transport property. ZnPc:C$_{60}$ solar cells with BF-DPB:F$_6$-TCNNQ (10 wt% DC) are depicted in Figure 7.5 (left), whereby the HTL is deposited either from gas phase or spin-coated from different solvents. With o-xylene or DMF as solvent, the jV curves exhibit a strong s-shaped behavior. Efficiencies of solar cells with these solution-processed HTLs stay far behind the reference solar cell.[2] In contrast, the solar cells with THF as HTL solvent do not show an s-shaped jV curve when merged and processed in N$_2$ atmosphere (Figure 7.5 right). Consequently, further investigations in

---

[2] A detailed examination of these solar cells is done in Section 7.2.1.

this study are carried out with THF as solvent. It is a non-halogenated solvent and, with this, more eco-friendly than typical halogenated solvents like chlorobenzene or chloroform, which are commonly used for the solution-processing of polymer absorbers.

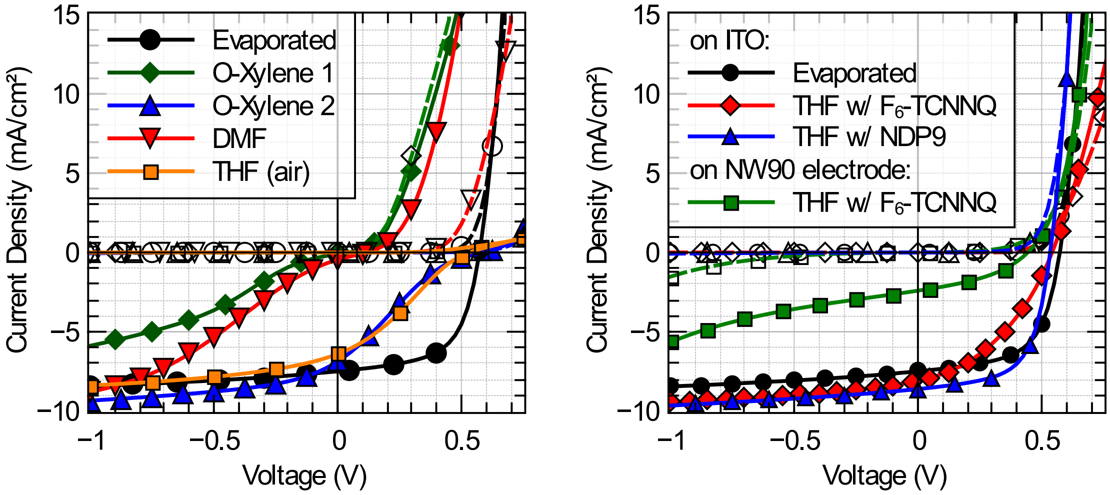

Figure 7.5.: jV curves of ZnPc:C_{60} solar cells on ITO with BF-DPB:F_6-TCNNQ (10 wt%) as HTL and different processing conditions. **Left:** HTL processed from different solvents or co-evaporation. **Right:** HTLs processed from THF in a N_2-filled glovebox. Additionally, a solar cell with NW90 as bottom electrode is depicted.

7.2.1. F_6-TCNNQ and NDP9 as p-Dopant

Intrinsic BF-DPB exhibits conductivities lower than 1×10^{-8} S/cm.[116] Sufficient charge carrier transport is not possible with such low conductivites. To increase HTL conductivity, BF-DPB is doped with molecules exhibiting a LUMO energy lower than the HOMO energy of BF-DPB. F_6-TCNNQ (LUMO of 5.37 eV [202]) and the proprietary 'NDP9'[3] (Novaled AG, Germany) are investigated since they exhibit good functionality in organic solar cells with vacuum-deposited HTLs.[81, 82, 118] For a successful blend of dissolved BF-DPB with one of these dopants, they need to be dissolvable in the same solvents. Luckily, this is the case; F_6-TCNNQ and NDP9 are soluble in THF, DMF and o-xylene. The color of the dopant-containing solution turns reddish brown nearly immediately. After mixing with BF-DPB, the color stays reddish brown.

To examine whether spin-coated thin-films of these composites fulfill the electronic functionality of an HTL, OSCs with ZnPc:C_{60} as absorbing layer are prepared. As this absorbing system is reliable and well studied, failure mechanisms can be attributed to the HTL. Several information about the s-HTL can be extracted with the analysis of

---

[3] The LUMO of this molecule is not public. Experiments show that this material is able to dope hosts down to a HOMO level of 5.6 eV.[72]

the jV curves. If the conductivity is too low, the FF decreases. Misaligned energy levels lead to injection or extraction barriers at the interface between s-HTL and electrode or absorbing system – s-shaped jV curves emerge.[182]

Figure 7.5 shows the jV curves of solar cells with different s-HTL processing conditions. All photovoltaic performance parameters are listed in Table 7.1. As reference solar cell with ITO electrode, an evaporated HTL (e-HTL) with a thickness of 30 nm is used that exhibits V_{OC}, j_{SC}, FF, and PCE values of 0.56 V, 7.5 mA/cm^2, 61 %, and 2.56 %, respectively. Solar cells with o-xylene or DMF as HTL solvent and F_6-TCNNQ as p-dopant exhibit PCEs lower than 1 %. With THF processed in air, the PCE is also lower than 1 %. All these solar cells exhibit strong s-shaped jV curves. This leads to the assumption that the solvents harm the organic materials such that extraction or injection barriers occur at the interfaces.

When mixing and spin-coating the s-HTL in THF inside of a nitrogen-filled glovebox (Fig. 7.5 right), V_{OC} and j_{SC} are comparable to the reference. A FF of 38 % reduces the PCE to 1.64 %. The HTL is functional, but an insufficient conductivity introduces additional series resistance in the device. Most likely, the F_6-TCNNQ is not doping the BF-DPB adequately. Using NDP9 instead of F_6-TCNNQ improves the device performance further such that V_{OC} and FF values are comparable to the reference. The j_{SC} (8.6 mA/cm^2) is even 13 % higher.[4] A proof of principle is performed by fabricating a solar cell on a silver nanowire electrode with an F_6-TCNNQ-doped s-HTL. The efficiency of 0.41 % is rather limited but a working solar cell is obtained. The low j_{SC} is attributed to a low s-HTL conductivity such that device areas far away from a nanowire are not contributing to current generation. This effect is investigated in detail in Section 7.2.4.

Concluding this preliminary study, working devices on ITO with THF as solvent and NDP9 as dopant are fabricated, if they are processed in inert atmosphere. Thus, the following investigations are done using only this material system.

---

[4] Note that the solar cell efficiencies are not mismatch-corrected. Therefore, the absolute j_{SC} values are not reliable. A comparison among identically measured samples is nonetheless possible.

Table 7.1.: Characteristic solar cell fingerprints of ZnPc:C_{60} solar cells with different HTL processing conditions. The solar cells have an assumed area of 6.25 mm^2 and are not mismatch-corrected. Illumination intensity equals 100 mW/cm^2.

Type	j_{SC} (mA/cm^2)	V_{OC} (V)	FF (%)	PCE (%)
with F_6-TCNNQ as p-dopant (10 wt% DC):				
Evaporated	7.5	0.56	61.1	2.56
O-Xylene (batch 1)	0.12	0.054	10.8	7×10^{-4}
O-Xylene (batch 2)	6.9	0.58	20.6	0.82
DMF	0.46	0.17	16.7	0.013
THF (air)	6.6	0.53	27.8	0.97
THF (glovebox)	7.9	0.544	38.2	1.64
THF on NW90 (glovebox)	2.4	0.44	38.9	0.41
with NDP9 as p-dopant (10 wt% DC):				
THF (glovebox)	8.6	0.54	61.0	2.8

7.2.2. Optical and Electrical Properties of BF-DPB:NDP9 Processed from Tetrahydrofuran

Prior to the implementation of the s-HTL into organic solar cells, an analysis of the charge-transfer process in solution is carried out. This is necessary, as the doping process might be different due to the changed processing technique. Furthermore, single layers of the doped s-HTL are investigated by means of spectroscopy and conductivity measurements.

BF-DPB:NDP9 in Solution

To investigate when and where charge-transfer complexes are formed, transmission spectra of BF-DPB, NDP9, and BF-DPB:NDP9 (10 wt%) dissolved in THF are recorded (Figure 7.6 a). The overall molecule ratio in respect to THF at a concentration of 1 mg/ml is only 1:9000 with a given molar mass of 720.941 g/mol (BF-DPB) and 72.11 g/mol (THF).

BF-DPB is transparent over the whole visible spectrum above 410 nm, corresponding to the optical bandgap of 3.02 eV. NDP9 is transparent above 800 nm, has an absorption dip around 685 nm, and an absorption edge at 560 nm. The blend of both materials shows a deep orange color (Figure 7.6 b), exhibits an absorption edge at 550 nm and two absorption dips: a broad one in the near-infrared (NIR) region approximately at 1500 nm and a narrow one at 685 nm. The broad NIR absorption dip is not the sum of the two neat materials and can be attributed to the interaction between dopant and host molecules. The emerging absorption feature may indicate the formation of a metastable hybrid molecule [159] between host and dopant (cf. Sec. 2.1.3). This hybrid molecule exhibits a smaller effective bandgap than the two isolated molecules and is thus responsible for the NIR absorption. Still, the distinct absorption dip around 685 nm in the blend leads to the assumption that many dopant molecules are not forming this hybrid state.

The solution – prepared in a UV-protected nitrogen atmosphere and stored in dark and inert atmosphere – is stable for at least 45 min. However, a 5 min exposure to ambient fluorescent tube light is changing the color to a darkish brown (Figure 7.6 c) with a vanishing NIR peak and a red-shift of the main absorption edge to 800 nm. This indicates a UV-light-activated breakup of this hybrid molecule and a damage of the primary materials.

These spectroscopic investigations suggest that the doping process via the formation of a charge-transfer complex is already happening in solution, although the overall molecule concentration is rather low.

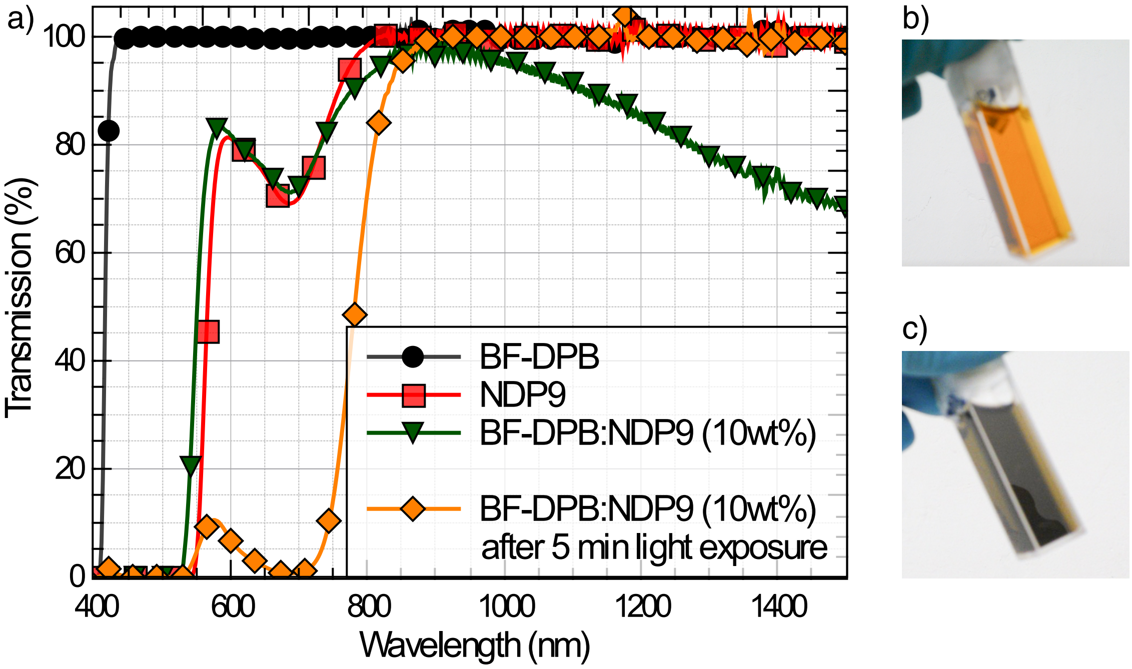

Figure 7.6.: a) Solvent transmission spectra in THF of BF-DPB, NDP9, and BF-DPB:NDP9 (10 wt%) before and after 5 min of ambient tube light irradiation. The neat THF transmission spectra is subtracted from all spectra to show only material transmission. Material concentration in THF is 1 mg/ml. Photographs of a solution of BF-DPB:NDP9 (10 wt%) **b)** before and **c)** after 5 min of ambient tube light irradiation.

BF-DPB:NDP9 Single Layers

Solutions of BF-DPB:NDP9 in THF with different doping concentrations (DCs) and an overall material concentration of 10 mg/ml are spin-coated onto glass substrates. The optical and electrical properties of the thin-films are studied and compared to vacuum-deposited reference layers. Vacuum-deposition is the deposition technique commonly used for this material. Figure 7.7 (left) shows the transmission spectra for 0 wt% and 10 wt% doping concentration with e-HTL and s-HTL. For a better comparison, the spectra are normalized to their value at 800 nm where no influence on the DC is observed.

All layers show a generally similar behavior: they are very transparent in the regime from 400 to 800 nm. A strong absorption dip arises around 400 nm that can be related to the optical bandgap of BF-DPB. The glass substrate causes a strong transmission cutoff below 300 nm. With increasing DC, two absorption dips around 500 nm and 700 nm occur in both, the spin-coated and the vacuum-deposited layers. Figure 7.7 (right) shows the emergence of the dip at 500 nm for intermediate DC of the s-HTL.

The conductivity is measured for evaporated and solution-processed samples. Figure 7.8 shows that the conductivity increases up to a value of 3×10^{-4} S/cm with increasing doping concentration for both deposition techniques. Two observations lead to the assumption that the actual doping efficiency is slightly lower in s-HTL than in e-HTL layers. First, the dopant absorption dips are more pronounced in spin-coated layers, especially the intrinsic dopant absorption at 700 nm (see Fig. 7.7). Second, conductivity values for the s-HTL lag behind the ones from vacuum-deposition for doping concentrations of 1 and 5 wt%, being more pronounced for the lower doping concentration.

Furthermore, the absorption coefficient α is calculated from the transmission spectra using Equation 7.1 and a layer thicknesses d of 30 nm (e-HTL) or 100 nm (s-HTL).

$$\alpha = \frac{-\ln(T_{\text{vis}}/92)}{d} \tag{7.1}$$

They are in the range of 7×10^3 to $12 \times 10^3\,\text{cm}^{-1}$ and 18×10^3 to $24 \times 10^3\,\text{cm}^{-1}$ for the s- and e-HTL, respectively. The calculation reveals that α of the s-HTL is half as much as the one from e-HTL. This behavior is explained by the different growth mechanism for the two deposition techniques. As evaporated layers often show a higher crystallinity than solution-processed ones, the up to 10 % stronger e-HTL film absorption in comparison to the s-HTL in the wavelength regime from 400 to 550 nm supports this assumption.[205, 256] Two further effects induced by solution-processing may have an influence on the resulting layer. On the one hand, the two materials fall below their solubility limit at different stages of solvent evaporation. This could lead to clustered dopant molecules within the matrix, consequently resulting in a lower doping efficiency and a higher intrinsic dopant absorption. Both is visible in the transmission spectra (absorption dip at 500 nm) and the conductivity (lower at low DC as compared to the e-HTL). On the other hand, main parts of the solution are removed from the substrate during spin-coating. An inhomogeneous molecule distribution in the solution might affect the resulting ratio between dopant and host, leading to a lower dopant or host concentration. However, the high intrinsic dopant absorption in s-HTL thin-films is not supporting this hypothesis. It is assumed that the DC in the film is very similar to the DC in solution.

Concluding this part, the electronic functionality of the materials as hole transport layer is maintained after solution-processing in THF and the conductivities for high DC are similar to the e-HTL layers.

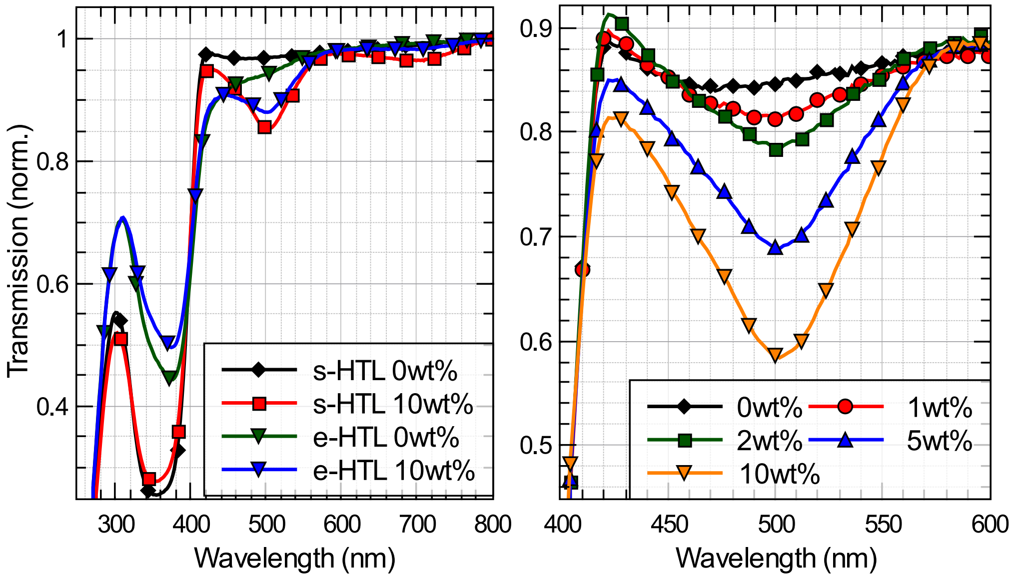

Figure 7.7.: Left: Normalized transmission spectra of spin-coated (s-HTL) and evaporated (e-HTL) BF-DPB:NDP9 layers on glass with 0 wt% and 10 wt% doping concentration. For better comparability, the measured values are normalized at 800 nm which corresponds to a total transmission of (87.3 ± 0.5) % (s-HTL) and (90.6 ± 0.5) % (e-HTL). The different transmission values between 300 nm and 800 nm are due to different layer thicknesses. **Right:** Transmission values for s-HTL with (0, 1, 2, 5 and 10) wt%. The spectra are normalized at 800 nm.

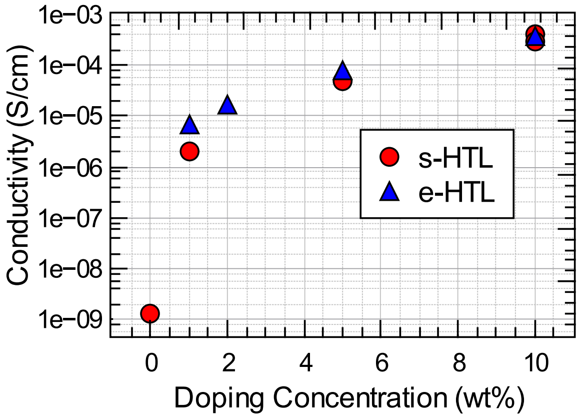

Figure 7.8.: Conductivity of solution-processed and evaporated BF-DPB:NDP9 layers with different doping concentrations.

7.2.3. Silver Nanowire Electrode Planarization with Solution-Processed BF-DPB:NDP9

Continuing this study, the planarization effect of the s-HTL on a rough AgNW electrode is investigated. SEM and AFM images are acquired before and after the deposition of a s-HTL on AgNW networks with glass as substrate. First, the influence of the dopant on s-HTL topography is investigated by acquiring AFM images of the thin-films with different doping concentrations (Figure 7.9). All films look very similar with a R_{rms} of (0.6 ± 0.3) nm. The topography is not influenced by the dopant. Thus, the planarization study on AgNW electrodes is performed exemplarily with undoped BF-DPB as s-HTL.

Investigations on the s-HTL planarization capability are done with AgNWs deposited on glass substrates. AgNW diameters of 90 nm (NW90) and 35 nm (NW35) are used. They are in the range of the most common wire diameters in literature and yield very good electrode performance.[35, 108, 211, 234] Figure 7.10 (a) shows a tilted view onto a neat NW90 electrode. The nanowires loosely lie over each other with weak contact to the substrate, resulting in a highly non-uniform topography. The same NW90 electrode is shown after s-HTL coating in Figure 7.10 (b). Here, the nanowires are buried in the s-HTL film and the electrode appears to be compressed in height. Capillary forces during solvent evaporation are leading to this AgNW network compression.[82] The junctions are still the highest point of the electrode but they are covered with BF-DPB as well. Some quantitive information can also be extracted from AFM images (Fig. 7.10 c, d), as the R_{rms} is reduced from 73 nm without s-HTL to 41 nm with s-HTL.

For the NW35 electrode with thinner nanowires, a similar study is done using AFM. Untreated NW35 electrodes (Figure 7.11 a, c) exhibit a peak-to-valley height D_{ptv} of 200 nm on $(10 \times 10)\,\mu\mathrm{m}^2$ image size and 170 nm on smaller scale ($(2 \times 2)\,\mu\mathrm{m}^2$). The wire contours are very defined. After s-HTL deposition (Figure 7.11 b, d), D_{ptv} values are 100 nm and 25 nm for large and small image sizes, respectively. Washed-out AgNW contours indicate soft slopes of HTL material along the nanowires. On large image size, just a few junctions increase the D_{ptv} value up to 100 nm. A drastic reduction from 170 nm to 25 nm is observed on small area.

Both imaging techniques reveal that the electrode topography is planarized in a distinct manner for both nanowire diameters with this small molecule material, even if the initial D_{ptv} values exceed the thickness (approximately (100 ± 10) nm) of the deposited thin-film. The SEM/AFM examinations and the observation of washed-out contours lead to the conclusion that BF-DPB is gathering around and on top of the nanowires and nanowire junctions. This indicates a strong smoothening effect on the initially very rough AgNW topography.

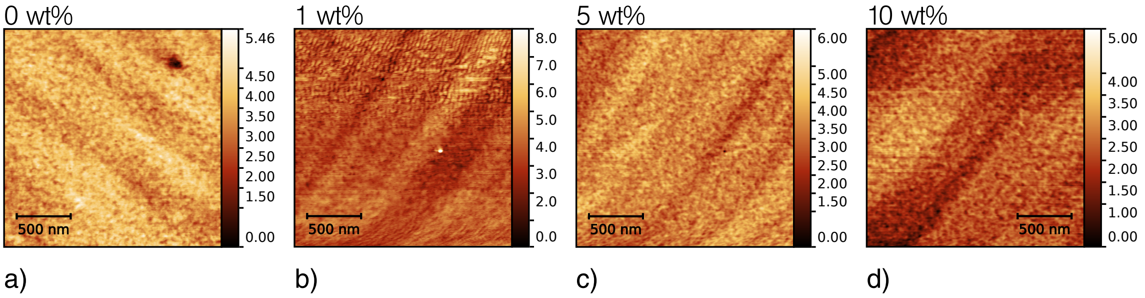

Figure 7.9.: AFM images of s-HTL thin-films on glass with **a)** 0 wt%, **b)** 1 wt%, **c)** 5 wt% and **d)** 10 wt% doping concentration. Scale values are stated in nm.

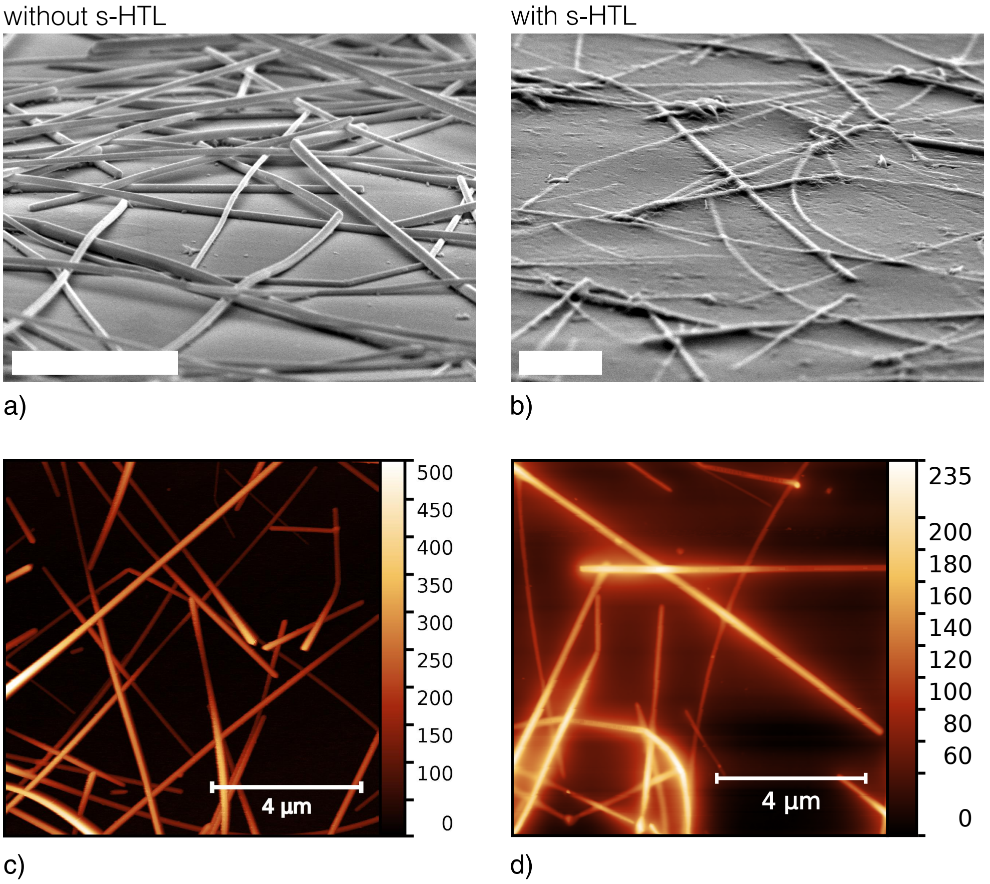

Figure 7.10.: Top: SEM images showing the **a)** untreated and **b)** the planarized NW90 electrode with s-HTL (0 wt% DC). Samples are tilted with an angle of 75 °, scalebars represent 2 µm. **Bottom:** AFM images of **c)** untreated and **d)** planarized NW90 electrode. Scale values are stated in nm.

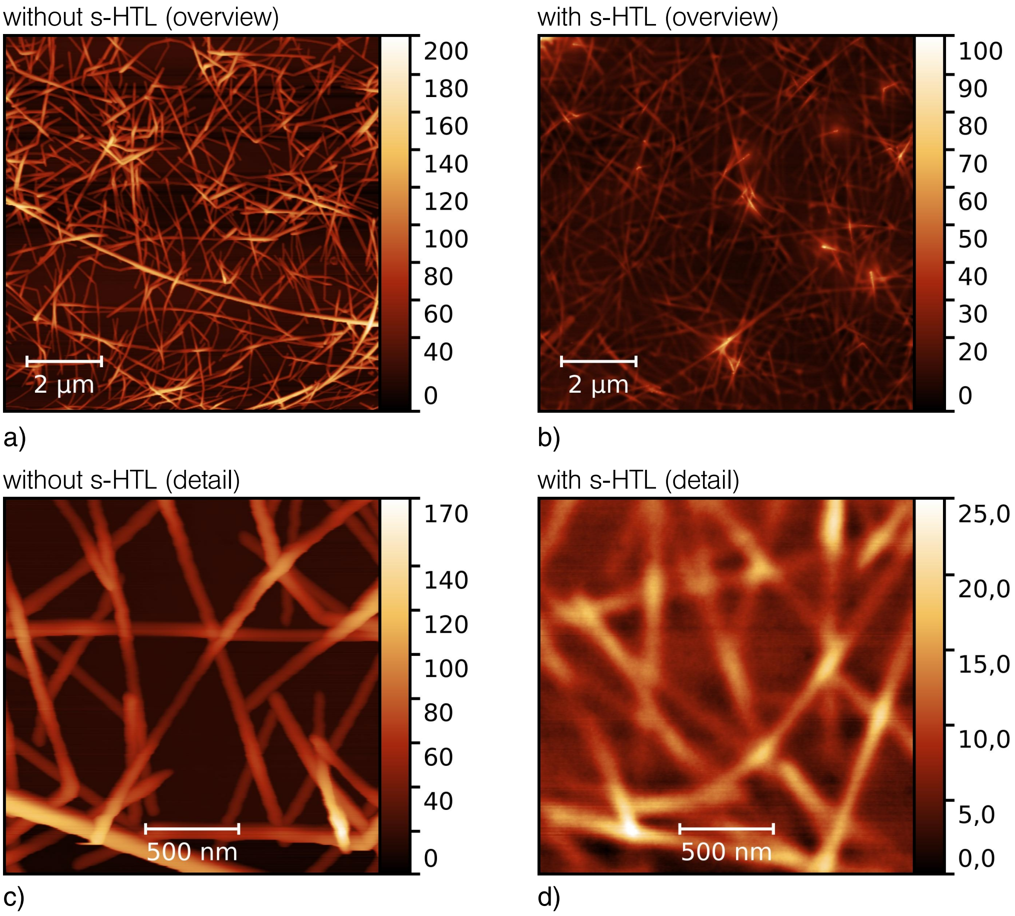

Figure 7.11.: AFM images of NW35 electrode. **a), c)** Without s-HTL. **b), d)** With undoped s-HTL. Scale values are stated in nm.

7.2.4. Investigating the Impact of Microscopic Network Voids on the Macroscopic Solar Cell Performance

Silver nanowire electrodes have a fundamentally different microscopic structure than common TCOs. TCO electrodes constitute a uniform, closed layer. A charge carrier needs to travel only in vertical direction through a device to reach the highly conductive electrode. This pathway is not longer than 100 nm in most OPV charge carrier transport layers (Fig. 7.12 a). In contrast, AgNW electrodes exhibit voids between the wires, ranging up to a size of square micrometers (cf. Fig. 7.10). The voids need to be filled by a transport layer. A charge carrier, located above such a void, needs to travel through the organic layer filling in vertical and lateral direction to reach the nanowire network (see Figure 7.12 b). These higher distances entail higher requirements on the conductivity of the charge carrier transport layer. If not fulfilled, the macroscopic OPV device performance suffers from a hindered charge carrier transport. This issue is similar to the electrode requirements discussed in Section 3.1, but on a different length scale.

In this section, the impact of the microscopic void-like AgNW electrode structure on OPV device performance is investigated with respect to the s-HTL conductivity.

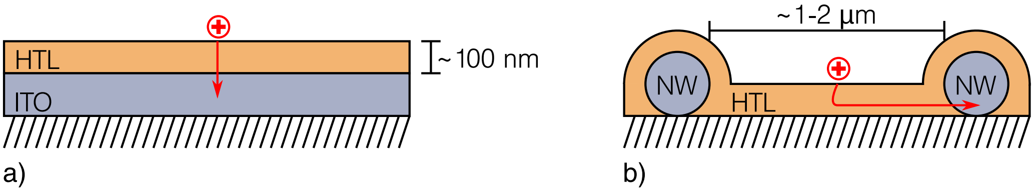

Figure 7.12.: Charge carrier transport on **a)** ITO or **b)** AgNW electrode. A charge carrier has to travel up to 100 nm or 1 to 2 µm in the case of ITO or AgNW networks, respectively.

Organic solar cells with a ZnPc:C_{60} bulk heterojunction as active layer are built. For a comparison of the different deposition techniques, ITO electrodes are coated with e-HTL and s-HTL. NW90 electrodes are planarized with s-HTL. The HTL conductivity is varied by changing the doping concentration in a range from 0 to 10 wt%. jV curves taken under illumination and characteristic device parameters for OSCs on NW90 and ITO electrodes are shown in Figure 7.13 left, Figure 7.14, and Table 7.2, respectively.

All devices with undoped HTL (0 wt%) have a low performance in common due to extremely low HTL conductivities of approximately 1×10^{-9} S/cm (cf. Fig. 7.8). Remarkably, the OSC on NW90 exhibits a diode-like behavior while on ITO, nearly no current is flowing through the device with s-HTL. A strong 's' shape in the jV curve is observed with e-HTL (Fig. 7.14 left). A maximum power conversion efficiency (PCE) of 2.3 % is achieved on ITO/e-HTL (5 wt%), NW90 (10 wt%) exhibits comparable PCEs. Solar cells on ITO have a decreasing V_{OC} down to 0.5 V for increasing DC. On NW90 electrode, the V_{OC} remains at 0.49 V for DC greater than 0 wt%. The j_{SC} for all ITO-based devices with a DC greater than 0 wt% is very similar for all s-HTL devices and

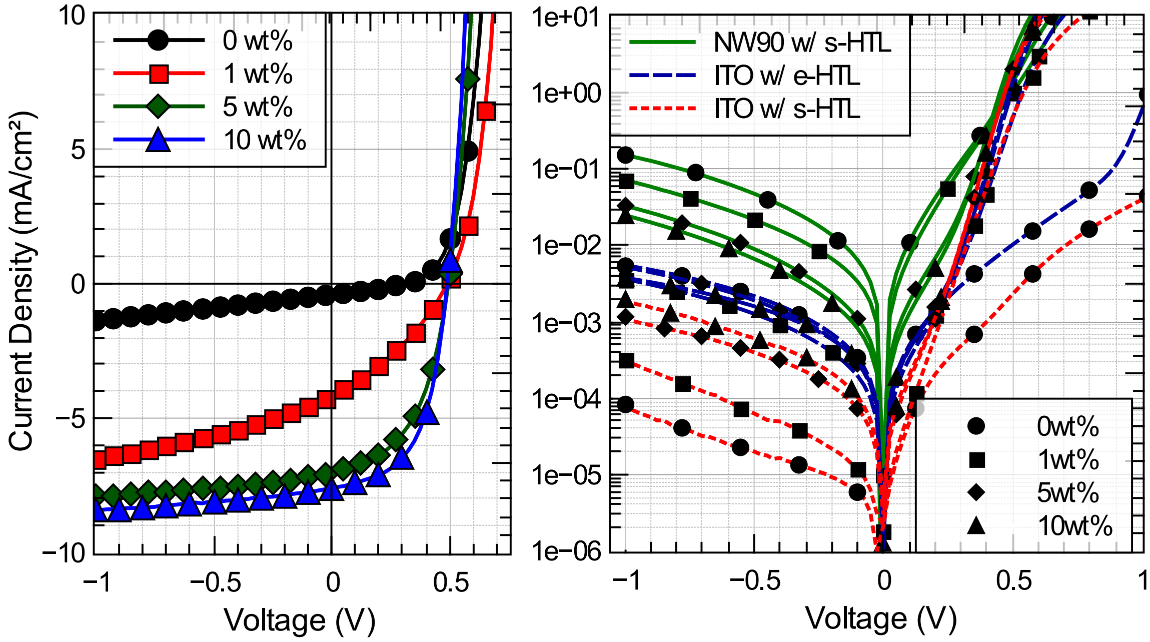

Figure 7.13.: jV curves of ZnPc:C_{60} solar cells with varied doping concentration of the s-HTL. **Left:** On NW90 electrode with 100 mW/cm^2 illumination. **Right:** Dark jV curves on NW90 electrode with s-HTL and on ITO with e- or s-HTL.

with slight deviations on e-HTL devices.

On NW90 electrodes, the j_{SC} is strongly increasing with DC and reaches $7.6\,\mathrm{mA/cm^2}$ (10 wt%), which equals the best j_{SC} for ITO-based devices. The FF is increasing with higher DC for every electrode type, but with stronger extent on NW90 electrode. The best FF value of 60 % is reached for the e-HTL device on ITO with 10 wt% DC while the FF equals 55 % with s-HTL (10 wt% DC). Dark jV curves (Fig. 7.13 right) reveal that the leakage current densities for the devices are in different orders of magnitude. OSCs on NW90 have the highest values indicating high leakage, while the s-HTL on ITO performs even better than the e-HTL reference. It is assumed that the roughness of the NW90 electrode still leads to additional leakage currents in the device. The dark currents of the s-HTL devices on ITO are even lower than with the reference deposition method. This might be due to an extremely smooth surface with R_{rms} values below 1 nm (cf. Fig. 7.9).

For the dependence of V_{OC} on the DC (for DC greater than 0 wt%), an ohmic contact between the electrode and the HTL is considered due to the presence of dopant molecules and a small energetic barrier between the ITO with a work function around 5 eV and the HTL HOMO energy level of 5.23 eV. This results in a higher V_{OC} for low DC.[126] With increasing DC, the Fermi level in the HTL shifts towards the HOMO which increases injection barriers between the HTL and the BHJ. The V_{OC} gets smaller.[183] Further, a direct contact of p-doped HTL and BHJ is not favorable. The dopants act as recombination centers and traps for charge carriers, leading to a worsening of V_{OC} and j_{SC}. This might explain the different V_{OC} in the case of e-HTL and s-HTL. On

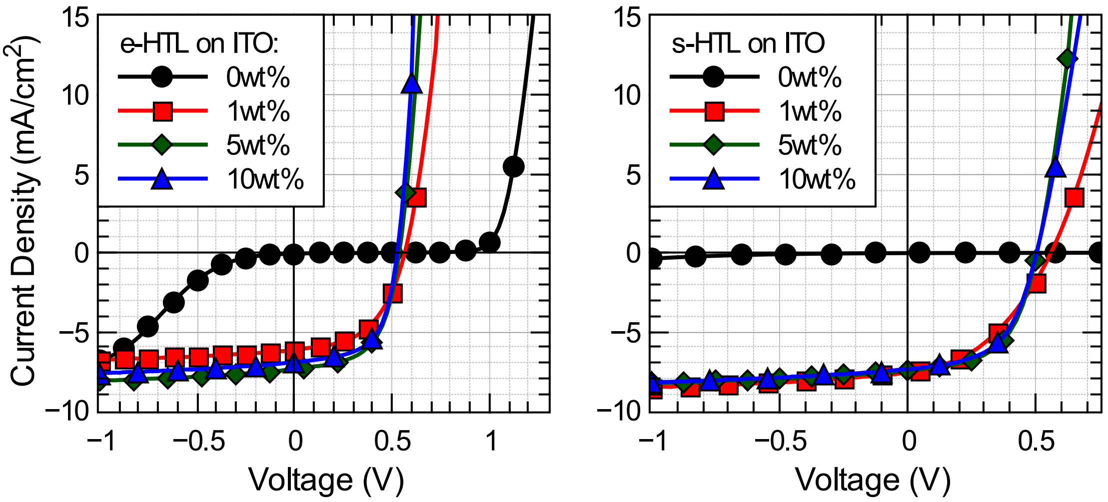

Figure 7.14.: jV characteristics of illuminated ZnPc:C_{60} solar cells on ITO with **Left:** 30 nm e-HTL and **Right:** 90 nm s-HTL.

an AgNW electrode, the work function of silver (4.3 eV) leads to higher energetical barriers at the interfaces, but the independence from DC needs further investigation. The key for understanding the strong variation of j_{SC} with varying DC on NW90 electrode is the interplay between HTL conductivity and the microscopic electrode structure. The voids in the silver nanowire mesh are in the square micrometer range and filled with the s-HTL. A charge carrier that is located far away from a nanowire needs to overcome micrometeres in lateral direction within the HTL to reach the highly conductive AgNW network, and vice versa. If the lateral HTL conductivity is too low, this process leads to a decreased effective active area, resulting in a reduced j_{SC}. For ITO-based devices, the charge carrier needs to cross the HTL only 30 to 100 nm in vertical direction to reach the transparent electrode, which is less lossy due to the smaller distance (cf. Fig. 7.12).

An equivalent circuit model is employed to quantify the effect of j_{SC} variation on AgNW electrodes and to relate it to HTL conductivities. A simulation of 2500 ideal, photo-generating diodes is conducted in a discretized $(1 \times 1)\,\mu\mathrm{m}^2$ area surrounded by the nanowire network. The HTL is implemented in the simulation as interconnected serial resistances between the diodes and the nanowire grid in lateral direction (cf. Fig. 6.1, p. 78 in the Experimental Section). The sheet resistance R_{S} of the HTL equivalent is varied and the resulting device performance is calculated. R_{S} is derived using the equation $R_{\mathrm{S}} = 1/(\sigma \cdot d)$ with HTL conductivity σ and a fixed HTL thickness d of 90 nm. The percentage loss in PCE compared to the PCE of a device with the highest investigated HTL conductivity is plotted in Figure 7.15. For simulated devices, an efficiency loss can be observed that emerges at 1×10^{-5} S/cm with 5 % and increases to 85 % at 1×10^{-8} S/cm. The loss in real devices appears to be 20 % already at 1×10^{-4} S/cm and reaches nearly 100 % at 1×10^{-9} S/cm. Although the behavior

Table 7.2.: Photovoltaic performance parameters of ZnPc:C_{60} OSCs in respect of s-HTL doping concentration and bottom electrode with e- or s-HTL (NW90 electrode with s-HTL). Values are always from the best pixel. The active area is 6.44 mm^2. Current densities are corrected for spectral mismatch.

DC	ITO		NW90	ITO		NW90
(wt%)	e-HTL	s-HTL	s-HTL	e-HTL	s-HTL	s-HTL
	V_{OC} (V)			FF (%)		
0	0.41	0.36	0.32	15	19	33
1	0.57	0.56	0.49	51	41	34
5	0.54	0.51	0.49	57	55	50
10	0.53	0.50	0.49	60	55	55
	j_{SC} (mA/cm^2)			PCE (%)		
0	0.04	0.01	0.4	0	0	0.04
1	6.2	7.6	4.2	1.8	1.8	0.7
5	7.4	7.5	7.0	2.3	2.1	1.7
10	6.9	7.4	7.6	2.2	2.0	2.1

is more steep and pronounced for real devices, it is shown that the measured HTL conductivity is in the range where losses in the device performance are observed. Due to a hindered current transport through the nanowire voids in the simulation, the j_{SC} goes down. The size of the real AgNW network is most likely not exactly 1 µm^2 and varies over the whole network. This reasons the deviant behavior between simulation and experiment.

Furthermore, the FF for simulated devices is also dependent on the HTL conductivity. This explains the stronger FF dependence on NW90 than on ITO electrode devices. The HTL is introducing serial resistances in lateral direction additionally to the vertical direction.

The simulation elucidates that the R_{S} of the HTL is the only driving force leading to FF and j_{SC} losses in organic solar cells if voids within the electrode have to be bridged by the HTL.

This investigation leads to two straightforward solutions for containing losses in organic solar cells when embedding AgNW electrodes. Voids in the micrometer range necessitate a conductivity greater than 1×10^{-4} S/cm of the HTL to maintain a lossless macroscopic device perfomance. Vice versa, if the HTL conductivity cannot be enhanced due to physical limitations, a reduction of the mesh size should be able to compensate the insufficient HTL conductivity. For example, realization is possible by using NW35 electrodes (cf. Fig. 7.11) which provide a smaller mesh size at a similar electrical and optical performance.

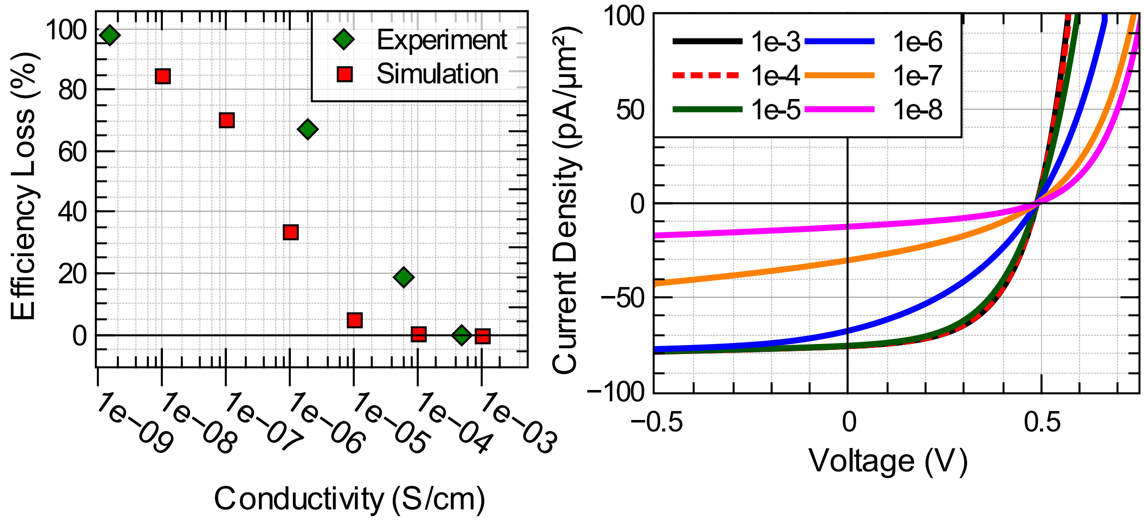

Figure 7.15.: Left: PCE loss in NW90 OSCs compared with the PCE loss in simulated devices in dependence of HTL conductivity. The loss is always given in respect to the PCE of the device with highest HTL conductivity. **Right:** Simulated jV curves of solar cells in dependence of the HTL conductivity in S/cm. The cells have an active area of 1 µm^2 representing one AgNW network void.

7.2.5. Efficient OPV Devices Using an Oligothiophene Donor

To further show the potential of the AgNW/s-HTL hybrid system, solar cells with a highly efficient donor are fabricated. ITO, NW90, and NW35 – planarized by an s-HTL with a thickness of (100 ± 10) nm – are employed as transparent bottom electrodes. Organic solar cells on ITO with a 90 nm thick e-HTL serve as fully evaporated reference devices. DCV5T-Me is chosen as donor in a p-i-n solar cell architecture (Fig. 7.16 d) due to its potential for highly efficient OSCs.[72, 140] For matching the HOMO level of DCV5T-Me (5.66 eV), a 5 nm thin layer of BPAPF:NDP9 (HOMO 5.6 eV) is inserted, followed by additional 5 nm of intrinsic BPAPF. Corresponding jV curves and photovoltaic performance parameters are depicted in Fig. 7.16 and Table 7.3, respectively. The reference solar cells on ITO/e-HTL show a maximum PCE of 5.37 %. The OSCs with s-HTL exhibit a PCE of 3.7 % on NW90, 4.05 % on ITO, and 4.4 % on NW35 electrode. The dark jV curves (Fig. 7.16 b) reveal that leakage currents in backward direction are in the range of 1×10^{-3} mA/cm^2 for ITO/e-HTL, 1×10^{-2} mA/cm^2 for ITO/s-HTL and NW35, and 1×10^{-1} mA/cm^2 for NW90. Despite the fact that the fully evaporated reference cell shows higher j_{SC}, FF and PCE values than the s-HTL devices, the V_{OC} for all devices is the same. This can be attributed to the inserted intrinsic BPAPF layer which prevents direct contact between dopant and bulk heterojunction. From all devices with s-HTL, the j_{SC} is around (20 ± 5) % lower than the reference j_{SC}. FF, saturation S, and PCE is best on NW35 and worst on NW90.

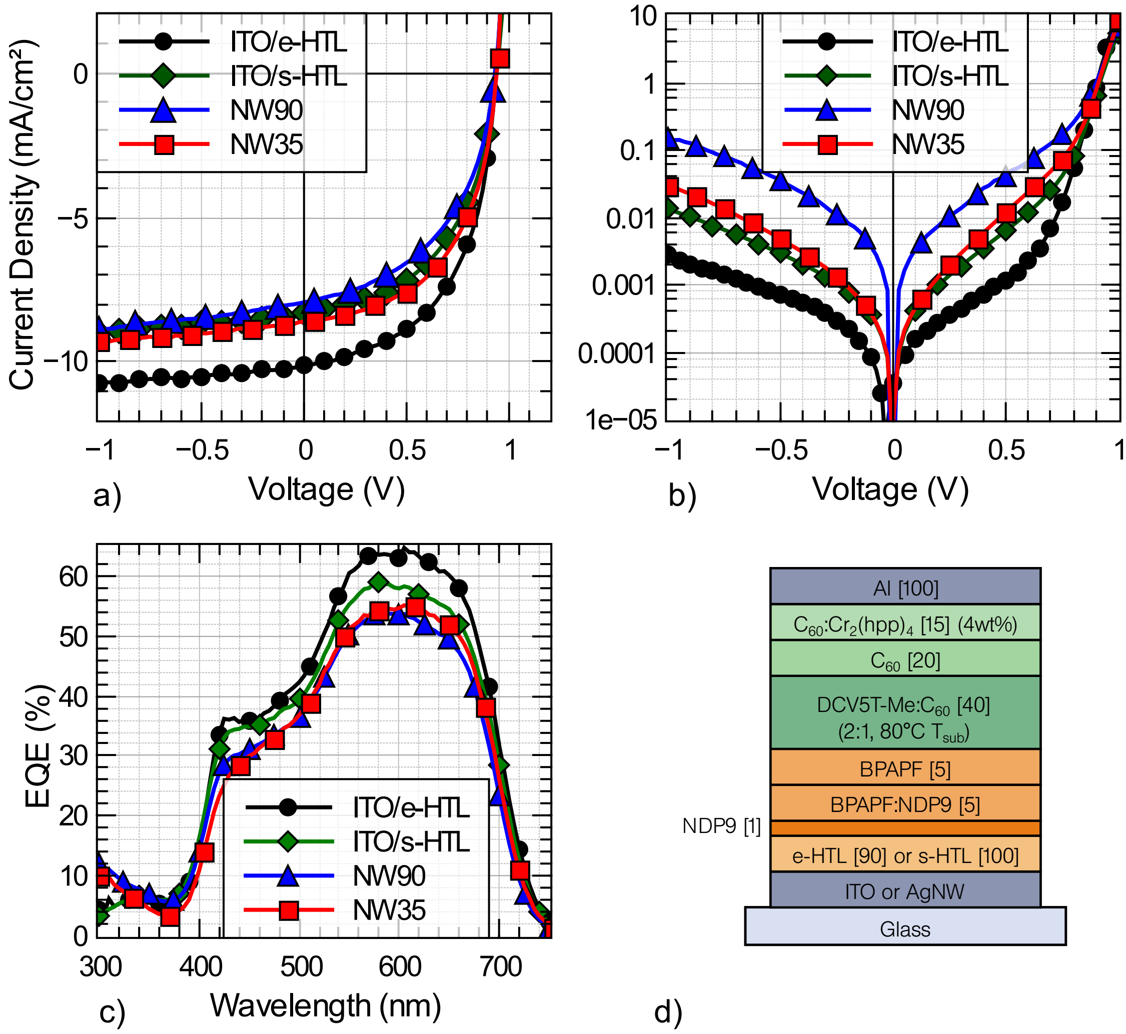

Figure 7.16.: a) Illuminated and mismatch-corrected jV characteristics of DCV5T-Me:C_{60} solar cells on different electrodes with e- or s-HTL (10 wt% doping concentration). **b)** Dark jV characteristics with logarithmic scale of j. **c)** External quantum efficiency, measured at short circuit condition. **d)** Schematic solar cell stack. Bracket values are stating the layer thickness in nm.

Hereby, saturation S is defined as

$$S = \frac{j(-1V)}{j_{\mathrm{SC}}} \tag{7.2}$$

and quantifies leakage properties of illuminated solar cells.

Dark currents in the negative voltage regime are always much higher for NW90 electrodes. On NW35, they are comparable to ITO. The saturation shows a similar trend: the NW35 value of 1.08 is close to the reference value of 1.06 and even better than the ITO/s-HTL device. The highest value of 1.1 is observed on NW90. A higher saturation value and higher dark current are attributed to roughness-induced leakage

Table 7.3.: Characteristic device parameters of DCV5T-Me:C_{60} solar cells, 4 pixels averaged, best value in brackets. Where no deviation is stated, the mean deviation is smaller than 1 %.

	V_oc (V)	j_sc (mA/cm^2)	FF (%)	Saturation	PCE (%)
ITO e-HTL	0.94	10.1 ± 0.1 (10.23)	54.9 ± 0.7 (55.8)	1.06	5.2 ± 0.1 (5.37)
ITO s-HTL	0.94	8.0 ± 0.2 (8.3)	51.3 ± 0.4 (51.6)	1.10	3.9 ± 0.1 (4.05)
NW90	0.9 ± 0.1	7.9 ± 0.4 (7.95)	48.9 ± 0.8 (49.2)	1.1 ± 0.3 (1.12)	3.5 ± 0.9 (3.7)
NW35	0.94	8.4 ± 0.1 (8.6)	53.0 ± 0.7 (54.1)	1.08	4.2 ± 0.1 (4.4)

and a suboptimal diode behavior. Furthermore, the mesh size in the NW35 is smaller as compared to a NW90 electrode, which leads to a decreased requirement on the HTL conductivity.

The largest discrepancy in efficiency compared to the reference devices comes from a loss in j_SC which is in the range of (20 ± 5) %. This loss is also visible on ITO/s-HTL devices, meaning that it is not caused by the void-like AgNW electrode. A possible explanation could be a different growth and morphology of the vacuum-deposited BPAPF and DCV5T-Me:C_{60} layers due to a different morphology of spin-coated/vacuum-deposited HTLs. It might influence either the charge carrier generation or the transport into adjacent layers. However, a detailed understanding of the morphological impact of DCV5T-Me:C_{60} solar cells in p-i-n architecture has not yet been achieved. A mismatch of the electrical field distribution within the absorbing layer due to optical reasons can be excluded because all thicknesses and materials for e-HTL and s-HTL on ITO are the same.

Summarizing, it is demonstrated that OSCs on NW35 with s-HTL yield efficiencies up to 4.4 %, which is higher than the efficiency of OSCs on NW90 and also on ITO with s-HTL. Still, a device performance worsening due to topography-induced leakage currents on NW90 electrodes is observed which are not present on NW35 electrodes. In conclusion, the nanowire topography has no negative influence anymore on the device perfomance with NW35 electrodes and s-HTL.

7.2.6. Conclusion

A solution-processed small molecule hole transport layer is introduced consisting of host (BF-DPB) and p-dopant (NDP9) with tetrahydrofuran as solvent. Spectral analysis reveals that the actual doping process takes place in the THF solution. The conductivity of the solution-processed material composite could be tuned over several orders of magnitude up to 3×10^{-4} S/cm by controlling the doping concentration nearly as sufficient as with the vacuum deposition technique.

The interplay between the highly conductive but void-like nanowire mesh together with a low-conductive s-HTL filling is investigated by fabricating ZnPc:C_{60} organic solar cells. One finding is that void-like electrodes like AgNW electrodes may reduce the macroscopic device perfomance, if the conductivity of the charge carrier transport material is too low. In our case of micrometer-large voids on NW90 electrodes, a s-HTL with a conductivity greater than 1×10^{-4} S/cm is able to prevent losses in j_{SC} and FF.

By showing solar cells with PCEs reaching 4.4 % on AgNW electrodes, a solution-processed small molecule hole transport layer is demonstrated that is capable of planarizing silver nanowire networks. The planarization is sufficient even in the case where the deposited layer thickness is less than the peak-to-valley height of the AgNW network. The efficiency on AgNW/s-HTL electrode is with 4.4 % even higher than on the reference ITO/s-HTL device (4.05 %).

This investigation moreover emphasizes a general difficulty when using void-like electrodes in combination with low-conductive organic materials. The trade-off between electrode void size and conductivity of charge carrier transport materials need to be taken into account when developing new concepts for ITO-free organic devices.

7.3. Spiro-TTB Doped with NDP9 as Hole Transport Layer

Another hole transport material is spiro-tetra(p-methyl-phenyl)-benzidine (Spiro-TTB).[281, 285] The molecule core consists of two interconnected molecular π-systems using a shared sp^3-hybridized carbon atom, the so-called spiro-compound (cf. Figure 7.3 on p. 84). This concept improves the morphological stability, prevents crystallization below the glass transition temperature T_{g}, stabilizes emission properties in the case of fluorescent dyes, and entails a higher solubility in organic solvents.[248, 250] Thus, spiro-linked organic molecules are widely used in many different optoelectronic applications like OLEDs [97, 175, 290], organic lasers [135, 271] and dye-sensitized solar cells.[136, 213] Nowadays, spiro-linked hole transport materials attract attention in the context of perovskite solar cells (PSCs) and help improving their power conversion efficiencies.[63, 77, 150]

Spiro-TTB is a hole transport material widely used at the IAPP. It has an ionization potential[5] of 5.25 eV, a hole mobility[6] of $(5.7 \pm 0.5) \times 10^{-5}\,\mathrm{cm^2/(V\,s)}$, and a conduc-

---

[5] 10 nm Spiro-TTB on ITO substrate, measured with ultraviolet photoelectron spectroscopy by Martin Schwarze (IAPP).

[6] Measured in OFET geometry.[250]

tivity of $1.9 \times 10^{-4}\,\mathrm{S/cm}$ with 5 wt% NDP9 as dopant.

In this section, a short analysis of the feasibility as doped, solution-processed HTL is presented. The layer formation is investigated by means of spectroscopic and topographic analysis on glass and on AgNW electrodes. Further, the application of Spiro-TTB:NDP9 as a hole transport layer in perovskite solar cells on ITO and AgNW electrodes is investigated.

Tetrahydrofuran is used for dissolving Spiro-TTB due to its positive results with BF-DPB (cf. Section 7.2). A concentration of dissolved Spiro-TTB in THF is tested up to 15 mg/ml, proving sufficient solubility. Although F_6-TCNNQ is a suitable p-dopant in reference devices with evaporated HTL that leads to conductivities up to $1.8 \times 10^{-5}\,\mathrm{S/cm}$, NDP9 is used because F_6-TCNNQ showed poor stability in THF solution (cf. Section 7.2.1). The spin-coated layers of Spiro-TTB:NDP9 have a thickness of $(55 \pm 3)\,\mathrm{nm}$. A doping concentration of 4 wt% with NDP9 is set, as conductivity measurements with NDP9 for evaporated films show sufficient conductivities also for doping concentrations below 10 wt% (Figure 7.17). A conductivity of $(6.0 \pm 0.1) \times 10^{-5}\,\mathrm{S/cm}$ (4 wt% DC) is measured and lies within a value expected for such DC. Thus, the doping is nearly as efficient as in evaporated layers.

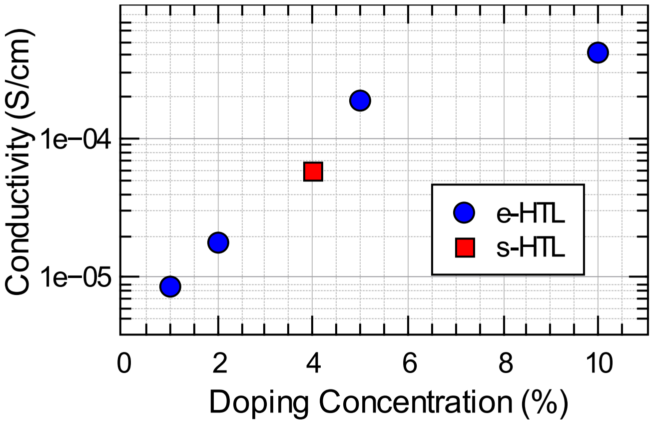

Figure 7.17.: Conductivity of evaporated (e-HTL) or solution-processed (s-HTL) Spiro-TTB:NDP9 thin-films in dependence on doping concentration.

Figure 7.18 depicts transmission measurements of Spiro-TTB (4 wt% DC) on glass and on NW90 electrode in comparison to solution-processed BF-DPB (10 wt% DC). On glass, the Spiro-TTB layer is highly transparent down to 400 nm which corresponds to the optical band gap of 3.25 eV. A weak absorption dip arises at $(500 \pm 5)\,\mathrm{nm}$ and can be attributed to the dopant absorption (cf. Fig. 7.7 (left) on p. 90). The averaged transmission T_{vis} equals $(85 \pm 5)\,\%$ on glass and $(77 \pm 5)\,\%$ on NW90. T_{vis} of the bare NW90 electrode equals $(84 \pm 1)\,\%$. The difference in T_{vis} of Spiro-TTB on glass and on NW90 can be fully attributed to the AgNW absorption. Compared to BF-DPB with a T_{vis} of $(81 \pm 5)\,\%$ on glass and $(73 \pm 5)\,\%$ on NW90, the transmission is 4 % higher. Also the absorption at 700 nm is weaker as compared to BF-DPB.

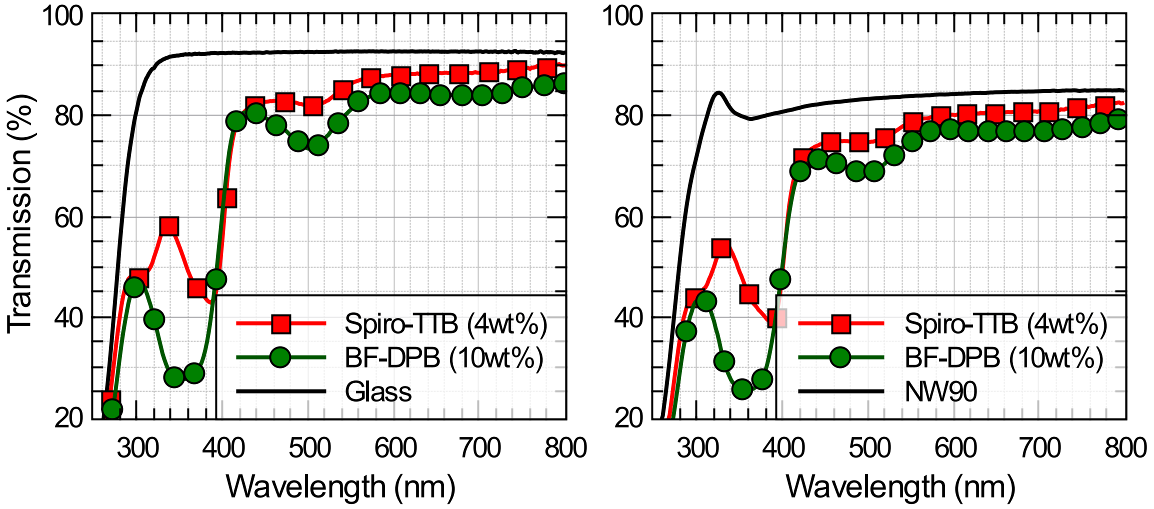

Figure 7.18.: Transmission graphs of Spiro-TTB in comparison to BF-DPB, both solution-processed from THF. **a)** On glass substrates. **b)** On glass/NW90 substrates.

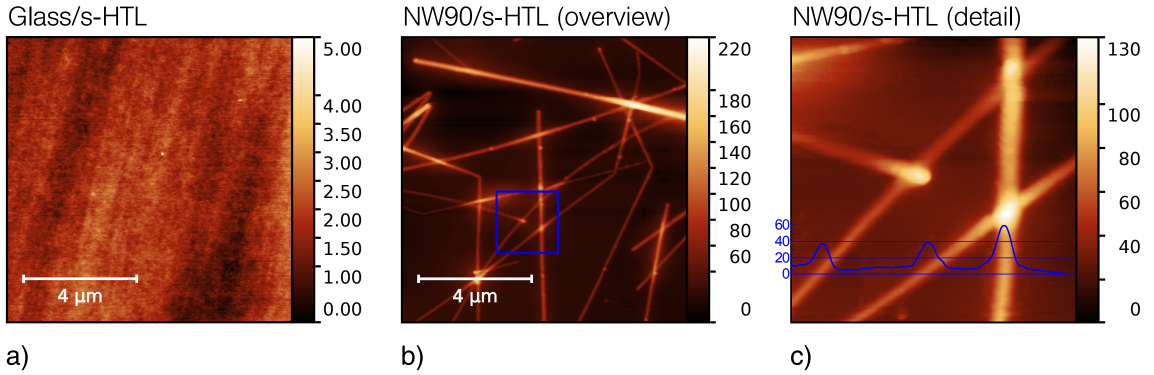

Figure 7.19.: AFM images of solution-processed Spiro-TTB **a)** on glass substrates and **b), c)** on NW90 electrodes. The blue square in b) gives the location of the detail view in c). A profile scan is superimposed in c). All values are given in nm.

The thin-film topography and the planarization effect on NW90 electrodes is studied using AFM (Figure 7.19). On glass, the roughness R_{rms} equals (0.4 ± 0.1) nm which is nearly as smooth as glass itself. On NW90, the wires seem to glow, indicating soft slopes at the wire edges. The superimposed profile scan in Figure 7.19 (c) shows a wire height of 40 to 60 nm. The wires, which usually have a height of 90 nm, are sunken into the Spiro-TTB. Also the wire junctions seem to be capped with organic material. The planarization behavior is very similar to the planarization with solution-processed BF-DPB (cf. Section 7.2.3). With this, solution-processed Spiro-TTB is promising as HTL on NW bottom electrodes in OSCs.

The Spiro-TTB s-HTL is implemented in organohalide perovskite solar cells (PSCs, cf. Section 2.2.3) as a first test of its functionality in an optoelectronic device (the layer stack is depicted in Figure 7.20 right). The perovskite solar cell type is chosen for two reasons. First, perovskite photovoltaics is a highly investigated research field in the last 4 years, since Lee et al. showed outstanding power conversion efficiencies.[151] Second, Polander et al. reported the use of evaporated, doped Spiro-TTB as hole transport material and achieved with this material the highest PCE in comparison to other investigated HTLs.[77] However, many groups reported a strong hysteresis behavior in the measurement of PSCs.[20, 83] This hystersis is not as strong with the layer architecture used in our study.

Figure 7.20 (left) depicts the jV curves of PSCs with s-HTL on ITO and NW90 as well as e-HTL on ITO (reference); photovoltaic performance parameters are listed in Table 7.4. The PSC with s-HTL shows a maximum PCE of 10.3 %, compared to 10.9 % for the PSC with e-HTL. PSCs on NW90 electrode do not work – no current is flowing through the device.

Discussing these results, the solution-processing of the HTL on ITO provides full functionality. No difference in PCE within the standard error is observed. A direct contact of dopant and perovskite layer is not decreasing the device performance, which has been the case with ZnPc:C_{60} solar cells and BF-DPB (cf. Section 7.2.4). The isolating behavior on NW90 is not expected. In contrast, a too rough surface topography due to the presence of nanowires would lead to a shunted device with ohmic jV behavior and high currents flowing. By means of electron microscopy, the NW90 device is analyzed further. In Figure 7.21 (a) and (b), an area with the top electrode is imaged. The nanowires are still strongly visible with insulating areas around some wires. The topography (Fig. 7.21 b) reveals a rough surface, which is remarkable as nearly 500 nm of material (perovskite, organics and metal) are deposited on top of the AgNW electrode. A smoothening and a vanishing of the NW90 topography is expected at such a high layer thickness. Fig. 7.21 (c) shows an area without top contact where a similar behavior is observed. The perovskite layer forms directly on the surface because it is a co-deposition of methylammonium iodide (CH_3NH_3I) and lead chloride ($PbCl_2$). Thus, the nanowire surface topography might induce a disturbed crystallization leading to phenomenons as seen in Figure 7.21.

These investigations show that doped Spiro-TTB with NDP9 is a solution-processable HTL. The conductivity is similar to evaporated reference layers. The implementation as HTL in a perovskite solar cell reveals that the electronic functionality is conserved; all s-HTL interfaces provide ohmic contacts. NW90 electrodes are planarized in a distinct manner. However, the growth of a perovskite layer on the NW90/s-HTL surface is difficult and leads to a solar cell failure. More investigations are needed on this issue to successfully create ITO-free perovskite solar cells with high PCEs.

Nonetheless, the working perovskite solar cell with an efficiency over 10 % on ITO confirms the proof of principle with a doped, solution-processed Spiro-TTB HTL.

Table 7.4.: Photovoltaic perfomance parameters of perovskite solar cells with spin-coated Spiro-TTB:NDP9 (4 wt%) on ITO or NW90 electrode with 6.25 mm^2 cell area. Illumination intensity is 100 mW/cm^2, the measurement is not mismatch-corrected. Values are averaged over 4 identically fabricated devices (the best value is stated in brackets). The reference solar cells with e-HTL are fabricated in the same chambers. Values are averaged over 8 to 12 devices on 3 to 5 substrates.

	V_{oc} (mV)	j_{sc} (mA/cm^2)	FF (%)	PCE (%)
ITO/e-HTL	970 ± 30	14.9 ± 0.9	63 ± 6	9 ± 1
(from [77])	(968)	(16.1)	(70)	(10.9)
ITO/s-HTL	930 ± 20	14.7 ± 0.8	64 ± 3	9 ± 1
	(963)	(15.9)	(66)	(10.3)
AgNW/s-HTL	no current flow			

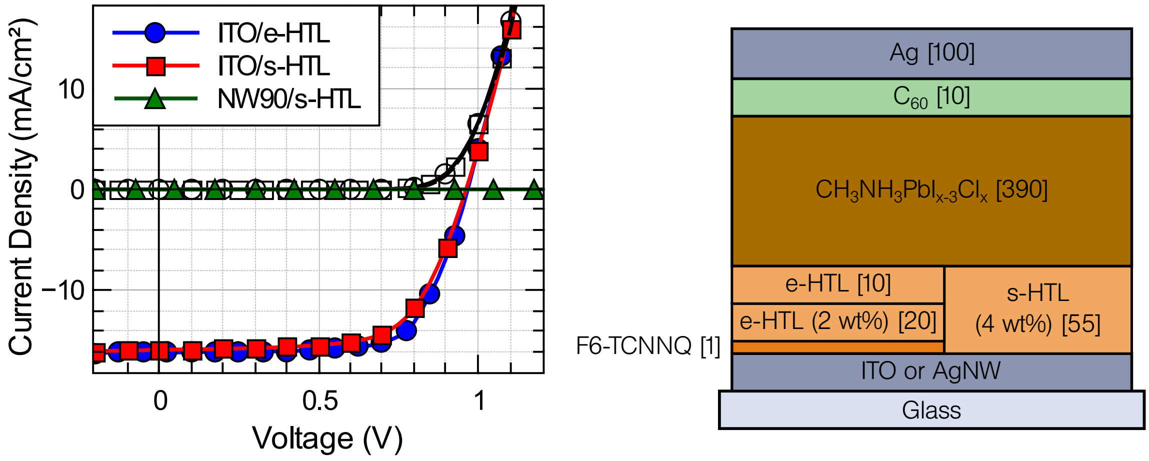

Figure 7.20.: **Left:** jV curves of perovskite solar cells with s-HTL or e-HTL on ITO or NW90 electrode. The s-HTL consists of 55 nm solution-processed Spiro-TTB:NDP9 (4 wt%). As e-HTL, 20 nm of Spiro-TTB:F_6-TCNNQ (2 wt%) and 10 nm undoped Spiro-TTB are used. **Right:** Schematic layer sequence of the perovskite solar cells. The layer thickness is stated in brackets.

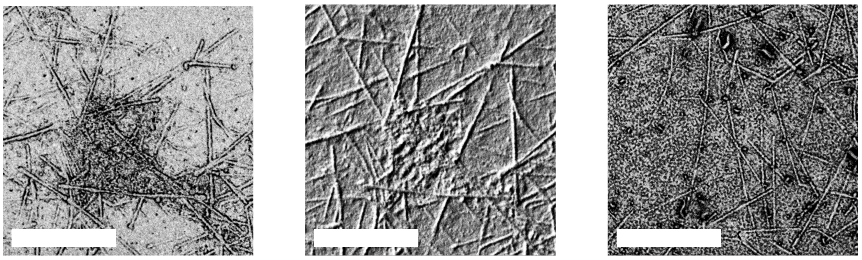
a) b) c)

Figure 7.21.: SEM images of a perovskite solar cell on NW90 electrode. **a)** Whole device including top electrode. **b)** Same as a), but using the topographic mode of the SEM. **c)** Aside the top electrode. All scale bars represent 10 µm.

7.4. Solution-Processed Electron Transport Layers

Since good results have been achieved using solution-processed small molecule materials as HTL, in this chapter corresponding investigations on the electron transport side are presented. By employing solution-processed ETLs (s-ETL), one would be able to also fabricate n-i-p devices, which normally show higher efficiencies and improved stability than p-i-n architectures.[32, 144, 231] Furthermore, the interface from electron transport layer (ETL) to electrode would be different due to a LUMO of approximately 4 eV needed for properly contacting the acceptor, e. g. C_{60}. While using ITO with a work function of 5 eV, an energetic difference at the ITO/ETL interface in the range of 1 eV needs to be conquered as compared to only 0.2 eV at the ITO/HTL interface (cf. Section 7.2). This might be more challenging than in the case of an HTL. Nonetheless, silver exhibits a work function of 4.3 eV. In this case, the energetic barrier would be rather low with an ETL and fairly high with HTLs. The latter case could be shown by investigations presented in Section 7.2.4.

Two ETL materials are investigated: n,n-bis(fluoren-2-yl)-naphtalenetetracarboxylic diimide (Bis-HFl-NTCDI) and 1,4,5,8-napthalenetetracarboxylic dianhydride (NTCDA); their chemical structure is depicted in Figure 7.3 on p. 84. The first one is developed and synthesized in-house and commonly used as evaporated ETL in our institute.[72, 80, 168] The latter one is a organic semiconductor frequently used in various applications such as organic thin-film transistors [274, 280] and OSCs [43], and in basic investigations of organic semiconductor properties. It provides a high electron mobility (cf. Table 7.5), has a remarkably low price, and was the first matrix material used for controlled n-type doping of small molecule organic semiconductors.[283] Falkenberg et al. reported n-doped NTCDA as ETL in p-i-n organic solar cells, exhibiting higher j_{SC} values than for other electron transport materials.[168, 230] However, the implementation in n-i-p solar cells failed because of a strong NTCDA crystallization during vacuum deposition. A roughness larger than the average film thickness caused shunts in the solar cells.[229] The approach of a solution-processed NTCDA ETL is intended to solve the challenges concerning rough layers as smoother layers are expected from the solution-processing.

In order to achieve high electron conduction, n-doping is necessary. Solubility of n-dopants in similar solvents as the matrix material needs to be considered as well as stability. Many n-dopants are not airstable due to a very low HOMO level such that the molecule is easily oxidized (cf. Section 2.1.3). To increase stability, newly designed molecules come along as airstable dimers without doping functionality. As soon as they break up during evaporation or under heating, they get activated within the film.[74, 143]

Two n-dopants are used in this study: dimeric rhodocene (Rh-D) [143] and the dimeric benzimidazoline-radical $(2\text{-cyc-DMBI})_2$. Both molecule structures are shown

Table 7.5.: Comparison of properties of evaporated NTCDA and Bis-Hfl-NTCDI.

	NTCDA	Bis-Hfl-NTCDI
Mobility ($cm^2/(V\,s)$)	3×10^{-3} [291]	3.1×10^{-6} [a]
Electron affinity (eV)	4.02 [242]	3.8
UPS Ionization Potential (eV)	8	6.55
Conductivity [b] (S/cm)	1×10^{-4}	2×10^{-4}
Price (€/g)	3.5[c]	–

a: measured in OFET geometry by Dr. Moritz P. Hein
b: with 7 wt% doping of $W_2(hpp)_4$
c: price from Sigma-Aldrich, 03/01/2016

in Figure 7.3 on p. 84. Moreover, these dopants can be deposited from liquid as well as from gas phase, which enables good opportunity for an easy comparison of spin-coated and co-evaporated n-doped ETLs.

The attempt of dissolving Bis-HFl-NTCDI failed. It is nearly insoluble in many different organic solvents like ethanol, tetrahydrofuran, chlorobenzene, dichloromethane, and chloroform. The addition of trifluoroacetic acid should protonate the molecule for improved solubility, but the molecule stays insoluble. Therefore, no further investigations are carried out with Bis-HFl-NTCDI.

NTCDA is soluble in dimethylformamide (DMF) and dimethylsulfoxide (DMSO) [261] up to a concentration of 10 mg/ml and does not dissolve in halogenated solvents like chlorobenzene. The latter fact is insofar interesting as many polymer solar cells are spin-coated from those halogenated solvents, e. g. chlorobenzene, dichlorobenzene, or chloroform. Consequently, a subjacent NTCDA layer will not get dissolved during polymer absorber deposition. This enables the possibility of integrating small molecule ETLs in inverted polymer solar cells which has not been shown up to now. The rhodium dopant shows only slight solubility in DMF up to 2.5 mg/ml which is sufficient for a doping concentration up to 20 wt%.

Morphological properties of NTCDA, doped with 5 wt% Rh-D, are investigated by means of atomic force microscopy (Figure 7.22). Vacuum-deposited layers with a thickness of 20 nm exhibit a D_{ptv} of 75 nm and a roughness of (8 ± 2) nm. Due to pronounced island-growth, NTCDA molecules form large crystallites such that the substrate is still visible between them. It provides an unfavorable foundation for the absorber deposition. In contrast, spin-coated, 15 to 20 nm thin n-NTCDA layers show a smaller grain size and a much smoother roughness R_{rms} of (2.0 ± 0.5) nm than the evaporated reference films. Thus, the layer itself exhibits superior morphology than evaporated NTCDA. However, the substrate wetting is not optimal up to now: channels without material are visible after solvent evaporation.

The conductivity of solution-processed n-NTCDA layers with 5 wt% doping concentration is determined to be $(2 \pm 1) \times 10^{-4}$ S/cm. They are similar as the reference value

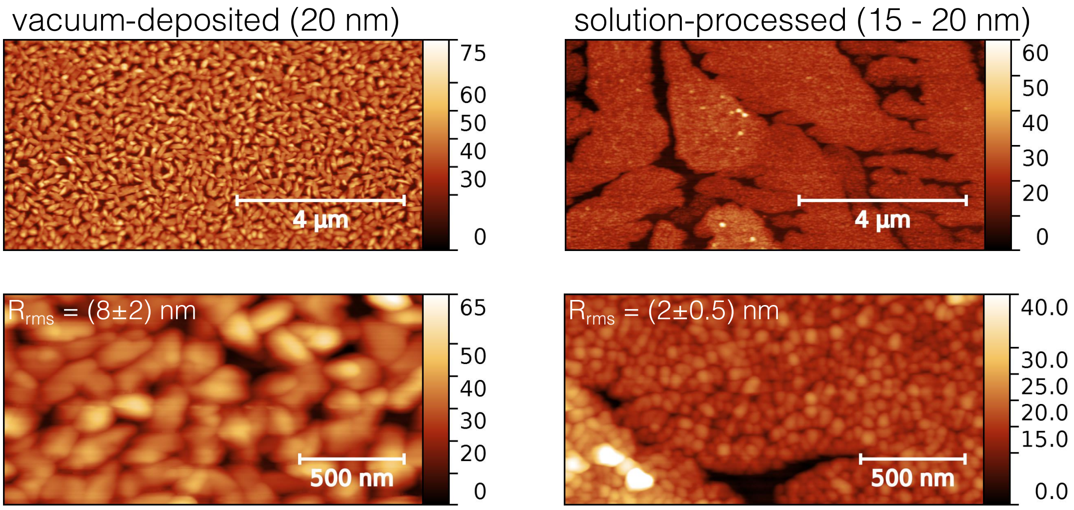

Figure 7.22.: AFM images of NTCDA layers on ITO substrates. All scale values are given in nanometers. **Left:** Spin-coated. **Right:** Vacuum-deposited.

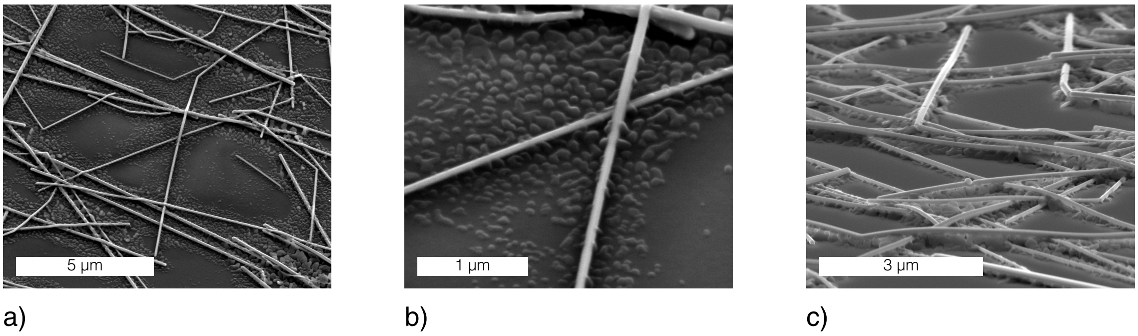

a)

b)

c)

Figure 7.23.: SEM images of NW90 electrodes covered with spin-coated NTCDA. **a), b)** Top view. **c)** Substrate is tilted with an angle of 70 degree.

of vacuum-deposited NTCDA films (cf. Tab. 7.5).

Silver exhibits a work function of approximately 4.3 eV, which fits much better to the LUMO of NTCDA than the work function of ITO. Hence, silver nanowires should be a good material in terms of electrical contact. Consequently, the planarization capability of ETL-covered AgNW networks is investigated. n-NTCDA is spin-coated onto NW90 electrodes and SEM images are acquired. Figure 7.23 shows these images and reveals that the area between the silver nanowires is not covered with material at all. Only a few NTCDA particles are gathering at the wires. Even more (as visible from the tilt view in Fig. 7.23 c), they are attracted between nanowires and substrate, thereby increasing substrate roughness. A planarizing effect is not observed, thus, the NTCDA deposition does not work as expected. Substrate wetting seems to be a reasonable cause for this behavior as in the case of ITO. More effort is needed to increase wetting on AgNW electrodes as well as the layer thickness. A 20 nm thin NTCDA layer is not enough to sufficiently planarize these electrodes. Therefore, solubility needs to be increased by using NTCDA derivatives with soluble ligands [102] or by modifying solvent properties. However, the synthesis, purification and characterization of new derivatives is a time-consuming process and not within the scope of this thesis. Therefore, investigations of ETL planarization on AgNW electrodes are not continued.

However, the solution-processed NTCDA layer with the rhodium dopant turns out to be a suitable material combination on flat ITO electrodes. Thus, it is now implemented in polymer solar cells to study its electronic functionality as ETL and the stability against further solution processing on top of it. For this purpose, PTB7:$PC_{71}BM$ solar cells are fabricated on ITO substrates according to the layer sequence in Figure 7.24 (left).[7] The active material PTB7 is a widely used commercially availabe polymer donor yielding high efficiencies with $PC_{71}BM$ as acceptor.[24, 66] Both materials are dissolved in chlorobenzene. As reference ETL, the polymer PFN is used. It is a 5 to 10 nm thin surface modifier that creates a strong permanent dipole, leading to a work function reduction of ITO to 4.1 eV (cf. Sec. 2.2.3.[144]
Figure 7.24 (right) shows the jV curve of solar cells with n-NTCDA. They eyhibit V_{OC}, j_{SC}, FF, and PCE values of $(600 \pm 60)\,\mathrm{mV}$, $(16 \pm 1)\,\mathrm{mA/cm^2}$, $(54 \pm 7)\,\%$, and $(5.4 \pm 0.8)\,\%$, respectively. Compared to a reference with PFN as 5 nm thin ETL ($V_{OC} = (740 \pm 2)\,\mathrm{mV}$, $j_{SC} = (18.1 \pm 0.1)\,\mathrm{mA/cm^2}$, $FF = (66 \pm 2)\,\%$, $\mathrm{PCE} = (8.8 \pm 0.3)\,\%$), all parameters are worse with strong deviations in the OSC employing n-NTCDA. A possible reason for this decrease is a non-ohmic contact between n-NTCDA and ITO or PTB7:$PC_{71}BM$ that reduces the V_{OC}. The lower j_{SC} might be caused by the incomplete substrate coverage. Further, it is unclear whether a contact of rhodium dopant and absorber layer leads to an additional worsening of the performance parameters.

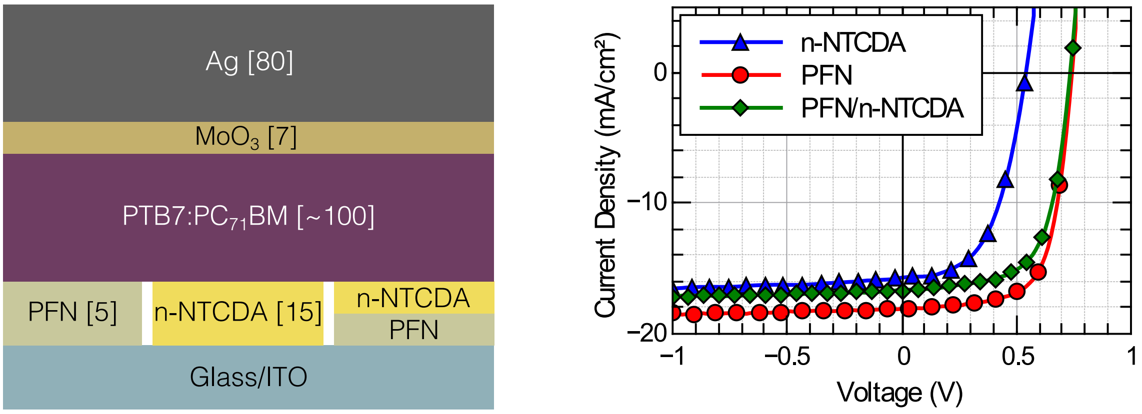

Figure 7.24.: Left: Schematic layer stack of PTB7:$PC_{71}BM$ solar cells with three different ETL combinations. **Right:** Illuminated jV curves of the PTB7:$PC_{71}BM$ solar cells. Active area is 10 mm^2, the solar cells are not corrected for spectral mismatch.

The combination of PFN and n-NTCDA as subsequently deposited layers leads to a strong improvement of all photovoltaic performance parameters. V_{OC} ($(732 \pm 5)\,\mathrm{mV}$) and FF ($(64 \pm 2)\,\%$) are very close to the reference value. Only the j_{SC} is still distinctly lower ($(16.6 \pm 0.1)\,\mathrm{mA/cm^2}$). A PCE of $(7.7 \pm 0.3)\,\%$ shows a strong improvement as

---

[7] Processing details can be found in the Experimental Section 4.5.2.

compared to bare n-NTCDA as ETL. It is concluded from this investigation that n-NTCDA is functioning as ETL and is not dissolved by further spin coating steps with halogenated solvents. Nonetheless, two issues need to be adressed for a successful implementation. First, wetting properties have to be improved to achieve reproducible and homogeneous layers. This could be achieved by adding surfactants like the fluorosurfactant 'Zonyl FS-300'[89, 155], octoxinol 9, or polyethylene glycole to the NTCDA solution.[214] Second, the interface between electrode and n-NTCDA seems to be the bottleneck for the electrical contact. It needs to be improved by reducing energetic barriers due to an unfavorable energy level alignment. This could be done via contact doping or by adjusting the electrode work function.

One impetus for the solution-processing of NTCDA has been the bad performance of small molecule n-i-p OSCs with evaporated NTCDA. In comparison to polymer-based solar cells, the small molecule active layers are much more prone to rough surfaces due to their lower thicknesses. The impact of ETL processing technique is investigated by fabricating ZnPc:C_{60} solar cells on either solution-processed or vacuum-deposited NTCDA. A neutral benzimidazoline-radical dimer, (2-cyc-DMBI)$_2$, is used as airstable n-dopant which can be processed from liquid and gas phase (see chemical structure in Figure 7.3 on p. 84).[74]
Figure 7.25 shows the layer sequence of the fabricated solar cells and the jV curves for the respective OSCs with e- and s-ETL. A doping concentration of 5 wt% is used for both processing techniques. Photovoltaic performance parameters are stated within the jV plot. The OSC with evaporated NTCDA (e-ETL) exhibits an efficiency smaller than 1 %. This is mainly caused by strong leakage currents in the dark jV curves, showing nearly no diode-like jV behavior anymore. In contrast, with the solution-processed n-NTCDA, the solar cell exhibits a PCE of 2.3 %. The V_{OC} is with 0.59 V very high for ZnPc:C_{60} solar cells (cf. Section 7.2.4). Only the FF of 50 % is not as good as possible; 60 % can be reached for similar devices. Further enhancement might be made by controlling and investigating the electronic interface between electrode and ETL.
However, the improvement in PCE from 0.94 % to 2.3 % – just by changing the ETL deposition process from thermal evaporation to spin coating – is remarkable and indicates the feasibility of the s-ETL in small molecule OPV.

In summary, NTCDA is introduced as solution-processable electron transport material for organic solar cells. Solution-processed thin-films show improved morphology with reduced layer roughness as compared to vacuum-deposited films. The reduction of roughness is benefitial for the application in n-i-p organic solar cells. Furthermore, a conductivity in the 1×10^{-4} S/cm regime is measured when doped with an airstable and soluble rhodium dopant. PTB7:PC$_{71}$BM polymer n-i-p solar cells with n-NTCDA as ETL exhibit PCEs up to 8 %. It shows that the electronic functionality of the n-doped NTCDA is available and that the layer is not affected by further solvent treatment. For small molecule ZnPc:C_{60} solar cells, an improvement in PCE from

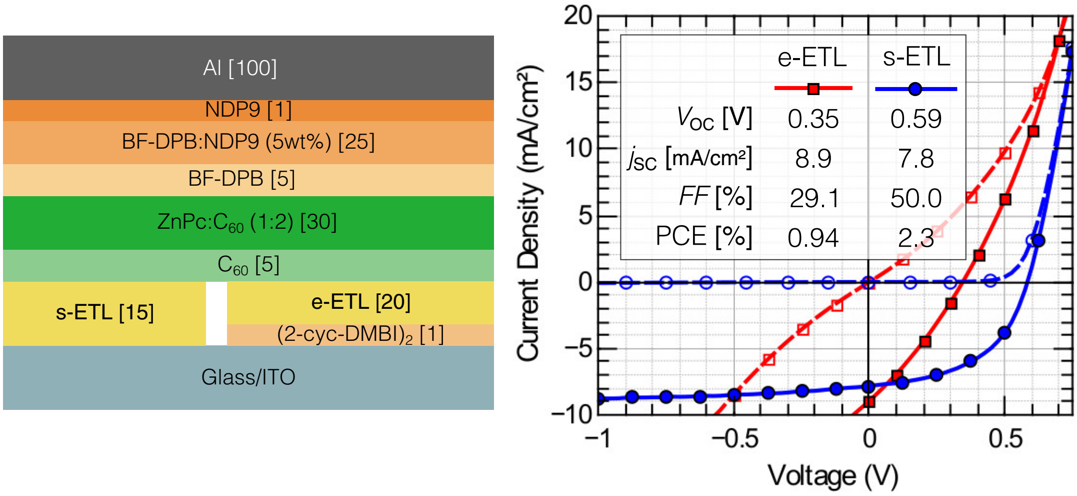

Figure 7.25.: ZnPc:C_{60} solar cells with solution-processed and evaporated NTCDA with 5 wt% (2-cyc-DMBI)$_2$ as ETL. **Left:** Schematic layer stack. **Right:** jV curves in dark (empty symbols) and under AM1.5G illumination with 100 mW/cm^2 intensity (full symbols). The solar cells have an active area of 6.44 mm^2, the performance is not corrected for spectral mismatch.

0.94 % (e-ETL) to 2.3 % (s-ETL) is observed. The situation on AgNW networks is still challenging, as bad wetting leads to non-planarized and rarely covered electrodes. However, NTCDA is very inexpensive and enables good control over conductivity and optimization of the polymer solar cells on ITO. Thus, it is a promising addition to the current research on cathode interlayers and on interface engineering in polymer solar cells.

7.5. Summary

In this chapter, a comprehensive study of solution-processable and dopable charge carrier transport layers is presented. The doping process of the hole transport material BF-DPB with the p-dopant NDP9 already takes place in THF solution and is for high doping concentrations as efficient as for co-evaporated reference layers. It is shown that BF-DPB:NDP9 is a suitable material combination for the planarization of silver nanowire electrodes. Small molecule solar cells with DCV5T-Me:C_{60} as efficient absorber system are fabricated, reaching efficiencies up to 4.4 % on NW35 electrodes and 4.1 % with ITO bottom electrodes. The interplay between HTL conductivity and microscopic network structure is investigated and the impact on the macroscopic device performance is evaluated. A minimum HTL conductivity of approximately 1×10^{-4} S/cm is needed on NW90 electrodes with 1 µm^2 large network voids to prevent losses in j_{SC} and FF. An equivalent circuit model simulation validates the findings and solely refers the performance variations to the HTL conductivity in combination with the AgNW network structure.

Solution-processed Spiro-TTB:NDP9 (4 wt%) is investigated as s-HTL in perovskite solar cells. PCEs up to 10.3 % are reached on ITO as compared to 10.9 % with the standard e-HTL. Solar cells on NW90 electrodes are not working, which is most probably due to an unfavorable growth of the perovskite on rough nanowire layers.

Furthermore, electron transport layers are introduced for solution-processing and the application in n-i-p polymer solar cells. NTCDA is shown to be soluble in dimethylformamide and dopable with a rhodium dopant or a DMBI derivative, leading to conductivities up to $(2 \pm 1) \times 10^{-4}$ S/cm. Polymer solar cells with PTB7:$PC_{71}BM$ show efficiencies up to 8.0 % with n-NTCDA and prove its ability to resist halogenated solvent treatment. Also n-i-p small molecule solar cells with ZnPc:C_{60} are demonstrated reaching PCEs of 2.3 % with solution-processed n-NTCDA. AgNW electrodes are not planarized by the ETL solvent processing due to a weak wettability and a relatively low NTCDA solubility in DMF.

8. Buried Silver Nanowires in an Insulating Polymer

In this chapter, an approach for the planarization of silver nanowire networks is investigated whereby the silver nanowires are embedded in an insulating polymer. This polymer serves as flexible and ultrathin substrate. AgNW-polymer composites with three different polymers are tested by basic optical, electrical, and topographical analysis (Section 8.3).
To prove the applicability of this flexible electrode, organic solar cells with a fullerene-free cascade layer architecture (Section 8.4) or a DCV5T-Me:C_{60} bulk heterojunction (Section 8.5) are manufactured. Furthermore, degradation studies with both OSC types are performed in a humid climate under continuous illumination. The intrinsic degradation behavior is evaluated with devices on ITO that are protected against moisture ingress with a glass-glass encapsulation. As flexible encapsulation, thin-films of alumina (AlO_x) are employed. The degradation of fully-flexible, encapsulated devices is studied and main degradation mechanisms are discussed.

8.1. Introduction

The implementation of AgNW networks as transparent bottom electrode into optoelectronic organic thin-film devices is a big challenge. For this purpose, the inherently large surface roughness needs to be reduced. As the network consists of single nanowires with diameters in the range of 30 to 100 nm, they pile up creating height differences greater than 60 nm with steep slopes on the substrate surface. This topography does not provide a suitable surface for organic devices with thicknesses that are often below 100 nm. Therefore, planarization or smoothening methods of AgNW networks are required.

In the previous chapter (Chapter 7), AgNW planarization has been realized using solution-processed small molecule hole transport layers made of BF-DPB or Spiro-TTB as matrix and NDP9 as dopant. They act as planarization/smoothening layer as well as hole transport layer for a selective charge carrier transport. Organic solar cells comprising AgNW electrodes with this solution-processed HTL show a similar performance as compared to ITO as bottom electrode.

However, using an HTL as planarization layer has some implications on the architecture of the solar cell. Obviously, one needs to employ a p-i-n type solar cell, which is a structure commonly used. In some cases, an n-i-p type solar cell is favorable due to a higher stability and higher power conversion efficiencies.[32, 148, 231] With an HTL above the transparent bottom electrode, this can only be realized by utilizing more sophisticated p-n-i-p structures that employ a highly doped recombination interface.

In the present chapter, a different approach for planarization is utilized. The silver nanowire network is buried in a transparent and nonconductive polymer.[152] This technique enables a very smooth and conductive nanowire-polymer composite without the need for further planarization steps.

8.2. Electrode Fabrication

A schematic description of the process is depicted in Figure 8.1. First, the silver nanowires are deposited on a rigid glass substrate via spin or spray coating. Second, the liquid polymer is deposited via spin coating on top of the nanowires. Subsequently, the polymer needs a heat or UV treatment to get solidified. Third, the polymer is peeled off carefully from the glass substrate with a pair of tweezers. The polymer is now the new substrate with the side previously looking to the glass substrate being the conductive surface.

In the course of this study, AgNWs with a diameter of 90 nm (NW90) or 35 nm (NW35) are used and deposited via spin or spray coating on glass substrates. Subsequently, the polymer is deposited onto the AgNW network. In some cases, a layer of PEDOT:PSS (AI4083) is spin-coated before or after the silver nanowire deposition.
Three different polymers are investigated. All process parameters are summarized in Table 8.1. On the one hand, a transparent polyimide formula (PI) is used ('VTEC PI-080-051').[57, 152] Polyimides are a family of plastics containing imide monomers. The chemical structure of the backbone is shown in Figure 8.2 (a). It is cured via heating at 110 °C for 10 min followed by 100 °C for 50 min. After curing, it is temperature-stable up to 316 °C,[302] highly transparent, and provides high mechanical stability and low water absorption. Another polymer is polydimethylsiloxane (PDMS, see Fig. 8.2 b) which is a colorless, inert, non-toxic, and non-flammable elastomer. PDMS applications span a wide range from contact lenses [287] to lighting encapsulation.[95] PDMS 'Sylgard® 184' consists of a two-component system with a base:crosslinker ratio of 10:1. It cures already at room temperature within 48 h. For a faster polymerization, a moderate temperature treatment of 100 °C for 30 min can be utilized.
As third option, the proprietary 'Norland Optical Adhesive 63' (NOA63) is used (Fig. 8.2 c).[56, 75] It contains mercapto ester monomers and cures under UV-illumination. This enables processing under a low temperature and with short treatment times, which is desirable in terms of large area R2R fabrication processes.

Table 8.1.: Processing parameters for PDMS, polyimide and NOA63. Spin coating parameters are given with the revolution speed (1/min) and the spin time (s) in brackets. If values are connected via an '& ', these steps are carried out subsequently.

Polymer	Heat/UV	Temperature (°C)	Time (min)	Spin coating parameter
PDMS	Hotplate	60	240	Petri dish
Polyimide	Hotplate	100 & 110	10 & 50	500(20) & 800(90)
NOA63	UV	RT	30	500(20) & 1200(30)

8.3. Optical, Electrical and Topographical Properties

In order to examine the functionality of the electrodes as bottom electrode in organic solar cells, the bare electrode needs to be characterized prior to the integration in organic thin-film devices. For all three polymers, the feasibility of the electrode fabrication and sample handling as well as the optoelectrical properties are investigated. Also of huge importance is the reduction in roughness of the AgNW electrode as it is a measure for the planarization capability of this approach.

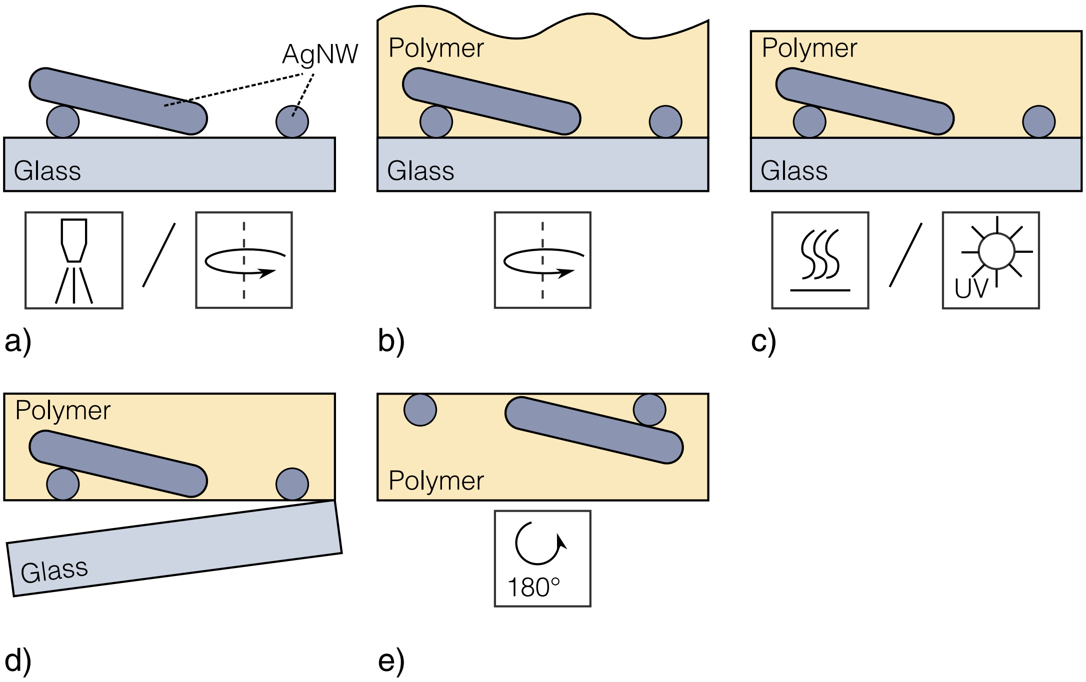

Figure 8.1.: Schematic process description of the electrode production. **a)** Silver nanowires are deposited on a glass substrate via spin or spray coating. **b)** The polymer is spin-coated on top of the AgNW network. **c)** The polymer is cured by heating or UV treatment. **d)** The AgNW-polymer composite is peeled off from the glass substrate. **e)** After turning the sample, a flexible substrate with embedded AgNWs is obtained.

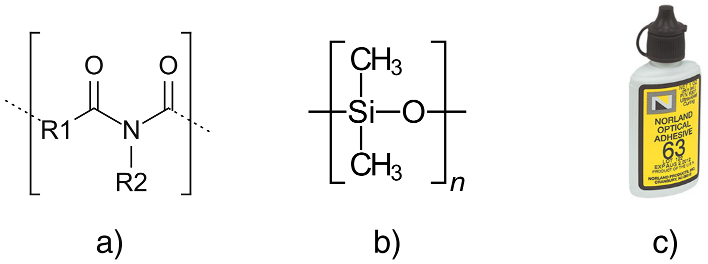

Figure 8.2.: Polymers used in this study. **a)** Polyimide, **b)** polydimethylsiloxane (PDMS), and **c)** 'Norland Optical Adhesive 63' (NOA63).

8.3.1. Polydimethylsiloxane

The material investigated first is PDMS.[53] Base and crosslinker are merged shortly before the usage. PDMS layer formation is done by filling the liquid PDMS into a small petry dish[1] with a glass/NW35 sample lying on the ground. This petri dish is then transferred onto a hotplate at 60 °C for 4 h. After curing, the PDMS layer is peeled out of the petri dish and exhibits a thickness of 1 to 2 mm. A neat PDMS layer is fabricated following the same recipe, but without substrate.

The total transmission spectrum T_t is recorded for the neat PDMS layer. Sheet resistance values R_S are measured before and after performing the peel-off process for the PDMS/NW35 sample. Additionally, SEM images are acquired before and after the transfer process.

The neat PDMS sample shows an ultra-high transmission value $T_{\mathrm{t},550}$ of 94.3 % at a thickness of 1 to 2 mm. It is even more transparent than glass with a $T_{\mathrm{t},550}$ of 92 %. After peeling off the PDMS/NW35 from the glass, no R_S could be measured although the glass/NW35 sample has been conductive before. The SEM images (Figure 8.3) show that nanowires are not transferred over the whole sample area. In areas where the nanowires are transferred, damage is visible in terms of strong kinks. Obviously, an electric connection between the nanowires – and with this a conductive PDMS/NW35 layer – cannot be established.

The reason for this deformation eventually lies in the elastic properties of PDMS in combination with the peel-off process. Nanowires that are embedded get stretched during the peel-off and bend strongly during contraction of the PDMS after peel-off. No further pre- or post-treatment such as O_2 plasma cleaning or the introduction of a PEDOT:PSS layer on top or below the AgNW mesh improved the result.

In summary, PDMS is basically a promising candidate as electrode substrate material as it is non-toxic, highly transparent, flexible and stretchable. However, a conductive electrodes is not achieved, which is contradictory to the underlying literature where no such difficulties have been observed.[53] Consequently, investigations with this polymer are not continued.

---

[1] The reason for avoiding spin coating is the too low viscosity of PDMS. After spin coating, the material flows away from the substrate during the long curing procedure.

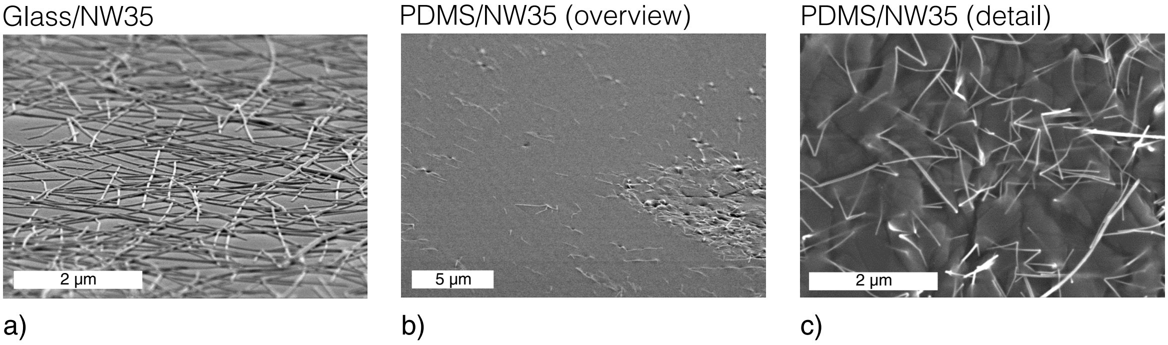

Figure 8.3.: SEM images of **a)** NW35 deposited on glass and **b), c)** NW35 buried in PDMS after peel-off. Courtesy of Dr. Nelli Weiß.

8.3.2. Polyimide

Polyimide (PI) is a one-component system containing the organic solvent n-methyl-pyrrolidone (NMP).[293] After spin coating the liquid PI (cf. Table 8.1), the layer is cured on a hotplate at 110 °C for 10 min and subsequently at 100 °C for 50 min. The resulting thickness of the layer is $(7.5 \pm 0.5)\,\mu\mathrm{m}$. PI layers are deposited on glass, glass/AgNW, and glass/AgNW/PEDOT:PSS. As PEDOT:PSS formulation, AI4083 is used. Subsequently, the layers are peeled off with a pair of tweezers from the glass substrate while the sample is still hot.

Transmission measurements of the different samples are shown in Figure 8.4. Corresponding T, R_S, and FOM (Φ_De) values are summarized in Table 8.2. The neat polyimide exhibits a transmission $T_{\mathrm{t},550}$ of 87.7 % including the glass substrate. PI absorption sets in at 360 nm. Adding a layer of AI4083 marginally reduces the $T_{\mathrm{t},550}$ to 86.6 %. The silver nanowire electrodes on PI with NW90/AI4083 and NW35/AI4083 exhibit a $T_{\mathrm{t},550}$ of 78.5 % and 71.3 %, respectively. Here, the transmission is measured without glass substrate to characterize the flexible transparent electrode.

Table 8.2.: Transmission, sheet resistance, and Φ_De values of polyimide and AgNW electrodes with PI.

Sample	$T_{\mathrm{t},550}$ (%)	T_vis (%)	R_S ($\Omega/\square$)	Φ_De
Glass/PI	87.7	73.3	–	–
PI/AI4083/NW90	78.5	64.2	17.6	130
PI/AI4083/NW35	71.3	57.7	15.3	90
ITO	82	80.7	26	122

Also sheet resistance measurements are carried out. A sample with silver nanowires buried in polyimide exhibits no measurable conductivity after peel-off. For samples of NW35 or NW90 in PI with an interlayer of AI4083, R_S values of $17.6\,\Omega/\square$ and $15.3\,\Omega/\square$ are measured, respectively.

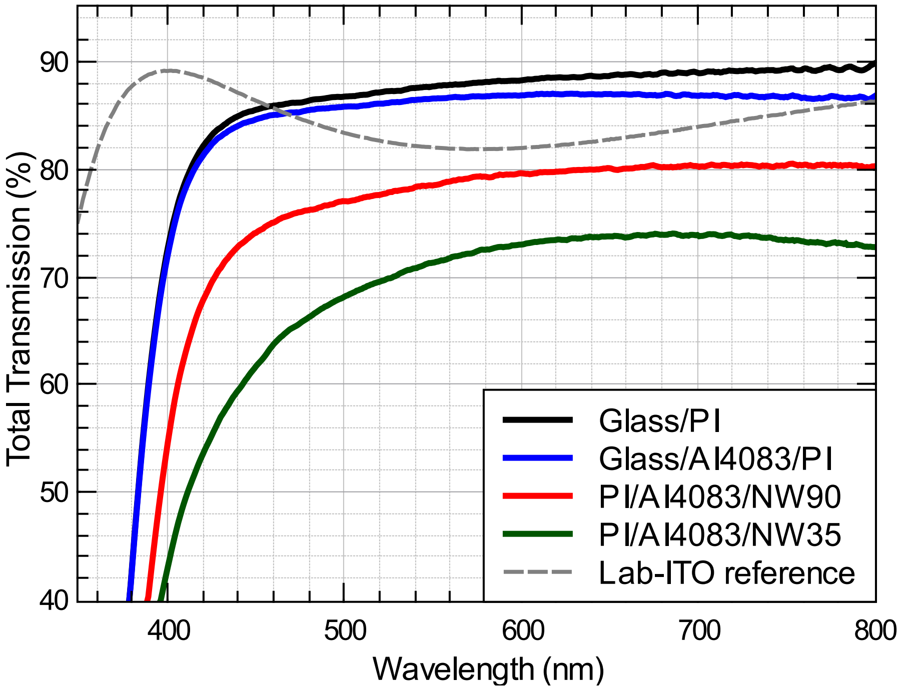

Figure 8.4.: Transmission graphs of polyimide, polyimide with PEDOT:PSS (AI4083), NW90 with AI4083 in PI, and NW35 with AI4083 in PI.

As in the case of PDMS (cf. Section 8.3.1), only nonconductive layers are achieved when untreated silver nanowires are buried in PI. However, the insertion of a layer of PEDOT:PSS onto the AgNWs prior to the PI coating results in a conductive layer. A look at the SEM images in Figure 8.5 gives an explanation of this behavior. Without PEDOT:PSS interlayer (Fig. 8.5 a), the nanowires are visible, but blurry. It seems that they sink into the PI. In contrast, the SEM image of the sample with PEDOT:PSS as interlayer shows nanowires with defined contours. They are lying directly below the surface of the PI. Moreover, the AFM image (Fig. 8.5 c) of this sample reveals interesting information: the peak-to-valley height of this sample is only 30 nm, and the surface roughness R_{rms} is (2.5 ± 0.5) nm, which is a dramatic decrease compared to the neat NW90 electrode on glass. With such low R_{rms} values, the implementation of organic thin-film devices should be possible. Also an AFM phase contrast is visible (Fig. 8.5 d). This is an evidence that AgNWs are looking out of the surface, as phase changes often indicate material changes on the measured surface. Thus, the PEDOT:PSS interlayer leads to a compression or tightening of the network such that the PI cannot penetrate the interstices of wires and wire junctions. A conductive layer, which is also accessible from the outside, remains after PI coating and peel-off.

The transmission of the PI layers is much worse than for the PDMS, taking the small substrate thickness of (7.5 ± 0.5) µm into account. The sample exhibits a slightly light-orange color which can be explained with the absorption below 380 nm. By adding

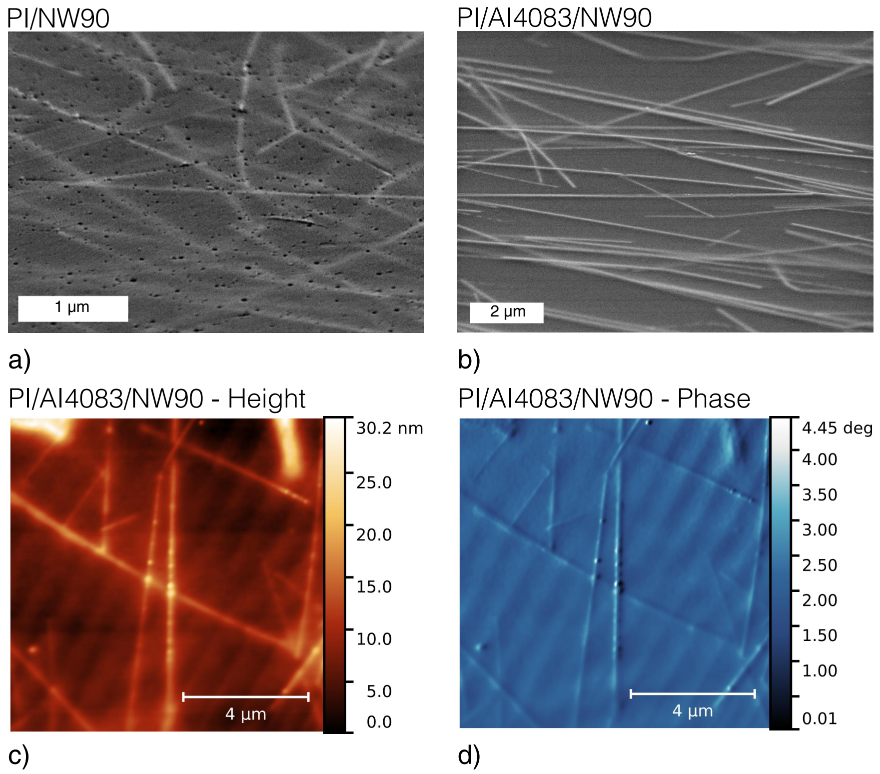

Figure 8.5.: Top: SEM images of silver nanowires buried in polyimide under an tilting angle of 70°. **a)** The polyimide coating is carried out on top of the neat silver nanowire electrode. **b)** A layer of PEDOT:PSS (AI4083) is spin-coated onto the AgNWs before depositing the PI. **Bottom:** AFM image of AgNWs with PEDOT:PSS (AI4083) buried in PI. **c)** Height and **d)** phase information.

the PEDOT:PSS interlayer, it loses roughly 1 % transmission compared to the neat PI which is acceptable in respect of its necessity for the formation of a conductive AgNW layer later on. However, the transmission of the electrode drastically decreases when introducing the silver nanowires although the glass is removed for these measurements. The loss compared to the PI layer is 9.2 % for the NW90 electrode type. This is expected, as the transmission loss on bare glass due to bare silver nanowires is also around 8 to 10 % with comparable R_{S} values. In case of NW35, the loss equals 16.4 % which is much more compared to the standard glass/NW35 electrode, where the reduction in $T_{\mathrm{t,550}}$ is only 10 to 12 %. For all nanowire samples, the typical plasmonic absorption is not visible anymore due to the PI absorption. However, the PI/AI4083/NW35 electrode has a spectrally broad transmission loss that reaches far beyond 500 nm. Possibly, the plasmonic absorption is still visible, but strongly broadens due to the embedment in PI. This absorption might be much stronger than for the NW90 electrode, as the wire diameter and the nanowire mesh size is much smaller compared to the NW90 electrode. Comparing the FOM values (cf. Table 8.2), a decrease by a factor of three compared to a glass/NW90 electrode (FOM $\approx$ 400) is observed, which can be attributed rather to the transmission loss than to a decrease in R_{S}.

Summarizing this section, conductive PI/AgNW transparent electrodes with a maximum $T_{t,550}$ of 78.5 % and a R_S as low as 15.3 Ω/□ are fabricated. This is achieved by introducing an interlayer of PEDOT:PSS that prevents the PI from penetrating the interstices of the wires. Drastic reduction of the surface roughness R_{rms} from 30 nm for the neat AgNW electrode down to (2.5 ± 0.5) nm is observed. These investigations offer a good foundation for the fabrication of OPV devices on this type of electrode (see Section 8.4.1), even if the transmission – and with this the FOM – is worse than the neat NW90 electrodes on glass.

8.3.3. Optical Adhesive 'NOA63'

NOA63 is introduced in this section as the third polymer investigated within this study. In contrast to the heat-curable polymers PDMS and polyimide, NOA63 is a polymer that cures under UV illumination with a maximum intensity between 350 to 380 nm wavelength. It offers temperature stability from −15 °C to 90 °C, which is in the range of usual OPV operating temperatures.[2]

The electrode fabrication follows the general description in Section 8.2 and the detailed processing denoted in the Experimental Section 4.4. To enhance wettability properties of the electrode for the deposition of adjacent solution-processed layers (e. g. PEDOT:PSS), argon plasma treatment is carried out. The impact on the electrode surface is studied using atomic force microscopy.

Silver Nanowires with 35 nm Diameter

Transmission graphs and AFM images of various NOA63/NW35 electrodes are plotted in Figure 8.6 and 8.8, respectively. Values for transmission, sheet resistance, and the corresponding FOM are summarized in Table 8.3.

Table 8.3.: Transmission and R_S values of NOA63 layers on glass, NW35 on glass and the NW35 on glass after the NOA63 deposition and curing. One sample was kept on a hotplate at 140 °C for 30 min prior to the NOA63 deposition.

	$T_{t,550}$ (%)	T_{vis} (%)	R_S (Ω/□)	FOM
Glass/NOA63	91.8	89.2	–	–
Glass/NW35 (no heat)	83.6	81.7	22 ± 2	175 ± 15
Glass/NW35 (heat)	84.0	82.8	18 ± 2	225 ± 25
Glass/NW35/NOA63 (no heat)	84.1	78.0	18.5 ± 0.2	222 ± 2
Glass/NW35/NOA63 (heat)	84.3	78.5	17.0 ± 0.2	248 ± 3

Note that all transmission measurements in Figure 8.6 are performed including the glass substrate. In Figure 8.7, transmission measurements and the corresponding

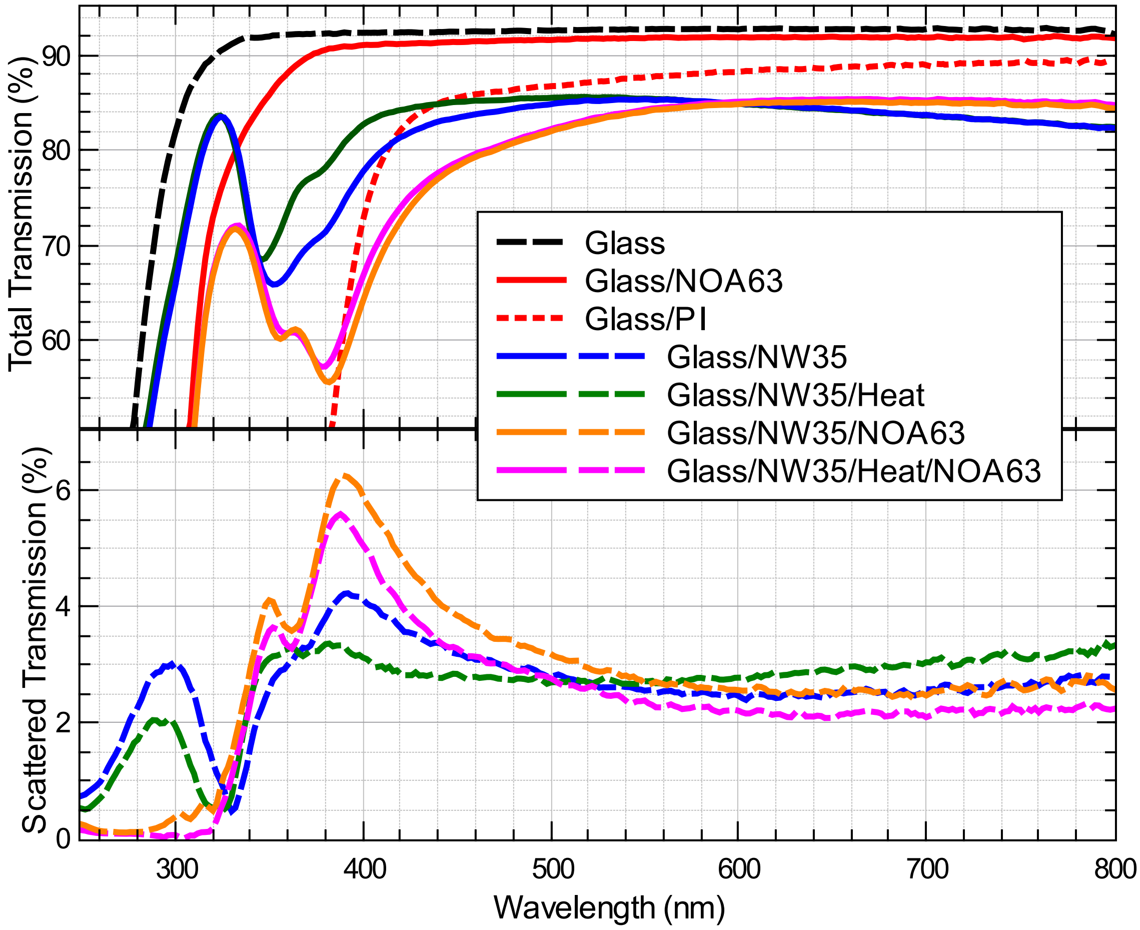

Figure 8.6.: Total transmission T_t and scattered transmission ($T_s = T_t - T_d$) spectra for glass, NOA63 on glass, PI on glass, and NW35 on glass with and without heat treatment and after NOA63 deposition.

$T_{t,550}$ and T_{vis} are visualized before and after the peel-off process from the glass. The transmission decreases for the neat NOA63 layer compared to NOA63 on glass by approximately 1 %. This small change is referred to different reflection properties of the NOA63 interface. Before peel-off, one NOA63 side sticks to the glass. That interface changes during peel-off such that air is the adjacent medium after peel-off with a different refractive index. In contrast, the transmission increases less than 1 % while having NW35 buried in the polymer film throughout the removal of the glass substrate. It is assumed that the nanowires give a different plasmonic reaction, depending on their contact medium – glass or air. The plasmonic interaction changes, which is indicated by the strongest difference in the two transmission spectra at 380 nm. This absorption dip is related to the plasmon resonance of the nanowires (cf. Section 3.3.4). Considering the application in solar cells, a transmittance change of 1 % has no significant influence on the device performance. In conclusion, it is reasonable to measure the electrode transmission including the glass substrate without falsifying the results. Even more, the electrode perfomance is somewhat underestimated.

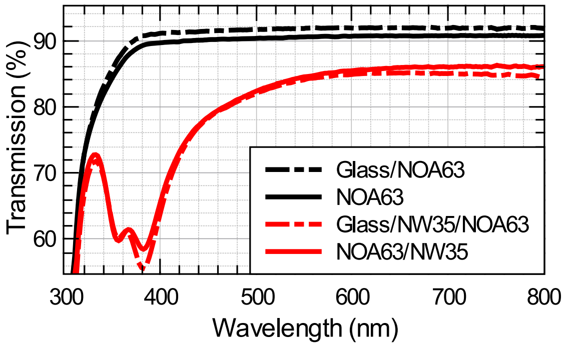

	$T_{t,550}$ (%)	T_{vis} (%)
Glass/NOA63	91.8	89.2
NOA63	90.5	88.1
Glass/NW35/NOA63	84.1	78.0
NOA63/NW35	84.5	78.8

Figure 8.7.: Left: Transmission measurements of NOA63 and NOA63/NW35 with and without the glass substrate. **Right:** Transmission values of NOA63 and NOA63/NW35 with and without glass substrate.

Continuing the optical analysis of the NOA63/NW35 layers, several observations can be drawn from Figure 8.6. First, the neat polymer film exhibits high transparency of greater than 90 % down to 370 nm and a high absorption is observed below 310 nm. These properties result in a colorless appearance. Furthermore, the NOA63 is much more transparent than the previously discussed polyimide. Second, the unheated NW35 network on glass exhibits a plasmon resonance absorption in the wavelength range of 320 to 420 nm. Upon network heating, the plasmon absorption decreases in width and strength and the sheet resistance decreases from $(22 \pm 2)\,\Omega/\square$ to $(18 \pm 2)\,\Omega/\square$. Both effects can be explained with the heating procedure: the junction resistance decreases and thus the network R_S. At the same time, the nanowires lay tighter on the glass, which reduces the scattering behavior of the AgNWs.[46]
Third, the overall transmission of the electrode is reduced by 3 to 4 % after the NOA63 coating while the $T_{t,550}$ stays nearly constant. The reduction in T_{vis} is mainly due to an increased and slightly red-shifted absorption in the plasmonically active region between 330 to 440 nm. Additionally, the NOA63 absorption edge contributes to a lower T_{vis}. Interestingly, the spectra for heated and non-heated NW35 electrodes become nearly the same again after the NOA63 coating. Due to a slightly lower R_S of the electrode, a heating step is nevertheless preferred but not necessary for NW35. Last but not least, the scattering of the NOA63/NW35 electrode increases from 3 to 4 % to a maximum of 6 % at 390 nm, where the plasmonic activity reaches the highest absorption. This again suggests that the NOA63 has an influence on the interaction between nanowire and light due to a changed refractive index[2] and a different dielectric constant than air. The FOM reaches 248 ± 3 for the heat-treated NOA63/NW35 electrode which is similar to the FOM of the reference NW35 electrode on glass.

Another important property is the electrode planarization capability of this process. This issue is investigated using atomic force microscopy on the electrode surface. Furthermore, the impact of argon plasma on the surface texture is studied. Typically,

---

[2] The refractive index of NOA63 is 1.56.[2]

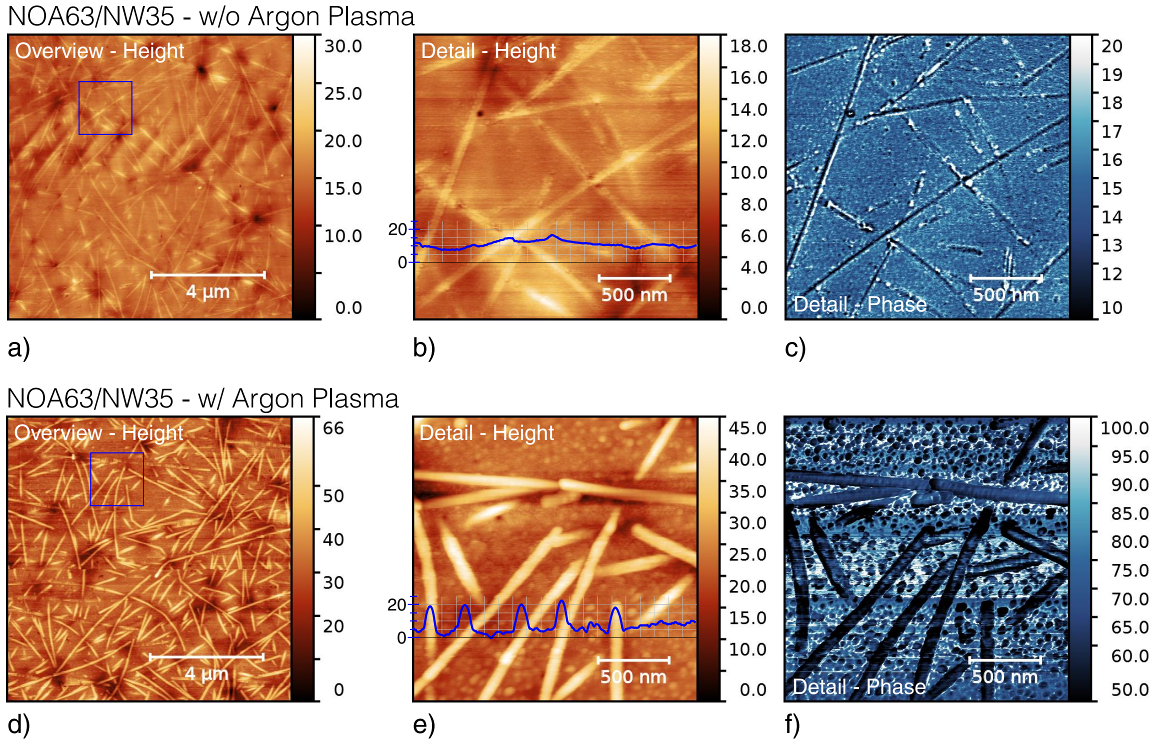

Figure 8.8.: AFM images of silver nanowires with 35 nm diameter buried in NOA63. The blue squares in a) and d) indicate the position of the detail scan. The blue curves in b) and e) represent profile scans through the black lines. All height scale values are stated in nm, all phase scale values are stated in degree. **Top:** Untreated electrode surface. **a), b)** Height informatione. **c)** Phase information of b). **Bottom:** Electrode surface after 10 min of argon plasma treatment. **d), e)** Height information. **f)** Phase information of e).

an argon plasma treatment changes the surface wettability. This is sometimes necessary for depositing adjacent organic interlayers, e. g. PEDOT:PSS or small molecule charge carrier transport layers (cf. Section 8.4). However, the impact on the NOA63 polymer surface is not clear, as argon plasma treatment has the ability to ablate soft material.[288] Figure 8.8 (top) shows the AFM images of the untreated surface. In Fig. 8.8 (bottom), the electrode surface is analyzed after 10 min of argon plasma treatment at a pressure of 4×10^{-1} mbar. For the untreated sample, the maximum peak-to-valley height D_{ptv} equals 30 nm on a large image size of $(10 \times 10)\,\mu\mathrm{m}^2$; a surface roughness $R_{\mathrm{rms}} < 1$ nm is determined. The nanowires are visible, but the contrast to the polymer surface is very weak. On a smaller image size of $(2 \times 2)\,\mu\mathrm{m}^2$, a line scan shows that the wires protrude from the polymer with a height of less than 5 nm. Additionally, the phase information (also $(2 \times 2)\,\mu\mathrm{m}^2$) exhibits a phase contrast with a very small width at areas where nanowires are visible. After exposing the surface to argon plasma, R_{rms} and D_{ptv} increase to (5 ± 1) nm and 66 nm on large image size, respectively. Now, the AgNWs are distinctly exposed with a height of ≈ 15 nm. The phase information reveals a phase contrast that is strongly broadened at the nanowire positions.

Comparing these measurements with each other, the argon plasma frees the nanowires by ablating 10 to 15 nm of polymer. This hypothesis is supported by the changed structure of the polymer, which looks more grainy after the treatment. On the one hand, the treatment increases the surface roughness. This behavor is not wanted in general as a stronger roughness complicates the fabrication of thin-film devices. On the other hand, the wires are exposed with stronger extent. This could increase the electrical contact to adjacent conductive layers, as it additionally removes insulating residuals like e. g. PVP or capping NOA63 from the wires.

Silver Nanowires with 90 nm Diameter

As the processes and results are very similar for AgNWs with the NW90 compared to the NW35 electrode type, this section just very briefly discusses the main differences between NW35 and NW90 in terms of processing and their electrical and optical properties.

Fabricating a NOA63/NW90 electrode differs only in one step from NW35: Directly after the deposition of NW90s on glass, a post-treatment is required to achieve full conductivity of the network. Therefore, an annealing step on a hotplate at 210 °C for 90 min in air is employed. This method is not suitable for temperature-sensitive polymer substrates, but shows the feasibility of NW90 with NOA63 in principle. An alternative process that uses much lower temperature has been developed by Weiß et al. where a high relative humidity of 80 % and a low temperature of only 70 °C is applied for 30 min.[46] This process is tested with positive results in this study, but not further investigated as the temperature reduction is not the main purpose of these experiments.

Graphs of the total and the scattered amount of transmitted light through glass/NW90 electrodes before and after the NOA63 deposition are shown in Figure 8.9. $T_{\mathrm{t},550}$ values develop from 83.3 % to 84.1 % after heating to 81.4 % for the glass/NW90/NOA63 electrode. T_{vis} is 82.0 %, 82.9 % and 78.5 % before, after the annealing, and after the NOA63 coating, respectively. Furthermore, the amount of scattered light is much larger in case of NW90 electrodes. It reaches values up to 10.5 % on glass and 14.3 % if embedded in NOA63. Similar NW35 samples scatter light up to 4.1 % on glass and 5.5 % in NOA63. The sheet resistance of the NW90 electrode changes from $(130 \pm 30)\,\Omega/\square$ before annealing to $(12.5 \pm 0.3)\,\Omega/\square$ after annealing to $(15.2 \pm 0.1)\,\Omega/\square$ after the NOA63 deposition and peel-off. This final R_S value is slightly better while the T_{vis} is exactly the same compared to the heated NOA63/NW35 electrode. However, when looking at Figure 8.9, it gets clear that the NW90 samples exhibit a more homogeneous spectral transmission distribution. The plasmonic absorption dip is very weak and nearly vanishes after NOA63 deposition. In contrast, this absorption gets even stronger and broader for NW35. This leads to the assumption that the visible appearance of the NW90 electrode is more colorless.

Which type of AgNWs is chosen for OPV application thus depends more or less on two considerations: first, the processability of the AgNWs might be more convenient with one type of AgNWs. In our case, the NW35 without the need for further annealing steps are simplifying the processing. Second, it depends on the type of solar cell chosen for fabrication onto this electrode. On the one hand, the spectral EQE should match the electrode transmission to achieve an optimal photocurrent generation. On the other hand, when using e. g. weakly conductive organic materials, a well chosen mesh size of the network might play an important role for efficient charge carrier collection (cf. Chapter 7). The scattering behavior of the AgNW electrode attracts further consideration. High light scattering might be benefitial for light absorption in OPV devices or homogeneous light outcoupling in OLEDs.[18, 97, 200]

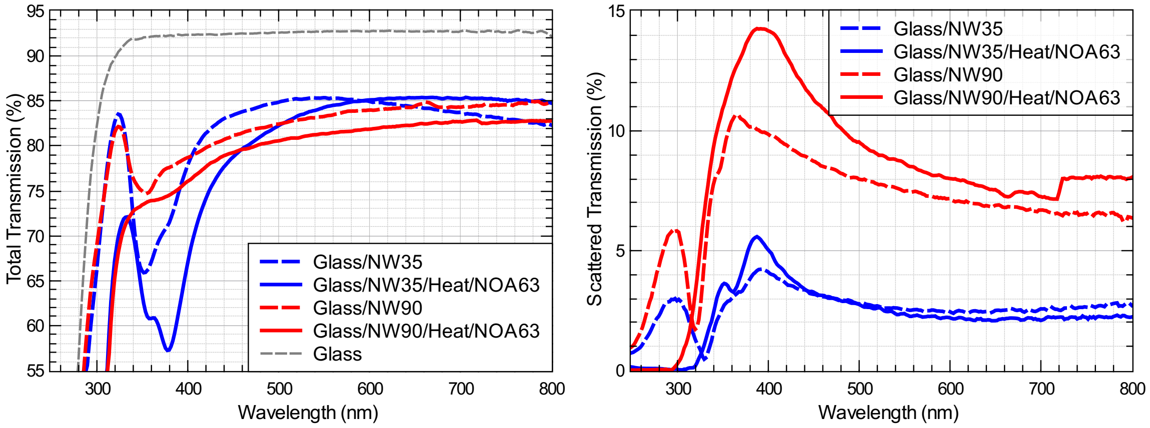

Figure 8.9.: Transmission spectra of NW35 (blue lines) and NW90 (red lines) electrodes on glass without heating (dashed lines) and after heat treatment and NOA63 deposition (solid lines). **Left:** Total Transmission. **Right:** Scattered amount of transmitted light.

Summary

Concluding this section, NOA63 is introduced as a single-component polymer providing the matrix material for the peel-off process. Transparent and conductive electrodes with NW35 are achieved reaching R_S values as low as $18.5\,\Omega/\square$ and a $T_{\mathrm{t},550}$ of $84\,\%$ directly after peel-off without any pre- or post-treatment of the nanowires. This is insofar remarkable, as a layer of PEDOT:PSS is a necessary part of creating conductive layers with polyimide (cf. Section 8.3.2). Now, processing steps involving water (e. g. the PEDOT:PSS coating) can be excluded from the electrode fabrication. It enables the possibility to transfer the processing fully to inert atmosphere (e. g. N_2), which reduces the probability and amount of trapped water in the polymer. Furthermore, it improves device stability and simplifies as well as shortens drying steps within device fabrication. A heat-treatment of the nanowires improves the sheet resistance even further to $17\,\Omega/\square$ at an improved $T_{\mathrm{t},550}$ of $84.3\,\%$.
AFM investigations on the planarization capability reveal extremely smooth surfaces

with an R_{rms} of roughly 1 nm. Additionally, an argon plasma treatment is capable of ablating NOA63 to improve the protrusion of nanowires out of the NOA63 without affecting the silver nanowires directly.

A comparison between NW90 and NW35 buried in NOA63 reveals comparable electrical properties. The total averaged transmission for both electrode types is very similar. Main difference is the spectral transmission distribution, which is much more homogeneous for NW90 than for NW35.

These investigations suggest that NOA63/AgNW layers are promising candidates for ITO-free and cost-effective electrodes as they are very smooth, flexible, transparent, and highly conductive.

8.4. Sexithiophene Cascade Organic Solar Cells

The previous investigations suggest that the implementation of this electrode type into thin-film organic solar cells seems reasonable. As testing device, a fullerene-free cascade architecture is chosen (cf. Section 2.2.3) that yields up to 8.4 % efficiency on ITO substrates.[55] Figure 8.10 (a) depicts the chemical structures of sexithiophene (α-6T), SubNc, and SubPc. The used layer stack is shown in Fig. 8.10 (b). Thereby, α-6T serves as thick donor layer that is in contact with SubNc and SubPc as two acceptor materials with similar LUMO and slightly different HOMO energies. This constellation accounts for efficient charge carrier generation, a simple sketch is depicted in Fig. 8.10 (c).

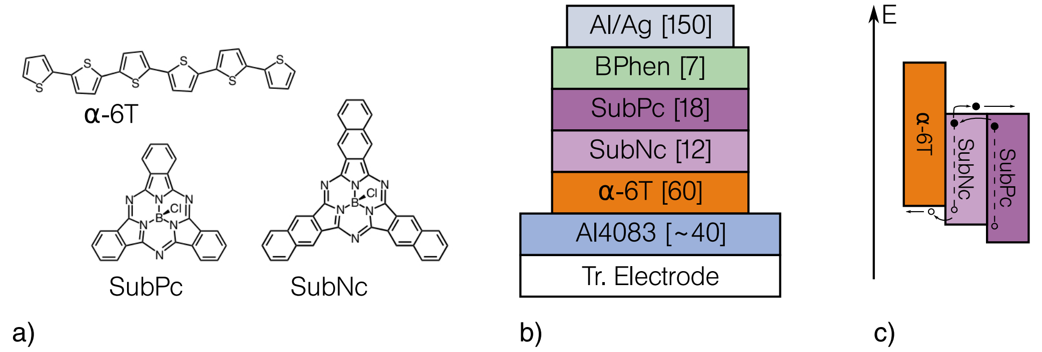

Figure 8.10.: a) Chemical structures of the active materials α-6T, SubPc and SubNc. **b)** Layer stack with thickness values in brackets (nm). The transparent electrode includes the substrate. **c)** Schematic process description of exciton dissociation and charge carrier movement. Adapted with permission from Cnops et al.[55]

8.4.1. Silver Nanowire Electrodes with Polyimide Substrate

This section deals with the applicability of the PI/AI4083/NW35 electrode in OSCs. It is tested by fabricating cascade organic solar cells (CSCs) (cf. Section 2.2.3). Electrodes

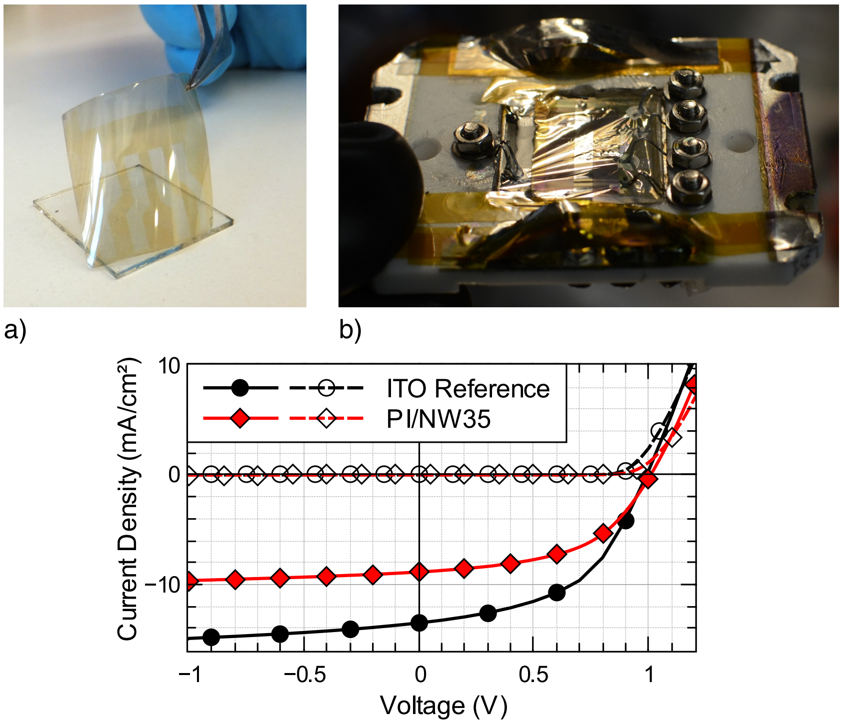

Figure 8.11.: Top: a) Photograph of a laser-structured PI/PEDOT:PSS/NW35 electrode directly after peel-off. **b)** PI substrate with evaporated cascade solar cell. The sample is mounted in a sample holder for the evaporation system 'UFO1'. **Bottom:** jV characteristics of a solar cell on PI/NW35 (red diamonds) and its ITO reference (black circles) under illumination with 100 mW/cm^2 (filled symbols) and in dark environment (empty symbols). The measurement is not mismatch-corrected, the assumed pixel area equals 6.25 mm^2.

are prepared following the procedure described in Section 8.3.2, with a slight change: directly after the deposition of silver nanowires on glass, a laser-scribing system is used to structure the electrode with the standard 4-finger layout (cf. Section 4.5). NW35s are used for the fabrication of transparent electrodes despite their worse aptitude as transparent electrode compared to NW90. A more reliable electrode fabrication and a more homogenous AgNW distribution after spin coating lead to this decision. A photograph of the electrode directly after the peel-off process can be found in Figure 8.11 (a). Although a layer of AI4083 already is in the electrode, the architecture of the cascade solar cell necessitates the deposition of another layer of low conductivity PEDOT:PSS (also AI4083) (cf. Experimental Section 4.4). Subsequently, the samples are heated out on a hotplate at 120 °C in ambient atmosphere for 15 min, followed by another heating under inert nitrogen atmosphere (30 min at 120 °C on a hotplate). The handling of the PI electrode is rather impractical, as it tends to coil up. The second AI4083 spin coating leads to material flowing beneath the substrate and a curling of the PI substrate. Thus, it complicates handling and mounting into the sample holder for the solar cell evaporation system (Figure 8.11 b). jV curves are acquired in inert nitrogen atmosphere.

The jV curves of a cascade solar cell on PI/AI4083/NW35/AI4083[3] and a reference on ITO/AI4083[4] are shown in Figure 8.11 (bottom). The CSCs on PI/NW35 and ITO exhibit power conversion efficiencies of 4.69 % and 6.85 %, respectively. All other values can be found in Table 8.4. This dramatic difference can be attributed solely to a strong divergence of j_{SC} which is on PI/NW35 just two third of the reference j_{SC}. All other values – V_{OC}, FF and S – are improved in case of the PI/NW35 CSC.

These results show that the electrical functionality of the electrode is working without a spot. The nanowire topography is sufficiently planarized to contain leakage currents, visible in the low value for S and a high FF. The V_{OC} is 20 mV larger on the PI/NW35 than on the ITO electrode. The most probable explanation here are indeed uncertainties in the solar cell fabrication. The discrepancy in j_{SC} becomes clear when comparing the transmission of the PI/NW35 and ITO electrodes (Fig. 8.4). On the one hand, the $T_{\mathrm{t},550}$ of the PI/NW35 electrode is roughly 10 % lower than $T_{\mathrm{t},550}$ of ITO. Additionally, the EQE of the CSC shows valuable contribution to the j_{SC} in the UV region of the spectrum below 400 nm.[55] In this region, the ITO electrode is transparent whereas the polyimide strongly absorbs. A significant reduction of T_{vis} by 23 % for the PI/NW35 electrode as compared to ITO accomodates this fact and explains the loss of j_{SC}.

Table 8.4.: Photovoltaic performance parameters of cascade solar cells with a device area of approximately 6.44 mm^2 on ITO or PI/NW35. Measurements are carried out in a nitrogen-filled glovebox under AM1.5G irradiation of 100 mW/cm^2. A spectral mismatch correction is not performed.

Electrode	V_{OC} (V)	j_{SC} (mA/cm^2)	FF (%)	S (a.U.)	PCE (%)
ITO	0.99	13.5	50.3	1.10	6.85
PI/NW35	1.01	8.86	51.5	1.09	4.69

Concluding this section, a working cascade solar cell on a flexible PI/NW35 electrode is shown for the first time with an efficiency of 4.7 %. The main discrepancy compared to a reference device on ITO (PCE 6.85 %) originates from a reduced j_{SC} due to an inferior transmission properties of this electrode. Additionally, the substrate handling is quite difficult and an even more complicated handling is expected for devices with larger areas. Moreover, the encapsulation against moisture ingress could become challenging with this kind of substrate.

---

[3] Short: PI/NW35

[4] Spin coating of the AI4083 layer is done at 4000/min|45 s, as the ITO needs no further smoothening. The AI4083 was only inserted for adjusting the energy levels of ITO and α-6T.

8.4.2. NOA63/NW35 Electrodes with Flexible Alumina Encapsulation[5]

Cascade solar cells on NOA63/NW35 electrodes are discussed in this part of the study. Two main aspects are investigated in the following: First, the NOA63/NW35 electrode is tested with respect to its functionality as bottom electrode in cascade solar cells. Second, the solar cells are aged in ambient climate conditions and continuous illumination. Therefore, an encapsulation against moisture ingress needs to be employed. An additional aim within this study is the fabrication of fully-flexible, encapsulated devices. As the electrode with the organic solar cell is already flexible, a flexible encapsulation is required.

Some additional experimental information is discussed as well as a detailed description of the techniques that enable the fabrication of flexible encapsulation barriers. Afterwards, the solar cells are investigated in terms of their general functionality and their degradation behavior in a simulated application environment. Furthermore, degradation mechanisms are identified and briefly discussed.

Experimental: Barrier Foil and Solar Cell Fabrication

For encapsulation purposes, three different possibilities are utilized. The encapsulation with glass is the most straightforward solution as glass nearly is a perfect barrier. Using a glass substrate protects the organic device against water ingress from the bottom. In order to protect it from the top as well, an encapsulation glass with a getter-containing cavity is glued on the substrate that encloses the device area (cf. Section 4.5). However, glass is rigid and therefore not suitable for the purpose of flexible devices. In this study, it is used as reference encapsulation to access information about the intrinsic degradation of the organic device due to chemical decomposition or the formation of interfacial energetic barriers.

As flexible alternative to glass encapsulation, alumina (AlO_x) is used. It is able to prevent water ingress down to a $WVTR$ of $3 \times 10^{-5}\,\mathrm{g/(m^2\,d)}$,[34] which puts it into the category of an *ultra-barrier*.[164] It is deposited via atomic layer deposition (ALD) and has a thickness of 20 nm. Two routes are followed to encapsulate the device. On the one hand, the AlO_x is deposited onto a planarized polyethylene naphtalene (pPEN) polymer web which then is laminated below or on top of the device with a Tesa® barrier glue. On the other hand, the AlO_x is directly deposited on top of the organic device. In this case, an additional PET foil is glued on top of this barrier layer with epoxy to prevent the layer from cracking and mechanical stress.[34] All steps are carried out in inert atmosphere.

The NOA63 electrodes are prepared following the explanations in Section 8.3.3.

---

[5] The content of this section is published in [5].

They are structured after nanowire deposition with the laser-scribing system to achieve the 4-finger layout (cf. Sec. 4.5). After the NOA63/NW35 peel-off, the electrode is laminated either onto a glass substrate or onto a barrier foil (pPEN with 20 nm AlO_x) with the proprietary Tesa® barrier glue. Subsequently, a layer of AI4083 is spin-coated with 2000 rpm on top of the electrode, and annealed on a hotplate (10 min at 120 °C in air and 12 h at 80 °C in N_2) to remove residual water.

Device Characterization

Various devices with different combinations of bottom electrode and top/bottom encapsulation are fabricated with a cascade layer architecture (Figure 8.10 b) and characterized in ambient atmosphere. The combinations and their respective solar cell fingerprints are summarized in Table 8.5, corresponding jV characteristics are depicted in Figure 8.12. EQE measurements and transmission spectra for the bottom electrode types are shown in Figure 8.13.
The solar cells on ITO exhibit a PCE of $(6.5 \pm 0.1)\,\%$[6], indepent of their encapsulation. The highest V_{OC}, j_{SC}, and FF values are 0.96 V, 11.3 mA/cm^2, and 63.5 %, respectively. Lowest saturation value is 1.063. With NW35 as bottom electrode, the highest efficiency of 5.61 % is reached with a glass-glass encapsulated CSC on NOA63/NW35 electrode, all other CSCs with NW35 exhibit PCEs around 5 % except the solar cell '# 9' which exhibits a maximum PCE of 2.8 %. The V_{OC} of the NW35 CSCs constantly lies between 0.95 V and 0.96 V with very small deviations on every sample. j_{SC} values are in the range of 8.5 to 9.2 mA/cm^2 for all NW35 samples except '# 9'. FF and saturation exhibit best values of 64.9 % ('# 4') and 1.058 ('# 5').

Several issues can be deduced comparing the different device types. First, the top encapsulation technique used does not impact the solar cell performance. This leads to the conclusion that there is no difficulty in depositing the AlO_x layer, the barrier glue, or the epoxy glue directly onto the aluminum cathode. Also, the processing is very reproducible. Only 2 samples out of 18 are damaged during the encapsulation resulting in non-working devices. Second, the main discrepancy in the PCE on NW35 is caused by the j_{SC} which is $(20 \pm 4)\,\%$ lower than the reference value on ITO. This loss can be explained with the EQE of the solar cells with different types of bottom electrodes. In the wavelength regime above 440 nm, the curves have a very similar shape and also similar values, only the EQE of ITO-based devices is 5 to 10 % higher. Going to wavelengths below 440 nm, the electrode types exhibit a deviating behavior mainly caused by the diverging electrode transmission. The EQE of ITO-based devices exhibits highest values as well. Notably, the NW35-based devices have the ability of transmitting light at short wavelength, which is visible in an EQE value of still 40 % at a wavelength of 300 nm. The combination with NOA63 leads to an absorption edge similar to ITO. Changing the bottom encapsulation from glass to pPEN/AlO_x gives

---

[6] Averaged over 6 samples containing 4 devices each.

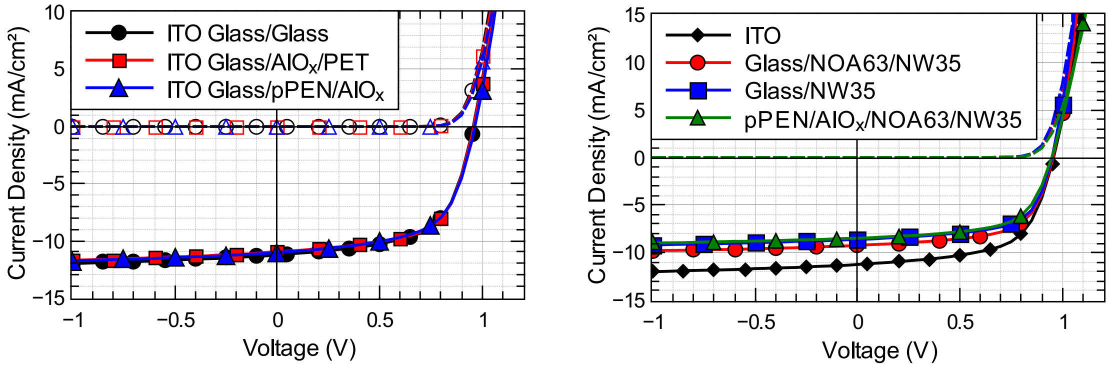

Figure 8.12.: jV characteristics of cascade solar cells, measured in air. Filled symbols and solid lines represent the solar cell under illumination, empty symbols and dashed lines show the jV behavior in dark environment. **Left:** CSCs on glass/ITO as bottom electrode. The solar cells are encapsulated with glass (circles), 20 nm AlO$_x$ directly deposited onto the solar cell and protected by an epoxy-glued PET sheet (red squares), and a pPEN sheet with 20 nm AlO$_x$, laminated with a barrier glue (blue triangles). **Right:** CSCs on ITO (black solid line), Glass/NW35 (blue squares), NOA63/NW35 laminated with a barrier glue on glass (red circles), or NOA63/NW35 laminated with a barrier glue on a pPEN sheet with 20 nm AlO$_x$ (green triangles) as bottom electrode.

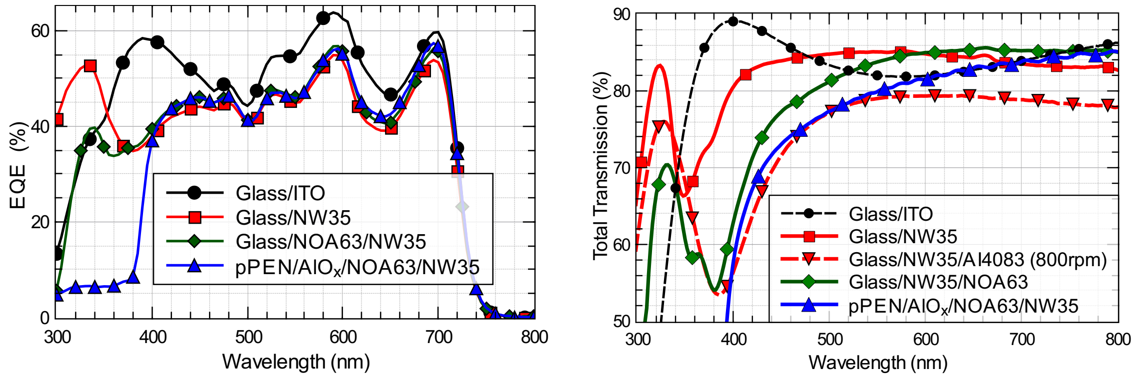

Figure 8.13.: **Left:** EQE of CSCs on different types of bottom electrodes. **Right:** Electrode transmission.

Table 8.5.: Photovoltaic performance parameters of cascade solar cells on ITO, NW35 and NOA63/NW35. All samples are encapsulated against moisture ingress. The used combination of substrate, electrode and encapsulation is stated under 'Type' as follows: [Bottom encapsulation] | [Electrode] | [Top encapsulation]. For every solar cell type, 2 samples containing 4 diodes each with an active area of 6.44 mm^2 are prepared under identical conditions. The yield states the amount of working diodes. All samples are measured in ambient atmosphere. The best value for every type is stated in brackets.

	Type	V_{OC} (V)	j_{SC} (mA/cm^2)	FF (%)	S (a.U.)	PCE (%)	Yield (x/8)
# 1	Glass | ITO | Glass w. Getter	0.96	10.9 ± 0.3 (11.3)	62.0 ± 0.8 (63.1)	1.066 (1.063)	6.47 ± 0.02 (6.61)	7
# 2	Glass | ITO | AlO$_x$/PET	0.96	10.9 ± 0.1 (11.0)	63.1 ± 0.2 (63.5)	1.067 (1.065)	6.61 ± 0.05 (6.68)	8
# 3	Glass | ITO | pPEN/AlO$_x$	0.96	10.8 ± 0.3 (11.1)	61.5 ± 0.4 (62.1)	1.068 (1.068)	6.4 ± 0.1 (6.51)	8
# 4	Glass | NW | Glass w. Getter	0.95	8.5 ± 0.2 (8.7)	64.1 ± 0.4 (64.9)	1.08 (1.066)	5.2 ± 0.1 (5.36)	8
# 5	Glass | NOA63-NW | Glass with Getter	0.95	9.0 ± 0.2 (9.2)	62.9 ± 0.8 (63.7)	1.059 (1.058)	5.4 ± 0.2 (5.61)	3
# 6	pPEN/AlO$_x$ | NOA63-NW | AlO$_x$/PET	0.95	8.6 ± 0.1 (8.7)	61 ± 1 (62.8)	1.061 (1.058)	5.0 ± 0.1 (5.1)	8
# 7	pPEN/AlO$_x$ | NOA63-NW | pPEN/AlO$_x$	0.95	8.7 ± 0.3 (9.1)	59 ± 4 (62.5)	1.07 ± 0.01 (1.064)	4.9 ± 0.2 (5.0)	6
# 8	Glass | NOA63-NW | pPEN/AlO$_x$	0.96	8.7 ± 0.1 (8.7)	62 ± 1 (62.4)	1.065 (1.061)	5.1 ± 0.1 (5.2)	3
# 9	Glass | NOA63-NW | AlO$_x$/PET	0.96	5 ± 2 (7.5)	35 ± 5 (39.3)	1.5 ± 0.3 (1.13)	1.7 ± 0.9 (2.8)	4

an additional EQE decrease as the absorption of the pPEN sheet already sets in at 400 nm.

All other values of the NW35 solar cells are similar or improved as compared to the reference on ITO. A maximum FF value of 64.9 % is reached on NW35 on glass ('# 4'). Here, the electrode exhibits an excellent R_S value of $(12 \pm 1)\,\Omega/\Box$ resulting in a very low series resistance. However, the necessity of a thick PEDOT:PSS planarization layer[7] results in an overall lower electrode transmission. This loss is also visible in the EQE and leads to a j_SC that is even lower than on NOA63/NW35 electrodes. Furthermore, the saturation value of this type is highest for all reasonable working devices, leading to the assumption that the planarization is not fully sufficient.

The fully flexible devices ('# 6' and '# 7') exhibit a maximum power conversion efficiency of 5.1 %. This is among the highest reported values in literature for ITO-free, fully-flexible, encapsulated small molecule organic solar cells. The only difficulty occurs during the lamination of the top encapsulation onto NOA63/NW35 electrodes that are already laminated on glass. Lamination with the epoxy glue encounters mechanical stress during curing. This leads to a corrugation of the solar cell and the top electrode, destroying parts of the solar cell. A microscope image of such an area is depicted in Figure 8.14 (c) in comparsion to unharmed areas of different samples (cf. Fig. 8.14 a, b).

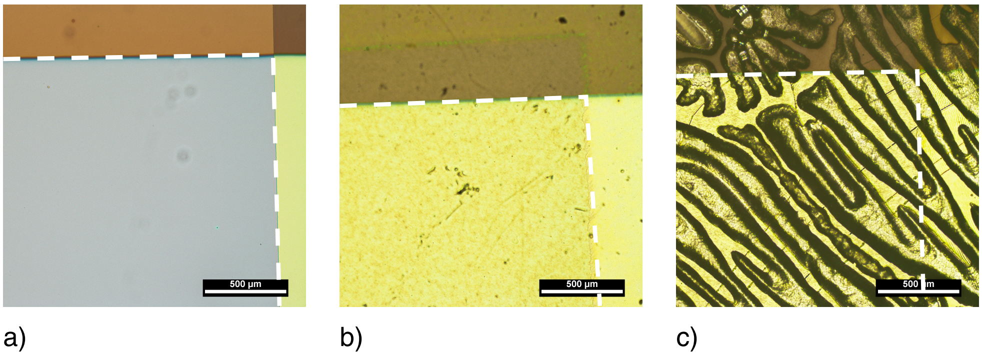

a) b) c)

Figure 8.14.: Optical microscope images of the solar cells encapsulated with 20 nm AlO_x followed by the lamination of a protective PET sheet with an UV-curable epoxy glue. Dashed lines indicate the active area, all scalebars represent 500 µm. Images are taken through the substrate side. **a)** ITO electrode. **b)** Fully-flexible NOA63/NW35 electrode. **c)** NOA63/NW35 electrode laminated on a glass substrate.

Overall, cascade solar cells are presented exhibiting a maximum PCE of 6.7 % on ITO, 5.6 % on NOA63/NW35 (glass-glass encapsulated), and 5.1 % as fully flexible device with NOA63/NW35 and a flexible encapsulation, all measured in ambient atmosphere. Two different thin-film AlO_x encapsulation techniques are successfully employed and show no significant influence on the device performance. The main loss mechanism is a reduced j_SC coming from a lower electrode transmission with NW35

---

[7] The AI4083 is deposited at a speed of only 800 rpm|60 s, resulting in a thickness of 80 nm on glass.

compared to ITO as bottom electrode. This is especially visible in the wavelength regime below 500 nm where the cascade architecture still gives a significant contribution to the photocurrent. Thus, the results are promising, as fully-flexible devices could potentially be processed with R2R technologies. Furthermore, facilitating a flexible ultra-barrier as encapsulation opens up the way for long-living flexible OPV.

Device Degradation

In the previous section, the first step towards fully-flexible encapsulated OPV has been taken by building CSC devices and characterizing them under ambient atmosphere. Highly efficient devices have been achieved. Nevertheless, a study of the degradation behavior of cascade solar cells in an environment simulating realistic outdoor applications has not been carried out up to now neither in literature nor in the scope of this thesis. However, this is an important investigation to complete the evaluation of this solar cell concept.

Consequently, the aging of the solar cells is studied under continuous illumination and a defined temperature and relative humidity. First, the setup and measurement method is briefly explained, followed by the evaluation of the degradation data. Subsequently, relevant degradation mechanisms are discussed and the applicability of this solar cell architecture is evaluated.

A climate cabinet is used for testing the solar cells under simulated AM1.5G illumination with an intensity of 100 mW/cm^2 (see Experimental Section 4.6). As climate environment, a relative humidity of 50 % and a temperature of 38 °C is set[8]. All solar cells are simultaneously mounted in the chamber and constantly illuminated; a self-made circuit board connects all devices to a SMU. IV curves are automatically taken every hour and relevant parameters are calculated. Solar cells are kept under open-circuit conditions in the time between the measurements.

The solar cells discussed in the previous section ('Device Characterization' in Table 8.5) are mounted into the climate chamber and aged under identical conditions for each device.

The degradation data – photovoltaic performance parameters over time and selected IV curves at different aging times – for the samples already discussed under Section 'Device Characterization' are depicted in Figure 8.15. The devices on ITO show a decrease by 50 % of their inital efficiency (D_{50}) within 240 to 330 h. The fully glass-glass encapsulated samples exhibit the longest lifetime. The V_{OC} stays nearly constant over all times. A PCE worsening originates from a reduction in j_{SC} and FF which is similar in shape. The IV curves show no exceptional behaviour except for very long aging times where a little s-kink is observed.

---

[8] Note, that the actual temperature in the solar cell is 5 to 10 K higher than the set-temperature due to illumination.

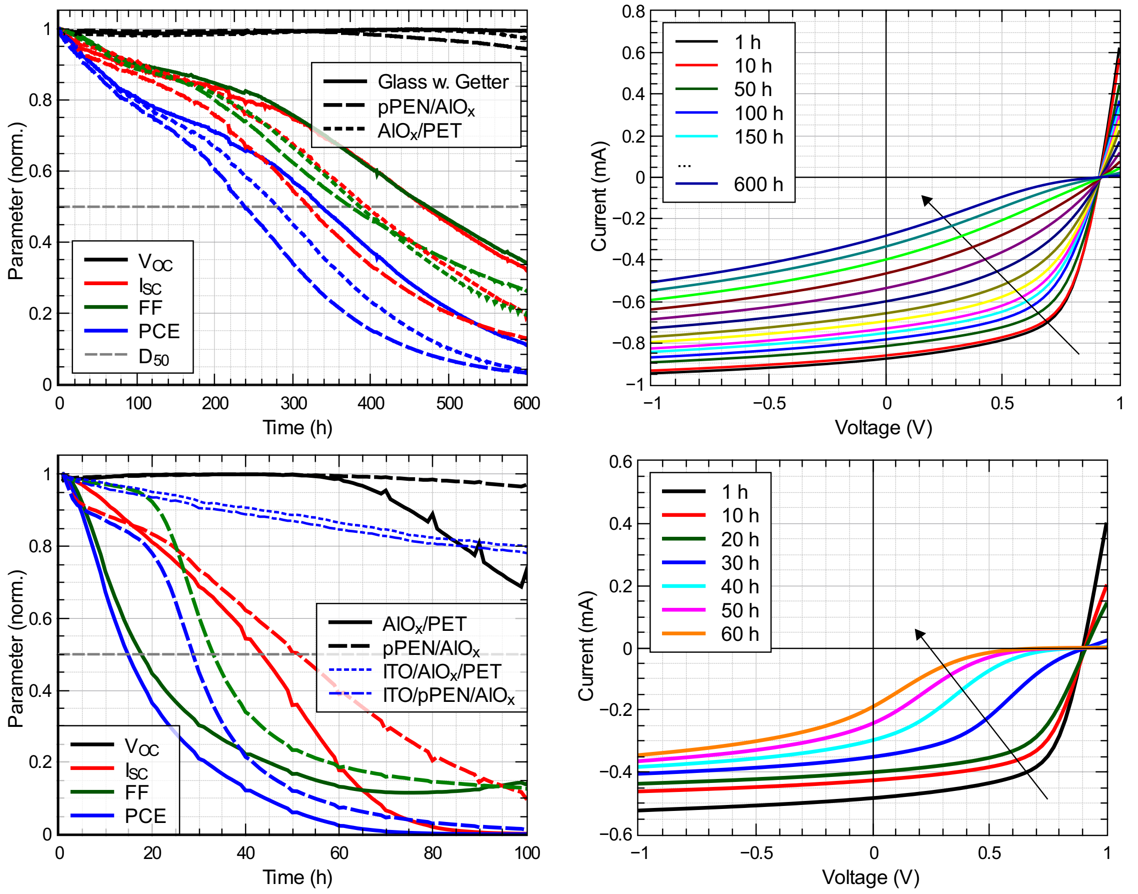

Figure 8.15.: Left: Development of characteristic CSC parameters over time. They are normalized to their starting value at 0 h. **Right:** IV curves at different aging times. **Top:** CSCs on ITO with different encapsulation: glass /w getter, pPEN/AlO$_x$ or AlO$_x$/PET. The IV curves are from the sample encapsulated with glass w/ getter. **Bottom:** Flexible CSCs on NOA63/NW35 with pPEN/AlO$_x$ bottom encapsulation and pPENAlO$_x$ or AlO$_x$/PET as top encapsulation. The IV curves are from the sample with pPEN/AlO$_x$ as top encapsulation.

The flexible solar cells reach D_{50} within 14 to 28 h. Here, the FF is the main factor for the PCE reduction over time. IV curves exhibit strong s-kinks, rising after approximately a day of aging.

Comparing and evaluating these results, two main findigs can be extracted. First, the cascade solar cells degrade very fast, even with an optimal encapsulation. A glass-glass encapsulated OSC with getter can reach D_{50} values up to 60 000 h,[145] but 1500 h for unencapsulated devices kept in air also have been reported.[253] The CSC degradation is therefore not caused by water or oxygen ingress into the device, but by intrinsic mechanisms, which will be discussed later. Employing thin-film encapsulation techniques accelerates the degradation slightly, but does not cause a drastic change in the degradation behaviour of the different fingerprints. However, a conclusive evaluation of the thin-film encapsulation cannot be carried out at such a fast device aging.

Second, the degradation happens even faster on NOA63/NW35 electrodes. Here, the degradation mechanism seems to be different to the degradation on ITO, as the s-kink occurs more early and with a stronger shape than on ITO. As organic layer architecture, processing, and aging conditions are identical to the ITO CSCs, the only reason for the significant degradation is connected to the NOA63/NW35 electrode. On the one hand, the electrode itself might degrade so that the charges cannot sufficiently be extracted by the contacts. An increase in series resistance would be the result which is in fact the case here (Fig. 8.15). Nam et al. reported on the R_S development of NOA/AgNW electrodes at 100 °C and observed an increase smaller than a factor of two within 14 days.[75] This finding does not support an electrode decomposition by itself within hours. On the other hand, acidic PEDOT:PSS might destroy the interface between cascade layers and electrode or has an impact on the electrode conductivity. This would explain the strong s-kink indicating a hindered charge extraction or injection.[127]
The role of PEDOT:PSS is investigated by performing experiments with the sole NOA63/AgNW electrode. Samples with NOA63/NW90 and NOA63/NW35 are placed on a hotplate at 50 °C in air (approx. 50 to 60 % RH). The resistance through the electrode is measured over time – once with an AI4083 layer, once without such a layer. Figure 8.16 shows the resistance development. A clear indication is visible that PEDOT:PSS causes a significant degradation which is independent from the choice of nanowire type. Without PEDOT:PSS, the resistance is nearly constant over one week of investigation.

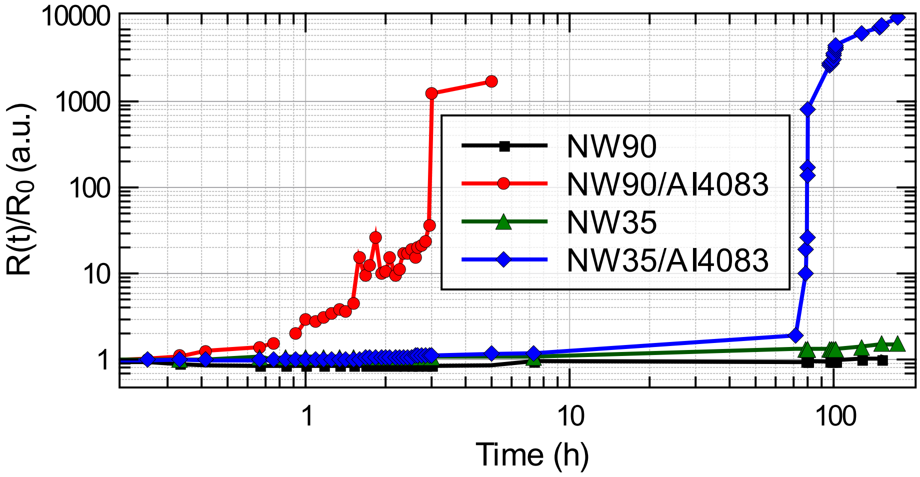

Figure 8.16.: Resistance change ($R(t)/R_0$) over time measured on NOA63/AgNW electrodes with and without a spin-coated layer of AI4083. As silver nanowires, NW90 and NW35 are used.

Intrinsic Cascade Solar Cell Degradation

In the following part, intrinsic CSC degradation mechanisms are discussed. Additional cascade solar cells are investigated to get further insights into the degradation mechanisms. A batch of CSCs on ITO according to the layer sequence in Figure 8.10 (page 126) but with an α-6T thickness varying from 30 to 75 nm in 15 nm steps is prepared, glass-glass encapsulated and aged in 38 °C, 50 % RH climate under illumination. Furthermore, CSCs without PEDOT:PSS are aged following the same procedure.
The inital solar cell fingerprints are summarized in Table 8.6. Figure 8.17 shows the degradation behavior for the α-6T thickness variation. The comparison of CSCs with and without a layer of AI4083 is depicted in Fig. 8.19.

The PCE of the CSC with 60 nm α-6T thickness exhibits 7.0 %, while a drop in PCE is obtained for thicker and thinner α-6T layers. With increasing α-6T thickness, the solar cell reaches the D_{50} earlier with 10 days difference between thickest and thinnest α-6T layer. The V_{OC} stays nearly constant while the degradation is caused by decreasing j_{SC} and FF values with a similar shape. The CSC without PEDOT:PSS has a PCE of 7.3 % and degrades within 61 h to D_{50}. The IV curves show a strong current decrease as soon as applied voltages are larger than V_{OC}.

These measurements suggest that the α-6T is the component that ages, at least in the case with AI4083. Several reasons substantiate this assumption. First, the cascade mechanism needs a high α-6T roughness to increase the interface to the SubNc and SubPc layers for efficient exciton splitting[9]. Sander et al. reported about a temperature- and UV-light-activated polymerization of α-6T molecules.[78] Although this might not happen in the solar cells discussed here, it shows that the α-6T is already affected by slight temperature and light ingress. A reorganization could cause a reduced interface area, leading to a decrease of charge carrier transport and generation capability, visible in degrading j_{SC} and FF values. This effect is less pronounced with a lower amount of α-6T molecules – the degradation is slower. Furthermore, Sander et al. report the formation of a radical prior to α-6T polymerization due to oxidation.[78] Thus, the α-6T molecules are more reactive, which could additionally lead to the formation of new molecule compounds with SubNc or SubPc (if such molecules are present). This assumption is supported by the change in the reflection spectra (Fig. 8.18) of a CSC before and after full degradation. The absorption dips can be attributed clearly to the different absorber materials. The strongest change happens in the spectral region of α-6T absorption[10].

The situation again looks very different in the case of ITO-based devices without PEDOT:PSS interlayer. Although the device efficiency is superior to all other CSCs fabricated within this study, the lifetime D_{50} is with only 61 h the shortest among all

---

[9] Cnops et al. measured a R_{rms} of 15.9 nm for 70 nm of α-6T, evaporated on Si/AI4083 substrates via AFM on $(2 \times 2)\,\mu\text{m}^2$ image size.[54]

[10] Note, that the absorption of α-6T is rather broad and reaches from 350 to 500 nm.

Table 8.6.: Solar cell fingerprints of cascade solar cells on ITO with x nm α-6T thickness ($x = (30, 45, 60, 75)$ nm). One sample containing four identical diodes of each kind per thickness is prepared, stated are always the values of the best pixel out of four.

$t_{\alpha\text{-6T}}$ (nm)	V_{OC} (V)	j_{SC} (mA/cm^2)	FF (%)	S (a.U.)	PCE (%)	D_{50} (h)
30 w/ AI4083	0.944	9.4	56.6	1.078	5.03	492
45 w/ AI4083	0.965	11.2	59.5	1.07	6.43	414
60 w/ AI4083	0.968	12.2	59.2	1.067	7.0	394
60 w/o AI4083*	0.98	12.1	61.8	1.07	7.28	61
75 w/ AI4083	0.969	11.7	60.1	1.067	6.8	232

*: This CSC is from another fabrication batch.

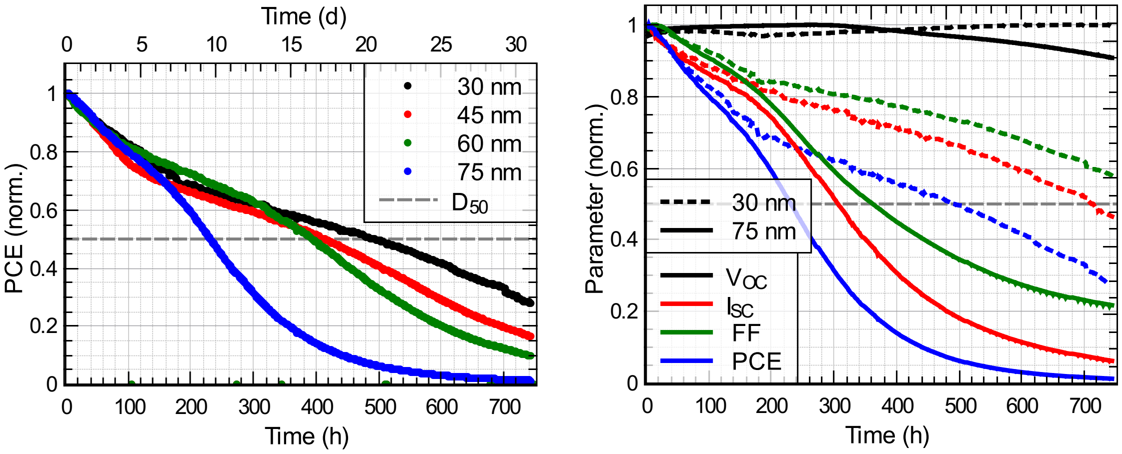

Figure 8.17.: Left: Normalized PCE of CSCs on ITO with α-6T thicknesses of (30, 45, 60 and 75) nm. All samples are glass/glass-encapsulated with getter. **Right:** Normalized parameter (V_{OC}, j_{SC}, FF, PCE) of CSCs on ITO with (30 and 75) nm

ITO-based CSCs. An interface effect is the reason for the fast degradation. Employing the highly doped PEDOT:PSS ensures an ohmic contact to ITO as well as to the α-6T. If the PEDOT:PSS is missing, already small changes in the energy levels generate energetic barriers. Either a change in the ITO workfunction or a decomposition of interfacial α-6T molecules – both due to constant illumination – is able to create an extraction barrier. This barrier is visible in the IV curves (Fig. 8.19 right) as the current flow through the device is hindered as soon as the direction of current flow changes ($V > V_{OC}$).

Summarizing the results of the whole degradation study on cascade solar cells, the following conclusions can be drawn. First, the α-6T within this layer sequence seems to be intrinsically unstable, at least under a continuous illumination and moderate temperatures. A maximum lifetime D_{50} lower than 500 h is measured. At the current state of investigation, it seems questionable whether this particular solar cell stack is applicable to a real outdoor environment. This result needs to be proven with other

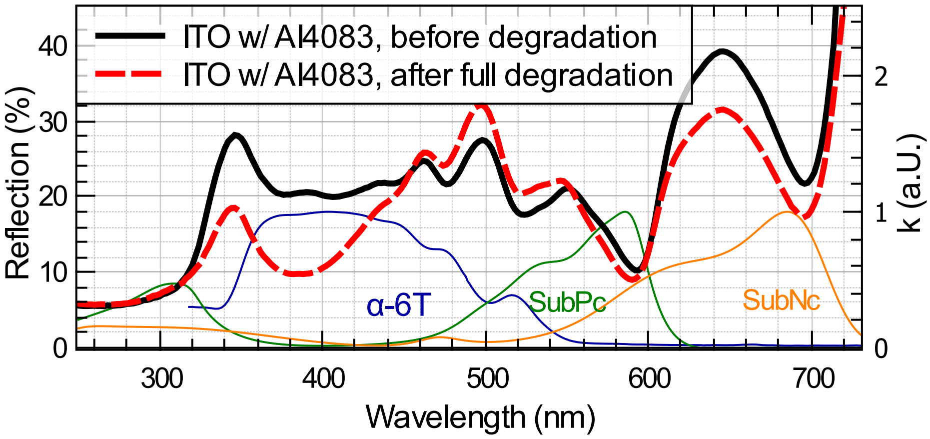

Figure 8.18.: Reflection measurements of a CSC device with 60 nm α-6T thickness before (solid line) and after degradation (dashed line). The thin solid lines show the normalized extinction coefficients k of α-6T, SubPc, and SubNc single thin-films.

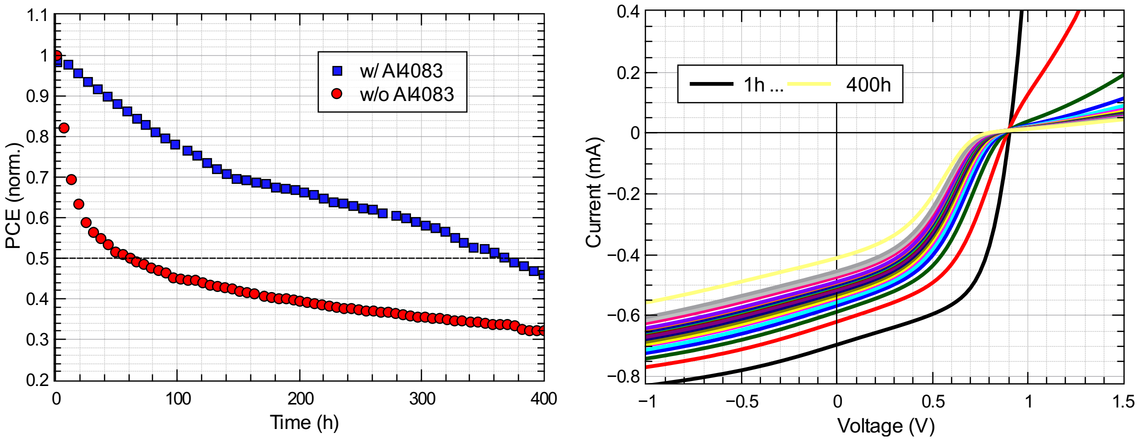

Figure 8.19.: Aging of CSCs on ITO with and without a layer of Al4083. **Left:** Normalized PCE. **Right:** IV curves of the CSC without Al4083, recorded at different aging times.

methodologies to get more insight on the molecular scale. Also the role of testing environment is not fully clarified, as solar cells are kept at open-circuit condition between the measurements. This is far away from a real situation where the solar cell is driven at the maximum power point for the whole operation time span.

Second, PEDOT:PSS is needed within the layer architecture to ensure a barrier-free charge carrier transport. On the other hand, PEDOT:PSS leads to a significant worsening of the flexible NOA63/AgNW electrode which results in a very short lifetime of these devices of only 30 h. Here, the use of pH-neutral PEDOT:PSS could improve the stability as well as a change to different hole transport layers, e. g. by using small molecules. First attempts are made replacing PEDOT:PSS by MeO-TPD or BF-DPB, but the efficiency stays behind those with PEDOT:PSS.

8.5. DCV5T-Me Solar Cells on NOA63/AgNW Electrodes [11]

In the previous section, it was shown that cascade organic solar cells with α-6T lack intrinsic stability leading to short lifetimes D_{50} of smaller than 500 h in a glass-glass encapsulated environment. On NOA63/AgNW electrodes, the lifetime is only 40 h. This effect is referred to a degradation related to the acidic PEDOT:PSS. However, PEDOT:PSS is a necessary layer in this device configuration to achieve high efficiencies. Moreover, the pPEN substrate reduces the j_{SC} due to an unfavorable overlap of EQE spectrum and pPEN absorption.

To circumvent these three issues, the material system is changed from a cascade architecture to a proven bulk heterojunction. As absorbing system, the small molecules DCV5T-Me and C_{60} are used as donor and acceptor, respectively (cf. Section 7.2.5 in Chapter 7). Three improvements in the device are expected: first, the DCV5T-Me:C_{60} system is highly efficient yielding efficiencies up to 9.5 % [72] and is known to be a stable material system. Second, the spectral EQE distribution is shifted more to the range of 400 to 700 nm. Thus, pPEN absorption below 400 nm has a much smaller impact on a reduced charge carrier generation. Third, there is no need to incorporate PEDOT:PSS in the layer sequence: vacuum-deposited small molecule materials can be used in the whole organic stack. This should solve stability issues connected to the acidity and hydrophilicity of PEDOT:PSS.

8.5.1. Organic Solar Cell Fabrication and Characterization

Organic solar cells are prepared according to the schematic layer stack in Figure 8.20 (left). NOA63/AgNW electrodes with NW35 and NW90 are employed as flexible transparent electrodes and bottom-encapsulated with pPEN/AlO_x. Organic solar cells with and without a PEDOT:PSS interlayer are fabricated to study its influence on device performance and lifetime. ITO on glass substrates serves as reference electrode and bottom encapsulation. The NOA63/AgNW electrodes including the pPEN/AlO_x barrier have a transmission T_{vis} and a sheet resistance R_{S} of $(77 \pm 7)\,\%$, $(17.5 \pm 0.5)\,\Omega/\square$ (NW35) and $(79 \pm 4)\,\%$, $(14.5 \pm 0.5)\,\Omega/\square$ (NW90). PEDOT:PSS reduces T_{vis} even further by 3 to 4 %. AgNW-based devices are top and bottom encapsulated with pPEN/AlO_x. For ITO-based devices, glass as bottom encapsulation and a getter-containing cavity glass or pPEN/AlO_x as top encapsulation is employed. jV curves of the illuminated devices and associated photovoltaic performance parameter are shown in Figure 8.20 (right) and Table 8.7, respectively. The ITO-based reference reaches a PCE of $(6.6 \pm 0.2)\,\%$ and $(7.0 \pm 0.1)\,\%$ with glass and pPEN/AlO_x top encapsulation, respectively. Small differences in V_{OC} and FF are caused by processing deviations. As in the case of

---

[11] The findings of this section are published in [4].

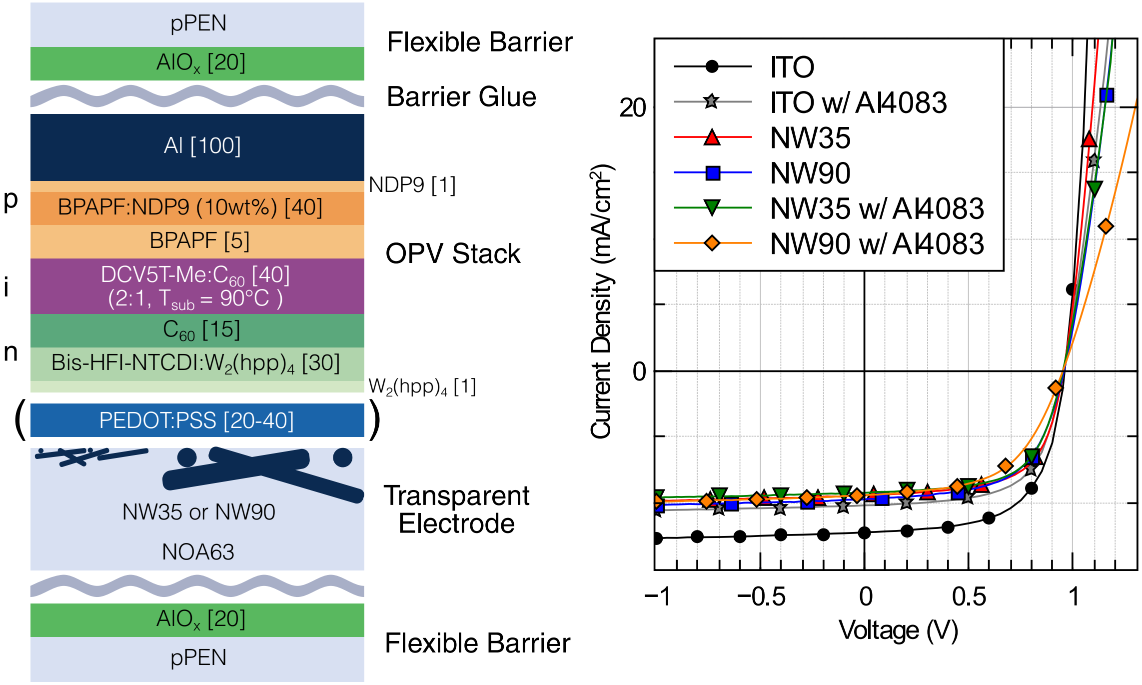

Figure 8.20.: Left: Schematic layer stack of flexible OSCs on NOA63/AgNW with pPEN/AlO$_x$ as top and bottom encapsulation. **Right:** jV curves of illuminated DCV5T-Me:C$_{60}$ solar cells on ITO, ITO with PEDOT:PSS, and NOA63/AgNW with NW90 or NW35.

cascade solar cells, the performance is not negatively influenced by the lamination of pPEN/AlO$_x$ barriers. By introducing a 20 nm thin interlayer of PEDOT:PSS (AI4083), the PCE is reduced by 13 % as compared to the reference. This loss is mainly caused by a reduced j_{SC}. The EQE spectra (Figure 8.21) shows that the spectrum is nearly similar to the reference in the spectral region up to 440 nm and is reduced by a maximum of 10 % above 440 nm.

The strong difference in j_{SC} between ITO and ITO/PEDOT:PSS devices might be explained with optical changes within the device due to the PEDOT:PSS layer. The reflection averaged from 424 to 700 nm (the spectral absorption region of DCV5T-Me) is (18 ± 2) % on bare ITO and only (12 ± 3) % on ITO/PEDOT:PSS. Back reflection at the transparent electrode leads to a microcavity effect which increases the absorption in the active layer and thus the j_{SC}.[153, 222] In case of ITO/PEDOT:PSS, a reduced reflectivity is observed, leading to a reduced absorption and j_{SC}.

On AgNW electrodes, PCEs of (5.6 ± 0.2) % (NW35) and (5.4 ± 0.1) % (NW90) are reached without PEDOT:PSS. By introducing the PEDOT:PSS layer, a reduced PCE of (5.4 ± 0.2) % (NW35) and (4.8 ± 0.2) % (NW90) is observed. Compared to ITO without PEDOT:PSS, the main loss mechanism is the j_{SC}. It is 16 to 19 % below the reference value. The pPEN absorption below 390 nm partly is responsible for it (cf. Fig. 8.21) and – as compared to cascade devices (cf. Fig. 8.13) – shows smaller losses in this region. However, distinct differences are present in the spectral region above 390 nm.

Table 8.7.: Photovoltaic performance parameters of DCV5T-Me:C_{60} solar cells on different transparent bottom electrodes. All AgNW-based devices are top and bottom encapsulated with pPEN/AlO_x. Top encapsulation for ITO-based devices is stated in brackets. For every solar cell type, 1 to 2 samples containing 4 devices each are prepared under identical conditions. The yield states the amount of working devices. Bracket values are always the highest measured within this category.

Type	j_{SC} (mA/cm^2)	V_{OC} (mV)	FF (%)	PCE (%)	Yield
ITO (glass)	11.5 ± 0.2	960 ± 1	60 ± 2	6.6 ± 0.2	3/4
	(11.6)	(961)	(62.3)	(6.8)	
ITO (pPEN/AlO_x)	11.7 ± 0.1	969 ± 1	62.3 ± 0.2	7.0 ± 0.1	4/4
	(11.7)	(969)	(62.5)	(7.1)	
ITO w/ AI4083 (glass)	10.2 ± 0.1	959 ± 1	61 ± 2	6.0 ± 0.2	8/8
	(10.23)	(961)	(63.3)	(6.2)	
NOA63/NW35	9.3 ± 0.4	955 ± 1	63.5 ± 0.3	5.6 ± 0.2	8/8
	(9.5)	(955)	(64.1)	(5.7)	
NOA63/NW90	9.7 ± 0.1	955 ± 1	59 ± 1	5.4 ± 0.1	6/8
	(9.8)	(957)	(59.8)	(5.6)	
NOA63/NW35 w/ AI4083	9.2 ± 0.1	952 ± 1	62 ± 2	5.4 ± 0.2	8/8
	(9.3)	(953)	(63.0)	(5.6)	
NOA63/NW90 w/ AI4083	9.4 ± 0.1	952 ± 1	53 ± 2	4.8 ± 0.2	8/8
	(9.7)	(953)	(55.3)	(5.0)	

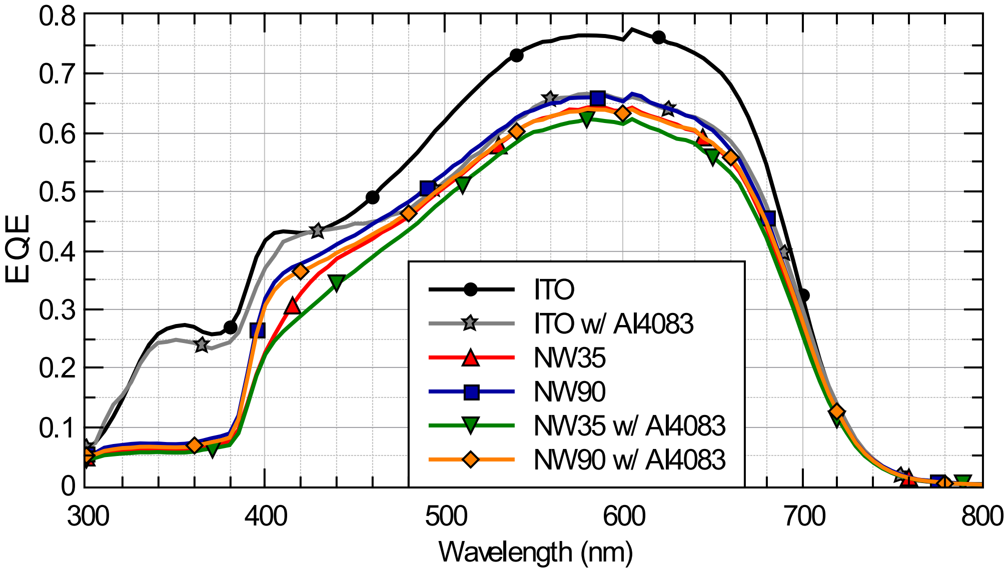

Figure 8.21.: External quantum efficiency of DCV5T-Me:C_{60} solar cells on ITO or AgNW (NW35 or NW90) electrodes, with and without PEDOT:PSS (AI4083).

Two reasons for the j_{SC} loss are assumed. The overall electrode transmission T_{vis} is below 80 % for the flexible electrodes which reduces the amount of light entering the device. Furthermore, the specular reflection in the relevant spectral region (400 to 700 nm) is determined to be (5.5 ± 0.2) %. Considering the microcavity effect previously discussed, a further reduced j_{SC} is reasonable.

The FF on NW35 is about 2 to 4 % better as compared to ITO due to a lower R_S of the electrode. At the same time, the NW90 electrode – which has the lowest R_S – exhibits lowest FF values of (59 ± 1) % and (53 ± 2) % with NW90 and NW90/PEDOT:PSS, respectively. A possible explanation of this behavior is given earlier in this thesis in Chapter 7, Section 7.2.4. The NW90 electrode exhibits large voids between the nanowires in the µm^2 range. They are much larger than on NW35. If the conductivity of the adjacent charge transport material is too low, charges are inefficiently transported to the highly conductive AgNW network. Doped Bis-HFl-NTCDI exhibits a conductivity of 2×10^{-4} S/cm (cf. Table 7.5 on p. 107). This is the crucial conductivity regime at which losses in FF and j_{SC} emerge.[6] However, it is contradictory that the sample with PEDOT:PSS exhibits a lower FF, as its conductivity should compensate the losses. In this case, it is assumed that accelerated degradation (see following Section 8.5.2) already reduced the device performance significantly.

8.5.2. Degradation in Illuminated 38 °C/50 % Climate

All organic solar cells investigated within this section exhibit a good initial performance. However, device efficiency is only one issue being adressed for improvement as compared to the cascade solar cells. The second big issue has been the very short lifetime of all devices in general, but especially the lifetime of NOA/AgNW-based devices. The degradation of the organic solar cells discussed in the last section is now studied. After initial characterization, the devices are put into the climate cabinet (cf. Experimental Section 4.6) and aged at 38 °C/50 % RH under constant AM1.5G illumination (100 mW/cm^2). IV curves are recorded every hour. Normalized PCEs over time for devices on ITO, ITO with PEDOT:PSS, and NOA/AgNW devices with and without PEDOT:PSS are plotted in Figure 8.22.

Utilizing ITO as bottom electrode (Fig. 8.22 a) with glass or pPEN/AlO$_x$ encapsulation shows a degradation within the first 200 h which is smaller than 6 % as compared to the inital PCE. In the case of a glass-glass-encapsulated sample, mostly intrinsic degradation (cf. Section 2.2.4) pathways are seen as water and oxygen is kept away from the device as good as possible. The degradation without PEDOT:PSS is rather slow, stating that DCV5T-Me:C$_{60}$ is an intrinsically stable material system. Although only 200 h have been measured, studies have been performed showing good stability up to 1600 h with an extrapolated D_{50} of approximately 6800 h.[33] The degradation with the pPEN/AlO$_x$ barrier happens with similar speed. Thus, the flexible barrier protects the device properly from water ingress.

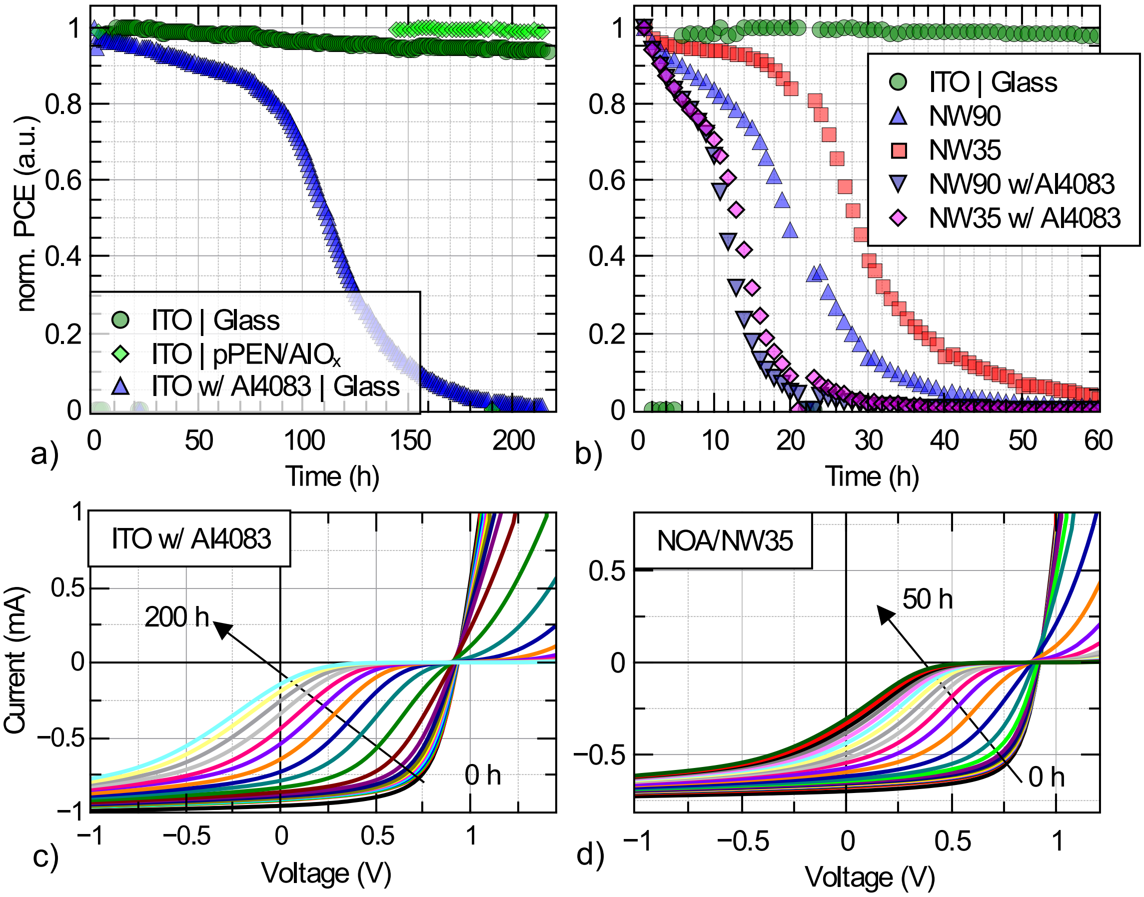

Figure 8.22.: Top: Normalized PCEs of DCV5T-Me:C_{60} devices over time in 38 °C/50 % RH climate. Samples are illuminated under AM1.5G conditions and 100 mW/cm^2 intensity. **a)** Devices on ITO and ITO with PEDOT:PSS (Al4083). **b)** Devices on NW35 and NW90 with and without Al4083. All nanowire electrodes are embedded in NOA63. **Bottom:** IV curves over time of **c)** ITO with PEDOT:PSS (10 h between curves) and **d)** NOA/NW35 without PEDOT:PSS (1 h between the curves).

With a PEDOT:PSS interlayer, devices age much faster such that D_{50} is reached already after 112 h. 98.5 % of the inital efficiency is lost after 200 h. Hence, PEDOT:PSS leads to a fast intrinsic degradation. This is already known for OPV and OLED devices [185, 246, 282] but occurs with a strong extent in this study. Several degradation mechanisms are possible: indium or PSS diffuses into the device or water uptake may reduce PEDOT:PSS conductivity. In the device, a formation of energetic barriers is visible in the IV curves of aged ITO/PEDOT:PSS samples (cf. Fig. 8.22 c). Deeper investigations of the exact cause are not performed within this study as it is not the primary scope.

On NOA/AgNW-based devices (Fig. 8.22 b), the situation looks quite different: OSCs without PEDOT:PSS exhibit D_{50} times of 29 h (NW35) and 20 h (NW90). With PEDOT:PSS, they degrade even faster within 12 to 14 h. IV curves (Figure 8.22 d) exhibit strong s-kinks.

Obviously, devices on NOA/AgNW electrodes degrade rather fast even without the use of PEDOT:PSS. Degradation speeds up further when introducing the PEDOT:PSS layer. It seems that the assumption within the scope of CSCs was only a part of the problem, as fast degradation persists without PEDOT:PSS. The *IV* curves (Fig. 8.22 d) suggest a barrier formation due to electrode degradation. To further analyze the cause of electrode breakdown, SEM images are acquired (Figure 8.23). Exemplarily, NOA/NW35 electrodes are aged in the same climate as OPV devices and compared to a freshly prepared one. As NOA63 is an UV-curable polymer, the effect of illumination is additionally investigated. One sample is thus protected against light incidence.

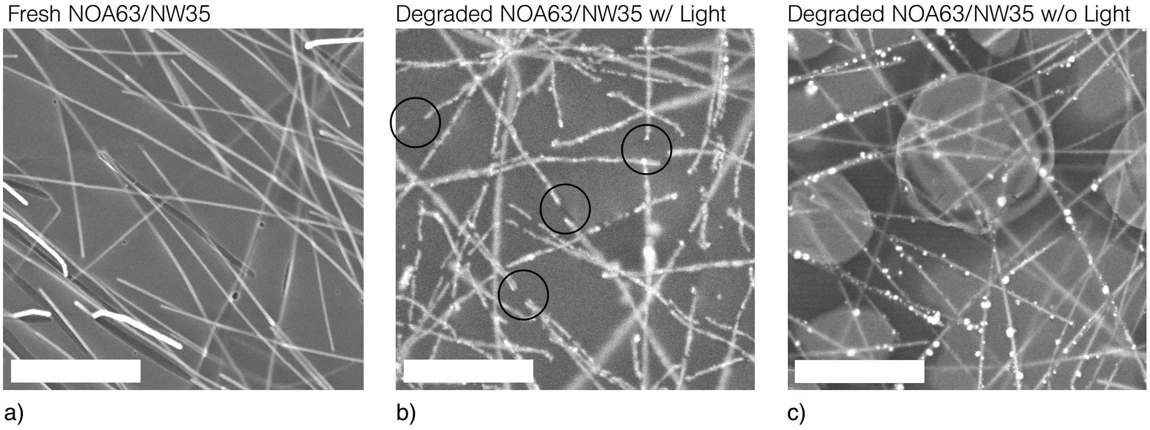

Figure 8.23.: SEM images of NW35 embedded in NOA63. **a)** Directly after deposition and peel-off. **b)** After one week of illumination in illuminated 38 °C/50 % RH climate. Exemplary areas are encircled where nanowires are detached from each other. **c)** After one week in climate but without illumination. The scalebars represent 1 µm.

Nanowires in the freshly prepared sample exhibit intact junctions and nanowires. In contrast, the degraded sample with light incidence shows many spots with destroyed nanowires. Over the entire area, nanowires have a grainy structure. If degradation happens without light incidence, a grainy structure is also visible, but the nanowires themselves are still intact. The SEM images substantiate the assumption of an electrode failure. The electrode decomposes and is destroyed under light incidence. Silver migration and transformation also cause the occurance of strong s-kinks in *IV* curves, as it changes the electrode surface. Although a complete understanding of these failure mechanisms is not achieved up to now, some conclusions are drawn. It is known that silver photooxidizes and photomigrates under light excitation.[98, 113] Additional sulfidization results in morphological changes in AgNWs during illumination possibly leading to this decomposition.[31] In an optoelectronic device, also electromigration of silver occurs, accelerating degradation processes.[86, 187] Furthermore, NOA is an UV-curable polymer containing mercapto esters. Incoming UV-light might additionally degrade NOA with reaction products causing silver nanowires to oxidize and sulfidize at further increased speed. Although many research groups have been using NOA for demonstrating working devices, the lifetime of NOA/AgNW-based devices has not been investigated until now. Nam et al. reported on the electrode stability with similar nanowires up to 16 d at 100 °C, 70 % *RH* but without illumination. With PEDOT:PSS present, its aciditiy and hydrophilicity adds another influence factor leading to further accelerated degradation.

8.6. Summary and Outlook

In this chapter, a planarization technique for silver nanowires is introduced whereby they are buried in an insulating polymer. This concept works well for the polymers polyimide and the optical glue 'NOA63' where a significant reduction of R_{rms} from 30 nm down to 1 to 2 nm is observed. The transmission $T_{\mathrm{t},550}$ and R_{S} for the best electrodes with NOA63/NW35 exhibit values up to 84.3 % and down to 17 Ω/□ proving excellent electrical and optical properties of this electrode type.
Further, the planarized AgNWs are employed as flexible bottom electrode in fully flexible organic solar cells and degradation studies under constant illumination and a climate of 38 °C/50 % *RH* are performed. A flexible and transparent moisture barrier consisting of 20 nm atomic layer deposited AlO_x is employed as top and bottom encapsulation which exhibits *WVTR*s down to $3 \times 10^{-5}\,\mathrm{g/(m^2\,d)}$. A fullerene-free cascade architecture and a DCV5T-Me:C_{60} bulk heterojunction are investigated as two different material systems for efficient charge generation. The cascade architecture yields efficiencies of 5.1 % for fully-flexible devices as compared to 7.0 % on ITO. Short lifetimes of <30 h and <500 h for flexible solar cells and fully glass-glass encapsulated ITO-based solar cells are obtained, respectively. A poor intrinsic stability of the α-6T is the reason for the fast degradation in case of glass-glass encapsulated ITO-based devices. A fast degradation of the NOA/AgNW/PEDOT:PSS composite is determined in fully-flexible cascade devices.
To circumvent the necessity of PEDOT:PSS and to increase efficiency and lifetime further, a DCV5T-Me:C_{60} bulk heterojunction is employed in an n-i-p solar cell which results in maximum efficiencies of 5.7 % and 7.2 % on AgNW and ITO electrodes, respectively. A decrease of the j_{SC} losses up to 5 % could be achieved due to a favorable OSC absorption spectrum in comparison to the cascade solar cell. ITO-based devices are reasonably stable, enabling extrapolated D_{50} lifetimes up to 6800 h. Nonetheless, D_{50}s of only (25 ± 5) h on NOA/AgNW electrodes show that intrinsic instabilities are caused by UV-driven photooxidation and photomigration of silver and not only due to PEDOT:PSS contact, as previously assumed.

Some further implications of this study are now discussed. The most challenging und least investigated issue is the low stability of NOA/AgNW electrodes under light incidence. Although stability investigations in humid air and under annealing suggest good stability,[57, 75] the influence of illumination seems to be tremendous and in case of organic solar cells inevitable. To the best of our knowledge, no study has investigated device degradation with this kind of electrode although many groups are using NOA63 as embedding polymer.[23, 56, 75]

Straightforward, a protection against UV light might improve the stability of AgNW electrode and plastic substrates. A possible degradation caused by the NOA63 might be solved by exchanging the polymer with alternatives like polyimide (as demonstrated) or other polymers. Moreover, the AgNWs could be protected by a thin layer of a metal oxide deposited prior to the spin coating of the polymer. This oxide layer would prevent direct contact between polymer and AgNWs without affecting electrical contact to subsequent organic layers. This principle has been shown already by Spechler et al. but they do not comment on longterm stability.[40] Another task is the optimization of the optical properties of AgNW electrode with a moisture barrier. The transmission needs to be increased, for example by omitting the second substrate for the AlO_x barrier layer. Moreover a careful adjustment of the specular electrode reflection would make use of the microcavity effect, improving active layer absorption.

The findings within this study show highest efficiencies reported up to now for small molecule devices on silver nanowires to best of our knowledge. As a first step towards competitive OPV, the material system enables large area roll-to-roll-processing and low production cost.

Part IV.

Conclusions and Future Prospects

9. Conclusions

In this thesis, the implementation of a novel transparent bottom electrode into various organic solar cell (OSC) types is investigated.

The transparent electrode consists of percolative silver nanowire (AgNW) networks that offer a high optical transparency T_t up to $(86 \pm 1)\,\%$ over the visible wavelength regime, including the glass substrate. Concurrently, sheet resistance values reach down to $(14 \pm 1)\,\Omega/\square$. These values are higher than commercially available indium tin oxide (ITO) electrodes.

Silver nanowires outperform ITO in some other aspects. First, they can be produced utilizing a simple and fast bottom-up synthesis. Second, electrode fabrication is carried out using solution-based deposition methods like spin or spray coating. Thus, transfer to large scale roll-to-roll processes is easily possible. Third, inherent flexibility of AgNW networks enables fabrication of fully-flexible organic devices.

Despite their advantages, AgNWs exhibit a high surface roughness and steep edges. An implementation as bottom electrode in thin-film OSCs is challenging. In order to avoid electrical shunt paths and short circuits, the AgNW electrodes need to be planarized. In this thesis, two different planarization approaches are investigated in detail.

Doped, Solution-Processed Small Molecule Charge Carrier Transport Layers

One core competence of the IAPP is the fabrication of small molecule organic solar cells via thermal deposition in an ultra-high vacuum. However, this directional deposition method is hardly capable of planarizing AgNW electrodes. The first approach investigated within this work introduces the transfer of the small molecule materials from vacuum-based to solution-based deposition techniques. Three different small molecule charge carrier transport layers are tested: BF-DPB[1] and Spiro-TTB[2] as the hole transport layer (HTL), and NTCDA[3] as the electron transport layer (ETL). Moreover, doping is necessary to increase the intrinsically low conductivity of the HTL/ETL.

Tetrahydrofuran is found as organic solvent for both HTL materials. It dissolves the materials up to a concentration of 10 mg/ml. Spin-coated layers of matrix BF-DPB and the proprietary dopant NDP9 exhibit conductivities up to $5 \times 10^{-4}\,\mathrm{S/cm}$ at $10\,\mathrm{wt}\%$

---

[1] N,N'-((diphenyl-N,N'-bis)9,9,-dimethyl-fluoren-2-yl)-benzidine

[2] 2,2',7,7'-tetra(N,N-ditolyl)amino-9,9-spiro-bifluorene

[3] 1,4,5,8-napthalenetetracarboxylic dianhydride

doping concentration, which are similar to thermally evaporated reference films. As small molecule doping in solution is rather uncommon, this process is investigated by means of optical spectroscopy. The formation of a hybrid molecule complex between host and dopant in THF is observed, proving the functionality of the doping process even from solutions.

Efficient small molecule OSCs with DCV5T-Me[4]:C_{60} as absorbing layer are fabricated with AgNW bottom electrodes. They reach efficiencies up to 4.4 % on AgNW electrodes in comparison to 4.1 % on ITO with identically fabricated HTLs.

Moreover, the effect of HTL conductivity on the macroscopic device performance is investigated. It is found that the square micrometer large voids within the AgNW network necessitate a minimum HTL conductivity of approximately 1×10^{-4} S/cm to prevent macroscopic efficiency losses. The results are confirmed by equivalent circuit simulations. This finding is of great importance for further studies on AgNW electrodes with low conductive organic charge carrier transport layers, as a careful tradeoff between network void size and HTL conductivity needs to be chosen.

With spin-coated Spiro-TTB:NDP9 hole transport layers, methylammonium lead iodide perovskite solar cells are fabricated. They exhibit an efficiency of (9 ± 1) % on ITO, which is similar to reference perovskite solar cells with evaporated Spiro-TTB HTL. Although the AgNW planarization with Spiro-TTB is similar to BF-DPB, a working perovskite solar cell on AgNWs is not achieved. Most likely, the perovskite layer growth on the AgNW topography failed.

On the ETL side, NTCDA is tested with a dimeric n-dopant. Both materials dissolve in dimethylformamide (DMF) and exhibit insolubility in chlorobenzene and probably other halogenated solvents. Therefore, NTCDA is suitable as ETL in n-i-p polymer solar cells. The applicability in devices is successfully demonstrated with solution-processed PTB7[5]:$PC_{71}BM$[6] solar cells, yielding power conversion efficiencies (PCEs) of (7.7 ± 0.3) % as compared to reference devices with PCEs of 8.8 %. The solution-processed NTCDA layers exhibit reduced roughness in comparison to evaporated NTCDA films. Implemented in evaporated n-i-p ZnPc[7]:C_{60} solar cells, a PCE of 2.3 % is obtained. Solution-processed NTCDA layers on AgNW electrodes do not show a planarization effect due to low layer thicknesses and an unfavorable surface wettability.

In summary, several solution-processed small molecule charge carrier transport layers are succesfully implemented in various organic solar cells. Using spin-coated HTLs on top of the AgNW bottom electrodes, additional planarization layers like PEDOT:PSS are made obsolete.

---

[4] 2,2-((3,4-dimethyl-[2,2:5,2:5,2:5,2-quinquethiophene]-5,5-diyl)bis(methanylylidene))dimalononitrile

[5] poly((4,8-bis[(2-ethylhexyl)oxy]benzo[1,2-b:4,5-b']dithiophene-2,6-diyl)(3-fluoro-2-[(2-ethylhexyl)carbonyl]thieno[3,4-b]thiophenediyl))

[6] phenyl C_{71} butyric acid methyl ester

[7] zinc phtalocyanine

Silver Nanowires Buried in an Insulating Polymer

The second planarization approach utilizes the embedment of AgNW electrodes in an insulating polymer. Polydimethylsiloxane (PDMS), polyimide, and an optical adhesive (NOA63) are tested as polymers for this purpose. The best achievements are obtained with NOA63, which results in a flexible, transparent, ultrathin, and highly conductive substrate of only 50 µm thickness. Sheet resistance values of $(14 \pm 1)\,\Omega/\square$ and averaged transmission over the visible part of the spectrum of $(84 \pm 2)\,\%$ are obtained, leading to Φ_{De} values up to 250. The high initial roughness of AgNW electrodes is dramatically reduced to R_{rms} values of $(2 \pm 1)\,\mathrm{nm}$, proving the exceptional planarization capabilities of this approach.

This type of transparent electrode is implemented in two different organic solar cell configurations. To further evaluate the applicability of this approach for future commercialization purposes, stability investigations are carried out under continuous illumination in a humid climate. Therefore, the devices are encapsulated with a flexible alumina thin-film, which serves as a diffusion barrier against moisture ingress.

On NOA63/AgNW electrodes, fullerene-free cascade organic solar cells with sexithiophene (α-6T) as donor are fabricated. They yield efficiencies of 5.6 % and 5.0 % with glass as encapsulation and as fully-flexible, encapsulated device, respectively. Glass-encapsulated reference devices on ITO exhibit PCEs of $(6.6 \pm 0.1)\,\%$. Furthermore, the efficiencies of fully-flexible encapsulated DCV5T-Me:C_{60} solar cells on NOA/AgNW electrodes are $(5.6 \pm 0.2)\,\%$, compared to $(6.6 \pm 0.2)\,\%$ on rigid samples utilizing ITO. The performance loss on NOA/AgNW electrodes is attributed to two effects: first, a reduced transmission of flexible encapsulation and electrode leads to a lower light intensity within the active layer and thus to a lower short circuit current density. Second, a lower reflection of the NOA/AgNW electrode in comparison to the ITO electrode reduces absorption further due to a reduced microcavity effect.

Device stability investigations reveal more insight into intrinsic and extrinsic degradation mechanisms. It is shown that cascade organic solar cells with α-6T lack intrinsic stability, as glass-encapsulated devices degrade to 80 % of their initial PCE within 300 h. α-6T is identified as the driving force behind the fast degradation. The DCV5T-Me:C_{60} solar cells prove good intrinsic stability greater than 1600 h. Tthe high quality of the flexible encapsulation is demonstrated, as a similar degradation behavior is observed by the alumina-encapsulated devices.

However, all fully-flexible encapsulated devices on NOA/AgNW fail within one to two days of operation. Here, several mechanisms are leading to this fast degradation: first, acidic PEDOT:PSS, which is included in the cascade solar cell stack, deteriorate the interface to the electrode. Then, silver is known to photo- and electromigrate, and it oxidizes in the presence of UV light. Further sulfurization of silver is assumed to take place.

In conclusion, highly efficient, fully-flexible, encapsulated, and ITO-free devices are fabricated with this planarization approach. Taking the aspect of electrode processing into account, upscaling to roll-to-roll processes is possible, as all fabrication steps are either solution-based or exclude high temperature treatment. Nevertheless, the operational stability of these devices is an unresolved issue up to now, with little research currently devoted to it.

If the aforementionend issues are solved, silver nanowire electrodes have the potential of replacing ITO as the industry-standard in many aspects. Performance, mechanical stability, low processing and material cost, and simple synthesis are key advantages of this technology that ITO can hardly provide.

10. Future Prospects

Efficiency of AgNW-Based Organic Solar Cells

Nearly all AgNW-based organic solar cells in this work exhibit a slightly lower power conversion efficiency in comparison to their ITO-based reference devices. The reason for this discrepancy has been determined to arise from optical considerations, as the electrical performance of AgNW-based devices is superior to those on ITO. Two possible approaches shall improve the device performance. The discussion takes place with regard to the findings in Chapter 8 where the AgNWs are buried in an insulating polymer.

1. The transmission of the whole electrode, which also includes the substrate, has to be optimized, especially in the case of utilizing the flexible alumina barrier. In the experiments presented in this thesis, the alumina layer needed to be implemented with an additional pPEN substrate, which caused additional parasitic absorption over the whole spectral range. An implementation of the barrier deposition directly into the electrode fabrication process, as depicted in Figure 10.1, would bypass the need for an additional substrate. Further minimization of substrate absorption would also be helpful, e. g. by successfully utilizing highly transparent polymers like PDMS or further reducing the substrate thickness.
2. As discussed in Section 8.5.1, the low specular reflection of AgNW-based electrodes hinders a strong development of the microcavity effect which occurs in ITO-based devices. Especially for thin absorbing layers, which are common in small molecule organic solar cells in contrast to polymer solar cells, the microcavity effect enhances the active layer absorption. Therefore, the insertion of an additional reflection layer between OSC and AgNWs could improve the microcavity effect in AgNW-based devices. A sketch is shown in Figure 10.2. Of course, it has to be taken care of the reflection strength, as light is also reflected before entering the device. Experiments with transparent metal films as electrode, performed by Dr. F. Nehm (IAPP) and published in [4], suggest that an electrode transmission of $(61 \pm 6)\,\%$ with a specular reflection of $(27 \pm 7)\,\%$ is sufficient to generate similar short circuit current densities as ITO-based reference devices.

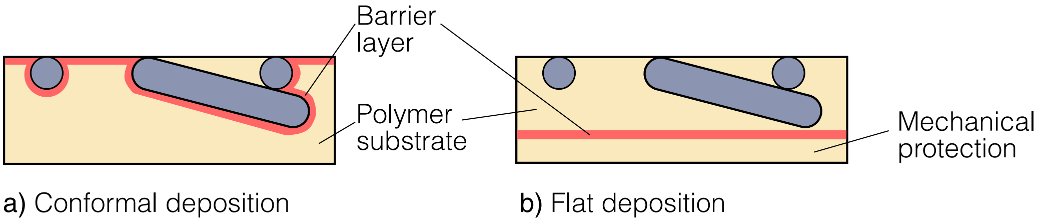

Figure 10.1.: Sketch for the implementation of the barrier. **a)** Using conformal deposition techniques like atomic layer deposition, the barrier may be deposited directly below the AgNWs. The substrate serves as mechanical protection at the same time. **b)** For flat layer deposition, the barrier may be inserted in the electrode fabrication processes as depicted here. The mechanical protection may be very thin and should consist of the same material as the polymer substrate or another highly transparent material.

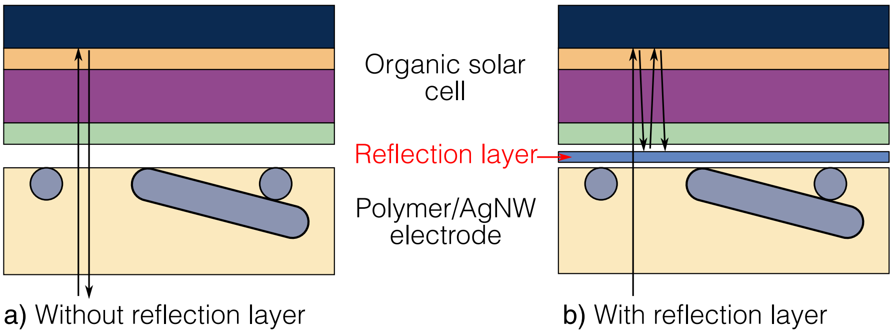

Figure 10.2.: Impact of a thin reflection layer on the light management in an organic solar cell. **a)** Without reflection layer. The light enters the solar cell and leaves it again after one reflection. **b)** With semitransparent reflection layer. The light enters the solar cell and is reflected again before leaving the device.

Stability of AgNW-Based Devices

The second issue concerns the stability of AgNW-based OSCs under operation. As shown in Section 8.4.2 and 8.5.2, the lifetime of these devices is extremely short. Consequently, approaches have to be implemented to increase stability.

1. Intrinsic stability of the silver nanowires could be improved by modifying their material. For example, Kim et al. showed increased stability of silver-nickel alloys in application of a metal grid.[65] This approach might be transferred to nanowire networks by synthesizing silver-nickel nanowires. AgNi nanowires have already been demonstrated by McKiernan et al., but not in the scope of OSC stability.[204]
2. Another approach might be the insertion of a conformally deposited metal oxide, as shown in Figure 10.1 a). It could prevent direct contact of the sulfur containing polymer and thus reduce the possibility of sulfurization. Also here, attempts are reported in literature by Spechler et al.[40] They use a titania sol-gel layer between the AgNWs and the polymer (polyimide in their case). However, stability

investigations were not carried out.

3. UV light is a crucial source of degradation, especially in polymers, which are used in OSCs as substrate, electrode, or active organic layers. On the one hand, it would be favorable to keep the UV light out of the device by adding a UV filter. However, this approach cuts off a significant portion of light, possibly leading to a reduced performance. On the other hand, UV-stable materials might be used. This could be reached by avoiding polymers as far as possible, or using only UV-stable polymers.

In summary, the aforementioned aspects need to be considered in future research to mature the promising technology of silver nanowire electrodes.

Appendix

Bibliography

[1] *Heliatek Press Release 02/16*. URL: http://www.heliatek.com/en/press/press-releases/details/heliatek-sets-new-organic-photovoltaic-world-record-efficiency-of-13-2 (visited on 02/08/2016) (see pp. 16, 29).

[2] *NOA63 information sheet*. URL: https://www.norlandprod.com/adhesives/noa%2063.html (visited on 07/10/2015) (see pp. 120, 122).

[3] D. Bi, W. Tress, M. I. Dar, P. Gao, J. Luo, C. Renevier, K. Schenk, A. Abate, F. Giordano, J.-P. Correa Baena, J.-D. Decoppet, S. M. Zakeeruddin, M. K. Nazeeruddin, M. Gra tzel, and A. Hagfeldt. "Efficient Luminescent Solar Cells based on Tailored Mixed-Cation Perovskites". *Science Advances* 2.1 (Jan. 2016). DOI: 10.1126/sciadv.1501170 (see p. 31).

[4] L. Bormann, F. Nehm, L. Sonntag, F.-Y. Chen, F. Selzer, L. Müller-Meskamp, A. Eychmüller, and K. Leo. "Degradation of Flexible, ITO-Free Oligothiophene Organic Solar Cells". *ACS Applied Materials & Interfaces* 8.23 (2016). DOI: 10.1021/acsami.6b02363 (see pp. 140, 154).

[5] L. Bormann, F. Nehm, N. Weiß, V. C. Nikolis, F. Selzer, A. Eychmüller, L. Müller-Meskamp, K. Vandewal, and K. Leo. "Degradation of Sexithiophene Cascade Organic Solar Cells". *Advanced Energy Materials* 6.9 (2016). DOI: 10.1002/aenm.201502432 (see p. 129).

[6] L. Bormann, F. Selzer, N. Weiß, D. Kneppe, K. Leo, and L. Müller-Meskamp. "Doped Hole Transport Layers Processed from Solution: Planarization and Bridging the Voids in Noncontinuous Silver Nanowire Electrodes". *Organic Electronics* 28 (2016). DOI: 10.1016/j.orgel.2015.10.007 (see pp. 49, 83, 143).

[7] C. R. Chu, C. Lee, J. Koo, and H. M. Lee. "Fabrication of sintering-free flexible copper nanowire/polymer composite transparent electrodes with enhanced chemical and mechanical stability". *Nano Research* (May 2016). DOI: 10.1007/s12274-016-1105-y (see p. 48).

[8] H. F. Dam. *Spin Coating*. 2016. URL: http://plasticphotovoltaics.org/lc/lc-fabrication/lc-coating/lc-spin.html (visited on 04/03/2016) (see p. 25).

[9] B. Dudley. *British Petroleum Statistical Review of World Energy*. Technical Report. British Petroleum, 2016, pp. 1–48 (see p. 1).

[10] J. Idier, W. Neri, C. Labrugère, I. Ly, P. Poulin, and R. Backov. “Modified silver nanowire transparent electrodes with exceptional stability against oxidation”. *Nanotechnology* 27.10 (Mar. 2016). DOI: `10.1088/0957-4484/27/10/105705` (see p. 59).

[11] D. Jacobs, K. Catchpole, F. Beck, and T. White. “A Re-Evaluation of Transparent Conductor Requirements for Thin-Film Solar Cells”. *J. Mater. Chem. A* 4 (2016). DOI: `10.1039/C6TA01670G` (see p. 39).

[12] W.-Y. Jin, R. T. Ginting, S.-H. Jin, and J.-W. Kang. “Highly Stable and Efficient Inverted Organic Solar Cells Based on Low-Temperature Solution-Processed PEIE and ZnO Bilayers”. *J. Mater. Chem. A* 4 (2016). DOI: `10.1039/C6TA00957C` (see p. 17).

[13] J. Kang, C.-G. Park, S.-H. Lee, C. Cho, D.-G. Choi, and J.-Y. Lee. “Fabrication of high aspect ratio nanogrid transparent electrodes via capillary assembly of Ag nanoparticles”. *Nanoscale* (2016). DOI: `10.1039/C6NR01896C` (see p. 46).

[14] J. Kim, W. J. da Silva, A. R. bin Mohd Yusoff, and J. Jang. “Organic devices based on nickel nanowires transparent electrode”. *Scientific Reports* 6.October 2015 (Jan. 2016). DOI: `10.1038/srep19813` (see p. 48).

[15] R. Meerheim, C. Körner, B. Oesen, and K. Leo. “10.4% Efficient triple organic solar cells containing near infrared absorbers”. *Applied Physics Letters* 108.10 (2016). DOI: `10.1063/1.4943653` (see pp. 16, 29).

[16] I. Salzmann, G. Heimel, M. Oehzelt, S. Winkler, and N. Koch. “Molecular Electrical Doping of Organic Semiconductors: Fundamental Mechanisms and Emerging Dopant Design Rules”. *Accounts of Chemical Research* 49.3 (Mar. 2016). DOI: `10.1021/acs.accounts.5b00438` (see p. 14).

[17] F. Selzer, C. Floresca, D. Kneppe, L. Bormann, C. Sachse, N. Weiß, A. Eychmüller, A. Amassian, L. Müller-Meskamp, and K. Leo. “Electrical limit of silver nanowire electrodes: Direct measurement of the nanowire junction resistance”. *Applied Physics Letters* 108.16 (Apr. 2016). DOI: `10.1063/1.4947285` (see p. 56).

[18] M. C. Suh, B. Pyo, and H. S. Kim. “Suppression of the viewing angle dependence by introduction of nanoporous diffuser film on blue OLEDs with strong microcavity effect”. *Organic Electronics* 28 (2016). DOI: `10.1016/j.orgel.2015.10.014` (see p. 125).

[19] J. Zhao, Y. Li, G. Yang, K. Jiang, H. Lin, H. Ade, W. Ma, and H. Yan. “Efficient Organic Solar Cells Processed From Hydrocarbon Solvents”. *Nature Energy* 1.2 (Jan. 2016). DOI: `10.1038/nenergy.2015.27` (see pp. 16, 30).

[20] D. Bryant, S. Wheeler, B. C. O'Regan, T. Watson, P. R. Barnes, D. A. Worsley, and J. Durrant. "Observable Hysteresis at Low Temperature in 'Hysteresis Free' Organic-Inorganic Lead Halide Perovskite Solar Cells". *The Journal of Physical Chemistry Letters* (2015). DOI: `10.1021/acs.jpclett.5b01381` (see p. 104).

[21] T. Cheng, Y. Zhang, W. Lai, Y. Chen, and W. Huang. "A rapid synthesis of high aspect ratio silver nanowires for high-performance transparent electrodes". *Chinese Journal of Chemistry* 33.1 (2015). DOI: `10.1002/cjoc.201400518` (see p. 55).

[22] S. Collavini, S. F. Völker, and J. L. Delgado. "Understanding the Outstanding Power Conversion Efficiency of Perovskite Based Solar Cells". *Angewandte Chemie International Edition* JUNE (2015). DOI: `10.1002/anie.201505321` (see p. 32).

[23] Y.-H. Duan, Y. Duan, X. Wang, D. Yang, Y.-Q. Yang, P. Chen, F.-B. Sun, K.-W. Xue, and Y. Zhao. "Highly flexible peeled-off silver nanowire transparent anode using in organic light-emitting devices". *Applied Surface Science* 351 (Oct. 2015). DOI: `10.1016/j.apsusc.2015.05.161` (see p. 147).

[24] L. K. Jagadamma, M. Al-Senani, A. El-Labban, I. Gereige, G. O. Ngongang Ndjawa, J. C. D. Faria, T. Kim, K. Zhao, F. Cruciani, D. H. Anjum, M. A. McLachlan, P. M. Beaujuge, and A. Amassian. "Polymer Solar Cells with Efficiency >10% Enabled via a Facile Solution-Processed Al-Doped ZnO Electron Transporting Layer". *Advanced Energy Materials* 5.12 (June 2015). DOI: `10.1002/aenm.201500204` (see pp. 30, 109).

[25] J. Jiu, J. Wang, T. Sugahara, S. Nagao, M. Nogi, H. Koga, and K. Suganuma. "Reliability of silver nanowire transparent electrode under atmospheric environment". In: *2015 IEEE 15th International Conference on Nanotechnology (IEEE-NANO)*. IEEE, July 2015, pp. 1390–1393. DOI: `10.1109/NANO.2015.7388896` (see p. 59).

[26] D. Kaduwal. "Roll-to-Roll Processing of ITO-free Organic Solar Cells". PhD Thesis. Albert-Ludwigs-Universität Freiburg im Breisgau, 2015 (see p. 27).

[27] B. Kan, M. Li, Q. Zhang, F. Liu, X. Wan, Y. Wang, W. Ni, G. Long, X. Yang, H. Feng, Y. Zuo, M. Zhang, F. Huang, Y. Cao, T. P. Russell, and Y. Chen. "A Series of Simple Oligomer-like Small Molecules Based on Oligothiophenes for Solution-Processed Solar Cells with High Efficiency". *Journal of the American Chemical Society* 137.11 (Mar. 2015). DOI: `10.1021/jacs.5b00305` (see p. 29).

[28] S. Kang, T. Kim, S. Cho, Y. Lee, A. Choe, B. Walker, S.-J. Ko, J. Y. Kim, and H. Ko. "Capillary Printing of Highly Aligned Silver Nanowire Transparent Electrodes for High-Performance Optoelectronic Devices". *Nano Letters* 15.12 (Dec. 2015). DOI: 10.1021/acs.nanolett.5b03019 (see pp. 48, 49, 57).

[29] Y. Kim, T. I. Ryu, K.-H. Ok, M.-G. Kwak, S. Park, N.-G. Park, C. J. Han, B. S. Kim, M. J. Ko, H. J. Son, and J.-W. Kim. "Inverted Layer-By-Layer Fabrication of an Ultraflexible and Transparent Ag Nanowire/Conductive Polymer Composite Electrode for Use in High-Performance Organic Solar Cells". *Advanced Functional Materials* 25.29 (Aug. 2015). DOI: 10.1002/adfm.201501046 (see pp. 48, 58).

[30] D. Langley. "Silver nanowire networks : effects of percolation and thermal annealing on physical properties". PhD Thesis. Grenoble University, 2015 (see pp. 51, 57).

[31] C. Mayousse, C. Celle, A. Fraczkiewicz, and J.-p. Simonato. "Stability of Silver Nanowire based Electrodes under Environmental and Electrical Stresses". *Nanoscale* 7 (2015). DOI: 10.1039/c4nr06783e (see pp. 45, 57, 59, 145).

[32] D. Nanova, M. Scherer, F. Schell, J. Zimmermann, T. Glaser, A. K. Kast, C. Krekeler, A. Pucci, W. Kowalsky, R. R. Schröder, and R. Lovrinčić. "Why Inverted Small Molecule Solar Cells Outperform Their Noninverted Counterparts". *Advanced Functional Materials* 25.41 (Nov. 2015). DOI: 10.1002/adfm.201502943 (see pp. 106, 114).

[33] F. Nehm. "Encapsulation and stability of organic devices upon water ingress". Dissertation. Technische Universität Dresden, 2015 (see pp. 32, 143).

[34] F. Nehm, H. Klumbies, C. Richter, A. Singh, U. Schroeder, T. Mikolajick, T. Mönch, C. Hoßbach, M. Albert, J. W. Bartha, K. Leo, and L. Müller-Meskamp. "Breakdown and Protection of ALD Moisture Barrier Thin Films". *ACS Applied Materials & Interfaces* 7.40 (Oct. 2015). DOI: 10.1021/acsami.5b06891 (see pp. 35, 129).

[35] K.-H. Ok, J. Kim, S.-R. Park, Y. Kim, C.-J. Lee, S.-J. Hong, M.-G. Kwak, N. Kim, C. J. Han, and J.-W. Kim. "Ultra-Thin and Smooth Transparent Electrode for Flexible and Leakage-Free Organic Light-Emitting Diodes". *Scientific Reports* 5 (2015). DOI: 10.1038/srep09464 (see p. 91).

[36] K.-T. Park, J. Park, J.-W. Park, and J. Hwang. "Maskless, site-selective, nanoaerosol deposition via electro-aerodynamic jet to enhance the performance of flexible Ag-grid transparent electrodes". *RSC Adv.* 5.56 (2015). DOI: 10.1039/C5RA04133C (see p. 46).

[37] B. Roth, G. A. Dos Reis Benatto, M. Corazza, R. R. Søndergaard, S. A. Gevorgyan, M. Jørgensen, and F. C. Krebs. "The critical choice of PEDOT:PSS additives for long term stability of roll-to-roll processed OPVs". *Advanced Energy Materials* 5.9 (2015). DOI: 10.1002/aenm.201401912 (see pp. 45, 57).

[38] F. Selzer. "Transparent Electrodes for Organic Solar Cells". Dissertation. TU Dresden, 2015 (see p. 48).

[39] F. Selzer, N. Weiß, D. Kneppe, L. Bormann, C. Sachse, N. Gaponik, A. Eychmüller, K. Leo, and L. Müller-Meskamp. "A Spray-Coating Process for Highly Conductive Silver Nanowire Networks as the Transparent Top-Electrode for Small Molecule Organic Photovoltaics". *Nanoscale* 7.6 (2015). DOI: 10.1039/c4nr06502f (see pp. 26, 49).

[40] J. A. Spechler, T. W. Koh, J. T. Herb, B. P. Rand, and C. B. Arnold. "A Transparent, Smooth, Thermally Robust, Conductive Polyimide for Flexible Electronics". *Advanced Functional Materials* (2015). DOI: 10.1002/adfm.201503342 (see pp. 147, 155).

[41] D. Spee, J. Rath, and R. Schropp. "Using hot wire and initiated chemical vapor deposition for gas barrier thin film encapsulation". *Thin Solid Films* 575 (Jan. 2015). DOI: 10.1016/j.tsf.2014.10.029 (see p. 34).

[42] D. M. Taylor. "Vacuum-thermal-evaporation: the route for roll-to-roll production of large-area organic electronic circuits". *Semiconductor Science and Technology* 30.5 (2015). DOI: 10.1088/0268-1242/30/5/054002 (see p. 27).

[43] J. Tian, C. Zhao, M. Wu, W. Xie, W. Mai, and P. Liu. *Thickness-dependence of S-shaped J-V curves of planar heterojunction organic solar cells containing NTCDA interlayer: Impedance-potential measurement and underlying mechanism*. 2015. DOI: 10.1016/j.solmat.2015.09.032 (see p. 106).

[44] M. L. Tietze, P. Pahner, K. Schmidt, K. Leo, and B. Lüssem. "Doped organic semiconductors: Trap-filling, impurity saturation, and reserve regimes". *Advanced Functional Materials* 25.18 (2015). DOI: 10.1002/adfm.201404549 (see p. 25).

[45] B.-Y. Wang, T.-H. Yoo, J. W. Lim, B.-I. Sang, D.-S. Lim, W. K. Choi, D. K. Hwang, and Y.-J. Oh. "Enhanced Light Scattering and Trapping Effect of Ag Nanowire Mesh Electrode for High Efficient Flexible Organic Solar Cell." *Small (Weinheim an der Bergstrasse, Germany)* (Jan. 2015). DOI: 10.1002/smll.201402161 (see pp. 55, 57, 58, 82).

[46] N. Weiß, L. Müller-Meskamp, F. Selzer, L. Bormann, A. Eychmüller, K. Leo, and N. Gaponik. "Humidity Assisted Annealing Technique for Transparent Conductive Silver Nanowire Networks". *RSC Adv.* 5.25 (2015). DOI: 10.1039/C5RA01303H (see pp. 57, 122, 124).

[47] B. J. Worfolk, S. C. Andrews, S. Park, J. Reinspach, N. Liu, M. F. Toney, S. C. B. Mannsfeld, and Z. Bao. "Ultrahigh electrical conductivity in solution-sheared polymeric transparent films". *Proceedings of the National Academy of Sciences* (2015). DOI: 10.1073/pnas.1509958112 (see pp. 31, 44).

[48] R.-C. Zhang, M.-Y. Wang, L.-Y. Yang, W.-J. Qin, and S.-G. Yin. "Polymer Solar Cells Using a PEDOT:PSS/Cu Nanowires/PEDOT:PSS Multilayer as the Anode Interlayer". *Chinese Physics Letters* 32.7 (July 2015). DOI: 10.1088/0256-307X/32/7/077202 (see p. 48).

[49] I. V. Anoshkin, A. G. Nasibulin, Y. Tian, B. Liu, H. Jiang, and E. I. Kauppinen. "Hybrid carbon source for single-walled carbon nanotube synthesis by aerosol CVD method". *Carbon* 78 (Nov. 2014). DOI: 10.1016/j.carbon.2014.06.057 (see p. 48).

[50] T. Araki, J. Jiu, M. Nogi, H. Koga, S. Nagao, T. Sugahara, and K. Suganuma. "Low haze transparent electrodes and highly conducting air dried films with ultra-long silver nanowires synthesized by one-step polyol method". *Nano Research* 7.2 (2014). DOI: 10.1007/s12274-013-0391-x (see p. 53).

[51] I. Burgués-Ceballos, N. Kehagias, C. M. Sotomayor-Torres, M. Campoy-Quiles, and P. D. Lacharmoise. "Embedded inkjet printed silver grids for ITO-free organic solar cells with high fill factor". *Solar Energy Materials and Solar Cells* 127 (Aug. 2014). DOI: 10.1016/j.solmat.2014.03.024 (see p. 47).

[52] S. Chen, L. Song, Z. Tao, X. Shao, Y. Huang, Q. Cui, and X. Guo. "Neutral-pH PEDOT:PSS as over-coating layer for stable silver nanowire flexible transparent conductive films". *Organic Electronics: physics, materials, applications* 15.12 (2014). DOI: 10.1016/j.orgel.2014.09.047 (see p. 57).

[53] T. Cheng, Y.-Z. Zhang, W.-Y. Lai, Y. Chen, W.-J. Zeng, and W. Huang. "High-performance stretchable transparent electrodes based on silver nanowires synthesized via an eco-friendly halogen-free method". *J. Mater. Chem. C* 2.48 (2014). DOI: 10.1039/C4TC01959H (see pp. 51, 58, 116).

[54] K. Cnops, B. P. Rand, D. Cheyns, B. Verreet, M. A. Empl, and P. Heremans. "[Supporting Information] 8.4% Efficient Fullerene-Free Organic Solar Cells Exploiting Long-Range Exciton Energy Transfer". *Nature Communications* 5 (2014). DOI: 10.1038/ncomms4406 (see p. 137).

[55] K. Cnops, B. P. Rand, D. Cheyns, B. Verreet, M. a. Empl, and P. Heremans. "8.4% efficient fullerene-free organic solar cells exploiting long-range exciton energy transfer." *Nature communications* 5 (2014). DOI: 10.1038/ncomms4406 (see pp. 29, 30, 126, 128).

[56] H.-F. Cui, Y.-F. Zhang, and C.-N. Li. “Flexible Organic Light-Emitting Devices with a Smooth and Transparent Silver Nanowire Electrode”. *Optical Engineering* 53.7 (2014). DOI: `10.1117/1.OE.53.7.077102` (see pp. 49, 58, 114, 147).

[57] D. S. Ghosh, T. L. Chen, V. Mkhitaryan, and V. Pruneri. “Ultrathin Transparent Conductive Polyimide Foil Embedding Silver Nanowires”. *ACS Applied Materials & Interfaces* 6.23 (2014). DOI: `10.1021/am505704e` (see pp. 58, 114, 146).

[58] M. Grätzel. “The light and shade of perovskite solar cells”. *Nature Materials* 13.9 (Aug. 2014). DOI: `10.1038/nmat4065` (see p. 32).

[59] J. Griffin, A. J. Pearson, N. W. Scarratt, T. Wang, D. G. Lidzey, and A. R. Buckley. “Organic photovoltaic devices incorporating a molybdenum oxide hole-extraction layer deposited by spray-coating from an ammonium molybdate tetrahydrate precursor”. *Organic Electronics* 15.3 (Mar. 2014). DOI: `10.1016/j.orgel.2013.12.028` (see p. 26).

[60] O. L. Griffith and S. R. Forrest. “Exciton management in organic photovoltaic multidonor energy cascades”. *Nano Letters* 14.5 (2014). DOI: `10.1021/nl501112z` (see pp. 29, 30).

[61] B. Han, Y. Huang, R. Li, Q. Peng, J. Luo, K. Pei, A. Herczynski, K. Kempa, Z. Ren, and J. Gao. “Bio-inspired networks for optoelectronic applications”. *Nature Communications* 5 (Nov. 2014). DOI: `10.1038/ncomms6674` (see pp. 47, 48).

[62] K. Harafuji, H. Sato, T. Matsuura, Y. Omoto, T. Kaji, and M. Hiramoto. “Degradation in organic solar cells under illumination and electrical stresses in air”. *Japanese Journal of Applied Physics* 53.12 (Dec. 2014). DOI: `10.7567/JJAP.53.122303` (see p. 17).

[63] N. J. Jeon, H. G. Lee, Y. C. Kim, J. Seo, J. H. Noh, J. Lee, and S. I. Seok. “o-Methoxy substituents in spiro-OMeTAD for efficient inorganic-organic hybrid perovskite solar cells.” *Journal of the American Chemical Society* 136.22 (2014). DOI: `10.1021/ja502824c` (see p. 101).

[64] Y. Jin, D. Deng, Y. Cheng, L. Kong, and F. Xiao. “Annealing-free and strongly adhesive silver nanowire networks with long-term reliability by introduction of a nonconductive and biocompatible polymer binder.” *Nanoscale* 6.9 (May 2014). DOI: `10.1039/c3nr05820d` (see p. 58).

[65] H. J. Kim, S. H. Lee, J. Lee, E. S. Lee, J. H. Choi, J. H. Jung, J. Y. Jung, and D. G. Choi. “High-durable AgNi nanomesh film for a transparent conducting electrode”. *Small* 10.18 (2014). DOI: `10.1002/smll.201400911` (see pp. 46, 155).

[66] J. K. Kim, I. Park, W. Kim, D. H. Wang, D.-G. Choi, Y. S. Choi, and J. H. Park. “Enhanced Performance and Stability of Polymer BHJ Photovoltaic Devices from Dry Transfer of PEDOT:PSS”. *ChemSusChem* 7.7 (July 2014). DOI: 10.1002/cssc.201400022 (see pp. 57, 109).

[67] H. Klumbies, L. Mueller-Meskamp, S. Schubert, T. Moench, M. Hermenau, and K. Leo. “Diffusion Barriers for Organic Devices and their Evaluation with Calcium Corrosion Tests”. *Society of Vacuum Coaters, 56th Annual Technical Conference Proceedings* (2014). DOI: 10.14332/svc13.proc.1116 (see p. 77).

[68] H. Klumbies, L. Müller-Meskamp, F. Nehm, and K. Leo. “Note: Influence of Calcium Corrosion on the Performance of an Adjacent Permeation Barrier”. *Review of Scientific Instruments* 85.1 (2014). DOI: 10.1063/1.4861536 (see p. 77).

[69] H. Klumbies, M. Karl, M. Hermenau, R. Rösch, M. Seeland, H. Hoppe, L. Müller-Meskamp, and K. Leo. “Water Ingress into and Climate Dependent Lifetime of Organic Photovoltaic Cells Investigated by Calcium Corrosion Tests”. *Solar Energy Materials and Solar Cells* 120 (2014). DOI: 10.1016/j.solmat.2013.10.023 (see p. 34).

[70] H. K. H. Lee, Z. Li, I. Constantinou, F. So, S. W. Tsang, and S. K. So. “Batch-to-batch variation of polymeric photovoltaic materials: Its origin and impacts on charge carrier transport and device performances”. *Advanced Energy Materials* 4.16 (2014). DOI: 10.1002/aenm.201400768 (see p. 31).

[71] Y. Liu, J. Zhao, Z. Li, C. Mu, W. Ma, H. Hu, K. Jiang, H. Lin, H. Ade, and H. Yan. “Aggregation and Morphology Control Enables Multiple Cases of High-Efficiency Polymer Solar Cells”. *Nature Communications* 5.9 (Nov. 2014). DOI: 10.1038/ncomms6293 (see p. 30).

[72] R. Meerheim, C. Körner, and K. Leo. “Highly Efficient Organic Multi-Junction Solar Cells with a Thiophene based Donor Material”. *Applied Physics Letters* 105.6 (2014). DOI: 10.1063/1.4893012 (see pp. 29, 82, 83, 85, 98, 106, 140).

[73] C. Murawski, C. Fuchs, S. Hofmann, K. Leo, and M. C. Gather. “Alternative P-Doped Hole Transport Material for Low Operating Voltage and High Efficiency Organic Light-Emitting Diodes”. *Applied Physics Letters* 105.11 (2014). DOI: 10.1063/1.4896127 (see p. 83).

[74] B. D. Naab, S. Zhang, K. Vandewal, A. Salleo, S. Barlow, S. R. Marder, and Z. Bao. “Effective solution- and vacuum-processed n-doping by dimers of benzimidazoline radicals”. *Advanced Materials* 26.25 (2014). DOI: 10.1002/adma.201400668 (see pp. 13, 83, 106, 110).

[75] S. Nam, M. Song, D.-H. Kim, B. Cho, H. M. Lee, J.-D. Kwon, S.-G. Park, K.-S. Nam, Y. Jeong, S.-H. Kwon, Y. C. Park, S.-H. Jin, J.-W. Kang, S. Jo, and C. S. Kim. “Ultrasmooth, Extremely Deformable and Shape Recoverable Ag Nanowire Embedded Transparent Electrode”. *Scientific reports* 4 (2014). DOI: `10.1038/srep04788` (see pp. 57, 58, 114, 136, 146, 147).

[76] F. Nehm, S. Schubert, L. Müller-Meskamp, and K. Leo. “Observation of feature ripening inversion effect at the percolation threshold for the growth of thin silver films”. *Thin Solid Films* 556 (2014). DOI: `10.1016/j.tsf.2014.01.067` (see pp. 40, 44).

[77] L. E. Polander, P. Pahner, M. Schwarze, M. Saalfrank, C. Koerner, and K. Leo. “Hole-transport material variation in fully vacuum deposited perovskite solar cells”. *APL Materials* 2.8 (Aug. 2014). DOI: `10.1063/1.4889843` (see pp. 101, 104, 105).

[78] A. Sander, R. Hammer, K. Duncker, S. Förster, and W. Widdra. “Thermally and photoinduced polymerization of ultrathin sexithiophene films”. *The Journal of Chemical Physics* 141.10 (Sept. 2014). DOI: `10.1063/1.4894437` (see p. 137).

[79] S. B. Sapkota, M. Fischer, B. Zimmermann, and U. Würfel. “Analysis of the degradation mechanism of ITO-free organic solar cells under UV radiation”. *Solar Energy Materials and Solar Cells* 121 (2014). DOI: `10.1016/j.solmat.2013.10.021` (see pp. 45, 57).

[80] S. Schubert, L. Müller-Meskamp, and K. Leo. “Unusually High Optical Transmission in Ca:Ag Blend Films: High-Performance Top Electrodes for Efficient Organic Solar Cells”. *Advanced Functional Materials* 24.42 (Nov. 2014). DOI: `10.1002/adfm.201401854` (see pp. 43, 106).

[81] S. Schubert, F. Schmidt, H. von Wenckstern, M. Grundmann, K. Leo, and L. Müller-Meskamp. “Eclipse Pulsed Laser Deposition for Damage-Free Preparation of Transparent ZnO Electrodes on Top of Organic Solar Cells”. *Advanced Functional Materials* (2014). DOI: `10.1002/adfm.201500569` (see p. 85).

[82] F. Selzer, N. Weiß, L. Bormann, C. Sachse, N. Gaponik, L. Müller-Meskamp, A. Eychmüller, and K. Leo. “Highly Conductive Silver Nanowire Networks by Organic Matrix Assisted Low-Temperature Fusing”. *Organic Electronics* 15.12 (2014). DOI: `10.1016/j.orgel.2014.09.030` (see pp. 49, 57, 85, 91).

[83] H. J. Snaith, A. Abate, J. M. Ball, G. E. Eperon, T. Leijtens, N. K. Noel, S. D. Stranks, J. T. W. Wang, K. Wojciechowski, and W. Zhang. “Anomalous hysteresis in perovskite solar cells”. *Journal of Physical Chemistry Letters* 5.9 (2014). DOI: `10.1021/jz500113x` (see p. 104).

[84] M. Song, H.-J. Kim, C. S. Kim, J.-H. Jeong, C. Cho, J.-Y. Lee, S.-H. Jin, D.-G. Choi, and D.-H. Kim. "ITO-free highly bendable and efficient organic solar cells with Ag nanomesh/ZnO hybrid electrodes". *J. Mater. Chem. A* 3.1 (2014). DOI: 10.1039/C4TA05294C (see p. 46).

[85] M. Song, J. H. Park, C. S. Kim, D.-H. Kim, Y.-C. Kang, S.-H. Jin, W.-Y. Jin, and J.-W. Kang. "Highly flexible and transparent conducting silver nanowire/ZnO composite film for organic solar cells". *Nano Research* 7.9 (2014). DOI: 10.1007/s12274-014-0502-3 (see p. 57).

[86] T.-B. Song, Y. Chen, C.-H. Chung, Y. M. Yang, B. Bob, H.-S. Duan, G. Li, K.-N. Tu, Y. Huang, and Y. Yang. "Nanoscale Joule Heating and Electromigration Enhanced Ripening of Silver Nanowire Contacts". *ACS nano* 8.3 (Mar. 2014). DOI: 10.1021/nn4065567 (see p. 145).

[87] M. L. Tietze. "Molecular Doping Processes in Organic Semiconductors investigated by Photoelectron Spectroscopy". Dissertation. TU Dresden, 2014 (see p. 12).

[88] B. Verreet, K. Cnops, D. Cheyns, P. Heremans, A. Stesmans, G. Zango, C. G. Claessens, T. Torres, and B. P. Rand. "Decreased Recombination Through the Use of a Non-Fullerene Acceptor in a 6.4% Efficient Organic Planar Heterojunction Solar Cell". *Advanced Energy Materials* 4.8 (June 2014). DOI: 10.1002/aenm.201301413 (see p. 30).

[89] J. Wang, C. Yan, W. Kang, and P. S. Lee. "High-efficiency transfer of percolating nanowire films for stretchable and transparent photodetectors." *Nanoscale* 6.18 (2014). DOI: 10.1039/c4nr02462a (see p. 110).

[90] H. Yamaguchi, J. Granstrom, W. Nie, H. Sojoudi, T. Fujita, D. Voiry, M. Chen, G. Gupta, A. D. Mohite, S. Graham, and M. Chhowalla. "Reduced Graphene Oxide Thin Films as Ultrabarriers for Organic Electronics". *Advanced Energy Materials* 4.4 (Mar. 2014). DOI: 10.1002/aenm.201300986 (see p. 35).

[91] B. Zeng, Z. H. Kafafi, and F. J. Bartoli. "Transparent electrodes based on two-dimensional Ag nanogrids and double one-dimensional Ag nanogratings for organic photovoltaics". *Journal of Photonics for Energy* 5.1 (2014). DOI: 10.1117/1.JPE.5.057005 (see p. 47).

[92] J. Burschka, N. Pellet, S.-J. Moon, R. Humphry-Baker, P. Gao, M. K. Nazeeruddin, and M. Grätzel. "Sequential deposition as a route to high-performance perovskite-sensitized solar cells". *Nature* 499.7458 (July 2013). DOI: 10.1038/nature12340 (see p. 28).

[93] R. Chen, S. R. Das, C. Jeong, M. R. Khan, D. B. Janes, and M. A. Alam. "Co-percolating graphene-wrapped silver nanowire network for high performance, highly stable, transparent conducting electrodes". *Advanced Functional Materials* 23.41 (2013). DOI: 10.1002/adfm.201300124 (see p. 59).

[94] D. Y. Choi, H. W. Kang, H. J. Sung, and S. S. Kim. "Annealing-free, flexible silver nanowire-polymer composite electrodes via a continuous two-step spray-coating method." *Nanoscale* 5.3 (Mar. 2013). DOI: 10.1039/c2nr32221h (see pp. 26, 57, 82).

[95] Corning. *Electronics Sylgard ® 184 Silicone Elastomer*. 2013 (see p. 114).

[96] J. Fahlteich, S. Amberg-Schwab, U. Weber, K. Noller, O. Miesbauer, C. Boeffel, and N. Schiller. "Ultra-High Barriers for Encapsulation of Flexible Displays and Lighting Devices". *SID Symposium Digest of Technical Papers* 44.1 (June 2013). DOI: 10.1002/j.2168-0159.2013.tb06219.x (see p. 35).

[97] W. Gaynor, S. Hofmann, M. G. Christoforo, C. Sachse, S. Mehra, A. Salleo, M. D. McGehee, M. C. Gather, B. Lüssem, L. Müller-Meskamp, P. Peumans, and K. Leo. "Color in the corners: ITO-free white OLEDs with angular color stability". *Advanced Materials* 25.29 (2013). DOI: 10.1002/adma.201300923 (see pp. 101, 125).

[98] N. Grillet, D. Manchon, E. Cottancin, F. Bertorelle, C. Bonnet, M. Broyer, J. Lermé, and M. Pellarin. "Photo-Oxidation of Individual Silver Nanoparticles: A Real-Time Tracking of Optical and Morphological Changes". *Journal of Physical Chemistry C* 117.5 (2013). DOI: 10.1021/jp311502h (see p. 145).

[99] F. Guo, X. Zhu, K. Forberich, J. Krantz, T. Stubhan, M. Salinas, M. Halik, S. Spallek, B. Butz, E. Spiecker, T. Ameri, N. Li, P. Kubis, D. M. Guldi, G. J. Matt, and C. J. Brabec. "ITO-Free and Fully Solution-Processed Semitransparent Organic Solar Cells with High Fill Factors". *Advanced Energy Materials* 3.8 (Aug. 2013). DOI: 10.1002/aenm.201300100 (see p. 37).

[100] M. Hösel and F. C. Krebs. *Large-scale Roll-to-Roll Fabrication of Organic Solar Cells for Energy Production*. December. 2013 (see p. 23).

[101] H. Hosseinzadeh Khaligh and I. a. Goldthorpe. "Failure of silver nanowire transparent electrodes under current flow." *Nanoscale research letters* 8.1 (May 2013). DOI: 10.1186/1556-276X-8-235 (see p. 59).

[102] M. Ichikawa, Y. Yokota, H.-G. Jeon, G. D. R. Banoukepa, N. Hirata, and N. Oguma. "Comparative study of soluble naphthalene diimide derivatives bearing long alkyl chains as n-type organic thin-film transistor materials". *Organic Electronics* 14.2 (Feb. 2013). DOI: 10.1016/j.orgel.2012.10.038 (see p. 108).

[103] Y. Jang, J. Kim, and D. Byun. "Invisible metal-grid transparent electrode prepared by electrohydrodynamic (EHD) jet printing". *Journal of Physics D: Applied Physics* 46.15 (2013). DOI: 10.1088/0022-3727/46/15/155103 (see p. 47).

[104] S. Kannappan, K. Palanisamy, J. Tatsugi, P.-K. Shin, and S. Ochiai. “Fabrication and characterizations of PCDTBT: PC71BM bulk heterojunction solar cell using air brush coating method”. *Journal of Materials Science* 48.6 (Mar. 2013). DOI: 10.1007/s10853-012-7010-1 (see p. 26).

[105] G. Khanarian, J. Joo, X. Q. Liu, P. Eastman, D. Werner, K. O’Connell, and P. Trefonas. “The optical and electrical properties of silver nanowire mesh films”. *Journal of Applied Physics* 114.2 (2013). DOI: 10.1063/1.4812390 (see p. 55).

[106] T. Kim, Y. W. Kim, H. S. Lee, H. Kim, W. S. Yang, and K. S. Suh. “Uniformly Interconnected Silver-Nanowire Networks for Transparent Film Heaters”. *Advanced Functional Materials* 23.10 (Mar. 2013). DOI: 10.1002/adfm.201202013 (see p. 49).

[107] M. Kohlstädt, M. Grein, P. Reinecke, T. Kroyer, B. Zimmermann, and U. Würfel. “Inverted ITO- and PEDOT:PSS-free polymer solar cells with high power conversion efficiency”. *Solar Energy Materials and Solar Cells* 117 (2013). DOI: 10.1016/j.solmat.2013.05.023 (see p. 43).

[108] J. Krantz, T. Stubhan, M. Richter, S. Spallek, I. Litzov, G. J. Matt, E. Spiecker, and C. J. Brabec. “Spray-Coated Silver Nanowires as Top Electrode Layer in Semitransparent P3HT:PCBM-Based Organic Solar Cell Devices”. *Advanced Functional Materials* 23.13 (Apr. 2013). DOI: 10.1002/adfm.201202523 (see pp. 26, 49, 91).

[109] F. C. Krebs, M. Hösel, M. Corazza, B. Roth, M. V. Madsen, S. a. Gevorgyan, R. R. Søndergaard, D. Karg, and M. Jørgensen. “Freely available OPV-The fast way to progress”. *Energy Technology* 1.7 (2013). DOI: 10.1002/ente.201300057 (see p. 27).

[110] D. A. Kunz, J. Schmid, P. Feicht, J. Erath, A. Fery, and J. Breu. “Clay-Based Nanocomposite Coating for Flexible Optoelectronics Applying Commercial Polymers”. *ACS Nano* 7.5 (May 2013). DOI: 10.1021/nn400713e (see p. 35).

[111] D. Langley, G. Giusti, C. Mayousse, C. Celle, D. Bellet, and J.-P. Simonato. “Flexible transparent conductive materials based on silver nanowire networks: a review.” *Nanotechnology* 24.45 (2013). DOI: 10.1088/0957-4484/24/45/452001 (see p. 48).

[112] D. Lee, H. Lee, Y. Ahn, Y. Jeong, D.-Y. Lee, and Y. Lee. “Highly stable and flexible silver nanowire-graphene hybrid transparent conducting electrodes for emerging optoelectronic devices.” *Nanoscale* 5.17 (Aug. 2013). DOI: 10.1039/c3nr02320f (see pp. 58, 59).

[113] G. P. Lee, Y. Shi, E. Lavoie, T. Daeneke, P. Reineck, U. B. Cappel, D. M. Huang, and U. Bach. "Light-Driven Transformation Processes of Anisotropic Silver Nanoparticles". *ACS Nano* 7.7 (July 2013). DOI: 10.1021/nn4013059 (see p. 145).

[114] J. Lee, P. Lee, H. B. Lee, S. Hong, I. Lee, J. Yeo, S. S. Lee, T.-S. Kim, D. Lee, and S. H. Ko. "Room-Temperature Nanosoldering of a Very Long Metal Nanowire Network by Conducting-Polymer-Assisted Joining for a Flexible Touch-Panel Application". *Advanced Functional Materials* (Apr. 2013). DOI: 10.1002/adfm.201203802 (see pp. 56, 57).

[115] H. Méndez, G. Heimel, A. Opitz, K. Sauer, P. Barkowski, M. Oehzelt, J. Soeda, T. Okamoto, J. Takeya, J. B. Arlin, J. Y. Balandier, Y. Geerts, N. Koch, and I. Salzmann. "Doping of organic semiconductors: Impact of dopant strength and electronic coupling". *Angewandte Chemie - International Edition* 52.30 (2013). DOI: 10.1002/anie.201302396 (see p. 14).

[116] T. Menke. "Molecular Doping of Organic Semiconductors A Conductivity and Seebeck Study". Dissertation. TU Dresden, 2013 (see pp. 12, 85).

[117] P. Pingel and D. Neher. "Comprehensive picture of p-type doping of P3HT with the molecular acceptor F4-TCNQ". *Physical Review B* 87.11 (Mar. 2013). DOI: 10.1103/PhysRevB.87.115209 (see p. 14).

[118] C. Sachse, L. Müller-Meskamp, L. Bormann, Y. H. Kim, F. Lehnert, A. Philipp, B. Beyer, and K. Leo. "Transparent, Dip-Coated Silver Nanowire Electrodes for Small Molecule Organic Solar Cells". *Organic Electronics* 14.1 (2013). DOI: 10.1016/j.orgel.2012.09.032 (see pp. 26, 57, 82, 85).

[119] C. Sachse, N. Weiß, N. Gaponik, L. Müller-Meskamp, A. Eychmüller, and K. Leo. "ITO-Free, Small-Molecule Organic Solar Cells on Spray-Coated Copper-Nanowire-Based Transparent Electrodes". *Advanced Energy Materials* (Sept. 2013). DOI: 10.1002/aenm.201300737 (see p. 48).

[120] S. Schubert, Y. H. Kim, T. Menke, A. Fischer, R. Timmreck, L. Müller-Meskamp, and K. Leo. "Highly doped fullerene C60 thin films as transparent stand alone top electrode for organic solar cells". *Solar Energy Materials and Solar Cells* 118 (2013). DOI: 10.1016/j.solmat.2013.08.017 (see pp. 39, 45, 78).

[121] S. Schubert, J. Meiss, L. Müller-Meskamp, and K. Leo. "Improvement of Transparent Metal Top Electrodes for Organic Solar Cells by Introducing a High Surface Energy Seed Layer". *Advanced Energy Materials* 3.4 (2013). DOI: 10.1002/aenm.201200903 (see pp. 37, 43, 44).

[122] A. Singh, H. Klumbies, U. Schröder, L. Müller-Meskamp, M. Geidel, M. Knaut, C. Hoßbach, M. Albert, K. Leo, and T. Mikolajick. "Barrier Performance Optimization of Atomic Layer Deposited Diffusion Barriers for Organic Light Emitting Diodes using X-Ray Reflectivity Investigations". *Applied Physics Letters* 103.23 (2013). DOI: 10.1063/1.4839455 (see p. 35).

[123] R. R. Sondergaard, M. Hösel, and F. C. Krebs. "Roll-to-Roll fabrication of large area functional organic materials". *Journal of Polymer Science, Part B: Polymer Physics* 51.1 (2013). DOI: 10.1002/polb.23192 (see pp. 26, 27, 45).

[124] S. D. Stranks, G. E. Eperon, G. Grancini, C. Menelaou, M. J. P. Alcocer, T. Leijtens, L. M. Herz, A. Petrozza, and H. J. Snaith. "Electron-Hole Diffusion Lengths Exceeding 1 Micrometer in an Organometal Trihalide Perovskite Absorber". *Science* 342.6156 (Oct. 2013). DOI: 10.1126/science.1243982 (see p. 32).

[125] J. G. Tait, B. J. Worfolk, S. a. Maloney, T. C. Hauger, A. L. Elias, J. M. Buriak, and K. D. Harris. "Spray coated high-conductivity PEDOT:PSS transparent electrodes for stretchable and mechanically-robust organic solar cells". *Solar Energy Materials and Solar Cells* 110 (Mar. 2013). DOI: 10.1016/j.solmat.2012.09.005 (see p. 26).

[126] M. L. Tietze, W. Tress, S. Pfützner, C. Schünemann, L. Burtone, M. Riede, K. Leo, K. Vandewal, S. Olthof, P. Schulz, and A. Kahn. "Correlation of open-circuit voltage and energy levels in zinc-phthalocyanine: C60 bulk heterojunction solar cells with varied mixing ratio". *Physical Review B - Condensed Matter and Materials Physics* 88.8 (2013). DOI: 10.1103/PhysRevB.88.085119 (see p. 95).

[127] W. Tress and O. Inganäs. "Simple experimental test to distinguish extraction and injection barriers at the electrodes of (organic) solar cells with S-shaped current–voltage characteristics". *Solar Energy Materials and Solar Cells* 117 (Oct. 2013). DOI: 10.1016/j.solmat.2013.07.014 (see p. 136).

[128] T. Wang, N. W. Scarratt, H. Yi, A. D. F. Dunbar, A. J. Pearson, D. C. Watters, T. S. Glen, A. C. Brook, J. Kingsley, A. R. Buckley, M. W. A. Skoda, A. M. Donald, R. A. L. Jones, A. Iraqi, and D. G. Lidzey. "Fabricating High Performance, Donor-Acceptor Copolymer Solar Cells by Spray-Coating in Air". *Advanced Energy Materials* 3.4 (Apr. 2013). DOI: 10.1002/aenm.201200713 (see p. 26).

[129] J. Widmer, M. L. Tietze, K. Leo, and M. Riede. "Open-circuit voltage and effective gap of organic solar cells". *Advanced Functional Materials* 23.46 (2013). DOI: 10.1002/adfm.201301048 (see p. 21).

[130] H. Wu, D. Kong, Z. Ruan, P.-C. Hsu, S. Wang, Z. Yu, T. J. Carney, L. Hu, S. Fan, and Y. Cui. “A Transparent Electrode based on a Metal Nanotrough Network”. *Nature nanotechnology* 8.6 (June 2013). DOI: `10.1038/nnano.2013.84` (see p. 47).

[131] Y. Ahn, Y. Jeong, and Y. Lee. “Improved thermal oxidation stability of solution-processable silver nanowire transparent electrode by reduced graphene oxide.” *ACS applied materials & interfaces* 4 (2012). DOI: `10.1021/am301913w` (see p. 59).

[132] D. Alemu, H.-Y. Wei, K.-C. Ho, and C.-W. Chu. “Highly conductive PEDOT:PSS electrode by simple film treatment with methanol for ITO-free polymer solar cells”. *Energy & Environmental Science* 5.11 (2012). DOI: `10.1039/c2ee22595f` (see p. 44).

[133] T. M. Barnes, M. O. Reese, J. D. Bergeson, B. A. Larsen, J. L. Blackburn, M. C. Beard, J. Bult, and J. Van De Lagemaat. “Comparing the fundamental physics and device performance of transparent, conductive nanostructured networks with conventional transparent conducting oxides”. *Advanced Energy Materials* 2.3 (2012). DOI: `10.1002/aenm.201100608` (see p. 41).

[134] S. M. Bergin, Y.-H. Chen, A. R. Rathmell, P. Charbonneau, Z.-Y. Li, and B. J. Wiley. “The effect of nanowire length and diameter on the properties of transparent, conducting nanowire films”. *Nanoscale* 4.6 (2012). DOI: `10.1039/c2nr30126a` (see pp. 54, 55).

[135] R. Brückner. “Coherence and Coupling of Cavity Photons and Tamm Plasmons in Metal-Organic Microcavities”. Dissertation. TU Dresden, 2012, pp. 1–135 (see p. 101).

[136] I. Chung, B. Lee, J. He, R. P. H. Chang, and M. G. Kanatzidis. “All-solid-state dye-sensitized solar cells with high efficiency.” *Nature* 485.7399 (May 2012). DOI: `10.1038/nature11067` (see p. 101).

[137] K. Ellmer. “Past achievements and future challenges in the development of optically transparent electrodes”. *Nature Photonics* 6.12 (2012). DOI: `10.1038/nphoton.2012.282` (see pp. 41, 43, 45, 55).

[138] C. J. Emmott, A. Urbina, and J. Nelson. “Environmental and Economic Assessment of ITO-Free Electrodes for Organic Solar Cells”. *Solar Energy Materials and Solar Cells* 97 (2012). DOI: `10.1016/j.solmat.2011.09.024` (see pp. 40, 43).

[139] M. V. Fabretto, D. R. Evans, M. Mueller, K. Zuber, P. Hojati-Talemi, R. D. Short, G. G. Wallace, and P. J. Murphy. “Polymeric Material with Metal-Like Conductivity for Next Generation Organic Electronic Devices”. *Chemistry of Materials* 24.20 (Oct. 2012). DOI: `10.1021/cm302899v` (see p. 44).

[140] R. Fitzner, E. Mena-Osteritz, A. Mishra, G. Schulz, E. Reinold, M. Weil, C. Körner, H. Ziehlke, C. Elschner, K. Leo, M. Riede, M. Pfeiffer, C. Uhrich, and P. Bäuerle. “Correlation of π-conjugated oligomer structure with film morphology and organic solar cell performance”. *Journal of the American Chemical Society* 134.27 (2012). DOI: `10.1021/ja302320c` (see p. 98).

[141] Y. Galagan, E. W. Coenen, S. Sabik, H. H. Gorter, M. Barink, S. C. Veenstra, J. M. Kroon, R. Andriessen, and P. W. Blom. “Evaluation of ink-jet printed current collecting grids and busbars for ITO-free organic solar cells”. *Solar Energy Materials and Solar Cells* 104 (Sept. 2012). DOI: `10.1016/j.solmat.2012.04.039` (see p. 39).

[142] E. C. Garnett, W. Cai, J. J. Cha, F. Mahmood, S. T. Connor, M. Greyson Christoforo, Y. Cui, M. D. McGehee, and M. L. Brongersma. “Self-limited plasmonic welding of silver nanowire junctions”. *Nature Materials* 11.3 (Feb. 2012). DOI: `10.1038/nmat3238` (see pp. 53, 57).

[143] S. Guo, S. B. Kim, S. K. Mohapatra, Y. Qi, T. Sajoto, A. Kahn, S. R. Marder, and S. Barlow. “n-Doping of Organic Electronic Materials using Air-Stable Organometallics”. *Advanced Materials* 24.5 (Feb. 2012). DOI: `10.1002/adma.201103238` (see pp. 13, 83, 84, 106).

[144] Z. He, C. Zhong, S. Su, M. Xu, H. Wu, and Y. Cao. “Enhanced power-conversion efficiency in polymer solar cells using an inverted device structure”. *Nature Photonics* 6.9 (Aug. 2012). DOI: `10.1038/nphoton.2012.190` (see pp. 30, 31, 106, 109).

[145] M. Hermenau. “Lebensdaueruntersuchungen an organischen Solarzellen”. PhD Thesis. TU Dresden, 2012, p. 249 (see pp. 32, 135).

[146] J.-W. Kang, Y.-J. Kang, S. Jung, D. S. You, M. Song, C. S. Kim, D.-G. Kim, J.-K. Kim, and S. H. Kim. “All-spray-coated semitransparent inverted organic solar cells: From electron selective to anode layers”. *Organic Electronics* 13.12 (Dec. 2012). DOI: `10.1016/j.orgel.2012.08.012` (see p. 26).

[147] Y. H. Kim, L. Müller-Meskamp, A. a. Zakhidov, C. Sachse, J. Meiss, J. Bikova, A. Cook, A. a. Zakhidov, and K. Leo. “Semi-transparent small molecule organic solar cells with laminated free-standing carbon nanotube top electrodes”. *Solar Energy Materials and Solar Cells* 96 (Jan. 2012). DOI: `10.1016/j.solmat.2011.10.001` (see p. 48).

[148] C. Koerner. “Oligothiophene Materials for Organic Solar Cells - Photophysics and Device Properties”. Dissertation. Technische Universität Dresden, 2012 (see pp. 23, 114).

[149] J. Lee, P. Lee, H. Lee, D. Lee, S. S. Lee, and S. H. Ko. "Very long Ag nanowire synthesis and its application in a highly transparent, conductive and flexible metal electrode touch panel". *Nanoscale* 4.20 (2012). DOI: `10.1039/c2nr31254a` (see pp. 49, 54, 58).

[150] M. M. Lee, J. Teuscher, T. Miyasaka, T. N. Murakami, and H. J. Snaith. "Efficient hybrid solar cells based on meso-superstructured organometal halide perovskites." *Science* 338.6107 (2012). DOI: `10.1126/science.1228604` (see pp. 31, 101).

[151] P. Lee, J. Lee, H. Lee, J. Yeo, S. Hong, K. H. Nam, D. Lee, S. S. Lee, and S. H. Ko. "Highly Stretchable and Highly Conductive Metal Electrode by Very Long Metal Nanowire Percolation Network". *Advanced Materials* (May 2012). DOI: `10.1002/adma.201200359` (see pp. 54, 55, 104).

[152] C. Y. Lin, D. H. Kuo, W. C. Chen, M. W. Ma, and G. S. Liou. "Electrical Performance of the Embedded-Type Surface Electrodes containing Carbon and Silver Nanowires as Fillers and One-Step Organosoluble Polyimide as a Matrix". *Organic Electronics: physics, materials, applications* 13.11 (2012). DOI: `10.1016/j.orgel.2012.06.047` (see pp. 58, 114).

[153] H.-W. Lin, S.-W. Chiu, L.-Y. Lin, Z.-Y. Hung, Y.-H. Chen, F. Lin, and K.-T. Wong. "Device Engineering for Highly Efficient Top-Illuminated Organic Solar Cells with Microcavity Structures". *Advanced Materials* 24.17 (2012). DOI: `10.1002/adma.201200487` (see p. 141).

[154] D. J. Lipomi, J. A. Lee, M. Vosgueritchian, B. C.-K. Tee, J. A. Bolander, and Z. Bao. "Electronic Properties of Transparent Conductive Films of PEDOT:PSS on Stretchable Substrates". *Chemistry of Materials* 24.2 (Jan. 2012). DOI: `10.1021/cm203216m` (see p. 45).

[155] Q. Liu, M. Ono, Z. Tang, R. Ishikawa, K. Ueno, and H. Shirai. "Highly efficient crystalline silicon/Zonyl fluorosurfactant-treated organic heterojunction solar cells". *Applied Physics Letters* 100.18 (2012). DOI: `10.1063/1.4709615` (see p. 110).

[156] A. Mityashin, Y. Olivier, T. Van Regemorter, C. Rolin, S. Verlaak, N. G. Martinelli, D. Beljonne, J. Cornil, J. Genoe, and P. Heremans. "Unraveling the Mechanism of Molecular Doping in Organic Semiconductors". *Advanced Materials* 24.12 (Mar. 2012). DOI: `10.1002/adma.201104269` (see p. 13).

[157] Y. Qi, S. K. Mohapatra, S. Bok Kim, S. Barlow, S. R. Marder, and A. Kahn. "Solution doping of organic semiconductors using air-stable n-dopants". *Applied Physics Letters* 100.8 (2012). DOI: `10.1063/1.3689760` (see p. 13).

[158] R. Rösch, D. M. . Tanenbaum, M. Jørgensen, M. Seeland, M. Bärenklau, M. Hermenau, E. Voroshazi, M. T. Lloyd, Y. Galagan, B. Zimmermann, U. Würfel, M. Hösel, H. F. Dam, S. a. Gevorgyan, S. Kudret, W. Maes, L. Lutsen, D. Vanderzande, R. Andriessen, G. Teran-Escobar, M. Lira-Cantu, A. Rivaton, G. Y. Uzunoğlu, D. Germack, B. Andreasen, M. V. Madsen, K. Norrman, H. Hoppe, and F. C. Krebs. "Investigation of the Degradation Mechanisms of a Variety of Organic Photovoltaic Devices by Combination of Imaging Techniques - the ISOS-3 Inter-Laboratory Collaboration". *Energy & Environmental Science* 5.4 (2012). DOI: 10.1039/c2ee03508a (see p. 32).

[159] I. Salzmann, G. Heimel, S. Duhm, M. Oehzelt, P. Pingel, B. M. George, A. Schnegg, K. Lips, R.-P. Blum, A. Vollmer, and N. Koch. "Intermolecular Hybridization Governs Molecular Electrical Doping". *Physical Review Letters* 108.3 (Jan. 2012). DOI: 10.1103/PhysRevLett.108.035502 (see p. 87).

[160] Y. Sun, G. C. Welch, W. L. Leong, C. J. Takacs, G. C. Bazan, and A. J. Heeger. "Solution-processed small-molecule solar cells with 6.7% efficiency." *Nature materials* 11.1 (Jan. 2012). DOI: 10.1038/nmat3160 (see p. 29).

[161] K. Vandewal, Z. Ma, J. Bergqvist, Z. Tang, E. Wang, P. Henriksson, K. Tvingstedt, M. R. Andersson, F. Zhang, and O. Inganäs. "Quantification of Quantum Efficiency and Energy Losses in Low Bandgap Polymer:Fullerene Solar Cells with High Open-Circuit Voltage". *Advanced Functional Materials* 22.16 (2012). DOI: 10.1002/adfm.201200608 (see p. 21).

[162] J.-S. Yu, I. Kim, J.-S. Kim, J. Jo, T. T. Larsen-Olsen, R. R. Søndergaard, M. Hösel, D. Angmo, M. Jørgensen, and F. C. Krebs. "Silver Front Electrode Grids for ITO-Free All Printed Polymer Solar Cells with Embedded and Raised Topographies, Prepared by Thermal Imprint, Flexographic and Inkjet Roll-to-Roll Processes". *Nanoscale* 4.19 (2012). DOI: 10.1039/c2nr31508d (see p. 27).

[163] Y. Zhou, C. Fuentes-Hernandez, and J. Shim. "A universal method to produce low–work function electrodes for organic electronics". *Science* 873.1985 (2012) (see p. 31).

[164] P. F. Carcia, R. S. Mclean, B. B. Sauer, and M. H. Reilly. "Atomic Layer Deposition Ultra-Barriers for Electronic Applications—Strategies and Implementation". *Journal of Nanoscience and Nanotechnology* 11.9 (2011). DOI: 10.1166/jnn.2011.5075 (see p. 129).

[165] M. T. Dang, L. Hirsch, and G. Wantz. "P3HT:PCBM, Best Seller in Polymer Photovoltaic Research". *Advanced Materials* 23.31 (Aug. 2011). DOI: 10.1002/adma.201100792 (see p. 30).

[166] D. Demeter, T. Rousseau, P. Leriche, T. Cauchy, R. Po, and J. Roncali. "Manipulation of the Open-Circuit Voltage of Organic Solar Cells by Desymmetrization of the Structure of Acceptor-Donor-Acceptor Molecules". *Advanced Functional Materials* 21.22 (Nov. 2011). DOI: 10.1002/adfm.201101508 (see p. 29).

[167] L. Erdmann, S. Behrendt, and M. Feil. *Kritische Rohstoffe für Deutschland*. Technical Report. Berlin: Institut für Zukunftsstudien und Technologiebewertung (IZT), 2011. URL: http://online-mittelstandsbank.de/kfw/de/I/II/Download%7B%5C_%7DCenter/Fachthemen/Research/PDF-Dokumente%7B%5C_%7DSonderpublikationen/Rohstoffkritikalitaet%7B%5C_%7DLF.pdf (see p. 43).

[168] C. Falkenberg. "Optimizing Organic Solar Cells - Transparent Electron Transport Materials for Improving the Device Performance". PhD thesis. Dresden: TU Dresden, 2011 (see p. 106).

[169] W. Gaynor, G. F. Burkhard, M. D. McGehee, and P. Peumans. "Smooth nanowire/polymer composite transparent electrodes." *Advanced Materials* 23.26 (July 2011). DOI: 10.1002/adma.201100566 (see pp. 43, 57, 58).

[170] D. S. Hecht, L. Hu, and G. Irvin. "Emerging Transparent Electrodes Based on Thin Films of Carbon Nanotubes, Graphene, and Metallic Nanostructures". *Advanced Materials* 23.13 (Apr. 2011). DOI: 10.1002/adma.201003188 (see pp. 41, 45).

[171] Y. H. Kim, C. Sachse, M. L. Machala, C. May, L. Mueller-Meskamp, and K. Leo. "Highly Conductive PEDOT:PSS Electrode with Optimized Solvent and Thermal Post-Treatment for ITO-Free Organic Solar Cells". *Advanced Functional Materials* (Feb. 2011). DOI: 10.1002/adfm.201002290 (see pp. 44, 45, 83).

[172] P. Kuang, J. M. Park, W. Leung, R. C. Mahadevapuram, K. S. Nalwa, T. G. Kim, S. Chaudhary, K. M. Ho, and K. Constant. "A new architecture for transparent electrodes: Relieving the trade-off between electrical conductivity and optical transmittance". *Advanced Materials* 23.21 (2011). DOI: 10.1002/adma.201100419 (see p. 46).

[173] D.-S. Leem, A. Edwards, M. Faist, J. Nelson, D. D. C. Bradley, and J. C. de Mello. "Efficient Organic Solar Cells with Solution-Processed Silver Nanowire Electrodes". *Advanced materials (Deerfield Beach, Fla.)* 23.38 (Oct. 2011). DOI: 10.1002/adma.201100871 (see p. 57).

[174] Q. N. Luu, J. M. Doorn, M. T. Berry, C. Jiang, C. Lin, and P. S. May. "Preparation and optical properties of silver nanowires and silver-nanowire thin films". *Journal of Colloid And Interface Science* 356.1 (2011). DOI: 10.1016/j.jcis.2010.12.077 (see p. 55).

[175] R. Meerheim, S. Olthof, M. Hermenau, S. Scholz, A. Petrich, N. Tessler, O. Solomeshch, B. Lüssem, M. Riede, and K. Leo. "Investigation of C60F36 as low-volatility p-dopant in organic optoelectronic devices". *Journal of Applied Physics* 109.10 (2011). DOI: 10.1063/1.3590142 (see pp. 83, 101).

[176] F. S. F. Morgenstern, D. Kabra, S. Massip, T. J. K. Brenner, P. E. Lyons, J. N. Coleman, and R. H. Friend. "Ag-Nanowire Films Coated with ZnO Nanoparticles as a Transparent Electrode for Solar Cells". *Applied Physics Letters* 99.18 (2011). DOI: 10.1063/1.3656973 (see p. 57).

[177] A. R. Rathmell and B. J. Wiley. "The synthesis and coating of long, thin copper nanowires to make flexible, transparent conducting films on plastic substrates." *Advanced materials (Deerfield Beach, Fla.)* 23.41 (Nov. 2011). DOI: 10.1002/adma.201102284 (see p. 48).

[178] M. C. Rosamond, A. J. Gallant, M. C. Petty, O. Kolosov, and D. A. Zeze. "A versatile nanopatterning technique based on controlled undercutting and liftoff". *Advanced Materials* 23.43 (2011). DOI: 10.1002/adma.201102708 (see p. 46).

[179] M. W. Rowell and M. D. McGehee. "Transparent electrode requirements for thin film solar cell modules". *Energy & Environmental Science* 4.1 (2011). DOI: 10.1039/c0ee00373e (see pp. 38, 39).

[180] C. W. Schlenker, V. S. Barlier, S. W. Chin, M. T. Whited, R. E. McAnally, S. R. Forrest, and M. E. Thompson. "Cascade Organic Solar Cells". *Chemistry of Materials* 23.18 (Sept. 2011). DOI: 10.1021/cm200525h (see p. 29).

[181] S. Schubert, H. Klumbies, L. Müller-Meskamp, and K. Leo. "Electrical Calcium Test for Moisture Barrier Evaluation for Organic Devices." *The Review of scientific instruments* 82.9 (Sept. 2011). DOI: 10.1063/1.3633956 (see p. 77).

[182] W. Tress. "Device Physics of Organic Solar Cells". Dissertation. TU Dresden, 2011 (see p. 86).

[183] W. Tress, K. Leo, and M. Riede. "Influence of Hole-Transport Layers and Donor Materials on Open-Circuit Voltage and Shape of I-V Curves of Organic Solar Cells". *Advanced Functional Materials* 21.11 (June 2011). DOI: 10.1002/adfm.201002669 (see p. 95).

[184] M. Wang, F. Xie, J. Du, Q. Tang, S. Zheng, Q. Miao, J. Chen, N. Zhao, and J. Xu. "Degradation mechanism of organic solar cells with aluminum cathode". *Solar Energy Materials and Solar Cells* 95.12 (Dec. 2011). DOI: 10.1016/j.solmat.2011.07.020 (see p. 33).

[185] J. M. Yun, J. S. Yeo, J. Kim, H. G. Jeong, D. Y. Kim, Y. J. Noh, S. S. Kim, B. C. Ku, and S. I. Na. "Solution-processable reduced graphene oxide as a novel alternative to PEDOT:PSS hole transport layers for highly efficient and stable Polymer solar cells". *Advanced Materials* 23.42 (2011). DOI: `10.1002/adma.201102207` (see p. 144).

[186] V. Zardetto, T. M. Brown, A. Reale, and A. Di Carlo. "Substrates for flexible electronics: A practical investigation on the electrical, film flexibility, optical, temperature, and solvent resistance properties". *Journal of Polymer Science, Part B: Polymer Physics* 49.9 (2011). DOI: `10.1002/polb.22227` (see p. 43).

[187] J. Zhao, H. Sun, S. Dai, Y. Wang, and J. Zhu. "Electrical Breakdown of Nanowires". *Nano Letters* 11.11 (2011). DOI: `10.1021/nl202160c` (see pp. 59, 145).

[188] J.-J. Zhu, C.-X. Kan, J.-G. Wan, M. Han, and G.-H. Wang. "High-Yield Synthesis of Uniform Ag Nanowires with High Aspect Ratios by Introducing the Long-Chain PVP in an Improved Polyol Process". *Journal of Nanomaterials* 2011 (2011). DOI: `10.1155/2011/982547` (see p. 54).

[189] R. Zhu, C.-H. Chung, K. C. Cha, W. Yang, Y. B. Zheng, H. Zhou, T.-B. Song, C.-C. Chen, P. S. Weiss, G. Li, and Y. Yang. "Fused silver nanowires with metal oxide nanoparticles and organic polymers for highly transparent conductors." *ACS nano* 5.12 (Dec. 2011). DOI: `10.1021/nn203576v` (see pp. 53, 58, 82).

[190] M. J. Allen, V. C. Tung, and R. B. Kaner. "Honeycomb carbon: a review of graphene." *Chemical reviews* 110.1 (Jan. 2010). DOI: `10.1021/cr900070d` (see p. 45).

[191] H. A. Atwater and A. Polman. "Plasmonics for improved photovoltaic devices". *Nature Materials* 9.10 (2010). DOI: `10.1038/nmat2866` (see p. 55).

[192] S. Bae, H. Kim, Y. Lee, X. Xu, J.-S. Park, Y. Zheng, J. Balakrishnan, T. Lei, H. Ri Kim, Y. I. Song, Y.-J. Kim, K. S. Kim, B. Özyilmaz, J.-H. Ahn, B. H. Hong, and S. Iijima. "Roll-to-roll production of 30-inch graphene films for transparent electrodes". *Nature Nanotechnology* 5.8 (Aug. 2010). DOI: `10.1038/nnano.2010.132` (see p. 45).

[193] S. Blumberg, O. Frank, and T. Hofmann. "Quantitative studies on the influence of the bean roasting parameters and hot water percolation on the concentrations of bitter compounds in coffee brew". *Journal of Agricultural and Food Chemistry* 58.6 (2010). DOI: `10.1021/jf9044606` (see p. 50).

[194] F. Bonaccorso, Z. Sun, T. Hasan, and A. C. Ferrari. "Graphene Photonics and Optoelectronics". *Nature Photonics* 4.9 (2010). DOI: `10.1038/nphoton.2010.186` (see p. 45).

[195] S. De and J. N. Coleman. "Are there fundamental limitations on the sheet resistance and transmittance of thin graphene films?" *ACS Nano* 4.5 (2010). DOI: 10.1021/nn100343f (see p. 38).

[196] S. De, P. J. King, P. E. Lyons, U. Khan, and J. N. Coleman. "Size effects and the problem with percolation in nanostructured transparent conductors." *ACS nano* 4.12 (Dec. 2010). DOI: 10.1021/nn1025803 (see pp. 40, 41, 51, 52, 53).

[197] A. Hagfeldt, G. Boschloo, L. Sun, L. Kloo, and H. Pettersson. "Dye-Sensitized Solar Cells". *Chemical Reviews* 110.11 (Nov. 2010). DOI: 10.1021/cr900356p (see p. 28).

[198] L. Hu, D. S. Hecht, and G. Grüner. "Carbon Nanotube Thin Films: Fabrication, Properties, and Applications". *Chemical Reviews* 110.10 (Oct. 2010). DOI: 10.1021/cr9002962 (see p. 48).

[199] L. Hu, H. S. Kim, J.-Y. Lee, P. Peumans, and Y. Cui. "Scalable coating and properties of transparent, flexible, silver nanowire electrodes." *ACS nano* 4.5 (May 2010). DOI: 10.1021/nn1005232 (see p. 55).

[200] M.-G. Kang, T. Xu, H. J. Park, X. Luo, and L. J. Guo. "Efficiency enhancement of organic solar cells using transparent plasmonic Ag nanowire electrodes." *Advanced materials (Deerfield Beach, Fla.)* 22.39 (Oct. 2010). DOI: 10.1002/adma.201001395 (see p. 125).

[201] S. Kirchmeyer, A. Elschner, K. Reuter, and W. Lovenich. *PEDOT: principles and applications of an intrinsically conductive polymer.* 2010 (see p. 44).

[202] P. K. Koech, A. B. Padmaperuma, L. Wang, J. S. Swensen, E. Polikarpov, J. T. Darsell, J. E. Rainbolt, and D. J. Gaspar. "Synthesis and Application of 1,3,4,5,7,8-Hexafluorotetracyanonaphthoquinodimethane (F6-TNAP): A Conductivity Dopant for Organic Light-Emitting Devices". *Chemistry of Materials* 22.13 (2010). DOI: 10.1021/cm1002737 (see pp. 83, 85).

[203] J.-Y. Lee, S. T. Connor, Y. Cui, and P. Peumans. "Semitransparent organic photovoltaic cells with laminated top electrode." *Nano letters* 10.4 (Apr. 2010). DOI: 10.1021/nl903892x (see p. 49).

[204] M. McKiernan, J. Zeng, S. Ferdous, S. Verhaverbeke, K. S. Leschkies, R. Gouk, C. Lazik, M. Jin, A. L. Briseno, and Y. Xia. "Facile Synthesis of Bimetallic Ag/Ni Core/Sheath Nanowires and Their Magnetic and Electrical Properties". *Small* 6.17 (Sept. 2010). DOI: 10.1002/smll.201000801 (see p. 155).

[205] S.-W. Park, J.-M. Choi, K. H. Lee, H. W. Yeom, S. Im, and Y. K. Lee. "Amorphous-to-crystalline phase transformation of thin film rubrene." *The journal of physical chemistry. B* 114.17 (May 2010). DOI: 10.1021/jp910459p (see p. 89).

[206] K. Vandewal, K. Tvingstedt, A. Gadisa, O. Inganäs, and J. V. Manca. “Relating the open-circuit voltage to interface molecular properties of donor:acceptor bulk heterojunction solar cells”. *Physical Review B* 81.12 (Mar. 2010). DOI: `10.1103/PhysRevB.81.125204` (see p. 21).

[207] P. Wei, J. H. Oh, G. Dong, and Z. Bao. “Use of a 1H-benzoimidazole derivative as an n-type dopant and to enable air-stable solution-processed n-channel organic thin-film transistors.” *Journal of the American Chemical Society* 132.26 (2010). DOI: `10.1021/ja103173m` (see p. 14).

[208] X.-Y. Zeng, Q.-K. Zhang, R.-M. Yu, and C.-Z. Lu. “A New Transparent Conductor: Silver Nanowire Film Buried at the Surface of a Transparent Polymer”. *Advanced materials (Deerfield Beach, Fla.)* 22.40 (Oct. 2010). DOI: `10.1002/adma.201001811` (see p. 58).

[209] S. Choi, W. J. Potscavage, and B. Kippelen. “Area-scaling of organic solar cells”. *Journal of Applied Physics* 106.5 (2009). DOI: `10.1063/1.3211850` (see pp. 16, 39).

[210] B. Dan, G. C. Irvin, and M. Pasquali. “Continuous and Scalable Fabrication of Transparent Conducting Carbon Nanotube Films”. *ACS Nano* 3.4 (Apr. 2009). DOI: `10.1021/nn8008307` (see p. 40).

[211] S. De, T. M. Higgins, P. E. Lyons, E. M. Doherty, P. N. Nirmalraj, W. J. Blau, J. J. Boland, and J. N. Coleman. “Silver Nanowire Networks as Flexible, Transparent, Conducting Films: Extremely High DC to Optical Conductivity Ratios.” *ACS nano* 3.7 (July 2009). DOI: `10.1021/nn900348c` (see pp. 48, 53, 91).

[212] M. Denhoff and N. Drolet. “The effect of the front contact sheet resistance on solar cell performance”. *Solar Energy Materials and Solar Cells* 93.9 (Sept. 2009). DOI: `10.1016/j.solmat.2009.03.028` (see p. 39).

[213] I.-K. Ding, N. Tétreault, J. Brillet, B. E. Hardin, E. H. Smith, S. J. Rosenthal, F. Sauvage, M. Grätzel, and M. D. McGehee. “Pore-Filling of Spiro-OMeTAD in Solid-State Dye Sensitized Solar Cells: Quantification, Mechanism, and Consequences for Device Performance”. *Advanced Functional Materials* 19.15 (Aug. 2009). DOI: `10.1002/adfm.200900541` (see p. 101).

[214] S. Ghosh, A. Gomathi, and C. N. R. Rao. “Stable Dispersions of Metal Oxide Nanowires and Nanoparticles in Water, Dimethylformamide and Toluene”. *Journal of Nanoscience and Nanotechnology* 9.9 (Sept. 2009). DOI: `10.1166/jnn.2009.1135` (see p. 110).

[215] C. Girotto, B. P. Rand, S. Steudel, J. Genoe, and P. Heremans. “Nanoparticle-based, spray-coated silver top contacts for efficient polymer solar cells”. *Organic Electronics* 10.4 (July 2009). DOI: `10.1016/j.orgel.2009.03.006` (see p. 26).

[216] S.-H. Hwang, Y. K. Kim, Y. Kwak, C.-H. Lee, J. Lee, and S. Kim. "Improved performance of organic light-emitting diodes using advanced hole-transporting materials". *Synthetic Metals* 159.23-24 (2009). DOI: 10.1016/j.synthmet.2009.09.015 (see p. 83).

[217] H. Ibach and H. Lueth. *Festkörperphysik*. Springer-Lehrbuch. Berlin, Heidelberg: Springer Berlin Heidelberg, 2009. DOI: 10.1007/978-3-540-85795-2 (see p. 15).

[218] C. S. Kim, S. S. Lee, E. D. Gomez, J. B. Kim, and Y. L. Loo. "Transient photovoltaic behavior of air-stable, inverted organic solar cells with solution-processed electron transport layer". *Applied Physics Letters* 94.11 (2009). DOI: 10.1063/1.3099947 (see p. 17).

[219] B. Kippelen and J.-L. Brédas. "Organic photovoltaics". *Energy & Environmental Science* 2.3 (2009). DOI: 10.1039/b812502n (see p. 18).

[220] G. Koishiyev and J. Sites. "Impact of sheet resistance on 2-D modeling of thin-film solar cells". *Solar Energy Materials and Solar Cells* 93.3 (Mar. 2009). DOI: 10.1016/j.solmat.2008.11.015 (see p. 39).

[221] A. Kojima, K. Teshima, Y. Shirai, and T. Miyasaka. "Organometal halide perovskites as visible-light sensitizers for photovoltaic cells". *Journal of the American Chemical Society* 131.17 (2009). DOI: 10.1021/ja809598r (see p. 31).

[222] Y. Long. "Improving Optical Performance of Inverted Organic Solar Cells by Microcavity Effect". *Applied Physics Letters* 95.19 (2009). DOI: 10.1063/1.3262967 (see p. 141).

[223] R. R. Lunt, N. C. Giebink, A. A. Belak, J. B. Benziger, and S. R. Forrest. "Exciton diffusion lengths of organic semiconductor thin films measured by spectrally resolved photoluminescence quenching". *Journal of Applied Physics* 105.5 (2009). DOI: 10.1063/1.3079797 (see p. 15).

[224] K. a. Sierros, N. J. Morris, K. Ramji, and D. R. Cairns. "Stress–Corrosion Cracking of Indium Tin Oxide Coated Polyethylene Terephthalate for Flexible Optoelectronic Devices". *Thin Solid Films* 517.8 (Feb. 2009). DOI: 10.1016/j.tsf.2008.10.031 (see pp. 43, 44).

[225] K. Vandewal, K. Tvingstedt, A. Gadisa, O. Inganäs, and J. V. Manca. "On the origin of the open-circuit voltage of polymer–fullerene solar cells". *Nature Materials* 8.11 (2009). DOI: 10.1038/nmat2548 (see p. 21).

[226] B. Walker, A. B. Tamayo, X.-D. Dang, P. Zalar, J. H. Seo, A. Garcia, M. Tantiwiwat, and T.-Q. Nguyen. "Nanoscale Phase Separation and High Photovoltaic Efficiency in Solution-Processed, Small-Molecule Bulk Heterojunction Solar Cells". *Advanced Functional Materials* 19.19 (Oct. 2009). DOI: 10.1002/adfm.200900832 (see p. 20).

[227] G. Zhang, W. Li, B. Chu, L. Chen, F. Yan, J. Zhu, Y. Chen, and C. S. Lee. "Cascade-energy-level alignment based organic photovoltaic cells by utilizing copper phthalocyanine as bipolar carrier transporting layer". *Applied Physics Letters* 94.14 (2009). DOI: 10.1063/1.3114379 (see p. 29).

[228] M. Campoy-Quiles, T. Ferenczi, T. Agostinelli, P. G. Etchegoin, Y. Kim, T. D. Anthopoulos, P. N. Stavrinou, D. D. C. Bradley, and J. Nelson. "Morphology evolution via self-organization and lateral and vertical diffusion in polymer:fullerene solar cell blends." *Nature materials* 7.2 (Feb. 2008). DOI: 10.1038/nmat2102 (see p. 30).

[229] C. Falkenberg, C. Uhrich, B. Maennig, M. K. Riede, and K. Leo. "1,4,5,8-naphthalene tetracarboxylic dianhydride as transparent electron transport material in organic p-i-n solar cells - art. no. 69990S". *Organic Optoelectronics and Photonics Iii* 6999 (2008). DOI: 10.1117/12.782340 (see p. 106).

[230] C. Falkenberg, C. Uhrich, S. Olthof, B. Maennig, M. K. Riede, and K. Leo. "Efficient p-i-n type organic solar cells incorporating 1,4,5,8- naphthalenetetracarboxylic dianhydride as transparent electron transport material". *Journal of Applied Physics* 104.3 (2008). DOI: 10.1063/1.2963992 (see p. 106).

[231] S. K. Hau, H.-L. Yip, N. S. Baek, J. Zou, K. O'Malley, and A. K.-Y. Jen. "Air-stable inverted flexible polymer solar cells using zinc oxide nanoparticles as an electron selective layer". *Applied Physics Letters* 92.25 (2008). DOI: 10.1063/1.2945281 (see pp. 106, 114).

[232] M. Joergensen, K. Norrman, and F. C. Krebs. "Stability/degradation of polymer solar cells". *Solar Energy Materials and Solar Cells* 92.7 (2008). DOI: 10.1016/j.solmat.2008.01.005 (see pp. 17, 32, 33, 45).

[233] M.-G. Kang, M.-S. Kim, J. Kim, and L. J. Guo. "Organic Solar Cells Using Nanoimprinted Transparent Metal Electrodes". *Advanced Materials* 20.23 (Dec. 2008). DOI: 10.1002/adma.200800750 (see pp. 46, 47).

[234] J.-Y. Lee, S. T. Connor, Y. Cui, and P. Peumans. "Solution-processed metal nanowire mesh transparent electrodes." *Nano letters* 8.2 (Feb. 2008). DOI: 10.1021/nl073296g (see pp. 48, 49, 57, 91).

[235] E. F. Aziz, A. Vollmer, S. Eisebitt, W. Eberhardt, P. Pingel, D. Neher, and N. Koch. "Localized charge transfer in a molecularly doped conducting polymer". *Advanced Materials* 19.20 (2007). DOI: 10.1002/adma.200700926 (see p. 14).

[236] a. K. Geim and K. S. Novoselov. "The rise of graphene". *Nature Materials* 6.3 (Mar. 2007). DOI: 10.1038/nmat1849 (see p. 45).

[237] C. Lungenschmied, G. Dennler, H. Neugebauer, S. N. Sariciftci, M. Glatthaar, T. Meyer, and A. Meyer. "Flexible, long-lived, large-area, organic solar cells". *Solar Energy Materials and Solar Cells* 91.5 (2007). DOI: 10.1016/j.solmat.2006.10.013 (see p. 39).

[238] H. Pang, Y. Yuan, Y. Zhou, J. Lian, L. Cao, J. Zhang, and X. Zhou. “ZnS/Ag/ZnS coating as transparent anode for organic light emitting diodes”. *Journal of Luminescence* 122-123 (Jan. 2007). DOI: `10.1016/j.jlumin.2006.01.232` (see p. 43).

[239] M. Schwoerer and H. C. Wolf. *Organic Molecular Solids.* Weinheim: Wiley-VCH Verlag, 2007 (see pp. 7, 10, 11, 15).

[240] K. Walzer, B. Maennig, M. Pfeiffer, and K. Leo. “Highly efficient organic devices based on electrically doped transport layers.” *Chemical reviews* 107.4 (Apr. 2007). DOI: `10.1021/cr050156n` (see p. 19).

[241] B. Wiley, Y. Sun, and Y. Xia. “Synthesis of Silver Nanostructures with Controlled Shapes and Properties”. *Accounts of Chemical Research* 40.10 (Oct. 2007). DOI: `10.1021/ar7000974` (see p. 54).

[242] C. K. Chan, E. G. Kim, J. L. Br??das, and A. Kahn. “Molecular n-type doping of 1,4,5,8-naphthalene tetracarboxylic dianhydride by pyronin B studied using direct and inverse photoelectron spectroscopies”. *Advanced Functional Materials* 16.6 (2006). DOI: `10.1002/adfm.200500402` (see p. 107).

[243] D. Etheridge, J.-M. Barnola, V. I. Morgan, L. P. Steele, R. J. Francey, R. L. Langenfelds, M. Meure, C. Trudinger, D. Ferretti, J. B. Miller, and J. W. C. White. *Ice Core CO2 Data.* 2006. URL: `ftp://ftp.ncdc.noaa.gov/pub/data/paleo/icecore/antarctica/law/law2006.txt` (visited on 06/09/2016) (see p. 2).

[244] C. Guillén and J. Herrero. “High conductivity and transparent ZnO:Al films prepared at low temperature by DC and MF magnetron sputtering”. *Thin Solid Films* 515.2 (Oct. 2006). DOI: `10.1016/j.tsf.2005.12.227` (see p. 41).

[245] H. Haken and H. C. Wolf. *Molekülphysik und Quantentheorie.* 4th ed. Berlin, Heidelberg: Springer-Verlag, 2006 (see p. 7).

[246] K. Kawano, R. Pacios, D. Poplavskyy, J. Nelson, D. D. Bradley, and J. R. Durrant. “Degradation of organic solar cells due to air exposure”. *Solar Energy Materials and Solar Cells* 90.20 (2006). DOI: `10.1016/j.solmat.2006.06.041` (see pp. 82, 144).

[247] E. Langereis, M. Creatore, S. B. S. Heil, M. C. M. van de Sanden, and W. M. M. Kessels. “Plasma-Assisted Atomic Layer Deposition of Al2O3 Moisture Permeation Barriers on Polymers”. *Applied Physics Letters* 89.8 (2006). DOI: `10.1063/1.2338776` (see p. 35).

[248] R. Pudzich, T. Fuhrmann-Lieker, and J. Salbeck. “Spiro compounds for organic electroluminescence and related applications”. *Advances in Polymer Science* 199.March (2006). DOI: `10.1007/12{\_}074` (see p. 101).

[249] D. R. Sahu, S.-Y. Lin, and J.-L. Huang. “ZnO/Ag/ZnO Multilayer Films for the Application of a Very Low Resistance Transparent Electrode”. *Applied Surface Science* 252.20 (2006). DOI: `http://dx.doi.org/10.1016/j.apsusc.2005.09.021` (see pp. 43, 44).

[250] T. P. I. Saragi, T. Fuhrmann-Lieker, and J. Salbeck. “Comparison of charge-carrier transport in thin films of spiro-linked compounds and their corresponding parent compounds”. *Advanced Functional Materials* 16.7 (2006). DOI: `10.1002/adfm.200500361` (see pp. 83, 101).

[251] M. C. Scharber, D. Mühlbacher, M. Koppe, P. Denk, C. Waldauf, A. J. Heeger, and C. J. Brabec. “Design rules for donors in bulk-heterojunction solar cells - Towards 10 % energy-conversion efficiency”. *Advanced Materials* 18.6 (2006). DOI: `10.1002/adma.200501717` (see p. 21).

[252] L. Schmidt-Mende and M. Grätzel. “TiO2 pore-filling and its effect on the efficiency of solid-state dye-sensitized solar cells”. *Thin Solid Films* 500.1-2 (Apr. 2006). DOI: `10.1016/j.tsf.2005.11.020` (see p. 28).

[253] Q. L. Song, M. L. Wang, E. G. Obbard, X. Y. Sun, X. M. Ding, X. Y. Hou, and C. M. Li. “Degradation of small-molecule organic solar cells”. *Applied Physics Letters* 89.25 (2006). DOI: `10.1063/1.2422911` (see p. 135).

[254] W. Brütting. *Physics of Organic Semiconductors.* Weinheim: Wiley-VCH Verlag, 2005 (see p. 7).

[255] W. Demtröder. *Molecular Physics.* Weinheim: Wiley-VCH Verlag, 2005 (see p. 9).

[256] T. Erb, U. Zhokhavets, G. Gobsch, S. Raleva, B. Stühn, P. Schilinsky, C. Waldauf, and C. J. Brabec. “Correlation Between Structural and Optical Properties of Composite Polymer/Fullerene Films for Organic Solar Cells”. *Advanced Functional Materials* 15.7 (July 2005). DOI: `10.1002/adfm.200400521` (see p. 89).

[257] T. Minami. “Transparent conducting oxide semiconductors for transparent electrodes”. *Semiconductor Science and Technology* 20.4 (Apr. 2005). DOI: `10.1088/0268-1242/20/4/004` (see p. 42).

[258] T. Minami. “Transparent conducting oxide semiconductors for transparent electrodes”. *Semiconductor Science and Technology* 20.4 (2005). DOI: `10.1088/0268-1242/20/4/004` (see p. 43).

[259] A. D. Pasquier, H. E. Unalan, A. Kanwal, S. Miller, and M. Chhowalla. “Conducting and transparent single-wall carbon nanotube electrodes for polymer-fullerene solar cells”. *Applied Physics Letters* 87.20 (2005). DOI: `10.1063/1.2132065` (see p. 48).

[260] B. Wiley, Y. Sun, B. Mayers, and Y. Xia. “Shape-Controlled Synthesis of Metal Nanostructures: The Case of Silver”. *Chemistry - A European Journal* 11.2 (Jan. 2005). DOI: `10.1002/chem.200400927` (see pp. 53, 54).

[261] Y. Ai, Y. Liu, T. Cui, and K. Varahramyan. “Thin film deposition of an n-type organic semiconductor by ink-jet printing technique”. *Thin Solid Films* 450.2 (Mar. 2004). DOI: `10.1016/j.tsf.2003.11.187` (see p. 107).

[262] J. S. Lewis and M. S. Weaver. “Thin-Film Permeation-Barrier Technology for Flexible Organic Light-Emitting Devices”. *IEEE Journal on Selected Topics in Quantum Electronics* 10.1 (2004). DOI: `10.1109/JSTQE.2004.824072` (see p. 35).

[263] M. M. Ling and Z. Bao. “Thin film deposition, patterning, and printing in organic thin film transistors”. *Chemistry of Materials* 16.23 (2004). DOI: `10.1021/cm0496117` (see p. 23).

[264] B. Maennig, D. Gebeyehu, P. Simon, F. Kozlowski, a. Werner, F. Li, S. Grundmann, S. Sonntag, M. Koch, K. Leo, M. Pfeiffer, H. Hoppe, D. Meissner, N. Sariciftci, I. Riedel, V. Dyakonov, J. Parisi, and J. Drechsel. “Organic p -i- n solar cells”. *Applied Physics A: Materials Science & Processing* 79.1 (June 2004). DOI: `10.1007/s00339-003-2494-9` (see p. 19).

[265] R. B. Pode, C. J. Lee, D. G. Moon, and J. I. Han. “Transparent conducting metal electrode for top emission organic light-emitting devices: Ca-Ag double layer”. *Applied Physics Letters* 84.23 (2004). DOI: `10.1063/1.1756674` (see p. 43).

[266] F. Yang, M. Shtein, and S. R. Forrest. “Controlled growth of a molecular bulk heterojunction photovoltaic cell”. *Nature Materials* 4.1 (2004). DOI: `10.1038/nmat1285` (see p. 82).

[267] N. Karl. “Charge carrier transport in organic semiconductors”. *Synthetic Metals* 133-134 (Mar. 2003). DOI: `10.1016/S0379-6779(02)00398-3` (see p. 11).

[268] D. Natelson. “Fabrication of metal nanowires”. *arXiv preprint cond-mat/0307600* (2003) (see p. 53).

[269] P. Peumans, S. Uchida, and S. R. Forrest. “Efficient bulk heterojunction photovoltaic cells using small-molecular-weight organic thin films.” *Nature* 425.September (2003). DOI: `10.1038/nature01949` (see p. 20).

[270] P. Peumans, A. Yakimov, and S. R. Forrest. “Small molecular weight organic thin-film photodetectors and solar cells”. *Journal of Applied Physics* 93.7 (2003). DOI: `10.1063/1.1534621` (see p. 18).

[271] T. Spehr, R. Pudzich, T. Fuhrmann, and J. Salbeck. “Highly efficient light emitters based on the spiro concept”. *Organic Electronics* 4.2-3 (2003). DOI: `10.1016/j.orgel.2003.08.002` (see p. 101).

[272] Y. Sun, B. Mayers, T. Herricks, and Y. Xia. “Polyol Synthesis of Uniform Silver Nanowires: A Plausible Growth Mechanism and the Supporting Evidence”. *Nano Letters* 3.7 (July 2003). DOI: `10.1021/nl034312m` (see p. 54).

[273] A. Werner. “N-type doping of organic thin films using a novel class of dopants”. Dissertation. Werner2003: TU Dresden, 2003 (see p. 14).

[274] M. Zhu, G. Liang, T. Cui, and K. Varahramyan. “Depletion-mode n-channel organic field-effect transistors based on NTCDA”. In: *Solid-State Electronics*. Vol. 47. 10. 2003, pp. 1855–1858. DOI: `10.1016/S0038-1101(03)00141-2` (see p. 106).

[275] M. Dressel and G. Gruener. *Electrodynamics of Solids: Optical Properties of Electrons in Matter*. Cambridge: Cambridge Univ Press, 2002 (see p. 40).

[276] Y. Sun, Y. Yin, B. T. Mayers, T. Herricks, and Y. Xia. “Uniform silver nanowires synthesis by reducing AgNO3 with ethylene glycol in the presence of seeds and poly(vinyl pyrrolidone)”. *Chemistry of Materials* 14.11 (2002). DOI: `10.1021/cm020587b` (see pp. 53, 56).

[277] M. S. Weaver, L. A. Michalski, K. Rajan, M. A. Rothman, J. A. Silvernail, J. J. Brown, P. E. Burrows, G. L. Graff, M. E. Gross, P. M. Martin, M. Hall, E. Mast, C. Bonham, W. Bennett, and M. Zumhoff. “Organic light-emitting devices with extended operating lifetimes on plastic substrates”. *Applied Physics Letters* 81.16 (2002). DOI: `10.1063/1.1514831` (see p. 35).

[278] M. Grätzel. “Photoelectrochemical cells”. *Nature* 414.6861 (Nov. 2001). DOI: `10.1038/35104607` (see p. 28).

[279] T. Stübinger and W. Brütting. “Exciton diffusion and optical interference in organic donor-acceptor photovoltaic cells”. *Journal of Applied Physics* 90.7 (2001). DOI: `10.1063/1.1394920` (see p. 16).

[280] L. Torsi, A. Dodabalapur, N. Cioffi, L. Sabbatini, and P. G. Zambonin. “NTCDA organic thin-film-transistor as humidity sensor: Weaknesses and strengths”. *Sensors and Actuators, B: Chemical* 77.1-2 (2001). DOI: `10.1016/S0925-4005(01)00664-5` (see p. 106).

[281] U. Bach, K. De Cloedt, H. Spreitzer, and M. Grätzel. “Characterization of Hole Transport in a New Class of Spiro linked obligotriphenylamine compunds”. *Advanced Materials* 12.14 (2000). DOI: `10.1002/1521-4095(200007)12:14<1060::AID-ADMA1060>3.0.CO;2-R` (see pp. 83, 101).

[282] M. P. de Jong, L. J. van IJzendoorn, and M. J. a. de Voigt. “Stability of the interface between indium tin oxide and polyethylenedioxythiophene / polystyrenesulfonate in polymer light-emitting diodes”. *Applied Physics Letters* 77.14 (2000). DOI: `10.1063/1.1315344` (see pp. 82, 144).

[283] a. Nollau, M. Pfeiffer, T. Fritz, and K. Leo. “Controlled n-type doping of a molecular organic semiconductor: Naphthalenetetracarboxylic dianhydride (NTCDA) doped with bis(ethylenedithio)-tetrathiafulvalene (BEDT-TTF)”. *Journal of Applied Physics* 87.9 (2000). DOI: `10.1063/1.373413` (see p. 106).

[284] P. Würfel. *Physik der Solarzellen*. 2nd ed. Heidelberg, Berlin: Spektrum Akademischer Verlag, 2000 (see p. 17).

[285] Frank Weissörtel. “Synthese und Charakterisierung spiroverknüpfter niedermolekularer Gläser für optoelektronische Anwendungen”. Dissertation. Universität Regensburg, 1999, p. 152 (see p. 101).

[286] H. Kim, C. M. Gilmore, A. Piqué, J. S. Horwitz, H. Mattoussi, H. Murata, Z. H. Kafafi, and D. B. Chrisey. “Electrical, optical, and structural properties of indium–tin–oxide thin films for organic light-emitting devices”. *Journal of Applied Physics* 86.11 (1999). DOI: `10.1063/1.371708` (see p. 43).

[287] D. G. Vanderlaan, I. M. Nunez, M. Hargiss, M. L. Alton, and S. Williams. *Soft contact lenses*. 1999 (see p. 114).

[288] J. P. Chang. “Kinetic study of low energy argon ion-enhanced plasma etching of polysilicon with atomic/molecular chlorine”. *Journal of Vacuum Science & Technology A: Vacuum, Surfaces, and Films* 15.4 (1997). DOI: `10.1116/1.580652` (see p. 123).

[289] S. R. Forrest. “Ultrathin Organic Films Grown by Organic Molecular Beam Deposition and Related Techniques.” *Chemical Reviews* 97.6 (1997). DOI: `10.1021/cr941014o` (see p. 23).

[290] J. Salbeck and F. Weissörtel. “Spiro linked compounds for use as active materials in organic light emitting diodes”. *Macromolecular Symposia* 125 (1997) (see p. 101).

[291] J. G. Laquindanum, H. E. Katz, A. Dodabalapur, and A. J. Lovinger. “n-Channel organic transistor materials based on naphthalene frameworks”. *Journal of the American Chemical Society* 118.45 (1996). DOI: `10.1021/ja962461j` (see p. 107).

[292] D. Stauffer and A. Aharony. *Introduction to Percolation Theory*. 2nd. Weinheim: Wiley-VCH Verlag, 1995 (see p. 49).

[293] M. Nishikawa, Y. Yokoyama, N. Bessho, D.-S. Seo, Y. Iimura, and S. Kobayashi. “Synthesis of a Novel Organic-Solvent-Soluble Polyimide and Its Application to Alignment Film for Liquid Crystal Displays”. *Japanese Journal of Applied Physics* 33.Part 2, No. 6A (1994). DOI: `10.1143/JJAP.33.L810` (see p. 117).

[294] J. S. Ishay, T. Benshalom-Shimony, A. Ben-Shalom, and N. Kristianpoller. “Photovoltaic effects in the Oriental hornet, Vespa orientalis”. *Journal of Insect Physiology* 38.1 (1992). DOI: `10.1016/0022-1910(92)90020-E` (see p. 2).

[295] C. W. Tang. "Two-layer organic photovoltaic cell". *Applied Physics Letters* 48.2 (1986). DOI: 10.1063/1.96937 (see p. 16).

[296] C. M. Lampert. "Heat mirror coatings for energy conserving windows". *Solar Energy Materials* 6.1 (1981). DOI: 10.1016/0165-1633(81)90047-2 (see p. 43).

[297] K. Rajkanan and R. Singh. "Absorption coefficient of silicon for solar cell calculations". *Solid-State Electronics* 22 (1979) (see p. 16).

[298] D. Meyerhofer. "Characteristics of resist films produced by spinning". *Journal of Applied Physics* 49.7 (1978). DOI: 10.1063/1.325357 (see p. 25).

[299] G. Haacke. "New figure of merit for transparent conductors". *Journal of Applied Physics* 47.9 (1976). DOI: 10.1063/1.323240 (see p. 40).

[300] G. E. Pike and C. H. Seager. "Percolation and conductivity: A computer study". *Physical Review B* 10.4 (Aug. 1974). DOI: 10.1103/PhysRevB.10.1421 (see p. 51).

[301] S. Kirkpatrick. "Percolation and Conduction". *Reviews of Modern Physics* 45.4 (1973). DOI: 10.1103/RevModPhys.45.574 (see p. 51).

[302] P. Delvigs, T. T. Serafini, and G. R. Lightsey. "Addition-type polyimides from solutions of monomeric reactants." *Journal of Applied Polymer Science* 16 (1972). DOI: 10.1002/app.1972.070160409 (see p. 114).

[303] D. Fraser and H. Cook. "Highly Conductive, Transparent Films of Sputtered InSnO". *Journal of the Electrochemical Society* May 2012 (1972) (see pp. 41, 43).

[304] A. F. Mayadas and M. Shatzkes. "Electrical-Resistivity Model for Polycrystalline Films: the Case of Arbitrary Reflection at External Surfaces". *Physical Review B* 1.4 (Feb. 1970). DOI: 10.1103/PhysRevB.1.1382 (see p. 43).

[305] A. Cottey. "The electrical conductivity of thin metal films with very smooth surfaces". *Thin Solid Films* 1.4 (Jan. 1968). DOI: 10.1016/0040-6090(68)90047-3 (see p. 43).

[306] S. R. Broadbent and J. M. Hammersley. "Percolation processes". *Mathematical Proceedings of the Cambridge Philosophical Society* 53.03 (July 1957). DOI: 10.1017/S0305004100032680 (see p. 49).

[307] R. E. Glover and M. Tinkham. "Conductivity of superconducting films for photon energies between 0.3 and 40kTc". *Physical Review* 108.2 (1957). DOI: 10.1103/PhysRev.108.243 (see p. 40).

[308] R. G. Chambers. "The Conductivity of Thin Wires in a Magnetic Field". *Proceedings of the Royal Society A: Mathematical, Physical and Engineering Sciences* 202.1070 (Aug. 1950). DOI: 10.1098/rspa.1950.0107 (see p. 56).

[309] R. B. Dingle. “The Electrical Conductivity of Thin Wires”. *Proceedings of the Royal Society A: Mathematical, Physical and Engineering Sciences* 201.1067 (May 1950). DOI: `10.1098/rspa.1950.0077` (see p. 56).

[310] R. S. Sennett and G. D. Scott. “The Structure of Evaporated Metal Films and Their Optical Properties”. *Journal of the Optical Society of America* 40.4 (Apr. 1950). DOI: `10.1364/JOSA.40.000203` (see p. 44).

[311] T. Foerster. “Energiewanderung und Fluoreszenz”. *Die Naturwissenschaften* 33.6 (1946). DOI: `10.1007/BF00585226` (see p. 15).

[312] K. Bädeker. “Über die elektrische Leitfähigkeit und die thermoelektrische Kraft einiger Schwermetallverbindungen”. *Annalen der Physik* 327.4 (1907). DOI: `10.1002/andp.19073270409` (see p. 37).

Danksagung/Acknowledgment

Es ist nachts halb eins. Übermorgen möchte ich die Arbeit abgeben und ich befinde mich inmitten der letzten Korrekturrunde. Eigentlich ein guter Zeitpunkt, um die ganze Sache etwas Revue passieren zu lassen. Hinter mir liegen fünf Jahre am IAPP, davon ziemlich genau dreieinhalb im Rahmen der Promotion. Ein halbes Jahr davon habe ich an der King Abdullah Uni in Saudi-Arabien verbracht während eines Forschungsaufenthalts. Das letzte halbe Jahr war hauptsächlich Schreibarbeit, was mal gut von der Hand ging, mal sehr zäh voranschritt. Aber schlussendlich habe ich es geschafft und muss an dieser Stelle sagen: ich hab es auch und gerade wegen Ihrer/eurer Hilfe geschafft! Auf das 'Ihr/euch' möchte ich jetzt etwas näher eingehen.

Den ersten Dank muss ich aufteilen: Einerseits habe ich Professor Karl Leo unglaublich viel zu verdanken. Nicht nur, dass er mein Doktorvater und Erstgutachter ist, der mir mit vielen hilfreichen Tipps und Tricks und mit seiner fairen und aufrichtigen Art viel weitergeholfen hat. Er hat es mir auch ermöglicht, ein halbes Jahr in Saudi-Arabien zu forschen und zu leben – auch dafür bedanke ich mich herzlich, denn es hat mich ungemein bereichert. Prof. Leo ist auch der Kopf des Instituts und hat in den letzten paarundzwanzig Jahren das IAPP zu dem gemacht was es ist. Andererseits möchte ich dem IAPP als solches großen Respekt zollen! Solch eine wunderbare Arbeitsatmosphäre, die so familiär und gleichzeitig so professionell wie möglich ist, war ein ganz großer Glücksgriff. Was genau den Charme ausmacht, weiß ich nicht, aber Hartmut Fröb, die Weihnachtsfeier, die Organic Days, der Kicker und das Klavier im Atelier, und das altehrwürdige Gebäude tragen sicher einiges dazu bei. Ich weiß, dass das alles den Umzug ins neue Gebäude überleben wird.
Dann danke ich Professor Frank Nüesch sehr für die freundliche Übernahme das Zweitgutachtens und die hervorragende Leitung des EU Projekts "Treasores", über welches ich finanziert wurde.
Dr. Lars Müller-Meskamp danke ich für die langjährige Begleitung und Betreuung vom kleinen SHK-Studenten, der noch ziemlich grün hinter den Ohren ist bis zum PhD Studenten in großen Teilen der Promotionszeit. Immer voller Ideen und Hingabe für die Sache und ein prima EnE-Arbeitsgruppenleiter. Der gesamten EnE-Arbeitsgruppe – aus welcher inzwischen die OrBas Gruppe hervorgegangen ist – danke ich für die exzellente Zusammenarbeit und auch für das gute soziale Gefüge. Dass immernoch ehemalige Mitglieder zu den EnE-Grill-und-Biertrink-Events kommen, spricht für sich.
Im Rahmen der EnE-Gruppe danke ich folgenden Leuten: Dr. Christoph Sachse als direkter Betreuer der Diplomarbeit, Mitglied der 12:30 Essensgruppe, Anhänger der Slow-Eat-Bewegung :) und immer für einen Plausch fernab der Physik zu haben.
Franz, der auch mehr ist als nur ein Kollege. Gemeinsam durch die Untiefen der Nanodrähte geschlängelt, hat die Arbeit und alles darüberhinaus mit dir viel Spaß gemacht. Danke! Fredi als wahnsinnig kompetenter Barrierenfachmann, der krass kickert, die besten Vorträge hält wie ich finde, der immer einen schlauen Rat auf den Lippen hat,

und der eine tolle Brettspielsammlung hat und zur Anwendung bringt :). BAHOTH! Danke dass es euch gibt!
Dank geht raus an Jakob und Matthias, meine beiden Masterstudenten. Durch die Betreuung von euch hab ich echt viel gelernt (ich hoffe, ihr auch ;)). Schade, dass ihr so schnell wieder weg wart und abseits der Uni euren Platz im jungen Arbeitsleben gefunden habt. Ich danke Luisa, Nelli, Yoonseok, Dhriti, Felix D. und Fan-Yu für die überaus angenehme Zusammenarbeit.
Danke an Janine, Natalia, Chris und Markus für eine tolle gemeinsame Büro-126-Zeit mit lecker Kuchen und Kaffe immer dann wenn der Bombenalarm losging (natürlich nur zu Testzwecken). Ich danke auch Prof. Torsten Fritz für die Installation der Klimaanlage, die uns im Sommer regelmäßig einen kühlen Kopf bewahren lässt.
Danke an den IAPP-Chor und den (ehemaligen) Leiter und die beiden Halbleiter (Haha) Andreas und Christian. Auch das war eine gute wöchentliche Abwechslung vom harten Forschungsdasein :).
Weiterer Dank geht raus an die vielen Leute, die das Leben und Arbeiten am IAPP so super gemacht haben: Martin S., Felix H. (auch fürs Korrekturlesen), David, Bernhard und Bernhard, Paul, Max, Axel (insbesondere fürs Flanken üben;), Andreas M., Böhmi, Ji-Ling, Marco, Toni, Vasilis, Donato, Koen und Irma (auch wenn du aus Jena kommst - da kann ich drüberhinwegsehen ;).
Dann – nicht zu unterschätzen – bin ich der IT bestehend aus Kai und Peter zu Dank verpflichtet - egal, ob Drucker, Computer, Mail, Netzwerkkrams, oder oder oder: Da wird man geholfen!
Danke an Johanna, Carla, Angelika und Annette für das Weiterhelfen bei sämtlichen bürokratischen Hürden, egal ob Dienstreiseabrechnung, Bestellverwirrungen oder anderen Dingen.

Einen eigenen kleinen Absatz bekommen die Techniker: Cheftechniker SVEN KUNZE und sein Fachadjutant Andreas – ohne die geht nix! Also ich meine gar nix. Wer macht das UFO ganz, wenn wieder jemand seine Sampleholder in den Handler fallen läst oder die Metallboote schrottet? Sven und Andreas. Wer lötet und bastelt die ganzen selbstgebauten Elektronikschnittstellen für die ganzen Messapparaturen? Sven und Andreas. Wer ist immer für ein kühles Pils zu haben? Sven und Andreas (und noch ein paar mehr ;). Wenn man sich lebensbejahende Sprüche anhören möchte, geht man zu wem? Sven und Andreas. Das lässt sich noch beliebig fortsetzen, aber es muss ja auch noch Platz für andere Menschen geben.
Auch das Lesker-Team um Tobias Günther, Andreas Wendel und Caroline Walde ist so unersetzlich, dass man es kaum in Worte fassen kann. Danke! In diesem Sinne auch Annette Petrich und Tina Träger für die Bereitstellung und Reinigung verschiedenster organischer Materialien.

Da ich in Saudi-Arabien auch viele tolle Menschen kennengelernt hab, muss ich an dieser Stelle auch ein großes "Shukran" dorthin schicken. Danke an Mohammed "Fifi" Alfaifi fürs Organisieren und Kümmern und Beantworten jeder Frage und Schwierigkeit, die manche Dinge an der KAUST so mitsichbringen. Danke an Professor Aram Amassian für die Aufnahme in seiner Gruppe. Danke an Max Babsy, Marios und MaxL Tietze für die gute gemeinsame Zeit im Labor und an den Abenden und in der Freizeit. *Hugs& Kisses* Und natürlich riesigen Dank an meine Band "Grape Apes", mit der es außerordentlich spaßig war, Musik zu machen. So viele Kulturen (Libanon, USA, Jordanien, Pakistan, Italien, Deutschland) die da aufeinandertrafen und es hat einfach super gefunzt: Danke, Nadia , Cacia, Ahmed, Moustapha, Zain, und Steve.

Auch außeruniversitär (man denkt es kaum ;) gibt es Leute, die mir wichtig sind hier zu lobpreisen. Ganz vorne natürlich die tollste Patchworkfamilie, die ich mir vorstellen kann. Dann bin ich dankbar, ein Teil dieses Erfuter Freundeskreis zu sein, der doch über die Jahre und über die verschiedenen Kontinente hinweg Bestand hat und sicher noch lange haben wird. Riesen Danke an die Stjärnevik Crew, voll super dass wir das gemacht haben. Danke an Körbi als entspanntester WG-Mitbewohner ever. Danke an das Oscar-Projekt-Trio (OPT), also an Ossi und Felix, dass wir schon so lange Musik zusammen machen und es viel Spaß macht. VOLL SCHÖN!
Und - last but not least - danke Tania 🌠, dass es dich gibt und du mich ziemlich genau seit Promotionsbeginn begleitest und für mich da warst und bist und wir hoffentlich noch lange eine wunderbare gemeinsame Zeit haben werden! Es ist schön mit dir! :)

Wer's bis hierhin geschafft hat: Danke, werter Leser, wer auch immer du bist.

Ende und out,

Ludi

Erklärung

Diese Dissertation wurde am Institut für Angewandte Physik/Photophysik – inzwischen Dresden Integrated Center for Applied Physics and Photonic Materials – der Fakultät Mathematik und Naturwissenschaften an der Technischen Universität Dresden unter wissenschaftlicher Betreuung von Prof. Dr. Karl Leo angefertigt.

Hiermit versichere ich, dass ich die vorliegende Arbeit ohne unzulässige Hilfe Dritter und ohne Benutzung anderer als der angegebenen Hilfsmittel angefertigt habe. Die aus fremden Quellen direkt oder indirekt übernommenen Gedanken sind als solche kenntlich gemacht. Die Arbeit wurde bisher weder im Inland noch im Ausland in gleicher oder ähnlicher Form einer anderen Prüfungsbehörde vorgelegt.

Weiterhin versichere ich, dass weder ein früheres erfolgloses Promotionsverfahren stattgefunden hat noch ein weiteres Promotionsverfahren anhängig ist. Ich erkenne die Promotionsordnung der Fakultät Mathematik und Naturwissenschaften der Technischen Universität Dresden vom 23.02.2011 in der aktuellen Fassung mit den durch den Fakultätsrat beschlossenen Änderungen vom 15.06.2011 und 18.06.2014 an.

Dresden, den 13. Juli 2016

Jan Ludwig Bormann